Computational Investigation of the Photochemistry and Spectroscopy of Cyclic Aromatic Hydrocarbons in Interstellar Ice Analogs

Divya Sharma

Submitted for the degree of Doctor of Philosophy (Chemistry)

Heriot-Watt University
Institute of Chemical Sciences
School of Engineering and Physical Sciences

May 2015

Abstract

This thesis describes the photochemistry and ultraviolet (UV) spectroscopy of cyclic aromatic hydrocarbons such as benzene and naphthalene, along with small water clusters and crystalline water ice clusters. Firstly, benzene and naphthalene interactions with small water hexamer (W_6) clusters, and then benzene interactions with crystalline water ice clusters are investigated. This thesis primarily focuses on the applications of a range of computational chemistry techniques to investigate and characterize excited states of these complex systems, which are generated following one-photon absorption. Benzene and naphthalene, as prototypical polycyclic aromatic hydrocarbons (PAHs), and water and crystalline ice clusters, taken as representative of interstellar ices, could also be considered as useful model systems to replicate polycyclic aromatic hydrocarbons (PAHs) in interstellar ices, and to study their behaviour under UV processing.

From coupled cluster (CC) benchmark studies on small water clusters up to water the pentamer, it is shown that that highly correlated linear-response coupled cluster methods such as CCSD and CC3 are important to consider while studying electronic excitations, as electron correlation effects play an important role in such systems, with double excitations playing a dominant role. However, triple excitations contributions calculated are negligible with CCSD and CC3 methods converging monotonically to similar results. The aggregation effect on water at CCSD level has shown a blue shift of ~ 0.7 eV in the central water molecule of water pentamer (C_{2v}) relative to water monomer (C_{2v}), and is in good agreement with the experimental blue shift of ~ 1 eV in condensed phase.

For both benzene- and naphthalene-bound water W_6 clusters, we have calculated interesting features of benzene- and naphthalene-mediated electronic excitations of the water W_6 cluster at wavelengths where photon absorption cross section of water is negligible i.e., above 170 nm. These excitations were originally absent in the isolated water W_6 cluster. Similar features are calculated for benzene-bound crystalline ice clusters, which also illustrate the effect of cyclic aromatic hydrocarbons on electronic excitations of ice clusters, and are also observed experimentally. The brightest $\pi \rightarrow \pi^*$ electronic transition of benzene and naphthalene is calculated to be red-shifted in wavelength and occurs with lower intensities after interacting with the water W_6 and ice clusters. The degeneracy of this transition is also slightly broken in benzene. We have

observed new electronic transition features such as charge transfer (CT), and locally diffuse Rydberg type excitation in these complexes. We have found a good performance of hybrid DFT functionals i.e. M06-2X and CAM-B3LYP in calculating vertical excitation energies of these complexes using time dependent density functional theory (TD-DFT).

Further, diffusion studies of the deuterium (D) atom have shown the importance of surface morphology in generating different potential sites and hopping characteristics of the D atom on crystalline and amorphous ice surfaces. D_2 formation is found to be efficient on the amorphous ice surface, with longer residence times of the D atom indicating a possibility of the deuterium atom getting trapped in such sites. There is then a further possibility of the diffusing D atom to recombine with the trapped D atom to form a D_2 molecule. However, such D atom trapping is a rare possibility on crystalline surface, as hopping is fast and thus the recombination process is not efficient on crystalline ice surface.

This thesis is dedicated to my beloved mother for her love and endless support from the Heaven.

Acknowledgements

The work presented in this thesis would not have been possible without the help and support of many people. First, and foremost, I am extremely thankful to my supervisor Prof. Martin Paterson for all his guidance and wise counseling throughout my research work. His seemingly endless list of suggestions and ideas, along with his down to Earth approach are very much appreciated. I sincerely thank Prof. Martin McCoustra for his help and ideas.

I also acknowledge the LASSIE FP7 Marie Curie Initial Training Network (ITN) and ERC for providing me funding to pursue the research presented in this thesis. I also thank all my colleagues and friends: Justyna, Therese, Russell, Peter, Nuno, Paul, Jeremy, Freda, Bethmini, Sameera, Gunnar, and Demian in the Heriot Watt University and LASSIE network for their support and useful discussions. I thank Russell, Tina, Paul, Freda, and Jeremy for proofreading my thesis.

Above all, my special thanks goes to my father, brother, sister, family and friends for their encouragement, love, and moral support which have made this work possible. They are equally entitled to share the honors of this work.

At last, but not least, I wish to express my gratitude to almighty for giving me strength, ability and good health that were necessary to complete this thesis.

List of Publications

[1] D. Sharma and M. J. Paterson, *The Structure and UV Spectroscopy of Benzene-Water (Bz-W_6) Clusters using Time-Dependent Density Functional Theory*, Photochem. Photobiol. Sci., 2014, **13**, 1549-1560.

[2] D. Sharma and M. J. Paterson, *Ground and excited states of Naphthalene-Water (Naphtha-W_6) Clusters: A Computational Study*, R. Soc. Chem. Adv., 2015, **5**, 28281-28291.

[3] D. Sharma, W. M. C. Sameera, Stefan Andersson, Gunnar Nyman, and Martin J. Paterson, *Computational study of the interactions between benzene and crystalline ice I_h: Ground and excited states*, Phys. Chem. Chem. Phys., 2015, *submitted*.

[4] D. Sharma, B. Seneviranthe, S. Andersson, G. Nyman, and M. J. Paterson*, Diffusion of deuterium atom on crystalline and amorphous ice*, 2015, *in preparation.*

[5] D. Sharma and M. J. Paterson, Excited state studies of small water clusters $(H2O)_{n=1-5}$ using Coupled cluster methods, 2015, *in preparation.*

Table of Contents

Chapter 1 - Introduction

1.1 Introduction

Photochemistry is the branch of chemistry that is concerned with the study of chemical reactions, isomerization and change in physical behaviour that may occur under the influence of light. Photochemical paths allow chemical reactions, which are inaccessible thermally, by overcoming large activation barriers in a short period of time. The absorption of light generally leads to the molecule in the excited state from where it can then de-excite to the ground state through different photo-physical radiative and non-radiative decay pathways. The light absorption by a molecular system can be measured via spectroscopic techniques such as absorption spectroscopy where absorption of light photons due to its interaction with a system is measured as a function of wavelength or frequency [1, 2]. The electronic and molecular structure of the system primarily determines the frequencies at which absorption lines occur in the spectrum, as well as their relative intensities [2].

In general, absorption lines are classified as rotational, or vibrational, or electronic depending on the nature of the quantum mechanical change induced in the molecule [1]. In the microwave spectral region, rotational lines occur due to change in the rotational state of a molecule. Vibrational lines occur when the vibrational state of a molecule is changed, whereas electronic lines are caused due to change in the electronic state of a molecule. Vibrational lines are typically found in the infrared (IR) region, whereas electronic lines are typically found in the visible (Vis) and ultraviolet (UV) region. The frequency of the absorption line is determined primarily by the energy associated with the quantum mechanical change. However, many factors such as external electric and magnetic fields, and interactions with neighbouring molecules can shift the frequencies. The shifts in frequencies are noticed for the gas phase molecule with respect to that in a liquid or solid phase as relatively strong interactions with neighbouring molecules are present in liquid and solid phases.

This thesis is focused on the applications of computational techniques to investigate the photochemistry and UV spectroscopy of cyclic aromatic hydrocarbons such as benzene, and naphthalene, as well as small water clusters and crystalline ice clusters. The interactions of benzene and naphthalene with small water clusters, along with

benzene interactions with crystalline ice clusters are studied computationally. However, the main focus in this thesis is to study the photochemistry and UV spectroscopy of benzene- and naphthalene-bound water clusters, and of benzene-bound crystalline ice clusters. This is also a useful model of an astrophysical relevance to replicate polycyclic aromatic hydrocarbons (PAHs) in interstellar ices, and to study their behaviour under UV processing. The diffusion of the deuterium (D) atom, a naturally occurring isotope of hydrogen, on both crystalline and amorphous ice surfaces, at the interstellar conditions, is also investigated. It is also an important model to study the role of diffusion in the formation of the D_2 molecule on interstellar ice surfaces.

Before introducing the theoretical background for the detailed description on the computational aspects involved in the work presented here, it is appropriate to introduce some simple concepts of astrochemistry that are relevant to this work.

This chapter begins with an introduction to the astrophysical background. A general overview of important astrophysical relevant concepts such as interstellar medium, interstellar dust grains and icy mantles, non-thermal processing of interstellar ices, polycyclic aromatic hydrocarbons (PAHs), the molecular family primarily studied in this thesis is presented below in Section 1.2. The relevant literature on the photo processing of laboratory models of interstellar ices is given in Section 1.3. Finally, the subsequent chapters are outlined in Section 1.4.

1.2 Astrophysical Background

Astrochemistry is a multidisciplinary field of research, bringing together the Astronomy, Astrophysics, Physics, and Chemistry fields, to explore the products, mechanisms and rates of the chemistry that dominates the Universe. It deals with the large time scale of the chemical evolution of astronomical objects, which may be thousands, or even millions of years, due to the low densities which exist in many astronomical regions [3]. It has been realized that cold dusty regions play a key role in the chemical evolution of the universe [4, 5]. Icy mantles are accreted on dust grains at low temperatures ($\leq$ 20 K) where the rich chemical complexity due to physical and chemical processes occurring at the surfaces of interstellar dust grains in such regions make them sites of star and planet formation [6].

1.2.1 The Interstellar medium (ISM)

It has been observed that vast clouds containing molecules and dust exist between the stars and the gravitational collapse of these clouds is the first step in the formation of new stars. The ISM represents the regions of space situated between stars within our galaxy containing a mixture of dust and gas, which is the reservoir of resources that forms stars and planetary systems [7]. These regions are of low densities that occupy 15 % of total mass of visible matter in our galaxy, the Milky Way. It is filled mainly with gas (99%), which is primarily composed of hydrogen (either molecular or atomic) followed by helium and trace amounts of carbon, nitrogen and oxygen, and about ~ 1% of dust grains [8, 9].

The ISM contains different environments showing large ranges in temperature (10–10^4 K) and densities (100–10^8 H atoms cm^{-3}). Different regions of the ISM can be classified depending on the density, size and temperature of a given cloud. For example in H I regions hydrogen is neutral in a cloud; in H II regions hydrogen is ionized, and in molecular clouds exists in molecular form [10]. Neutral and ionized clouds are sometimes referred as diffuse clouds, while molecular clouds are known as dense clouds. Diffuse clouds are the lowest density structures that are dominated by atomic hydrogen and typically have temperatures in the range 80-100 K.

Most of the dense clouds are held together by the increased gravitational attraction that arises as a result of their greater mass, while some are formed by the compression of diffuse clouds by shocks resulting from supernovae. The collisions between diffuse clouds may form Giant Molecular Clouds (GMCs), where dark clouds are dominated by molecular hydrogen (H_2) due to increased density. This increased molecular abundance results in a higher probability for chemical reaction and the attenuation of radiation that would lead to the photo-destruction of formed molecules. Thus temperatures become lower 10-50 K, as a result of the attenuation of radiation.

The star formation initiates when clumps within a dark cloud collapse further, which may occur due to collisions between clumps or shocks from nearby supernovae. For the formation of protostar, and small stars, a clump should collapse further by radiating some of the thermal energy out of the clump. It is suggested that molecules present in the collapsing clump could provide a mechanism for this by emitting energy through rotational, vibrational and electronic transitions [6]. This further collapse results in a hot core formation where temperature rises to around 2000 K. This temperature is high enough to cause dissociation of H_2 and may further cause ionization of H atoms as the

temperature rises. Finally, at very high temperatures around 10^6 K and sufficiently energetic conditions, nuclear fusion process can occur due to collisions between protons.

Table 1.1 List of known interstellar and circumstellar molecules as of 2012. ? indicates uncertain detection. [Source: http://science.gsfc.nasa.gov/691/cosmicice/interstellar.html]

2 atoms	3 atoms	4 atoms	5 atoms	6 atoms	7 atoms	>= 8 atoms
H_2	H_2O	NH_3	CH_4	CH_3OH	$CH_2CH(OH)$	CH_3COOH
CO	H_2S	H_2CO (?)	SiH_4	CH_3SH	c - C_2H_4O	$HC(O)OCH_3$
CSi	HCN	H_2CS	CH_2NH	C_2H_4	$HC(O)CH_3$	$HOCH_2C(O)H$
CP	HNC	C_2H_2	NH_2CN	$H(CC)_2H$	H_3C-CC-H	H_3C-CC-CN
CS	CO_2	HNCO	c - C_3H_2	CH_3CN	CH_3NH_2	H_2C_6
NO	SO_2	HNCS	l - C_3H_2	CH_3NC	$CH_2CH(CN)$	$H(CC)_3H$
NS	MgN	H_3O+	CH_2CN	$HCONH_2$	HCC-CC-CN	H_2C=CH-C(O)H
SO	MgNC	SiC_3	H_2COH^+	HCC-C(O)H	C_6H	CH_2CCHCN
HCl	NaN	C_3S	C_4Si	$HC3NH^+$	C_6H^-	C_7H
NaCl	N_2O	H_2CN	C_5	HC_4N		H_2NCH_2CN
KCl	NH_2	c - C_3H	HNCCC	C_5N		$(CH_3)_2O$
AlCl	OCS	l - C_3H	C_4H	C_5H		CH_3CH_2CN
AlF	CH_2	HCCN	C_4H^-	H_2CCCC		CH_3CH_2OH
PN	HCO	CH_3	HC(O)CN	H_2CCNH		CH_3C_4H
SiN	C_3	C_2CN	HCOOH?	C_5N^-		HCC-CC-CC-CN
SiO	C_2H	C_3O	HCC-CN	c-H_2C_3O		C_8H
SiS	C_2O	$HCNH^+$	HCC-NC			$CH_3C(O)NH_2$
NH	C_2S	$HOCO^+$				C_8H^-
OH	AlNC	C_3N^-				CH_3CHCH_2
C2	HNO	HCNO				$(CH_3)_2CO$
CN	SiN	HSCN				$HOCH_2CH_2OH$
HF	N_2H+	H_2O_2				H_3C-CH_2-C(O)H
FeO	SiNC					$CH_3(CC)_2CN$
LiH	c - SiC_2					HCC-CC-CC-CC-CN
CH	HCO^+					CH_3C_6H
CH^+	HOC^+					$HC(O)OCH_2CH_3$
CO^+	HCS^+					C_6H_6
SO^+	H_3^+					$CH_3CH_2CH_2CN$
SH	OCN^-					HCC-CC-CC-CC-CC-CN
O_2	CCP					
N_2	HCP					
CF^+						
PO						
AlO						

It is clear that interstellar molecules play an important role in astrophysical processes such as, star formation, and thus their formation and evolution has been the field of growing interest in astrochemistry. More than 140 different molecules have been identified in interstellar and circumstellar regions, most of them are organic in nature (See Table 1.1). They have been observed at wavelengths across the electromagnetic spectrum. Larger carbon-bearing species such as polycyclic aromatic hydrocarbons (PAHs) and fullerenes may also be present in interstellar gas or incorporated in dust and ice mantles [4, 11]. It is suggested that large amount of the cosmic carbon is locked in carbonaceous solids on dust grain.

1.2.2 Interstellar dust grains and Icy mantles

There is certain evidence of the presence of the interstellar dust [4, 5, 12], which accounts for 1% of total mass of the material in ISM. It is revealed from observations of gas phase species within clouds that carbon (C) and Silicon (Si) could be the main populations of dust grains, showing significant depletion of these elements, which results from them being locked up in the solid phase [13].

The physical and chemical processes occurring on these dust grain surfaces play a key role in the formation of molecular hydrogen and many other complex species. There are some species for which formation in the gas phase cannot be sufficiently efficient to account for the observed abundances that includes highly abundant molecules such as H_2, H_2O and CH_3OH. However, models have shown that grain surface mechanisms [14, 15] provide a route to properly account for the formation of these and other species on the surfaces of interstellar dust grains at low temperatures that cannot be formed efficiently in the gas phase.

Typical grain temperatures in dense clouds are 10 K, sufficient for the majority of atomic and molecular species to reside on the grain surface for significant periods of time. Freezing out of these atomic and molecular species on dust surface results in formation of icy mantles where large number of gas molecules is trapped in the icy mantles, as shown in Figure 1.1. Even such icy mantles containing less volatile species such as H_2O can be formed in warmer, and more diffuse regions.

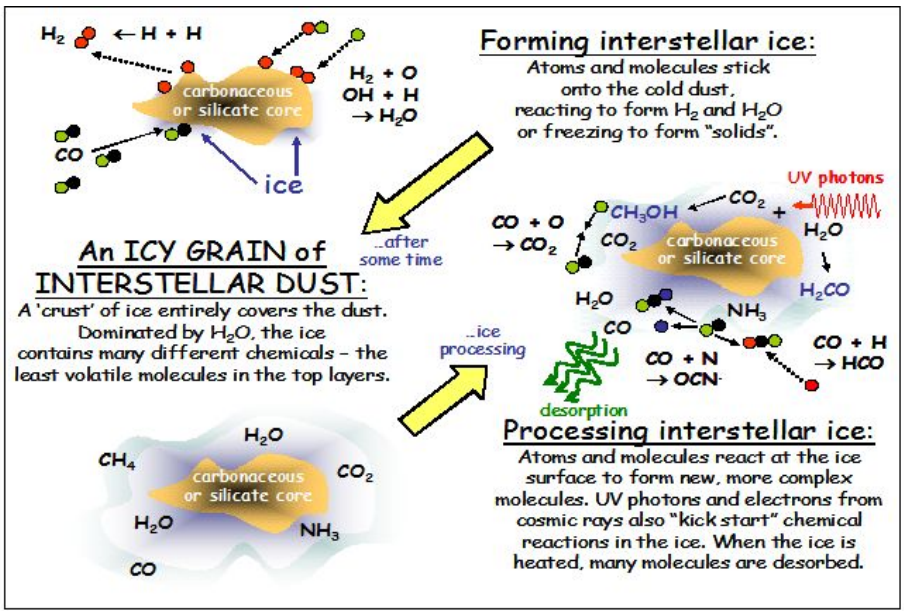

Figure 1.1 A cartoon depicting gas-grain interactions in the ISM leading to formation and processing of interstellar ices. [Source: http://lassie.u-cergy.fr]

Water ice has been observed as the most abundant ice in the Universe [11]. In the interstellar medium, H_2O ice was first detected in 1973 through infrared absorption feature at 3.1μm [16]. This absorption band is characteristic of the OH stretch of adsorbed bulk ice [17, 18]. Infrared observations have shown that apart from H_2O being most abundant molecule, the ices also contain significant amount of other molecules such as CO, CO_2 and CH_3OH, with very small traces of other species [19, 20]. It is realized that 90% of chemical processes during star formation occur on ice surfaces. Once formed, ices can be processed by both thermal and non-thermal mechanisms in the ISM. The work presented in this thesis focuses on the non-thermal processing of interstellar ices, particularly photon-stimulated processes.

1.2.3 Non-thermal Processing of interstellar ices

Non-thermal processing of ices involves irradiation of ices with photons and charged particles. Cosmic rays are the primary sources of charged particles. Depending on the energy, cosmic rays may cause different effects, where the highest energy cosmic rays upon collision with gas molecules can lead to the emission of gamma rays. The cosmic ray ionization of species can occur by lower energy cosmic rays that can lead to the generation of secondary electrons, which is most pronounced in the outer regions of dense clouds. Interstellar radiation field (ISRF) [21] representing photons in interstellar

medium contains contributions from nearby stars and emission both from dust and molecules such as PAHs [7]. Cosmic rays and UV light can induce chemical transformation in the ice and possibly desorption of the adsorbed species.

Astrochemical models have predicted that photo-desorption of H_2O by UV photons from the ISRF is efficient in the outer layers of both molecular clouds [22] and proto-planetary disks [23], which are diffuse regions with low densities. Lyman–alpha radiation is thought to dominate photon-driven processes deep within the molecular clouds due to strong attenuation of interstellar radiation field (ISRF) in these dense regions where radiation does not penetrate deeply into the clouds, and the source of this Lyman-alpha radiation is the recombination of electrons and protons caused by cosmic ray bombardment [24].

1.2.4 Polycyclic Aromatic Hydrocarbons (PAHs)

Polycyclic aromatic hydrocarbons (PAHs) are ubiquitously present in the ISM, which accounts up to 20 % of the galactic carbon and is thought to be among the most abundant organic compounds in the universe. They are likely to exist in the presence of water ice as either a part of the carbonaceous component of dust grain itself or as a component of icy mantles [11, 25]. They are a class of planar carbon bearing molecules that are highly stable due to their aromatic structures, which consist of fused benzene rings. In all PAHs, there is a delocalization of electrons in planes that are parallel to the plane of the molecule.

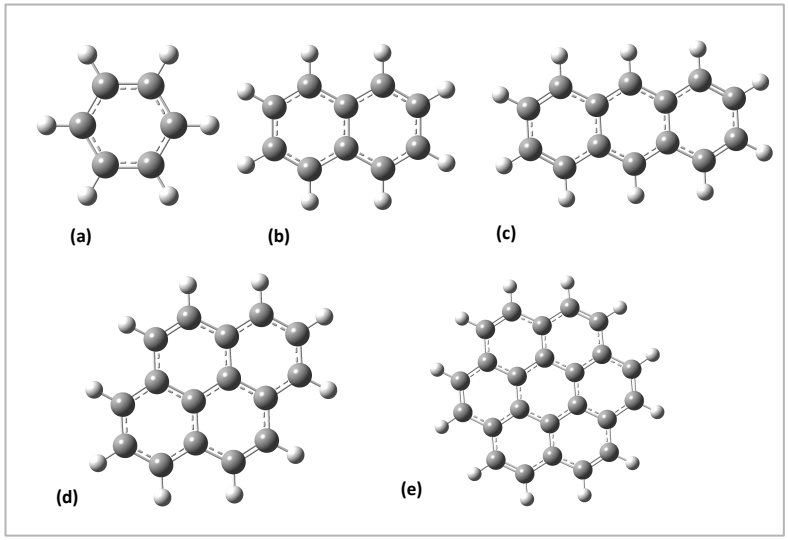

Figure 1.2 Structures of (a) benzene, (b) naphthalene, (c) anthracene, (d) pyrene, and (e) coronene.

Figure 1.2 shows the structures of benzene, along with some simple PAHs such as naphthalene, anthracene, pyrene, and coronene.

PAH molecules can be detected through both absorption and emission features. Being important component of the ISM, they can be used to probe different astrophysical environments. PAHs can efficiently absorb UV radiation to reach to excited electronic states, ultimately resulting with vibrational temperatures up to 1000K where excited molecule can undergo internal conversion and intersystem crossings to other electronic states, which results in IR emissions [26].

Figure 1.3 shows the energy level diagram for the various photo-physical pathways possible for a neutral PAH which includes radiative and non-radiative excitation and relaxation channels.

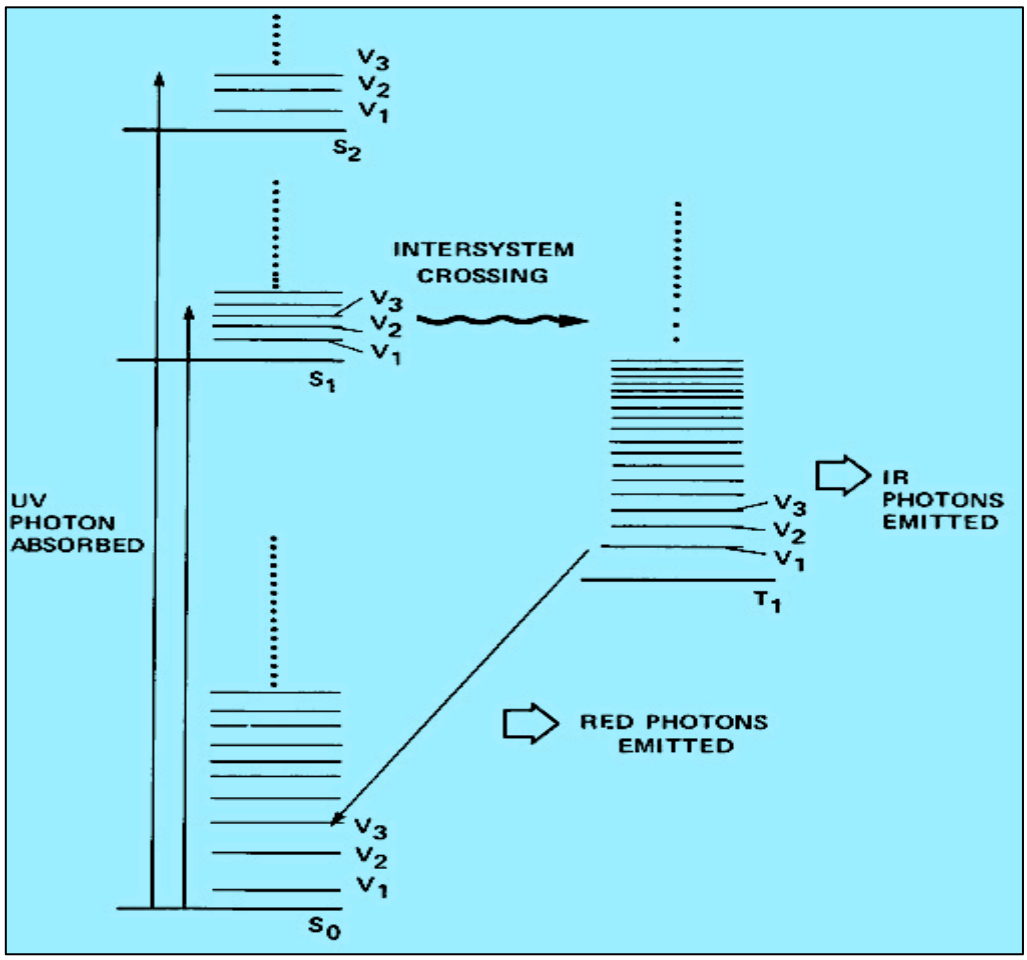

Figure 1.3 Jablonski diagram to illustrate the photophysics that drives IR and visible emission by neutral PAH molecules. From [26].

A neutral PAH molecule in its ground singlet state S_0, on absorbing a UV photon can be excited to different electronic excited states i.e. S_1, S_2, S_3, *etc*. The internal conversion (a non-radiative decay to lower excited state of same spin S_1) can then occur, followed by intersystem crossing (a radiationless decay between states of different spin) which populates the vibrational states in lowest lying triplet state T_1. The vibrational relaxation in T_1 can result in IR emissions or radiative phosphorescence process from T_1 state to ground state S_0 can result in visible emissions. Fluorescence, which is a radiative process from higher excited states S_1, S_2, S_3, etc to the ground state (S_o) of the same spin, is not shown here in Figure 1.3, as intersystem crossing dominates (about 90%) over fluorescence for these molecules.

PAHs are considered to be strong candidates for the carriers of broad interstellar infrared emission features observed at 3.3, 6.2, 7.8, 8.6 and 11.3 μm, commonly termed as Unidentified IR bands (UIRs) [27, 28]. They were first reported in the 1970s [29] and these aromatic infrared bands (AIBs) appear in diverse sources including stars, nebulae and many extragalactic sources. The detailed study of these UIRs emission features of PAHs and comparison to laboratory data is well presented in literature [28, 30]. It has been suggested that larger PAHs containing up to 500 carbon atoms would lead to broader emission features, while those containing 20 to 40 carbon atoms could result in sharp emission features [26].

The origin of the diffuse interstellar bands (DIBS) seen in the spectra of the astronomical objects in universe is still unknown and topic of debate for many years. PAHs and other large carbon bearing species are also thought to be responsible for these absorption features [31] and are generally attributed to electronic transitions in molecules and are typically observed towards dusty regions [32]. It has also been suggested that the strength of the DIBs is likely to be correlated with the extinction caused by interstellar dust.

In this thesis, to model complex molecules like PAHs within ice mantles, we have used benzene as a prototypical PAH compound to start with, for our computational convenience. Benzene is amongst the list of known interstellar molecules, and has been detected in the proto-planetary nebula CRL 618 [33]. We have also studied naphthalene that has also been identified in the ISM [34-36], taken as a representative of PAH family in the work presented in this thesis.

Benzene (C_6H_6) compound with its six membered ring of carbon atoms possess an interesting electronic structure and is a cyclic conjugated π electron system due to

overlap of π-orbitals on carbons forming a continuous ring of electron density and providing maximum stability. Qualitative molecular orbital (MO) picture of benzene shows that it has six π molecular orbitals, three of them are bonding molecular orbitals filled with all six π electrons while other three remain vacant, known as π^* anti-bonding molecular orbitals as shown in Figure 1.4. π_1 is the most stable bonding orbital with all in-phase combination while π_2 and π_3 orbitals have one node each. There are π_4 and π_5 orbitals with two nodes each and finally π_6 is the least stable totally anti-bonding orbital, with all out-of-phase combination having three nodes. The stability of the orbitals decreases due to increase in number of nodes with increase in energy.

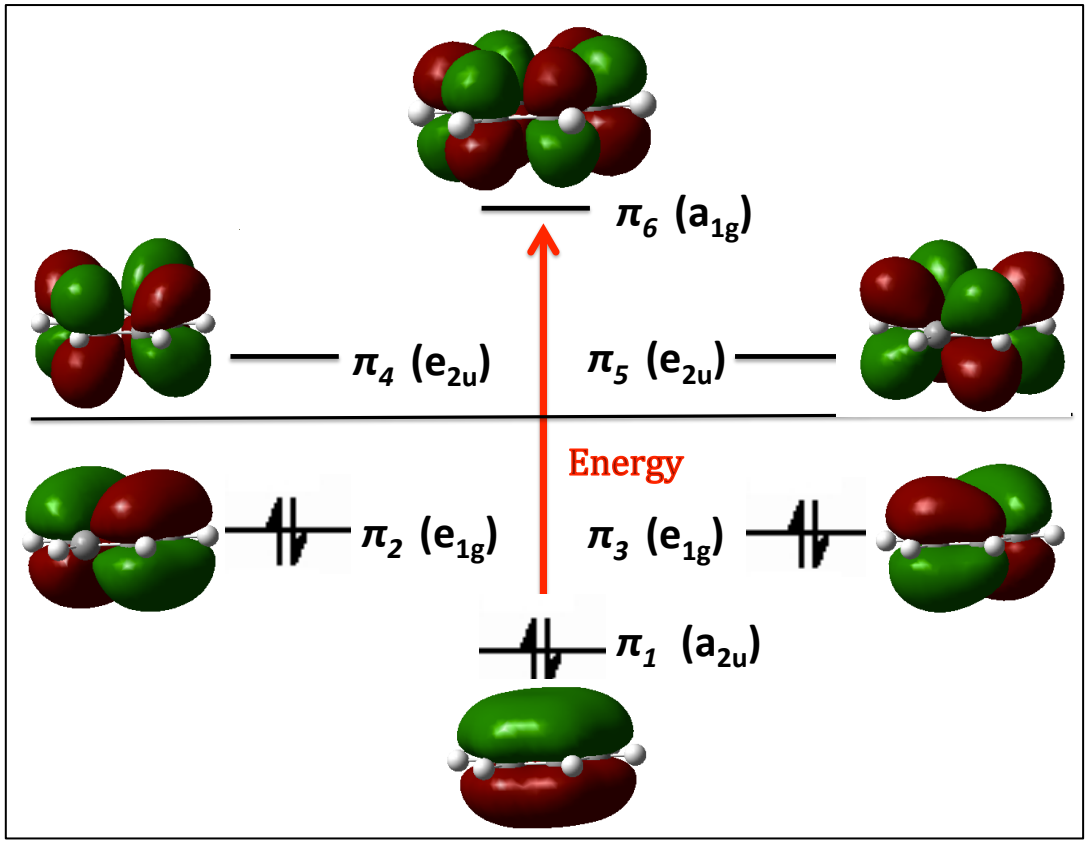

Figure 1.4 π molecular orbitals of benzene.

Benzene belongs to the D_{6h} point group, and the ground electronic state of benzene is $^1A_{1g}$, which is a totally symmetric singlet ground state, also referred to as $\tilde{X}\,^1A_{1g}$. The lowest energy electronic transition is the $\pi \rightarrow \pi^*$ promotion of an electron from the e_{1g} π bonding orbital to the e_{2u} π^*antibonding orbital. This leads to two non-equivalent electrons in e_{1g} and e_{2u} orbitals, which for D_{6h} symmetry results in the direct product

$e_{1g} \times e_{2u} = B_{1u} + B_{2u} + E_{1u}$. This results in six possible states, considering both singlets and triplets.

UV absorption spectra of benzene have been extensively studied in various states of aggregation [37, 38]. In the gas phase, it is well known that there exist three absorption bands in the near and far ultraviolet regions. The very weak first band at about 4.94 eV (or ~ 255 nm) is assigned to the singlet $^1A_{1g} \rightarrow {}^1B_{2u}$ transition. A moderately intense second band near 6.20 eV (or ~ 210 nm) is assigned to the singlet $^1A_{1g} \rightarrow {}^1B_{1u}$ electronic transition, whereas an extremely intense third band near 6.94 eV (or ~185 nm) corresponds to the singlet $^1A_{1g} \rightarrow {}^1E_{1u}$ transition. It has been established that these absorption bands are due to $\pi \rightarrow \pi^*$ singlet excitations of benzene. The lowest valence transitions of benzene from ground $^1A_{1g}$ state to excited states 1^1B_{2u} and 1^1B_{1u} are strictly electronically forbidden (or dipole forbidden) on symmetry grounds, while transitions to degenerate $^1E_{1u}$ excited states are dipole allowed electronic transitions. However, if the vibrational part of the wavefunction is considered, the lowest valence transitions of benzene become weakly allowed through vibronic transitions. The gas-phase UV absorption spectrum of benzene is shown in Figure 1.5.

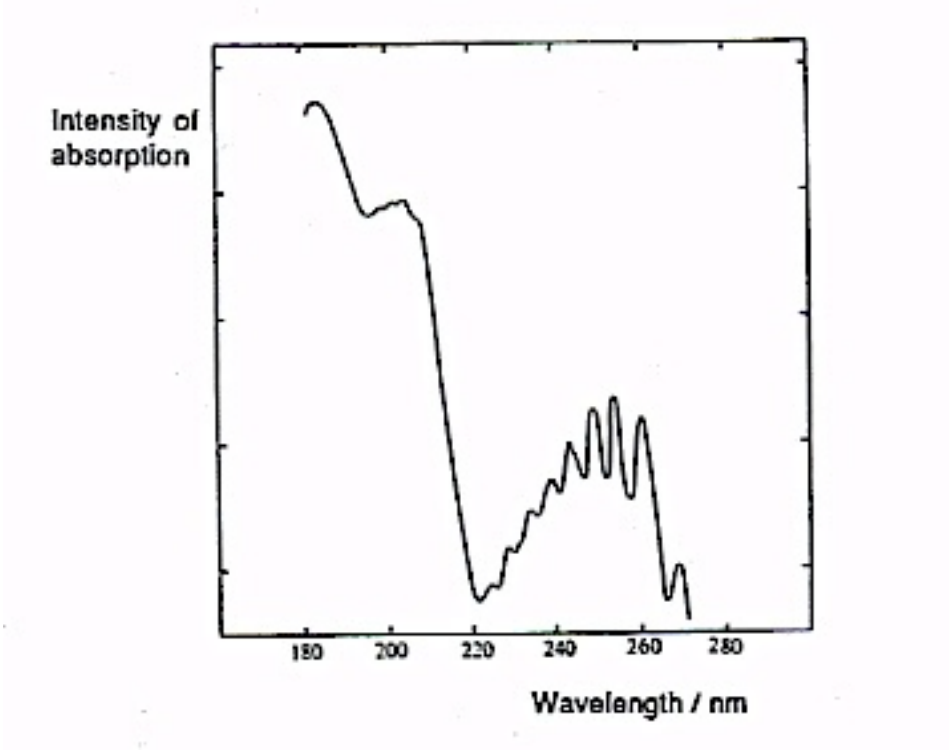

Figure 1.5 Ultraviolet/visible absorption spectrum of benzene showing vibrational fine structure [39].

Naphthalene belongs to the D_{2h} point group, and allows many transitions that are forbidden in benzene, due to its lower symmetry than benzene. There have been many theoretical [40-43] and experimental studies [44-47] on the excited state properties of naphthalene. The photochemistry of benzene and naphthalene are really interesting to study as it provides different photo-physical pathways for new products through different electronic transitions such as $\pi \rightarrow \pi^*$ (π bonding to π^* antibonding), $\sigma \rightarrow \pi^*$(σ bonding to π^* antibonding), $\pi \rightarrow \sigma^*$ (π bonding to σ^* antibonding), and also through charge transfer and non-radiative transitions.

1.3 Photon stimulated processes in ices

Photo dissociation and photo desorption of water ices are of particular interest to account for the astronomical observations of high gas-phase abundance of water in cold clouds, and also to understand their role in chemical evolution of icy mantles, which may lead to the formation of more complex molecules (Figure 1.6). There have been many experimental studies on the photon induced desorption of H_2O in an interstellar context. Only single photon processes were suggested to occur due to low photon fluxes prevalent in such astrophysical conditions.

Westley *et al*. [48, 49] studied H_2O desorption during irradiation with Lyman-α photons (121.6 nm), where photon energy is above the 7 eV threshold that is required for its absorption by H_2O molecules. Therefore, photodissociation of H_2O leads to H, and OH, H_2 and O, which subsequently reacted to form H_2O, HO_2, O_2 and H_2O_2. The two-photon desorption mechanism using photons at 248 nm has been studied by Nishi *et al*. [50], though such multi-photon processes are unlikely to be significant in the ISM due to low photon fluxes in astrophysical environments compared with those obtainable in the laboratory. An experimental study on the desorption of H_2O during photon irradiation with broadband VUV centred around 121 nm using Reflection-absorption infrared spectroscopy (RAIRS) has shown the photodissociation of bulk H_2O molecules, and desorption of surface bound H_2O molecules, confirming that photodesorption occurs only in the surface region [51]. OH, H_2 and O_2 photoproducts were also detected with the quadruple mass spectrometer (QMS). Different mechanisms were proposed for H_2O desorption where it was suggested that photodissociation products would desorb directly, result in H_2O desorption through recombination or kick-out, freeze-out (i.e. become thermalized) within the ice or recombine and freeze-out. Andersson *et al*. have also studied these mechanisms using molecular dynamics

simulations [52] and it was shown that majority of the H_2O desorption occurs through recombination. However, it was observed that that the kick-out mechanism might be dominant for the H_2O desorption upon photon irradiation at 157 nm [53].

It has been observed experimentally that UV irradiation of water ices cause reconstruction (crystallization/amorphization) of ices, and thus affect the morphology of the ice. The irradiation of crystalline ice with fast ions at low temperatures (T<100K) or by Lyman alpha photons were investigated and transformation of crystalline ice into amorphous ice was observed experimentally [54-56].

Chemical evolution of bulk ices during irradiation by ultraviolet (UV) light has been studied extensively [57, 58]. It was found that UV irradiation of H_2O ice containing CH_3OH, CO and NH_3 results in the formation of complex organic species including CO, CO_2, CH_4, HCO, H_2CO, CH_3CH_2OH, and other more complex species [43]. Similar studies performed with PAH molecules have suggested that chemical reactions induced in PAHs may play a significant role in the formation of complex organic species such as alcohols, quinones and ethers, during UV irradiation of water ice containing PAHs. The photon irradiation of mixed H_2O ices with H_2O/PAH ratios of between 800 and 3200 using broadband UV centred around 160 nm has indicated the addition of O and/or H atoms to the PAH molecules as detected by mass spectrometry. The IR data confirmed the presence of new functional groups, such as observed C=O stretching modes, indicated the formation of ketones, while OH stretching and bending modes indicated the formation of both aliphatic and aromatic alcohols. There is no evidence of breaking of the aromatic skeleton of the PAH molecules as clearly observed from these experiments. This is due to the high stability of these aromatic systems. The presence of some of the biologically important molecules, which have been detected in meteorites, was also noted in these experiments. However, processes (like photodesorption) occurring at a longer wavelength range cannot be ruled out as this experiment was conducted at a relatively small wavelength range.

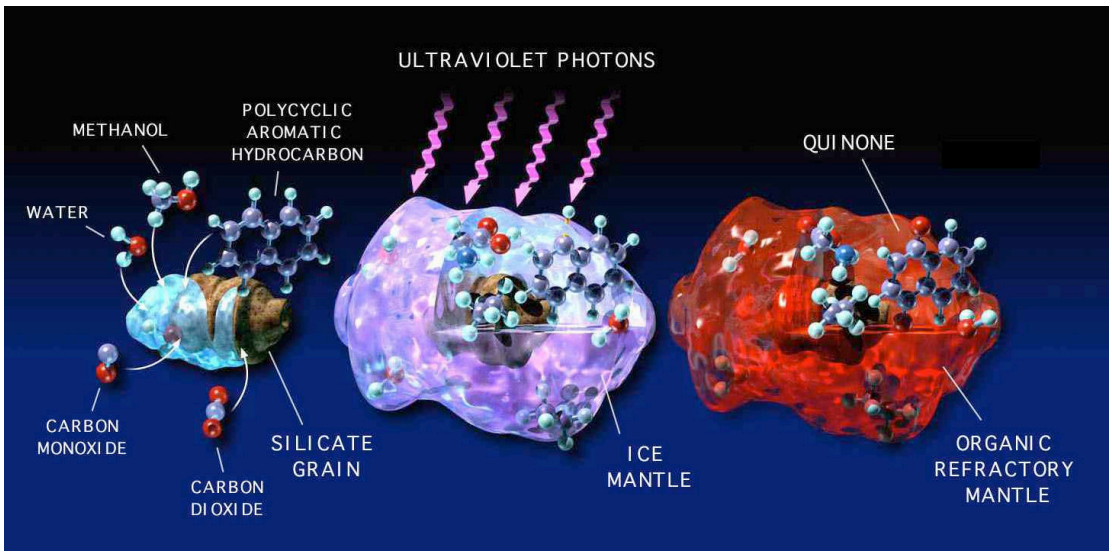

Figure 1.6 UV irradiation of ices involving both simple and more complex molecule. From [58].

A computational study has been performed to study the photoionization behaviour of benzene and small polycyclic aromatic hydrocarbons when they are embedded in a matrix of water ice using density functional theory (DFT) calculations [59]. It was found that ionization energies of benzene, naphthalene, anthracene, and pyrene are lowered by 1.5–2.1 eV in water ice. The time-dependent DFT calculations have shown that low lying vertical electronic excitation energies of both neutral and ionized species are unaffected by the ice matrix.

The UV absorption spectra of H_2O ice was studied experimentally [60]. It was observed that the first absorption band of the UV absorption spectrum is broadened and shifted by about 1.3 eV in condensed phase with respect to gas phase water [61]. There have been theoretical and computational studies on the excited state properties of small water clusters [62-64].

In the past decade, Zwier *et al*. have done detailed experimental studies on the Bz-W_n clusters using resonant ion-dip spectroscopy (RIDIRS) and resonant two-photon ionization (R2PI) techniques [65-67]. It was observed that the water O-H stretch spectra depends on the size of cluster and is sensitive to the number, strength and the type of hydrogen bonds in which it participates while C-H stretch in benzene was found insensitive to the size of water cluster with $n \leq 7$ [65]. For n = 3-5, the water cluster was considered to bind to benzene primarily through single water molecule on or near benzene six-fold axis and the O-H spectra was consist of free O-H stretches, π H-bonded O-H stretches and the single donor O-H stretches. The significant spectral signature was observed at $n \geq 6$ in O-H stretch spectra, showing new transitions that are

associated with the double-donor O-H stretches, which exist, in the more compact large Bz-W_n clusters. An experimental evidence predicted the change in shape of cluster from cyclic to non-cyclic at n = 6 such that Bz-W_6 cluster was found likely to exist as a cage shaped arrangement of six water molecules giving the lowest energy structure.

Recently, there have been growing interests in the UV processing of laboratory models of interstellar ices. A few experiments have been performed on photo processing of laboratory models of interstellar ices by UV radiation [68-74]. Thrower *et al.* have done experimental studies on photo-processes in model interstellar ices by modelling multilayer films of benzene & water deposited on the sapphire substrate at temperature of around 80 K [72]. It was investigated that three distinct photo-desorption mechanisms occur in such systems: (i) Direct adsorbate-mediated desorption of benzene, (ii) Indirect adsorbate–mediated desorption of water, and (iii) Substrate-mediated desorption of both benzene and water. The translational temperature of both desorbed species i.e. benzene and water molecule is found to be more than the ambient temperature of the complex system. The photodesorption of benzene from H_2O ice has shown a strong dependence of desorption of both benzene and water on the morphology of the ice [71].

Recent experimental study on photon- and electron- induced desorption from laboratory models of interstellar ice grains by mimicking the conditions found in dense interstellar clouds has been performed by Thrower *et al*. [70]. The desorption cross sections and first order rate constants for the desorption processes in benzene-water (Bz-W_n) complexes have been obtained. It was observed that photon absorption by benzene could make H_2O desorption possible at wavelengths where photon-absorption cross-section (i.e. the ability of a molecule to absorb a photon of a particular wavelength) for H_2O is negligible. The interstellar radiation field (ISRF) induced photo-desorption was found to be an important process in the indirect desorption of water, which occurs at the edges of dense interstellar clouds and at relatively long wavelengths, whereas the electron stimulated desorption channels and internal UV fields dominant deep within the dense clouds were found to play an important role in the direct desorption of water.

Computational studies on low lying excited states of Bz-W_n, (n = 1-6) complexes have been performed by Upadhyay *et al*. (2002) using configuration interaction method involving all the singly excited configurations (CIS) [75]. The binding energies of these clusters are also calculated and the complex of water dimer with benzene (Bz-W_2) is

found to be the most stable among the various complexes with high stability of Bz-W_6 complex too. It was found that the whole Bz-W_n complex as well as the water cluster W_n undergoes an expansion in size following excitation to lowest singlet excited states. The small blue shifts in the excitation energies are observed in the electronic absorption spectra in going from Bz-W_1 to higher complexes Bz-W_n, (n = 4-6).

The main objective of the work in this thesis project is to perform computational study on the UV spectroscopy and photochemistry of small water clusters, and cyclic aromatic hydrocarbons such as benzene and naphthalene. We have also modelled benzene- and naphthalene-bound water clusters as well as benzene-bound crystalline ice clusters, as of particular importance in order to mimic PAHs in interstellar icy structures and to get deep insight into the behaviour and role of PAHs in the model interstellar ices under UV field. There have been very few computational studies on the excited state properties of these systems and thus are the subject of main interest in our thesis. Furthermore, we have studied the deuterium (D) diffusion on crystalline and amorphous ice surfaces at astronomically relevant temperatures in detail, and also investigated the possible mechanism for the D_2 formation on ice surfaces.

1.4 Outline of this thesis

Further in this thesis, Chapter 2 introduces the theoretical background needed for the detailed description on the computational aspects involved in the work. A general theoretical background on the quantum mechanics as well as molecular mechanics approaches is discussed; along with its applicability on the molecular systems through computational techniques. This chapter primarily focuses on the description of a range of computational techniques employed for the calculations of ground and excited state properties of the systems involved in the work.

Chapter 3 primarily focuses on the lowest energy excited states of small water clusters i.e. from an isolated water molecule up to the water pentamer cluster. Detailed benchmark computations are performed using a range of high level electron structure methods including hierarchy of linear response coupled cluster (CC) methods and the time-dependent density functional theory (TD-DFT) methods. Excited state properties such as vertical excitation energies, oscillator strengths, and dipole moments are studied, and the effect of electron correlation on such excited states is investigated. The solvation or aggregation effect on the lowest lying excited state of the water monomer is studied.

Chapter 4 describes the spectroscopy and photochemistry of interstellar ice analogs i.e. benzene-water hexamer cluster is used as a model system to replicate such astrophysical environment. Detailed investigation of the important electronic transitions involved in such systems following photon absorption are performed using linear response time dependent DFT with a range of well developed DFT hybrid functionals.

In Chapter 5, we extend the work performed in Chapter 4 to truly polycyclic aromatics via naphthalene ($C_{10}H_8$), consisting of linearly fused two benzene rings. Both ground and excited states of the naphthalene-water hexamer water cluster are investigated using quantum chemical computational methods. The linear response time-dependent DFT with a range of well-developed DFT functionals is again used to study UV spectroscopy and photochemistry of naphtha-W_6 clusters.

In Chapter 6, we extend the work from Chapter 4 and replace the water hexamer cluster with a crystalline ice surface. Therefore, in this chapter computational investigation of the benzene adsorption on a crystalline ice surfaces is presented. The role of the dangling atoms of ice clusters on the benzene adsorption on crystalline ice is studied using the ONIOM (QM: AMOEBA) method. This work was carried out in collaboration, where a computational group at the University of Gothenburg implemented the AMOEBA force field in the ONIOM method. The UV spectroscopy of benzene-ice clusters is investigated using the TD-DFT method.

Further the work presented in Chapter 7 was carried out in collaboration with a computational group at the University of Gothenburg. This chapter describes the deuterium (D) atom diffusion on both crystalline and amorphous ice surfaces. Binding energies, barrier heights, hopping rate constants, residence times, and diffusion coefficients are computed. The rate constants are calculated using the quasi-quantum harmonic transition state theory (qq-HTST). The diffusion coefficients of the D atom on both amorphous and crystalline ice surfaces are calculated at astronomically relevant temperatures (T = 8-30 K) using the Adaptive Kinetic Monte Carlo (AKMC) method.

Chapter 8 gives an overview of all results and summarizes the work of this thesis.

Chapter 2 - Theoretical Background

2.1 Quantum-Mechanical Background

Quantum Mechanics (QM) is a fundamental branch of science that deals with the physical phenomena at molecular scale. The postulates of quantum mechanics state that physical properties of atoms and molecules are *quantized,* and thus physical quantities can only take certain *discrete* values and not continuous values [76]. The concepts of quantum mechanics includes the mathematical description of the concept of wave–particle duality of light and matter and Heisenberg's uncertainty principle. Quantum mechanics is an important tool to explain the behaviour of matter and its interactions with light, and provides a useful framework for describing many chemical problems in the field of chemistry.

2.1.1 The Schrödinger Equation

The main goal of most quantum chemical approaches is to find the approximate solutions of the time-independent, non-relativistic Schrödinger equation

$$\hat{H}\Psi_i\left(\overrightarrow{\mathbf{x}_1}, \overrightarrow{\mathbf{x}_2}, \ldots, \overrightarrow{\mathbf{x}_N}, \overrightarrow{R_1}, \overrightarrow{R_2}, \ldots, \overrightarrow{R_M}\right) = E_i\,\Psi_i(\overrightarrow{\mathbf{x}_1}, \overrightarrow{\mathbf{x}_2}, \ldots, \overrightarrow{\mathbf{x}_N}, \overrightarrow{R_1}, \overrightarrow{R_2}, \ldots, \overrightarrow{R_M}) \tag{2.1}$$

where $\hat{H}$ is the Hamilton operator corresponding to the total energy for a molecular system consisting of M nuclei and N electrons in the absence of magnetic or electric fields, which can be represented as,

$$\hat{H} = \hat{T}_n + \hat{T}_e + \hat{V}_{nn} + \hat{V}_{en} + \hat{V}_{ee} \tag{2.2}$$

where all the five components in Equation (2.2) of the Hamilton operator (in atomic units) can be written as

$\hat{T}_n$, the operator for the kinetic energy of the nuclei :

$$\hat{T}_n = -\sum_{A=1}^{M} \frac{1}{2M_A} \nabla_A^2 \tag{2.3}$$

$\hat{T}_e$, the operator for the kinetic energy of the electrons:

$$\hat{T}_e = -\sum_{i=1}^{N} \frac{1}{2} \nabla_i^2 \tag{2.4}$$

$\hat{V}_{nn}$, the operator for the Coulomb repulsion between the nuclei :

$$\hat{V}_{nn} = \sum_{A=1}^{M} \sum_{B>A}^{M} \frac{Z_A Z_B}{R_{AB}} \tag{2.5}$$

$\hat{V}_{en}$, the operator for the Coulomb attraction between electrons and nuclei:

$$\hat{V}_{en} = -\sum_{i=1}^{N} \sum_{A=1}^{M} \frac{Z_A}{r_{iA}} \tag{2.6}$$

$\hat{V}_{ee}$ = the operator for the Coulomb repulsion between electrons:

$$\hat{V}_{ee} = \sum_{i=1}^{N} \sum_{j>i}^{N} \frac{1}{r_{ij}} \tag{2.7}$$

where, M_A is the ratio of the mass of nucleus A to the mass of an electron, Z_A is the atomic number of nucleus A. r_{iA} is the distance between the i^{th} electron and A^{th} nucleus i.e. $r_{iA} = |\vec{r_i} - \vec{r_A}|$, and r_{ij} is the distance between the i^{th} and j^{th} electron i.e. $r_{ij} = |\vec{r_i} - \vec{r_j}|$. Similarly, $R_{AB} = |\overrightarrow{R_A} - \overrightarrow{R_B}|$ is the distance between the A^{th} nucleus and the B^{th} nucleus. Here, A and B run over the M nuclei while *i* and *j* denote the N electrons in the system.

The wave function Ψ_i $(\overrightarrow{\mathbf{x}_1}, \overrightarrow{\mathbf{x}_2}, \ldots, \overrightarrow{\mathbf{x}_N}, \overrightarrow{R_1}, \overrightarrow{R_2}, \ldots, \overrightarrow{R_M})$ depends on the 3N spatial coordinates (r_i), and the N spin coordinates (s_i) of the electrons, which are collectively termed as ($\mathbf{x}_i$), and the 3M spatial coordinates of the nuclei, (R_I). Ψ_i denotes the wave function of the i^{th} state of the system, that contains all information that can possibly be known about the quantum system under study. E_i stands for the energy of the i^{th} state described by wave function Ψ_i.

Without introducing any approximations, the total (exact) wave function can be written as a sum of products of nuclear and electronic wave functions, and is expanded in the complete set of electronic functions with the expansion coefficients being functions of the nuclear coordinates.

$$\Psi_{total} = \sum_{k} \Psi^{k}_{nuc}\{R_A\}\,\Psi^{k}_{elec}\{r_i;\ R_A\} \tag{2.8}$$

This total wave function is inserted into a time-independent Schrödinger equation (2.1) and on expansion leads to standard adiabatic equations, and non-adiabatic coupling terms that emerge due to coupling of electronic states via nuclear motion.

2.1.2 The Born Oppenheimer Approximation

The Schrödinger equation (2.1) can be further simplified if we take advantage of the significant differences between the masses of nuclei and electrons. Since nuclei are much heavier than the electrons, they are assumed to be stationary with respect to electronic motion. The electrons in a molecule move in the field of fixed nuclei and adjust quickly to any movement of nuclei. Thus electronic and nuclear motion can be treated separately, which is the basis of the Born Oppenheimer (BO) or clamped-nuclei approximation to simplify the complicated Schrödinger equation for a molecule [77, 78].

The non-adiabatic coupling terms are generally small due to large mass differences and can be neglected under BO approximation. However this BO approximation breaks down at electron degeneracies where electronic states are close in energy to one another. For example, one of the non-adiabatic coupling terms is closely related to the equation for derivative coupling vector [79],

$$\langle \Psi_i | \nabla_n | \Psi_j \rangle = \frac{\left\langle \Psi_i \left| \frac{\partial \hat{H}_e}{\partial q} \right| \Psi_j \right\rangle}{V_j - V_i} \quad \text{, for } i \neq j \tag{2.9}$$

where $\hat{H}_e$ is the electronic Hamiltonian operator, Ψ_i and V_i denotes the adiabatic wavefunction and the electronic energy of i^{th} electronic state, respectively. The value of a non-BO term goes to infinity, when difference of energies between two electronic states becomes zero i.e. denominator of Equation (2.9) becomes zero, the BO approximation completely breaks down and therefore the non-adiabatic coupling terms generated due to the coupling of electronic and nuclei motions have to be taken into account. When $\Delta V \neq 0$, the B0 approximation is still valid and the coupling terms can be neglected.

Under BO approximation, $T_n = 0$ as nuclei are fixed and repulsion between nuclei can be considered as constant i.e. V_{nn} = constant, so the electronic Hamiltonian describing the electron motion in the field of nuclei is as follows

$$\hat{H}_{elec} = \hat{T}_e + \hat{V}_{en} + \hat{V}_{ee} \tag{2.10}$$

and the solution of the electronic Schrödinger equation

$$\hat{H}_{elec}\Psi^i_{elec} = E^i_{elec}\Psi^i_{elec} \tag{2.11}$$

can be written as

$$\Psi^i_{elec} = \Psi^i_{elec}(\{r_i\};\{R_A\}) \tag{2.12}$$

which is an electronic wave function that depends explicitly on electron coordinates r_i but parametrically on the nuclear coordinates R_A, as does the electronic energy E_{elec} ,

$$E_{elec} = E_{elec}(\{R_A\}) \tag{2.13}$$

The total energy E_{tot} for fixed nuclei is the sum of E_{elec} and the constant nuclear repulsion term,

$$E_{tot} = E_{elec} + \sum_{A=1}^{M}\sum_{B>A}^{M}\frac{Z_A Z_B}{R_{AB}} \tag{2.14}$$

The total energy E_{tot} provides a potential for the nuclear motion. The solution of Schrödinger equation obtained by varying the molecular geometry over a range of nuclear coordinates R_A to obtain a different electronic energy at each geometry, gives E_{elec} as a function of R_A. This further defines the *Potential Energy Surface (PES)*: E_{tot} as a function of R_A.

The nuclear Hamiltonian in the average field of the electrons can be written as

$$\hat{H}_N = \hat{T}_n + \langle \hat{T}_e + \hat{V}_{en} + \hat{V}_{ee} \rangle + \hat{V}_{nn} \tag{2.15}$$

and the solution of the nuclear Schrödinger equation

$$\hat{H}_N \Psi_{nuc} = E\Psi_{nuc} \tag{2.16}$$

gives the nuclear wave function

$$\Psi_{nuc} = \Psi_{nuc}\{R_A\} \tag{2.17}$$

which describes the vibration, rotation, and translation of a molecule and E is the BO approximation to the total energy of (2.1) which includes electronic, vibrational, rotational, and translational energy. The attractive potential exerted on the electrons due to the nuclei i.e. the expectation value of the operator $\hat{V}_{en}$ in equation (2.10) is also often termed the external potential V_{ext}, in density functional theory, which will be discussed later in this chapter.

The wave function Ψ itself is not an observable, whereas physical interpretation can only be associated the square of the wave function that represents the probability of electrons 1, 2, …., N that are found simultaneously in volume elements $d\overrightarrow{\mathbf{x}_1}, d\overrightarrow{\mathbf{x}_2}, \ldots d\overrightarrow{\mathbf{x}_N}$ and can be written as

$$|\Psi_i (\overrightarrow{\mathbf{x}_1}, \overrightarrow{\mathbf{x}_2}, \ldots \overrightarrow{\mathbf{x}_N})|^2 d\overrightarrow{\mathbf{x}_1}, d\overrightarrow{\mathbf{x}_2}, \ldots d\overrightarrow{\mathbf{x}_N} \tag{2.18}$$

The probability of finding the N electrons anywhere in space must be exactly unity and a wave function which satisfies the Equation (2.19) is the normalized wave function.

$$\int \ldots \int |\Psi_i (\overrightarrow{\mathbf{x}_1}, \overrightarrow{\mathbf{x}_2}, \ldots \overrightarrow{\mathbf{x}_N})|^2 \; d\overrightarrow{\mathbf{x}_1}, d\overrightarrow{\mathbf{x}_2}, \ldots d\overrightarrow{\mathbf{x}_N} = 1 \tag{2.19}$$

Since electrons are indistinguishable, this probability must not change with respect to the interchange of the coordinates of **x** (both space and spin) of any two electrons (here *i* and *j*) i.e.,

$$\left|\Psi_i \left(\overrightarrow{\mathbf{x}_1}, \overrightarrow{\mathbf{x}_2}, \ldots \overrightarrow{\mathbf{x}_i}, \ldots, \overrightarrow{\mathbf{x}_j}, \ldots \overrightarrow{\mathbf{x}_N}\right)\right|^2 = \left|\Psi_i (\overrightarrow{\mathbf{x}_1}, \overrightarrow{\mathbf{x}_2}, \ldots \overrightarrow{\mathbf{x}_j}, \ldots, \overrightarrow{\mathbf{x}_i}, \ldots \overrightarrow{\mathbf{x}_N})\right|^2 \tag{2.20}$$

To satisfy the above condition Equation (2.20) by electrons, that are fermions with half-integral spin, the electronic wave function Ψ therefore must be antisymmetric with respect to interchange of the spatial and spin coordinates of any two electrons,

$$\Psi_i\left(\overrightarrow{\mathbf{x}_1}, \overrightarrow{\mathbf{x}_2}, \ldots \overrightarrow{\mathbf{x}_i}, \ldots, \overrightarrow{\mathbf{x}_j}, \ldots \overrightarrow{\mathbf{x}_N}\right) = -\Psi_i\left(\overrightarrow{\mathbf{x}_1}, \overrightarrow{\mathbf{x}_2}, \ldots \overrightarrow{\mathbf{x}_j}, \ldots, \overrightarrow{\mathbf{x}_i}, \ldots \overrightarrow{\mathbf{x}_N}\right) \quad (2.21)$$

which represents a quantum-mechanical generalization of Pauli's exclusion principle statement that "*no two electrons can occupy the same state"*. Thus the exact electron wave function must satisfy the *antisymmetry principle.*

2.1.3 Potential Energy Surface (PES)

A PES is a mathematical relationship linking molecular structure and resultant energy as mentioned above in Section 2.1.2. A molecule has minima on the PES, which corresponds to equilibrium structures of reactants and products, with the global minimum describing the most stable nuclear configuration. At both minima and saddle points, also termed as stationary points on PES, the energy gradient becomes zero and hence forces vanish at such points. The characterization of these stationary points as minima or saddle points can be done by calculating the second derivative of the energy with respect to nuclear positions (Hessian matrix), giving positive eigenvalues for minima, and *n*-negative eigenvalues for n^{th} order saddle points. First order saddle point generally describes a transition state (TS) between products and reactants. A multi-dimensional PES is shown in Figure 2.1.

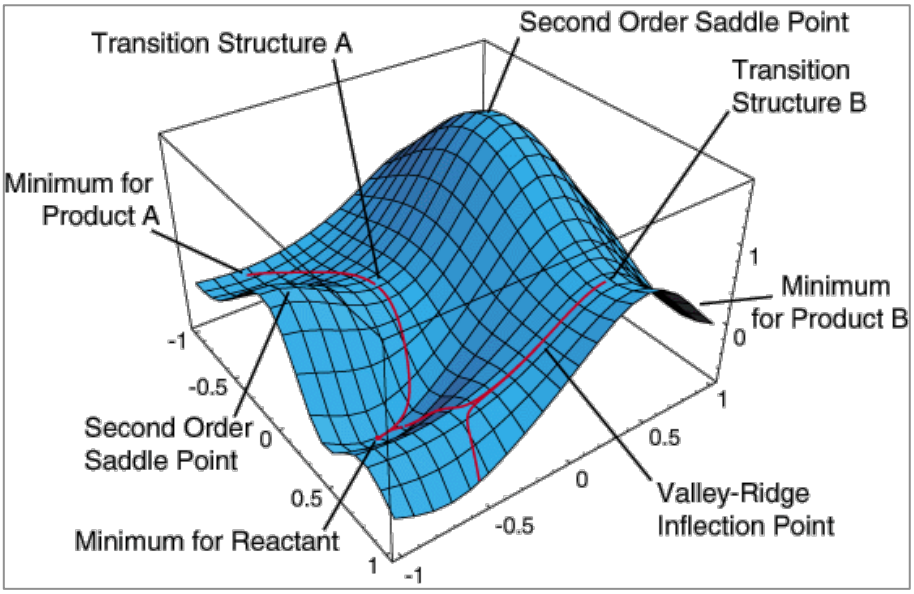

Figure 2.1 Multi-dimensional PES of a molecule. From [80].

In this thesis, the saddle point search between two local energy minima is performed by the activation-relaxation technique (ART) technique.

2.1.3.1 The Activation-Relaxation Technique

The activation-relaxation technique (ART) [81, 82] defines events in the surface energy landscape according to a two-step process: (a) the activation process starting from a local energy minimum to a nearby local saddle point: (b) the relaxation process where configuration is relaxed from this saddle point to a new minimum. For the activation process, we have used the modified version of ART, i.e. ART *nouveau* (ARTn) [83], which considers the eigenvector corresponding to the largest, negative eigenvalue of the Hessian to ensure a full convergence onto a saddle point.

In the activation process, the configuration is first pushed along a random direction until a negative eigenvalue appears. At each step along this trajectory, its total energy is relaxed in the hyperplane perpendicular to the step direction so that total energy and forces remain under control as the configuration leaves the harmonic well. Once the lowest eigenvalue passes a threshold (in our case 10^{-6}) and if it is negative, the convergence to the saddle point is started by pushing the configuration along the eigenvector corresponding to the negative eigenvalue, while minimizing the forces in all other directions. If the lowest eigenvalue doesn't change sign and remain negative this procedure leads to convergence to the first-order saddle point. If the lowest eigenvalue changes sign, and become positive, the iteration procedure is stopped and a new event is started. At the first order saddle point, all the eigenvalues of the Hessian except one are positive, and the energy landscape resembles a valley going down along the eigendirection corresponding to the negative eigenvalue.

The ART is designed to deal with systems with thousands of degree of freedom, where it is not appropriate to perform a direct diagonalization of the Hessian to extract eigenvalues and eigenvectors. We use the Lanczos algorithm [84] that performs well in extracting the lowest eigenvalues and corresponding eigenvectors.

For the relaxation process, we have used the conjugate gradient (CG) method [85]. Leaving the saddle point by steepest descent, we follow the floor of the valley to arrive at a nearby minimum.

The ARTn method is efficient in finding all first-order saddle points and new minima around a given minimum. It also defines trajectories connecting initial minimum-saddle point-final minimum as fully reversible and real activated paths.

2.1.4 Transition State Theory (TST)

The most widely employed approach for studying reaction rates invloving species that are undergoing reaction at or near thermal-equilibrium conditions is the transtion state theory (TST). In the framework of classical transition state theory (TST) [86], under the assumption of harmonic approximation for vibrational modes, the transition rate constant can be written as [87]

$$k(T) = \frac{k_B T}{h} \frac{Q^{\ddagger}}{Q_R} e^{(-\Delta E/k_B T)} \tag{2.22}$$

where $Q^{\ddagger}$ and Q_R are the partition functions of the saddle point and the reactant, respectively. The classical barrier height is ΔE and is given as $\Delta E = E_{TS} - E_{min}$, that corresponds to the classical binding energy difference between the energy of the saddle point (E_{TS}) , and energy of the minimum (E_{min}).

It is important to consider quantum effects for light atoms carefully. The classical treatment of atomic motion is not accurate at low temperatures, and the zero point energy (ZPE) of the vibrational ground state is important and needs to be taken into account.

In the framework of harmonic transition state theory (HTST) [87, 88], the classical partition function for vibration is replaced by the quantum vibrational partition function to introduce ZPE into the rate expression, and the quantum vibrational partition function is given as [86]

$$Q_{vib} = \sum_i g_i e^{(-E_i/k_B T)} \tag{2.23}$$

where g_i is the degeneracy, and E_i is the vibrational energy of the i^{th} energy level.
The energy eigenvalues of the harmonic oscillator are,

$$E_n = \hbar\omega(n + 1/2), n = 0, 1, 2, 3, \ldots, \infty \tag{2.24}$$

Substituting in Equation (2.23), then Q_{vib} can be written as

$$Q_{vib} = \sum_{n=0}^{\infty} e^{(-(n+1/2)\,\hbar\omega/k_B T)} \tag{2.25}$$

where $g_i = 1$.

Using the defination of the hyperbolic function $sinh(x) = (e^x - e^{-x})/2$ and Equation (2.25), the vibrational partition function of an atom at transition state $Q_{vib}^{\ddagger}$ and at local minimum Q_{vib}^{min} can be obtained. Inserting $Q_{vib}^{\ddagger}$ and Q_{vib}^{min} into Equation (2.22), we can obtain the hopping rate constant that includes zero point energy (ZPE). The hopping rate constant using quasi-quantum harmonic transition state theory (qq-HTST) is $k_{qq-HTST}$ and can be written as

$$k_{qq-HTST}(T) = \frac{k_B T}{\hbar} \frac{\prod_{i=1}^{3} 2sinh\,(\hbar\omega_i^{min}/2k_B T)}{\prod_{i=1}^{2} 2sinh\,(\hbar\omega_i^{TS}/2k_B T)} e^{(-\Delta E/k_B T)} \tag{2.26}$$

where ω^{min} and ω^{TS} are the angular frequencies of the harmonic vibrational modes at the local minima and transition state, respectively.

Hopping Rate constant for $\Delta E^{VAG} < 0$

The barrier height measured between the reactant and saddle point at zero point energy levels (ΔE^{VAG}) can be written as

$$\begin{aligned} \Delta E^{VAG} &= \left(E_{TS} + \sum_{i}^{D-1} \frac{\hbar\omega_{\ddagger,i}}{2}\right) - \left(E_{min} + \sum_{i}^{D} \frac{\hbar\omega_{R,i}}{2}\right) \\ &= \left(E_{TS} + \sum_{i}^{2} \frac{\hbar\omega_{\ddagger,i}}{2}\right) - \left(E_{min} + \sum_{i}^{3} \frac{\hbar\omega_{R,i}}{2}\right) \end{aligned} \tag{2.27}$$

for the modes of one deuterium atom where D denotes the number of vibrational modes, ω is the angular frequency, and here VAG stands for vibrational adiabatic ground state.

For $\Delta E^{VAG} > 0$, qq-HTST provides reasonable hopping rates k for each hop using Equation (2.26), and behaves properly. But for $\Delta E^{VAG} < 0$, qq-HTST doesn't provide accurate values for k, as the Boltzmann factor becomes very large for negative VAG, and leads to improper behaviour.

Considering the nature of the hop, whether the transition is endoergic or exoergic, this problem can be approached in two ways. If the quantum energy of the reactant is

more than the quantum energy of the product, then the transition is considered as exoergic, i.e. for $E_{R_q} > E_{P_q}$, and the transition is endoergic for $E_{R_q} < E_{P_q}$.

The expressions for E_{R_q} and E_{P_q} can be given as

$$E_{R_q} = E_R + \sum_i^3 \frac{\hbar\omega_{R,i}}{2} \tag{2.28}$$

$$E_{P_q} = E_P + \sum_i^3 \frac{\hbar\omega_{P,i}}{2} \tag{2.29}$$

where E_R and E_P are the classical binding energy of the reactant and the product, respectively.

For exoergic transition with $\Delta E^{VAG} < 0$ the rate constant is considered to be $min\,[k_B T/h, v_{min}^R]$, where v_{min}^R is the minimum vibrational frequency of the reactant. For endoergic transition with $\Delta E^{VAG} < 0$, the qq-HTST rate equation is modified and rate Equation (2.30) is used which can be given as

$$k_{endo}(T) = k_b \frac{\prod_j^3 2sinh\,(\hbar\omega_j^R/2k_B T)}{\prod_j^2 2sinh\,(\hbar\omega_j^P/2k_B T)} e^{(-\Delta E/k_B T)}\, e^{(hv_{min}^P/2k_B T)} \tag{2.30}$$

where k_b is the rate constant of the hop in backward direction.

If this backward hop has $\Delta E^{VAG} > 0$, then $k_b = k_{qq-HTST}$. If the backward hop is exoergic and $\Delta E^{VAG} < 0$, then $k_b = min\,[k_B T/h, v_{min}^R]$. The barrier height is the classical binding energy difference between the energy of the reactant and the product i.e. $\Delta E = E_P - E_R$. A zero point energy (ZPE) correction term for the product is included in the rate equation (i.e. last exponential term in Equation (2.30)) as ZPE is also included in the partition functions.

2.1.4.1 Adaptive kinetic Monte Carlo (AKMC) method

A popular method for modeling state-to-state molecular dynamics is the Adaptive kinetic Monte Carlo (AKMC) [89, 90] method. In this thesis, AKMC is used for long timescale simulation in crystalline and amorphous ice surfaces for determining kinetic processess such as diffusion.

The primary task of the AKMC simulations is to search for possible processes, which are determined by performing a large number of saddle point searches, which separates the current state i.e. a local minimum on the potential energy surface (PES) from its neighbouring minima [91]. These searches are carried out using the minimum mode following algorithm. These processes are stored in the so-called table of events (TOE). In order to propagate the dynamics within AKMC, a list of all possible rates leading away from the current stable state to any other state is required and these are then used to populate the TOE. A transition between states is assumed to be first order, and the rate of the transition is calculated from the harmonic approximation to the transition state theory (hTST). Each process leading to a new state is tabulated in rate table and one transition is selected with a probability proportional to its rate. The transition time is drawn from a first-order distribution for the total rate of escape from the state. The saddle point search procedure then starts over in the new state. If the system revisits a state, the TOE that has been constructed in a previous visit can be reused.

Once the TOE is known for a specific temperature, it is simple to perform KMC simulations at other temperatures [92]. Since the process barriers and prefactors are temperature independent, one can simply recalculate the rates for a new temperature using the harmonic transition state theory expression (2.31)

$$k = v\, e^{(-E_b/kT)} \tag{2.31}$$

where v is the process prefactor and E_b is the energy barrier.

The KMC trajectories give the position (r) of the atom on the ice surface as a function of time (t). Thus, diffusion coefficients, D, can be calculated using the Einstein-Smoluchowski Equation (2.32) for two-dimensional diffusion.

$$D = \lim_{t\to\infty} \frac{1}{4t} \langle |r(0) - r(t)|^2 \rangle \tag{2.32}$$

where $\langle |r(0) - r(t)|^2 \rangle$ is the mean-squared displacement.

2.1.5 The Variational Principle

Now in order to solve the electronic Schrödinger equation (2.11) for an arbitrary molecular system, we need to find the eigenfunctions Ψ_i and corresponding eigenvalues E_i of the Hamiltonian operator $\widehat{H}$ of that system. Once the Ψ_i are determined, all properties of interest can be obtained by applying the appropriate operators to the wave function. The mean value of a particular observable O will be equal to the expectation value of the corresponding appropriate operator $\hat{O}$ by using a normalized wave function.

$$\langle O \rangle = \langle \Psi \left| \hat{O} \right| \Psi \rangle \tag{2.33}$$

The *variational principle*, one of the fundamental principles in all quantum-chemical applications, provides a systematical approach to find the exact wave function of the ground state Ψ_0 i.e. the state that delivers the lowest energy E_0.

The *variational principle* states that the expectation value of the Hamiltonian operator $\widehat{H}$ from any guessed trial wave function Ψ_{trial} will be an *upper bound* to the true energy of the ground state [93]:

$$\langle \Psi_{trial} \left| \widehat{H} \right| \Psi_{trial} \rangle = E_{trial} \geq E_0 \tag{2.34}$$

where the equality hold only if Ψ_{trial} is identical to the exact ground state wave function Ψ_0. The trial wave function must be normalized and must satisfy the appropriate boundary conditions. In the framework of the *variational principle*, we need to minimize the energy functional E [Ψ_{trial}] by searching through all acceptable N-electron wave functions. The minimum value of the energy computed by trial wave function is taken as the variational estimate of the exact ground state energy E_0.

2.2 Electronic Structure Methods

Electronic structure methods use a quantum mechanical approach to solve the electronic Schrödinger equation (2.11) for any molecular system [78, 93-95]. An exact solution to the Schrödinger equation is impossible to compute for most of the complex many-electron systems. However, simple assumptions and procedures make it possible to obtain approximate solutions for such systems. Electronic structure methods are

characterized as *ab-initio* methods or semi-empirical methods depending on the various mathematical approximations to its solution [94]. The former generates solutions without any reference to experimental data. The latter involves fitting to experimental data to simplify the computations. Density Functional methods [93, 94] are another important class of electronic structure methods widely popular these days and are discussed below in Section 2.2.2. The *ab-initio* and semi-empirical methods are considered as wave function methods due to use of approximate wave function to obtain the ground or excited state properties of the system whereas in density functional methods, total electron density fully describes the ground state properties of the system.

2.2.1 Wavefunction Methods

2.2.1.1 The Hartree-Fock Approximation

The Hartree-Fock (HF) method is the central and the simplest *ab-initio* method in quantum chemistry to solve the electronic Schrödinger equation. In HF approximation, an antisymmeterized product of N one-electron wave functions forms the N-electron wave function and is often termed a Slater determinant [78, 93, 94] as given in Equation (2.35).

$$\Psi(\mathbf{x}_1, \mathbf{x}_2, \ldots, \mathbf{x}_N) = (N!)^{-1/2} \begin{vmatrix} \chi_i(\mathbf{x}_1) & \chi_j(\mathbf{x}_1) & \cdots & \chi_k(\mathbf{x}_1) \\ \chi_i(\mathbf{x}_2) & \chi_j(\mathbf{x}_2) & \cdots & \chi_k(\mathbf{x}_2) \\ \vdots & \vdots & & \vdots \\ \chi_i(\mathbf{x}_N) & \chi_j(\mathbf{x}_N) & \ldots & \chi_k(\mathbf{x}_N) \end{vmatrix} \tag{2.35}$$

where the factor $(N!)^{-1/2}$ is a normalization factor. These one-electron functions $\chi_i(\mathbf{x}_i)$ are called molecular spin orbitals, which are composed of the product of a spatial orbital $\phi_i(\vec{r}_i)$ and one of the two spin functions, $\alpha(s\uparrow)\ or\ \beta(s\downarrow)$.
The spatial orbitals as well as spin orbitals are orthonormal such that

$$\int \chi_i^*(\mathbf{x})\chi_i(\mathbf{x})\mathrm{d}\mathbf{x} = \langle\chi_i|\chi_j\rangle = \delta_{ij} \tag{2.36}$$

where the Kronecker delta δ_{ij} equals to 1 for $i = j$ and 0 for $i \neq j$.

The variational principle is used to obtain the lowest energy Slater determinant and the resulting optimized set of molecular orbitals obtained are eigenfunctions of an effective one-electron non-linear Fock operator ($\hat{F}$) where,

$$\hat{F}_i = -\frac{1}{2}\nabla_i^2 - \sum_{A=1}^{M}\frac{Z_A}{r_{iA}} + V_i^{HF}(j) \tag{2.37}$$

where the 'first' and the 'second' term in Equation (2.37) are the one electron terms which correspond to kinetic energy of the electron and the potential energy due to the electron–nucleus interaction, respectively. The third term $V_i^{HF}(j)$ is the Hartree-Fock potential, which accounts for the average repulsion experienced by the i^{th} electron due to the presence of remaining N-1 electrons.

The Hartree-Fock potential $V_i^{HF}(j)$ consists of two components i.e. the Coulomb operator $\hat{J}$ and the Exchange operator $\hat{K}$ and can be written as [93]:

$$V_{HF}(\vec{\mathbf{x}}_1) = \sum_{j}^{N}(\hat{J}_j(\vec{\mathbf{x}}_1) - \hat{K}_j(\vec{\mathbf{x}}_1)) \tag{2.38}$$

The Coulomb operator $\hat{J}$ is defined by its effect on orbital $\chi_i(\vec{\mathbf{x}}_1)$ as:

$$\hat{J}_j(\vec{\mathbf{x}}_1)\chi_i(\vec{\mathbf{x}}_1) = \left[\int |\chi_j(\vec{\mathbf{x}}_2)|^2 \frac{1}{r_{12}} d\vec{\mathbf{x}}_2\right]\chi_i(\vec{\mathbf{x}}_1) \tag{2.39}$$

where it describes the repulsive potential an electron at position $\vec{\mathbf{x}}_1$ in spin orbital χ_i experiences due to the average charge distribution of another electron described by orbital χ_j. Finally, this interaction is integrated over all space and spin coordinates.

The Exchange operator $\hat{K}$ represents the exchange contribution to the HF potential, and has no classical interpretation. It can only be defined through its effect when operating on a spin orbital $\chi_i(\vec{\mathbf{x}}_1)$ as:

$$\hat{K}_j(\vec{\mathbf{x}}_1)\chi_i(\vec{\mathbf{x}}_1) = \int \chi_j^*(\vec{\mathbf{x}}_2)\frac{1}{r_{12}}\chi_i(\vec{\mathbf{x}}_2)\, d\vec{\mathbf{x}}_2\, \chi_j(\vec{\mathbf{x}}_1) \tag{2.40}$$

It is described mathematically that exchange correlation arises due to the antisymmetry of the Slater determinant, and exists only for electrons of like (or parallel) spins as a consequence of the Pauli exclusion principle, that states that two or more electrons of the same spin can't occupy the same spatial orbital.

The Hartree-Fock equation (2.37) is non-linear and therefore we have a pseudo-eigenvalue problem that must be solved iteratively. The technique used for solving the Hartree-Fock equation is called the *self-consistent field* (SCF) procedure since the orbitals are derived from their own effective potential. In this procedure, we start by using a 'guessed' set of orbitals, with which the HF equations are solved. The resulting new set of orbitals is then used in the next iteration and so on until self-consistency is reached i.e. until the spin orbitals used to construct the Fock operator are the same as its eigenfunctions.

2.2.1.2 Linear Combination of Atomic Orbitals (LCAO)

The Hartree-Fock SCF problem is usually solved through the introduction of a finite basis set to expand the molecular orbitals. The molecular orbital can be expanded into a set of atomic orbitals basis functions by using a linear combination of atomic orbitals (LCAO):

$$\phi_i = \sum_{\mu} C_{\mu i} \varphi_{\mu} \tag{2.41}$$

As the basis set φ_{μ} becomes more and more complete, the expansion (2.41) leads to a more accurate representation of the exact molecular orbitals.

Using the Roothaan-Hall approach to solve the HF equation numerically by introducing a set of known spatial basis functions, the differential HF equation can be converted to a set of algebraic *Roothaan-Hall equations* that can be solved by standard matrix techniques [96]. The problem of calculating the Hartree-Fock molecular orbitals is now reduced to the problem of calculating the set of expansion coefficients $C_{\mu i}$.

The Roothaan equations can be written as a single matrix equation [77]

$$\mathbf{FC} = \mathbf{SC\varepsilon} \tag{2.42}$$

where **F** and **S** are the *Fock matrix* and the *overlap matrix* , respectively. The **C** matrix is the matrix of the expansion coefficients, $C_{\mu i}$, which describes the molecular orbitals,

and $\boldsymbol{\varepsilon}$ is a diagonal matrix of the orbital energies ε_i.

2.2.1.3 Basis Sets

A basis set is a set of functions that gives the mathematical description of orbitals within a system where each atom within a molecule is assigned a group of basis functions to approximate its orbitals, as mentioned above in Section 2.2.1.2. Larger basis sets approximate the orbitals more accurately to ensure that it accounts for the regions of space where the electrons are likely to be found i.e. enlarging the basis set helps to reach the complete basis set limit and to perform the quantum chemical calculations with more accuracy [78, 94]. In the early days of quantum chemistry, the Slater type orbitals (STOs) [97] were used as basis functions due to their similarity with the eigenfunctions of the Schrödinger equation for the one electron system, of the form $e^{-\zeta r}$. STOs possess exponential decay at long range and a cusp at short range, and have an advantage in that they have direct physical interpretation. From a computational point of view, the STOs have the severe shortcoming that most of the required integrals are very difficult to compute.

STOs can be approximated as linear combinations of Gaussian orbitals. In the modern computational chemistry, the standard basis set uses basis functions which are composed of a linear combination of gaussian functions of the form $e^{-\alpha r^2}$ to form the orbitals. Such basis functions are termed as contracted functions, and the component gaussian functions are referred to as primitives. A basis function consisted of one gaussian function is termed as uncontracted function.

The minimal basis sets contain the minimum number of basis functions needed to cover all the atomic orbitals for each neutral atom in the molecule. STO-3G is the most common minimal basis set that uses three gaussian primitives per basis function [98]. The one way to improve the basis set for flexible description of the occupied molecular orbitals is by increasing the number of basis functions per atom.

Pople and co-workers [99-101] introduced split valence basis sets with the typical notation X-YZG for split-valence double zeta (DZ) basis set, where X represents the number of primitive gaussians comprising each core atomic orbital basis function, Y and Z tells that each valence orbital is composed of two basis functions of different size, where the first basis function is composed of linear combination of Y primitives gaussian functions and the second basis function is composed of linear combination of Z primitives gaussian functions. The 3-21G and 6-31G are commonly known split-

valence double-zeta (DZ) basis sets. Similarly split-valence triple-zeta (TZ) basis sets such as 6-311G, use three different size basis functions for each valence atomic orbital.

Further improvements in the basis set can be performed by introducing polarization functions [102, 103] i.e. by adding functions of higher angular momentum than the highest occupied orbitals in the neutral atom that allow orbitals to change shape. For example, polarized basis sets add *p*-functions to hydrogen, *d*-functions to carbon, nitrogen etc., and *f*- functions to transition metals. The most commonly used polarized basis set for medium sized systems is 6-31G(d) basis set, also known as 6-31G*, is the Pople-type 6-31G basis set with *d*-functions added to heavy atoms. Another popular polarized basis set is 6-31G(d,p), also written as 6-31G**, which add *p*-functions to hydrogen atoms in addition to *d*-functions on all other atoms.

Further basis set variations can be brought about by the inclusion of diffuse functions [104] which are large size versions of s and p functions that allow orbitals to occupy larger region of space. For example, the 6-31+G(d) basis set is the 6-31G(d) basis set with diffuse functions added on non hydrogen atoms, denoted by plus (+) sign in Pople-type basis set. The double plus (++) sign in basis set 6-31++G(d) indicates that diffuse functions are added to the hydrogen atoms as well. Diffuse functions are very important for systems where electrons are relatively far from the nucleus such as molecular system with significant negative charge, molecules with lone pairs, anions, systems in their excited state and so on.

Some of the most widely used basis sets are developed by Dunning and coworkers, [105-107] which converge to the complete-basis-set (CBS) limit. These are known as correlation-consistent polarized-valence X-zeta (cc-pVXZ) basis set, where X is called the cardinality of the basis (double, triple, quadruple,…). Here each higher level involves the addition of one set of higher angular momentum functions, and the addition of another set of functions for each angular momentum already present i.e. they include successively larger shells of polarization functions (*d, f, g,* etc.). The augmented version further adds diffuse functions to the cc-pVXZ basis set, termed as aug-cc-pVXZ basis set. We have often employed these basis sets for geometry optimization of complex systems as well as for calculating excitation energies, which are often used for high level calculations on complex systems.

2.2.1.4 Basis Set Superposition Error (BSSE)

For most of the quantum chemistry calculations, it is not practical to use a complete basis set, as it is computationally very demanding. Therefore, using finite basis sets can lead to basis set superposition error (BSSE). BSSE is zero in the limit of a complete basis set, and adding more basis functions will not give any improvement. When the atoms of interacting molecules (or of different parts of the same molecule) approach one another, their basis functions overlap. For example, in the dimer, basis functions from one molecule can help compensate for the basis set incompleteness on the other molecule, and vice versa, thus effectively increasing its basis set and improving the calculation of derived properties such as energy.

One way of assessing BSSE is the *Counterpoise* (CP) correction [108]. In this method the BSSE is estimated as the difference between monomer energies with the regular basis and the energies calculated with the full set of basis functions for the whole complex [94]. Four additional energy calculations are required to calculate counterpoise energy correction ΔE_{CP}, which is defined in equation (2.43).

$$\Delta E_{CP} = E(A)^*_{ab} + E(B)^*_{ab} - E(A)^*_a - E(B)^*_b \tag{2.43}$$

The energies of fragment A and B are calculated using the basis set *a* and *b,* respectively, for molecule A and B, and the energies of each of the two fragments are calculated with the geometry they have in the complex, also these geometries in the complex environment are indicated by * symbol. Other two additional energy calculations of each of the fragments at the complex geometry are then obtained using the full *ab* basis set. This implies that the energy of A is calculated in the presence of both the normal *a* basis functions and with the *b* basis functions of fragment B, but without the B nuclei present, and vice versa. Such basis functions are often referred to as ghost orbitals that are located at fixed points in space. Thus the fragment energy for A will be lowered due to these ghost functions, since a basis becomes more complete. The complexation energy or binding energy of the AB complex is given in equation (2.44).

$$\Delta E_{complexation} = E(AB)^*_{ab} - E(A)_a - E(B)_b \tag{2.44}$$

The counterpoise energy correction ΔE_{CP} is then subtracted from the complexation energy to get the counterpoise-corrected complexation energy, $\Delta E_{complexation} - \Delta E_{CP}$. It is usual to find that the CP correction is larger for methods including electron correlation than at the HF (or DFT) level.

2.2.1.5 Electron Correlation

As discussed above in Section 2.2.1.1, in the Hartree-Fock method, each electron moves in an average field of all the other electrons and this time-averaged field approximates the exact instantaneous electron-electron repulsions, which leads to HF energy E_{HF} always larger (i.e. less negative) than the exact ground state energy E_0. This energy difference is called the correlation energy, which is a measure of error introduced through the HF scheme [94]:

$$E_{corr}^{HF} = E_0 - E_{HF} \tag{2.45}$$

In the Hartree-Fock scheme, the electrons are allowed to approach each other more closely than they should, which causes the electron-electron repulsion term to be too large resulting in $E_{HF} > E_0$. The electron correlation effects are manifested as *static* and *dynamic* correlation. *Static* correlation is important when there exist more than one non-equivalent configurations of similar magnitude in the wave function, whereas *dynamic* correlation accounts for the instantaneous Coulomb repulsion between electrons and consists of lots of small corrections to qualitatively correct wave functions.

There has been an extensive research in the development of methods to determine the electron correlation contributions accurately, and is still an active research area in the computational quantum chemistry.

2.2.1.6 Configuration Interaction (CI) Method

In order to properly account for the electron correlation effects, the Configuration Interaction (CI) method was developed, in which the many–electron wave function can be written as a linear combination of all substituted configurations (single, double, triple, etc.) that can be obtained by promoting electrons from occupied HF orbitals to virtual (empty) orbitals [94] :

$$\Psi^{CI} = \left(1 + \sum_{i}^{occ}\sum_{a}^{vir} c_i^a \ \Psi_i^a + \sum_{i<j}^{occ}\sum_{a<b}^{vir} c_{ij}^{ab} \ \Psi_{ij}^{ab} + \cdots\right)\Psi^{HF} \tag{2.46}$$

where Ψ^{HF} → HF reference determinant;

Ψ_i^a → Singly excited HF determinant (one electron from a doubly occupied molecular orbital within HF determinant swapped with a virtual orbital);

Ψ_{ij}^{ab} → Doubly excited HF determinant (two electrons from doubly occupied molecular orbitals swapped with two virtual orbitals);

$c_i{}^a$, c_{ij}^{ab},…. → CI expansion coefficients.

If CI expansion coefficients are optimized over all possible configurations for all states using the *variational* principle, one can obtain the exact wave function such that these optimal CI coefficients yield the wave function with the lowest energy. As the one-electron basis set approaches completeness, *the basis set correlation energy* i.e. the difference between the lowest eigenvalue obtained by performing a full CI and the Hartree-Fock ground state energy within the same basis set approaches the exact correlation energy [77]. This is considered as a benchmark to compare correlation energies calculation by other computational methods. Since the number of possible configurations grows very quickly as the basis functions used to describe orbitals are increased, it is a computationally prohibitive task to obtain exact full CI wave function for larger systems. Thus, it is practical to truncate CI wave function by adding only limited set of substituted configurations to HF reference i.e. by using methods like CIS (CI-Singles), CISD (CI-Singles and Doubles), CISDT (CI-Singles, Doubles and Triples), *etc.* However, the drawback of all these limited CI methods is that they are not *size-consistent* as now the energy of the system is not proportional to number of molecules in the system [77, 95].

2.2.1.7 Complete active space self-consistent field (CASSCF) method

There is one method that incorporates a full CI, named as the complete active space self-consistent field (CASSCF) method. The orbitals involved in the CI are known as active orbitals that exclude inner shell (fully occupied) orbitals and part of unoccupied high-energy orbitals of molecule (virtual orbitals) in all possible configurations and a

full CI is performed on this active space involving subset of orbitals [78, 94]. CASSCF method optimizes the active orbitals variationally for the CI wave function, in addition to the CI expansion coefficients.

CASSCF is an extremely flexible method and can be used for describing any kind of chemical bonding across the PES. It recovers some electron correlation, primarily 'static correlation' as it deals with many configurations and is also considered effective in correctly describing systems, for which HF does not give a correct reference wave function i.e. for describing ground degenerate states, bond breaking situation and modelling excited states.

2.2.1.8 Møller-Plesset (MP) Perturbation Theory

Another wave-function approach to account for the electron correlation is the Møller-Plesset (MP) perturbation theory [109], a post-HF method based on perturbation technique. It is based on adding electron-correlation effects to HF method by using the technique of Rayleigh-Schrödinger perturbation theory [77, 94].

The Hamiltonian is partitioned into two parts

$$\hat{H} = \hat{H}_0 + \lambda \hat{V} \tag{2.47}$$

where $\hat{H}_0$ is defined as the sum of one-electron Fock operators [77]

$$\hat{H}_0 = \sum_i \hat{F}^i = \sum_i [h_i + V_i^{HF}(j)] \tag{2.48}$$

and $'\lambda V'$ is the small perturbation applied to H_0 which accounts for the electron-correlation , where $'\lambda'$ is a parameter which is the measure of perturbation.

The perturbation operator $'\hat{V}'$ can be defined as

$$\hat{V} = \sum_{i<j} r_{ij}^{-1} - \sum_i V_i^{HF}(j) \tag{2.49}$$

The perturbed wave function and energy can be expressed as a power series in $'\lambda'$ as

$$\Psi_i = \Psi_i^{(0)} + \lambda^1\Psi_i^{(1)} + \lambda^2\Psi_i^{(2)} + \lambda^3\Psi_i^{(3)} \ldots \tag{2.50}$$

and

$$E_i = E_i^{(0)} + \lambda^1 E_i^{(1)} + \lambda^2 E_i^{(2)} + \lambda^3 E_i^{(3)} + \cdots \tag{2.51}$$

Thus on substituting these equations in time independent Schrödinger equation

$$\widehat{H}\Psi_i = E_i\,\Psi_i \tag{2.52}$$

and expanding the products and equating the coefficients on both sides of equation for each power of λ, leads to equations representing successively higher orders of perturbation. By solving these equations using properties of ortho-normality of $'\Psi'$ and hermiticity of $\widehat{H}_0$ operator, we get Hartree-Fock energy as

$$E_i^{HF} = E_i^{(0)} + E_i^{(1)} \tag{2.53}$$

where $E_i^{(0)}$ is given as

$$E_i^{(0)} = \langle\Psi_i^{(0)}\big|\widehat{H}_0\big|\Psi_i^{(0)}\rangle \tag{2.54}$$

and $E_i^{(1)}$ is given as

$$E_i^{(1)} = \langle\Psi_i^{(0)}\big|\widehat{V}\big|\Psi_i^{(0)}\rangle \tag{2.55}$$

By adding first perturbation to HF energy i.e. $E_i^{(2)}$ to E^{HF} yields MP2 energy, where MP2 is the second-order Møller-Plesset perturbation theory.

$$E_i^{MP2} = E_i^{HF} + E_i^{(2)} \tag{2.56}$$

where second-order energy $E_i^{(2)}$ is given as

$$E_i^{(2)} = \langle\Psi_i^{(0)}\big|\widehat{V}\big|\Psi_i^{(1)}\rangle = \sum_{n\neq i}\frac{\left|\langle\Psi_i^{(0)}\big|\widehat{V}\big|\Psi_n^{(0)}\rangle\right|^2}{E_i^{(0)} - E_n^{(0)}} \tag{2.57}$$

where $\Psi_i^{(1)}$ is expanded in the terms of the eigenfunctions of $\widehat{H}_0$, which are taken to be complete,

$$\Psi_i^{(1)} = \sum_n c_n^{(1)} \Psi_n^{(0)} \tag{2.58}$$

The first correction to the HF energy is always negative, thus lowering the total energy and this correction accounts for electron-correlation effects. Similarly higher order term corrections give the MP3, MP4, MP5 methods, which may not necessarily be convergent at higher orders. It is found that convergence can be slow, rapid, oscillatory, regular, highly erratic or simply non-existent, depending on the precise chemical system or basis set .

MP2 typically accounts for 80-90% of the correlation energy [94], and is a good standard method to estimate the energies of the loosely bound systems by properly accounting for the electron-correlation effects. Furthermore, MP2 represents a qualitatively superior alternative to the density functional methods to model dispersion (van der Waals) interactions [110, 111]. MP2 has been used extensively in computational chemistry as a benchmark method and is considered reliable for ground state geometry optimizations and to estimate the energies of loosely bound hydrogen bonded and dispersion bound complexes [112]. Although performance of MP2 methods for properties involving making or breaking electron pairs is substantially inferior to that of coupled cluster CCSD(T) and the best DFT methods, MP2 methods are generally useful for studying nonbonded interactions in both small and large systems and perform extremely well if one extrapolates to the basis set limit [113-115]. Such calculations are highly relevant in biological and materials science problems. We have also used this method for ground state geometry optimizations as well for calculating binding energies for our cluster systems.

2.2.1.9 Coupled Cluster Method

One of the popular wave function methods is the coupled cluster (CC) method that accounts for the electron correlation efficiently using the exponential cluster operator to construct the multi-electron wave function [94].

The excitation operator $\boldsymbol{T}$ can be defined as

$$\boldsymbol{T} = \boldsymbol{T_1} + \boldsymbol{T_2} + \boldsymbol{T_3} + \ldots + \boldsymbol{T_{N_{elec}}} \tag{2.59}$$

where the $\boldsymbol{T_i}$ operator acts on the Hartree-Fock reference wave function Ψ_0 to generate all the i^{th} excited Slater determinants.

$$\boldsymbol{T_1}\Psi_0 = \sum_{i}^{occ}\sum_{a}^{vir} t_i^a \ \Psi_i^a \tag{2.60}$$

$$\boldsymbol{T_2}\Psi_0 = \sum_{i<j}^{occ}\sum_{a<b}^{vir} t_{ij}^{ab} \ \Psi_{ij}^{ab} \tag{2.61}$$

where t represents the expansion coefficients, often termed as *amplitudes* in the CC method.

The configuration interaction (CI) wave function can be written as

$$\Psi_{CI} = (1 + \boldsymbol{T})\Psi_0 = (1 + \boldsymbol{T_1} + \boldsymbol{T_2} + \boldsymbol{T_3} \ + \ \ldots)\Psi_0 \tag{2.62}$$

On the other hand, the coupled cluster (CC) wave function is defined as

$$\Psi_{CC} = e^{\boldsymbol{T}}\Psi_0 \tag{2.63}$$

where exponential function can be expanded as a Taylor series:

$$e^{\boldsymbol{T}} = 1 + \frac{\boldsymbol{T}}{1!} + \frac{\boldsymbol{T}^2}{2!} + \frac{\boldsymbol{T}^3}{3!} + \cdots \ + \sum_{k=0}^{\infty}\frac{1}{k!}\boldsymbol{T}^k \tag{2.64}$$

Using equation (2.59) and (2.64), exponential cluster operator can be written as

$$e^{\boldsymbol{T}} = 1 + \boldsymbol{T}_1 + \left(\boldsymbol{T}_2 + \frac{1}{2}\,\boldsymbol{T}_1^2\right) + \left(\boldsymbol{T}_3 + \boldsymbol{T}_2\,\boldsymbol{T}_1 + \frac{1}{6}\boldsymbol{T}_1^3\right) + \left(\boldsymbol{T}_4 + \boldsymbol{T}_3\,\boldsymbol{T}_1 + \frac{1}{2}\boldsymbol{T}_2^2 + \frac{1}{2}\boldsymbol{T}_2\boldsymbol{T}_1^2 + \frac{1}{24}\boldsymbol{T}_1^4\right) + \cdots \tag{2.65}$$

, and the coupled cluster (CC) wave function becomes

$$\Psi_{CC} = \left(1 + \boldsymbol{T}_1 + \left(\boldsymbol{T}_2 + \frac{1}{2}\,\boldsymbol{T}_1^2\right) + \left(\boldsymbol{T}_3 + \boldsymbol{T}_2\,\boldsymbol{T}_1 + \frac{1}{6}\boldsymbol{T}_1^3\right) + \left(\boldsymbol{T}_4 + \boldsymbol{T}_3\,\boldsymbol{T}_1 + \frac{1}{2}\boldsymbol{T}_2^2 + \frac{1}{2}\boldsymbol{T}_2\boldsymbol{T}_1^2 + \frac{1}{24}\boldsymbol{T}_1^4\right) + \cdots\right)\Psi_0 \tag{2.66}$$

The first term in Equation (2.66) generates the reference HF, and the second term gives all singly excited states. The first contribution in parenthesis in Equation (2.66) generates all doubly excited states whereas the second and third contributions in parenthesis generate all triply and quadruply excited states respectively. Thus, additional terms at each excitation level are seen in the CC wave function in Equation (2.66) that arise due to the product of excitations, as compared to CI wave function shown in Equation (2.62).

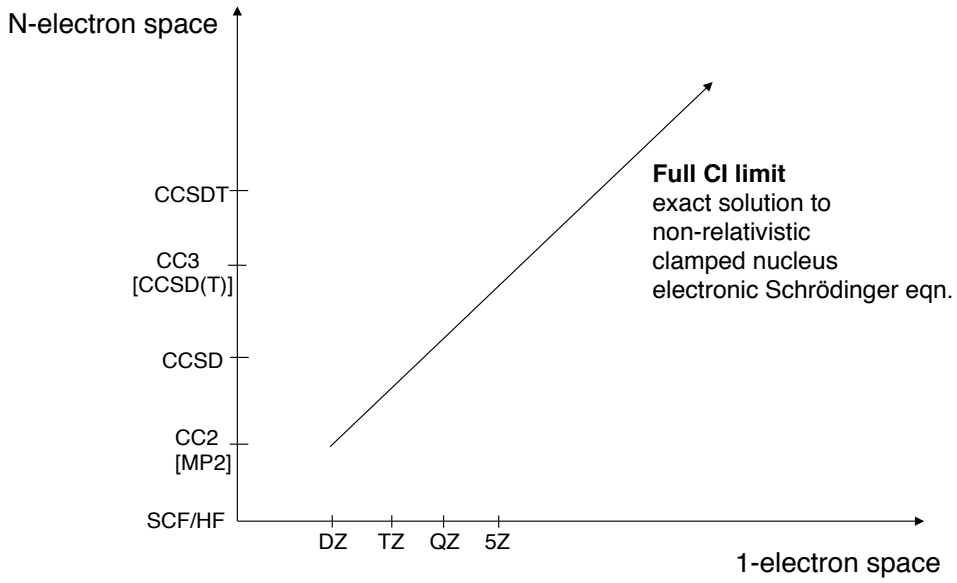

Figure 2.2 Two dimensional map illustrating the accuracy of coupled cluster methods against the quality of basis set from double zeta (DZ) to an infinite basis set and the full CI limit for the energy or any molecular property of the system.

The coupled cluster wave function is equivalent to full CI, if all the cluster operators up to $\boldsymbol{T}_N$ are included in **T,** as shown in Figure 2.2. However, this is impossible for all systems but the smallest systems. Analogous to CI method, the wave function needs to be truncated at some excitation level for CC method. Using $\boldsymbol{T} = \boldsymbol{T}_1 + \boldsymbol{T}_2$ in the $e^{\boldsymbol{T}}$operator gives the *Coupled Cluster Singles and Doubles* (CCSD) model [116], while using $\boldsymbol{T} = \boldsymbol{T}_1 + \boldsymbol{T}_2 + \boldsymbol{T}_3$ gives the *Coupled Cluster Singles, Doubles and Triples* (CCSDT) model [117]. CCSDT method is more expensive than CISDT method. CCSD in general is the most applicable method as higher orders such as CCSDT, CCSDTQ, *etc*. can only be used for very small systems, being computationally very demanding. Furthermore, two intermediate coupled cluster methods have been introduced, known as CC2 [118], and CC3 [119, 120]. The CC2 method is an approximation to the full

CCSD model, where the doubles contribution is approximated by the expression arising from the lowest non-vanishing order in Møller-Plesset (MP) perturbation theory. CC2 may loosely be defined as MP2 with the added feature of orbital relaxation arising from the singles. Similarly, CC3 is derived from full CCSDT by only including the triple contribution arising from the lowest non-vanishing in perturbation theory [94].

One important feature of CC methods is that excitations of higher order than the truncation of the $\boldsymbol{T}$ operator enter the amplitude equation. It is the inclusion of these products of excitations that makes coupled cluster theory size extensive, which is one of the advantages of using CC methods over CI methods.

2.2.2 Density Functional Methods

An alternative to the expensive wave function methods such as post Hartree-Fock methods MP2, configuration interaction (CI), multi-reference CI and coupled cluster CC) methods, is to use density functional methods to determine *electron correlation* effects efficiently. Density Functional Theory (DFT) has become the most successful and versatile quantum mechanical approach to study the electronic structure of matter. It can compute a great variety of ground state molecular properties i.e. molecular structures, vibrational frequencies, ionization energies, reaction paths, *etc.* at a relatively low computational cost as compared to other wave function methods.

The basis for DFT is the proof by Hohenberg and Kohn [121], which states that *the ground state electronic energy is determined completely by the electronic density ρ.* In wave function methods, the H_{elec} for an N-electron system depends on 4N variables (3N spatial and N spin variables), but electronic density depends on the same number of three spatial coordinates, independent of system size and therefore it avoid becoming increasingly complicated as the system increases in size. The goal of DFT methods is to find the exact form of a functional that connects the electron density with the energy [93], which is yet unknown.

2.2.2.1 Hohenberg- Kohn (HK) Theorems

The First HK-Theorem

It states that the external potential V_{ext} is a unique functional of the electron density ρ; since, in turn this potential fixes $\widehat{H}$, we see that the full many particle ground state is a unique functional of electron density [121]. Since the complete ground state energy is a

functional of the ground state electron density so must be its individual components,

$$E_0[\rho_0] = \int \rho_0(\vec{r}) V_{Ne}\, d\vec{r} + T[\rho_0] + E_{ee}[\rho_0] \tag{2.67}$$

The first term in Equation (2.67) is the potential energy due to the nuclei-electron attraction i.e. here $V_{ext} = V_{Ne}$ and depends on the system via N, $R_{A,}$ and $Z_{A.}$ The second and third terms which correspond to the kinetic energy of electrons and energy due to the electron-electron repulsion respectively, are system independent and can be collectively defined in the form of the Hohenberg-Kohn functional $F_{HK}[\rho_0]$,

$$F_{HK}[\rho_0] = T[\rho_0] + E_{ee}[\rho_0] \tag{2.68}$$

The Second HK-Theorem

This theorem states the *variational principle* that an energy functional $E^{HK}[\rho]$ delivers the lowest ground state energy E_0 if the true ground state density ρ_0 is used as a trial density [121].

$$E_{HK}[\rho] = \int \rho(\vec{r}) V_{Ne}\, d\vec{r} + F_{HK}[\rho] \geq E_0\,[\rho_0] \tag{2.69}$$

2.2.2.2 Kohn Sham Formalism

In modern DFT, the real system is replaced by a fictitious non-interacting system of same density as the real system, as suggested by Kohn and Sham (1965) [122]. In non-interacting system of electrons, electrons do not interact among themselves. The Hamiltonian for such a system can be expressed as a sum of one-electron operators, and has eigenfunctions that are Slater determinants of the individual one-electron eigenfunctions, and has eigen values that are simply the sum of the one-electron eigen values [78].

In the Kohn Sham formalism, the connection of this fictitious non-interacting system to the real system of interacting electrons is established by an introduction of Kohn-Sham orbitals φ_i and by choosing an effective external potential V_{ext} such that the electron density resulting from the summation of the moduli of the squared orbitals φ_i is same as the ground state density of the real system of interacting electrons.

The total electron density is then represented as [93]

$$\rho(r) = \sum_{\sigma} \sum_{i}^{occ} |\varphi_i(r,\sigma)|^2 \tag{2.70}$$

where $\varphi_i(r,\sigma)$ denotes Kohn-Sham orbitals. Here σ and r are the spin and position coordinates of the electrons, respectively.

The general DFT energy expression [94] is written as

$$E[\rho] = T_S[\rho] + E_{Ne}[\rho] + J[\rho] + E_{xc}[\rho] \tag{2.71}$$

where T_S : the kinetic energy of all electrons determined from a single Slater determinant;

E_{Ne} : the standard Coulomb electron-nuclei interaction term;

J : the classical Coulomb electron-electron repulsion term.

E_{xc} : an *exchange correlation* energy that includes kinetic correlation energy (that is not covered by T_S), potential correlation and exchange energy.

The minimization of the Kohn-Sham (KS) functional with respect to electron density leads to the Kohn-Sham equations,

$$\left(-\frac{1}{2}\nabla^2 - \sum_{A} \frac{Z_a}{|r_1 - R_A|} + \int \frac{\rho(r_2)}{|r_1 - r_2|} dr_2 + V_{XC}(r) \right) \varphi_i^{KS} = \varepsilon_i^{KS}\, \varphi_i^{KS} \tag{2.72}$$

whose solution yields Kohn-Sham orbitals $\varphi_i(r,\sigma)$ where

$$V_{XC}(r) \equiv \frac{\delta E_{XC}}{\delta \rho} \tag{2.73}$$

termed as exchange–correlation potential, is the functional derivative of E_{XC} with respect to ρ.

The total electronic energy is determined by solving KS equation under a self-consistent field (SCF) procedure (until ρ converges) and the converged ρ gives the total electronic energy from the energy expression given in Equation (2.71). The main goal of modern DFT is to find better approximations to the unknown functional E_{xc} and the corresponding potential V_{XC}, which would lead to exact energy, i.e. the correct

eigenvalue of the Hamiltonian operator of the Schrödinger equation and hence could describe the real system.

2.2.2.3 Exchange-Correlation Functionals

The exchange correlational functional E_{xc} is a unique mathematical form, whose form differs for different DFT methods [94]. The functional dependence of E_{xc} (sum of both exchange and correlation energy) on the electron density is often expressed in terms of energy per particle i.e. energy density ε_{xc}.

$$E_{xc}[\rho(r)] = \int \varepsilon_{xc}\,[\rho(r)]\rho(r)\,dr = \int \varepsilon_x\,[\rho(r)]\rho(r)\,dr + \int \varepsilon_c\,[\rho(r)]\,\rho(r)\,dr \tag{2.74}$$

Local Density approximation (LDA) functional

In LDA, the functional ε_{xc} depends only on the density at each point, i.e. $\rho(r)$, the local value of ρ, under the assumption that the density locally can be treated as a uniform electron gas. There has been development of many LDA exchange and correlation functionals [123], but this approach based on 'uniform electron density' approximation has certain limitations, usually resulting in strong over-binding in molecules. Thus it could be applied only for those systems where assumption of slow varying electron density is valid.

Generalized gradient approximation (GGA) functional

The improvement over the LDA approach is done by introduction of generalized gradient approximations (GGA's) in 1988 where the functional depends on both density, $\rho(r)$ and its gradients, $\nabla\rho(r)$ at each *r*. Becke, [124] developed the widely popular GGA exchange functional (B or B88) as a correction to LDA exchange energy which is often combined with the popular 'LYP' correlation functional by Lee, Yang and Parr, [125] to obtain BLYP calculation. The PBE, PW91, KT3 are some other popular GGA's functional.

Meta-GGA (MGGA) functional

The next step in the improvement of GGA's functional involved the capture of more non-local effects which led to the development of MGGA functionals [94], that allow exchange and correlation functionals to depend also on second order derivative of the electron density ($\nabla^2\rho$) i.e. the Laplacian, along with $\rho(r)$ and its gradient $\nabla\rho(r)$. Alternatively, in MGGA formalism, the functional dependence on the orbital kinetic-energy density 'τ' can be included, and τ is defined as

$$\tau(r) = \frac{1}{2}\sum_{i}^{occ} |\nabla\varphi_i(r)|^2 \tag{2.75}$$

where the $'\varphi'$ are the Kohn-Sham orbitals.

BR, B95, VSXC, PKZB, TPSS, t-HCTH are well developed meta-GGA functionals. Meta-GGA calculations are found to be more accurate than GGA calculations at the same computational cost.

Hybrid Functionals

Hybrid functionals include a mixture of Hartree-Fock (HF) exchange with DFT exchange-correlation, which can be written as

$$E_{XC} = aE_X^{HF} + (1-a)E_{XC}^{DFT} \tag{2.76}$$

where 'a' is an empirical constant to be optimized. Hybrid methods are also termed as adiabatic connection methods that connect the non-interacting system with the real system.

Becke in 1993, [126] first introduced the three parameter hybrid functional 'B3PW91' and then Stephens *et al.* [127] modified this functional to produce the most popular B3LYP (Becke, three-parameter, Lee-Yang-Parr) functional which is defined as

$$E_{XC}^{B3LYP} = (1-a)E_X^{LSDA} + aE_x^{HF} + bE_X^{B88} + (1-c)E_c^{LSDA} + cE_c^{LYP} \tag{2.77}$$

where a, b and c constants have typical values of a ~ 0.2, b ~ 0.7 and c ~ 0.8, and depends on the form of chosen GGA exchange E_x^{GGA} and correlational functional E_c^{GGA}.

E_X^{B88}corresponds to the Becke 88 exchange functional. It is found that the inclusion of exact HF exchange improves the calculated results quite often, where B3LYP functional incorporates 20% of exact Hartree-Fock exchange.

A further development in hybrid functionals is by Truhlar and co-workers, [128, 129] who developed meta-hybrid functionals such as M05, M05-2X, along with the M06 suite of functionals M06, M06-2X and M06-HF, which differ by the amount of exact Hartee-Fock exchange they incorporate into the exchange-correlation functional. M06 incorporates 27% of exact HF exchange, whereas M06-2X and M06-HF contains 54% and 100% of exact HF exchange, respectively. The suite of M06 functionals, being highly non-local, are found to perform fairly well than the standard hybrids for systems involving non-covalent interactions, and modelling electronic excitation energies to valence and Rydberg states. In order to correctly account for the non-Coulomb part of exchange functionals, which typically dies off too rapidly and gives inaccurate results at large distances, the long-range corrected functionals were introduced [130-132]. LC-wPBE, Coulomb-attenuating method CAM-B3LYP, wB97X, wB97XD are some well-developed long range corrected functionals where wB97XD functional also include empirical atom-atom dispersion corrections [130].

Further addition to hybrid functionals is the double hybrids, which combine exact HF exchange with an MP2-like correlation to a DFT calculation. B2PLYP, B2PLYPD are some of the popular double hybrids, where B2PLYPD also includes empirical dispersion [133]. These double hybrid calculations are computationally very expensive for larger systems as it scales as MP2 rather than DFT.

2.3 Force Field or Molecular Mechanics (MM) methods

Another popular branch of computational methods for molecular modelling is the Force field method, also referred as Molecular Mechanics (MM) method that use the laws of classical physics to predict the structures and properties of molecules. The “building blocks” in force field methods are atoms, where the molecules are treated as mechanically connected systems of atoms. MM calculations are based upon the interactions among nuclei. The electrons are not treated explicitly as being not considered as individual particles in MM theory and thus electronic effects are implicitly included in force fields via its parameterization.

Many molecular mechanics methods were developed with each one characterized by different force fields [134-142]. The parameter sets and functional form of

interatomic potential are usually empirical as they are based on numerous approximations and derived from different types of experimental data.

In general, the total force field or MM energy of the molecular system can be written as sum of different interaction terms, each describing different types of strain possible in a molecular system [94].

$$E_{MM} = E_{stretch} + E_{bend} + E_{torsion} + E_{oop} + E_{cross} + E_{vdW} + E_{ES} \qquad (2.78)$$

where $E_{stretch}$ represents the energy function for stretching a bond between two atoms, E_{bend} is the energy required for bending an angle, $E_{torsion}$ is the torsional energy for rotation around a bond, and E_{oop} and E_{cross} describes out-of-plane bending and bond-angle cross coupling, respectively. The last two terms E_{vdW} and E_{ES} correspond to the non-bonded atom-atom interactions i.e. van der Waals (vdW), and electrostatic contributions, respectively.

Most standard force fields use a "fixed atomic point charge" model where each atom is assigned a fixed value for the atomic charge; it is thus the use of the fixed charges that the atom is unable to respond directly to the molecular environment and remain unaffected by the local electrostatic environment. Non-polarizable (fixed charge) models cannot fully capture many-body effects such as electronic polarization. Extensive research and developments in force fields have led to models that account for many-body effects via electronic polarization in which a particle's charge is influenced by electrostatic interactions with its neighbours. Polarizable empirical force fields offer a clear and systematic improvement in functional form over fixed charge models [143-145]. Some popular polarizable bio-molecular force fields are from the Amber, CHARMM, and OPLS/PFF, and AMOEBA consortia. The quality of a force field calculation depends on the appropriateness of the mathematical form of the energy expression, and the accuracy of the parameters. The main advantage of force field methods is the speed with which calculations can be performed that makes molecular mechanics computations quite inexpensive in computational time, and that also enables MM methods to treat very large systems containing thousands of atoms.

2.3.1 AMOEBA Force Field

The AMOEBA polarizable force field has been explained in detail in literature [143, 144, 146, 147]. For this potential energy model, the total interaction energy among atoms is expressed as

$$U = U_{bond} + U_{angle} + U_{b\theta} + U_{oop} + U_{torsion} + U_{vdW} + U_{elec}^{perm} + U_{elec}^{ind} \quad (2.79)$$

where the first five terms describe the short-range valence interactions corresponding to the bond stretching, angle bending, bond-angle cross coupling, out-of-plane bending, and torsional rotation, respectively. The last three terms correspond to the nonbonded interactions i.e. van der Waals (vdW), permanent electrostatic, and induced electrostatic contributions.

In AMOEBA, the pairwise additive vdW is described by Halgren's buffered 14-7 function [148], that yields a slightly "softer" repulsive region than the Lennard-Jones 6-12 function, but a steeper repulsion at very short range than typical Buckingham exp-6 formulations. AMOEBA utilizes permanent electrostatic multipole moments through the quadrupole at each atom [143, 144], and atomic multipole moments are derived from high-level *ab initio* quantum mechanical calculations of the small molecules using Stone's distributed multipole analysis (DMA) [149, 150]. The inclusion of permanent dipoles and quadrupoles allows for an accurate description of molecular electrostatic potentials and errors in the molecular electrostatic potential are shown to reduce by orders of magnitude upon complementing atomic monopoles with dipole and quadrupole moments [151-153].

AMOEBA force field has shown significant improvement over fixed charge (nonplarizable) models by explicitly including many-body effects such as electronic polarization [143, 144, 154], and treats both intra- and intermolecular polarization consistently via Thole's damped interactive induction models based upon distributed atomic polarizabiltities [155]. In this interactive induction scheme, an induced dipole produced at any site further polarize all other sites, and such mutual induction continues until the induced dipoles at each site reach convergence. One key feature of Thole's model is that point dipole interactions are replaced with interactions between smeared dipoles to produce damping of polarization interaction at very short range to avoid the so-called polarization catastrophe and thus, yields the energies in better agreement with *ab initio* results.

Successful applications of AMOEBA force field to study the wide range of properties of gas-phase clusters, liquid water, and ice crystals have been given in several publications [144-146].

In this thesis, the AMOEBA force field is used for the ONIOM(QM:MM) calculations for ground state geometry optimizations of benzene bound ice clusters.

2.3.2 Water Models

Water, due to its highly polarizable, hydrogen bonded nature and other interesting properties, has been the focus of many experimental and computational studies. In computational chemistry, many different types of water models have been developed to study and explore the structure and properties of water [156-162]. These water models are used for the simulation of liquid water, water clusters, aqueous solutions, *etc*. Further such models can be distinguished depending upon number of interaction points (sites), nature of the model whether rigid or flexible, and accountability of the polarization effects in the water model.

The simplest water models are rigid in nature, which rely on the non-bonding interactions, where bonding interactions are treated implicitly. Coulomb's law models the electrostatic interactions, whereas dispersion and repulsive interactions are modeled by the Lennard-Jones (12-6) potential. The potential for models such as TIP3P and TIP4P can be represented as

$$E_{pq} = \sum_{i}^{p} \sum_{j}^{q} \frac{k_C q_i q_j}{r_{ij}} + \frac{A}{r_{OO}^{12}} - \frac{B}{r_{OO}^{6}} \tag{2.80}$$

where k_C ~ 332.1 Å kcal/mol is the electrostatic constant; q_i represent the partial charges relative to the charge of the electron; r_{ij} gives the distance between two atoms or charged sites; and A and B are the Lennard-Jones parameters. In most water models, the Lennard-Jones term applies only to the interaction between the oxygen atoms.

The three-site models are one of the popular water models that are computationally efficient, and are widely applicable in many molecular simulations. In the three-site model, there are three interaction sites corresponding to the three atoms of the water molecule, with each site carrying a point charge [161, 162]. Some popular 3-site models are SCP, SCP/E, TIP3P, *etc*. In the CHARMM force field, slightly modified TIP3P potential model is implemented, where Lennard-Jones parameters are placed on the

hydrogen atoms too, in addition to the one on oxygen [163]. Most of the 3-site models use a rigid geometry as of the actual water molecules, except the SCP (single point charge) model. In SCP model, water has an ideal tetrahedral shape with HOH angle of 109.47° instead of the observed angle of 104.5°, whereas with a further refinement SPC/E model also adds an average polarization correction to the potential energy function. Further improvement is the flexible SPC water model developed after the re-parameterization of the three-site SPC water model, which accounts flexibility. An anharmonic O-H stretching is considered and thus the dynamical behaviour is well described.

In the four-site models, one dummy atom (X) is added near the oxygen atom along the bisector of the HOH angle of the three-site models such that the electrostatic distribution around the water molecule is improved [156-158, 164]. The dummy atom carries a negative charge. The 4-site TIP4P model is widely used for the simulation of biomolecular systems. There have been significant developments in TIP4P models by subsequent re-parameterization, and some popular models are the TIP4P-Ew model, the TIP4P/Ice, TIP4P/2005, TIP4P/2005f, *etc.* The parameters for some of the 3-site and 4-site water models are listed in Table 2.1.

Table 2.1 The parameters for some of the 3-site and 4-site water models.

	SPC/E [161]	**TIP3P** [160]	**TIP4P** [165]	**TIP4P/2005** [157]	**TIP4P/2005f** [166]
$r_{(OH)}$, Å	1.0	0.9572	0.9572	0.9572	0.9419
$r_{(OM)}$, Å	-	-	0.150	0.1546	0.1546
HOH, deg	109.47	104.52	104.52	104.52	107.4
$A \times 10^{-3}$, kcal Å^{12}/mol	629.4	582.0	600.0	731.3	747.0
B, kcal Å^{6}/mol	625.5	595.0	610.0	736.0	744.0
q(O)	−0.8476	−0.834	-	-	-
q(H)	+0.4238	+0.417	+0.52	+0.5564	+0.5564
q(X)	-	-	−1.04	−1.1128	−1.1128

The 5-site model such as TIP5P model with five interaction sites, add dummy atoms that carry the negative charge to represent the lone pairs of the oxygen atom. It has a tetrahedral-like geometry. Further, re-parameterization of TIP5P gives the TIP5P-E model. The 5-site models are computationally very expensive as the computational cost of a water simulation increases with the number of interaction sites in the water model.

2.4 Quantum Mechanics/ Molecular Mechanics (QM/MM) methods

One of the limitations of the MM methods is that molecular mechanics methods cannot treat chemical problems where electronic effects predominate such as describing bond breaking/forming or electron transfer reactions. It is important to consider electron structure methods in such situations. But if the system of interest is too large to treat entirely by electronic structure methods, then one can use hybrid methods that are designed for modelling such cases. Such hybrid methods are often referred as Quantum Mechanics-Molecular Mechanics (QM/MM) methods [167-170] where the system is partitioned into an electronically important region that requires QM treatment and the remaining system is treated classically by force field methods i.e. the MM approach, as shown in Figure 2.3.

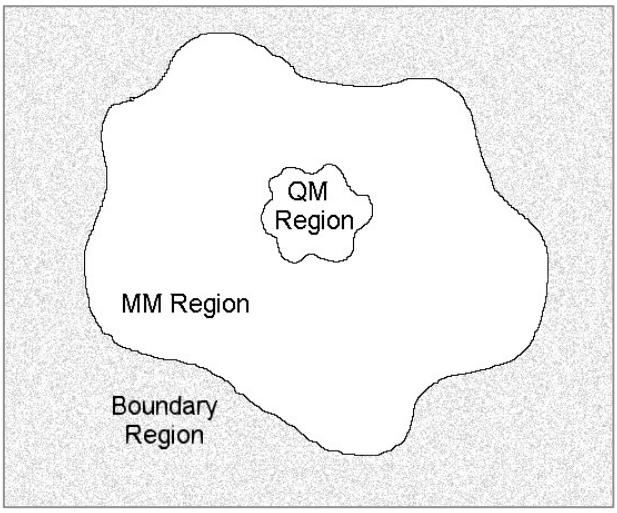

Figure 2.3 Pictorial representation of QM/MM approach. [Source: anusf.anu.edu.au]

Thus, QM/MM is a molecular simulation methodology that couples both Quantum Mechanics and Molecular Mechanics approaches, and is highly efficient for treating large systems by combining the accuracy of quantum approach with the speed of MM approach. The computational cost scales as $O(N^2)$ for MM treatment, where N is number of atoms in the system, while it scales as $O(N^3)$ to $O(N^4)$ for QM treatment for simple *ab-initio* calculations, where N stands for the number of basis functions.

The Hamiltonian and resultant energy of the system is divided into three parts,

$$H_{tot} = H_{QM} + H_{MM} + H_{QM-MM} \tag{2.81}$$

$$E_{tot} = E_{QM} + E_{MM} + E_{QM-MM} \tag{2.82}$$

where H_{QM} and H_{MM} corresponds to the Hamiltonian in isolated QM and MM regions, respectively. The actual difficulty arises in the calculation of H_{QM-MM} part, i.e. in the calculation of interaction energy between two regions. Different schemes have been proposed to model this interaction term correctly by introducing the concepts of mechanical embedding, electronic embedding and polarizable embedding [94].

Mechanical embedding provides the lowest level of interaction where the interactions between the QM and MM regions are treated at the MM level. The bonded (stretching, bending, and torsional) interactions and non-bonded (electrostatic and van der Waals) interactions of the two regions are included in the interaction term. There is no interaction between the electronic parts of the two regions, thus the wave function of the QM region does not respond to changes in the MM region.

The next level of improvement is called electronic embedding, in which partial charges on the MM atoms can be incorporated into the QM Hamiltonian, and the QM atoms thus feel the electric potential due to all the MM atoms. The MM region polarizes the electronic density of the QM region and thus the wave function in the QM region becomes coupled to the MM geometry. A further improvement can be made by allowing the QM atoms also to polarize the MM region such that electric field generated by the QM region influences the MM electric moments. This is often termed as polarizable embedding. This implementation substantially increases the computational cost, and is not commonly used for calculating very large systems, so the electronic embedding approximation is employed in most of the QM/MM calculations.

2.4.1 ONIOM(QM:MM) method

The ONIOM (our own n-layered integrated molecular orbital and molecular mechanic) method [168, 171-173] is one of the most popular hybrid methods, especially designed to deal with large systems, and enables the methods of different accuracy to combine together to produce results at the desired accuracy at reduced computational time. The high level methods deal with electronic structure methods (QM approach) while low-level methods involve force field methods (MM approach). The original ONIOM model only used mechanical embedding for the QM/MM interface, but electronic embedding has also been implemented in recent extensions.

In the two-layer scheme of ONIOM, the small model system (chemically active portion of the real system) is treated by both high and low levels methods, while the large real system is treated by low-level method only. Thus the energy of the real system at high-level accuracy can be calculated as [94]

$$E^{ONIOM}(real\ system, high\ level) = E^{high}(small\ model\ system) + E^{low}(real\ system) - E^{low}(small\ model\ system) \quad (2.83)$$

Similarly, the three-layer model incorporates a 'middle layer' which is treated by an intermediate level of theory between high and low level methods. This middle layer is the larger subset of the real system than the small model system, and it models the electronic effects of the molecular environment on the small model system. The energy of the real system using this 3-layer scheme is given as

$$E^{ONIOM}(real\ system, high\ level) = E^{high}(small\ model\ system) + E^{low}(real\ system) + E^{medium}(intermediate\ system) - E^{low}(intermediate\ system) - E^{medium}(small\ model\ system) \quad (2.84)$$

In the ONIOM model, derivatives can be constructed from the corresponding derivative of the underlying methods, and therefore using the ONIOM energy function, geometry optimization and vibrational analysis can be performed. The ONIOM method is highly applicable to large systems including cluster models of surfaces, modelling enzyme reactions and so on. ONIOM(QM:MM) applications on bio-molecular systems and transition metal complexes are very well known and are discussed in literature in detail [174-177].

2.5 Time-Dependent Molecular Properties

The interaction between light and matter can be considered classically or quantum mechanically as light either can be considered a classical electromagnetic wave or as a stream of photons. All charged particles in a molecule experience a force in the presence of an external electric field that perturbs their motions. In a classical sense, on the absorption of light by the molecule, an oscillating electric field $E(t)$ of light causes an oscillation of charges and these oscillating charges give rise to an induced polarization or induced dipole moment $\mu(t)$ in the molecule [178]. The polarizability of the molecule tells us about the ability or tendency of the molecule to become polarized by the oscillating electric field. The time dependent polarization can be expressed as a Taylor series in the electric field strength,

$$\mu(t) = \mu_0 + \alpha\, E(t) + \frac{1}{2}\beta E^2(t) + \frac{1}{6}\gamma E^3(t) + \cdots \tag{2.85}$$

where μ_0 is the permanent electric dipole moment of the molecule, α is the linear electric polarizability, β is the first-order (nonlinear) hyperpolarizability, and γ is the second-order hyperpolarizability of the molecule. The linear polarizability α as well as non-linear coupling constants β and γ depend on the frequency of the electric field, where α corresponds to the molecule's ability to undergo one photon absorption, while β and γ constants correspond to its tendency to undergo two-photon absorption.

In quantum mechanics, the probability of transition of a molecule from one eigenstate Ψ_1 to another eigenstate Ψ_2 after absorption of photon in the form of an oscillating electric field is given by $|M_{21}|^2$, which is square of the transition moment integral M_{21},

$$M_{21} = \int \Psi_2^* \,\hat{\mu}\, \Psi_1 d\tau \tag{2.86}$$

where $\hat{\mu}$ is the transition dipole moment operator.

Both the nuclear and electronic parts contribute to the dipole moment operator. So we divide $\hat{\mu}$ into two parts, with nuclear contribution μ_n and electronic contribution μ_e. Therefore, M_{21} can be written as

$$M_{21} \approx \int \Psi_{e2}^{*}\, \hat{\mu}_e\, \Psi_{e1}\, dr \int \Psi_{n2}^{*} \Psi_{n1}\, dR \tag{2.87}$$

The first integral defines the electronic selection rules. For the transitions between the states of different spin, this transition integral becomes zero and the transition is forbidden. If the symmetry of this integral spans the totally symmetric representation of the point group to which the molecule belongs then this integral is non-zero and the transition is allowed. Otherwise, the transition is forbidden.

The second integral in the above Equation (2.87) is the vibrational overlap integral between one eigenstate and another eigenstate and the square of this integral is called the Franck-Condon factor. The large value of Franck-Condon factor shows the large vibrational contribution to the transition probability, where there is a strong overlap of the vibrational ground state and excited state.

2.5.1 Response Theory

From a theoretical point of view, by studying the response of wave functions to the frequency dependent perturbations, one can retrieve the corresponding information about the molecular properties, which is the basis for response theory. Response theory methods are used to study excited states of the systems, with the assumption that the time-dependent perturbation is small. The time-dependent perturbation is of the form of oscillating electric field, and the interaction operator can be written as [178, 179]

$$\hat{V} = \sum_{y} \exp\left(-\mathrm{i}\omega_y t\right) \epsilon_y(\omega_y) \hat{P} \tag{2.88}$$

where $\hat{P}$ is a Hermitian operator, ω_y is the frequency, and $\epsilon_y(\omega_y)$ is a perturbation strength parameter.

The time-dependent expectation value of an observable, Q, which can be expanded in the orders of the perturbation,

$$\langle \Psi_0(t)|Q|\Psi_0(t)\rangle = \langle \Psi_0|Q|\Psi_0\rangle + \sum_{y} \epsilon_y(\omega_y) \langle\langle Q, P\rangle\rangle_{\omega_y} \exp\left(-\mathrm{i}\omega_y t\right) + \cdots \tag{2.89}$$

defines the linear response function $\langle\langle Q, P\rangle\rangle_{\omega_y}$. When P and Q are dipole operators, the linear response function is the dipole-dipole polarizability. The linear response function can be written in terms of the unperturbed eigenstates ($|\Psi_0\rangle, |\Psi_k\rangle$) of Hamiltonian H as

$$\langle\langle Q, P\rangle\rangle_{\omega_y} = \hat{\Pi}^{QP} \sum_k \frac{\langle\Psi_0|Q|\Psi_k\rangle\langle\Psi_k|P|\Psi_0\rangle}{\omega_y - \omega_k} \tag{2.90}$$

where $\hat{\Pi}^{QP} f_{xy} = f_{xy} + f_{yx}$. The excitation energies of the system are $\omega_k = E_k - E_0$, where E_0 and E_k represent the ground and excited state energy of the system, respectively. Thus poles of the linear response function gives excitation energies when $\omega_y = \omega_k$ i.e. the external frequency is equal to an excitation energy of the system, and the corresponding residues give one photon absorption (OPA) transition moments.

In photochemistry, response theory is used as a tool for evaluating transition moments between photochemical states of a molecular system. These response functions are sometimes referred to as polarization propagators if P and Q are number conserving operators (i.e. they do not correspond to adding or removing electrons from the system under study). From a computational point of view, as in the case of CI calculations, this quickly becomes expensive, and the methods need to be approximated. The simplest method of approximation is to truncate the propagator to only include single excitations and de-excitations, also known as random phase approximation (RPA). As with propagator methods a reference is required, one can use HF reference in TD-HF, and DFT reference in TD-DFT method [180]. TD-DFT method will be discussed in detail in next section. Similarly, if a CCSD reference is used, this will be the so-called equation of motion CCSD (EOM-CCSD) method [181, 182].

The other range of methods used are the coupled cluster response methods that use coupled cluster theory as a reference, and the expansion of the propagator as a function of the fluctuation potential is considered. The standard coupled cluster methods such as CCS, CC2, CCSD, CC3, and CCSDT have already been discussed in Section 2.2.1.8. One complication in CC theory is how singles are treated equivalently in their correlation expansion as well as in response calculations. This in practice involves the use of similarity transformed cluster operator of the type $\hat{O} = e^{-T_1} O\, e^{T_1}$, where T_1 is the cluster operator for the single excitations as already described above in Section 2.2.1.9. In coupled cluster response calculations, firstly the coupled cluster energy and

amplitudes for the reference state are calculated, and then the excitation energies of the system are calculated directly through the response eigenvalue equations. This means ground and excited state wave functions do not need to be optimized independently. In coupled cluster excitations, the expansion in terms of the fluctuation potential provides a way of systematically improving excitation energies using a coupled cluster wave function [183]. For CCSD reference wave functions for example, the propagator expansion is truncated at second order. This approach introduces a hierarchy of linear response coupled cluster methods that extends the improvements to excitation energies and transition moments too. The computational cost for these approximate models scales as N^4 for CCS, N^5 for CC2, N^6 for CCSD, N^7 for CC3 and N^8 for CCSDT, where N is the number of basis functions.

2.5.2 Time-Dependent Density Functional Theory (TD-DFT)

Though DFT methods are well developed to describe the ground state properties of the system, it can also be used to study the excited state properties with the help of response methods, under the framework of *time-dependent* DFT (TD-DFT) method [184-187].

The foundation of TD-DFT is the Runge-Gross (R-G) theorem, [184] which incorporates the time dependent density and potentials properly into DFT, and is a time dependent analogue of Hohenberg-Kohn theorem (1964) [121] for ground electronic states. R-G theorem states that there is a unique mapping between the time–dependent external potential, $v_{ext}(r,t)$ and the time dependent electron density, $\rho(r,t)$ for a fixed initial state.

Within the framework of Kohn-Sham formalism of non-interacting system, the time dependent density is written as,

$$\rho(r,t) = \sum_{\boldsymbol{\sigma}} \sum_{i}^{occ} |\varphi_i(r,\sigma,t)|^2 \tag{2.91}$$

where Kohn-Sham orbitals $\varphi_i(r,t)$ satisfy the time-dependent Kohn-Sham equations

$$i\frac{\partial}{\partial t}\varphi_i(r,t) = \left(-\frac{\nabla^2}{2} + v_s[\rho(r,t)]\right)\varphi_i(r,t) \tag{2.92}$$

with Kohn-Sham non-interacting potential $v_s[\rho](r,t)$ given as

$$v_s[\rho(r,t)] = v_{ext}(r,t) + \int \frac{\rho(r',t)}{|r-r'|} dr' + v_{xc}[\rho(r,t)] \tag{2.93}$$

and $v_{xc}[\rho(r,t)]$ is the exchange–correlation potential.

In the past few years, TD-DFT linear response theory has become the widely used method for extracting features like excitation energies, frequency-dependent response properties, and photo-absorption spectra of complex systems. Thus TD-DFT can be applied to systems dealing with relatively weak external fields, which can be considered as small external perturbation within linear response theory.

Now considering the external potential as

$$v_{ext}(r,t) = v_0(r) + v_1(r,t) \tag{2.94}$$

where $v_1(r,t)$ is a time dependent external perturbing potential and $v_0(r)$ is the usual attractive Coulomb potential between electron and nuclei.

The first order density response for *interacting* particles to the perturbation is obtained as

$$\rho(r,t) - \rho_0(r) \approx \rho_1(r,t) = \int dt \int dr'\, \chi(r,t,r',t') v_1(r',t') \tag{2.95}$$

where

$$\chi(r,t,r',t') = \frac{\delta\rho(r,t)}{\delta v_{ext}(r',t')} \Big| v_0 \tag{2.96}$$

is the interacting response function.

Similarly, Kohn-Sham response function of *non-interacting* particles is given as

$$\chi_s(r,t,r',t') = \frac{\delta\rho(r,t)}{\delta v_s(r',t')} \Big| v_{s[\rho_0]} \tag{2.97}$$

And the first order density response in terms of $\chi_s(r,t,r',t')$ can be written as

$$\rho_1(r,t) = \int dt' \int dr'\, \chi_s(r,t,r',t') v_{s,1}(r',t') \tag{2.98}$$

where

$$v_{s,1}[\rho(r,t)] = v_1(r,t) + \int \frac{\rho(r',t)}{|r-r'|} dr' + \int dt' \int dr' \, f_{xc}[\rho_0(r,t,r',t')]\rho_1(r',t') \quad (2.99)$$

with the exchange correlational kernel

$$f_{xc}[\rho_0(r,t,r',t')] = \frac{\delta v_{xc}[\rho_0(r,t)]}{\delta\rho(r',t')} \quad (2.100)$$

Using the Fourier transform of Equation (2.95), the frequency-dependent linear density response can be obtained and the first order density can be solved self-consistently.
The poles of the response function of the interacting system give electronic excitation energies, which can be characterized by solving the eigenvalue problem of form

$$\begin{pmatrix} \boldsymbol{P} & \boldsymbol{Q} \\ \boldsymbol{Q} & \boldsymbol{P} \end{pmatrix} \begin{pmatrix} \boldsymbol{X} \\ \boldsymbol{Y} \end{pmatrix} = \omega \begin{pmatrix} -1 & 0 \\ 0 & 1 \end{pmatrix} \begin{pmatrix} \boldsymbol{X} \\ \boldsymbol{Y} \end{pmatrix} \quad (2.101)$$

where $\boldsymbol{P} \rightarrow$ the energy difference between occupied and unoccupied orbitals combined with coupling matrix (response kernel integral including exchange correlation and Coulomb electron-electron interaction) ;
$\boldsymbol{Q} \rightarrow$ Coupling matrix;
$\boldsymbol{X}$ *and* $\boldsymbol{Y} \rightarrow$ linear response of the density matrix i.e. perturbed density in terms of mixing of occupied and unoccupied orbitals;
$\omega \rightarrow$ frequency of perturbation.
The residues at poles give transition moments and this is how TD-DFT combines with linear response theory to give excitation energies and subsequently transition moments. Linear response TD-DFT calculations for excited states are computationally less expensive than CI and CC methods and thus can be applied to many electron systems too. Though it has few limitations and drawbacks in modelling systems dealing with long-range forces, charge transfer states and quality of results obtained are functional-dependent. Despite of this fact, we have used TD-DFT methods for modelling excited states for our studies, using long range corrected hybrids and Truhlar's meta-hybrid functionals that are found to deal fairly better with charge transfer properties rather than standard functionals [128, 129].

Chapter 3 - Excited states of small water clusters $(H_2O)_{n=1-5}$

3.1 Introduction

Water is one of the most studied systems among all polyatomics due to its interesting properties and its important role in many geological, biological, and chemical processes [188]. The lowest excited state of an isolated water monomer in gas phase has been extensively studied in the past [62, 189-192]. It has been observed experimentally that the UV absorption spectrum of gas phase water shows two absorption bands at ~ 7.4 eV and ~ 10 eV [61]. The first absorption band has been found to be broadened and also blue-shifted by ~ 0.9 eV in liquid water [193, 194] and by ~ 1.3 eV in condensed phases [60]. The origin of the observed blue shift has often been discussed from a molecular perspective, where it is assigned to Rydbergization [195, 196] and/or solvent effects[197, 198], causing their excited states to be destabilized relative to their ground states.

It has been generally realized that many of the properties of the condensed phase water are linked to the extended hydrogen binding network, as hydrogen bonding interactions dominate among water molecules [188]. An increase of the liquid temperature causes a red shift in the position [199] and low energy edge [200] of the first absorption band, which has been related to changes in hydrogen bonding with increasing temperature.

A common feature of the absorption spectrum of larger water clusters has been observed which shows an increased blue shift and broadening of the first absorption band with increasing cluster size [201-205]. A qualitative analysis on large water clusters has suggested that the first absorption band holds contributions from transitions of different origins. Transitions involving under-coordinated water molecules at the cluster surface contribute to the low energy regime of the first absorption band, while transitions involving innermost molecules may contribute to the higher energy regime [205]. These results further support the notion that formation of additional hydrogen bonds to water molecules with increase in cluster size produce a blue shift in the excitation of that water molecule.

Hence, studying low lying valence excitations in the condensed phase water poses a challenge and further investigations to get the microscopic details that underline shifts

and broadening in peak positions is required. The information on the lowest excited state of water in liquid and ice phases is limited. Therefore, a computational study has been performed to investigate condensed-phase effects on the electronic spectrum of water using coupled cluster electronic structure methods [201]. The condensed phase blue shift of ~ 0.7 eV was noticed by comparing water monomer relative to the water pentamer, which was in good agreement with experiments. A few computational studies on low-lying singlet and triplet excited states of small water clusters have been performed using a range of electron structure methods including TD-DFT, CIS(D) and the equation of motion coupled cluster (EOM-CCSD) methods [62-64]. It was noticed that lowest excited state of each water cluster i.e. dimer (C_s), trimer (C_{2v}) and pentamer (C_{2v}) is non-dissociative for stretching of an OH bond that is hydrogen bonded to a neighbouring water molecule in an ice-like configuration, in contrast to the dissociative nature of the lowest excited state of an isolated water monomer upon OH stretching [62]. It further supports the experimental evidence [206] that suggests a significant lifetime for water excitations in amorphous ice.

The effects of hydrogen bonding on the ultraviolet absorption spectrum of the liquid water has been studied computationally and the detailed benchmark electronic structure calculations using high level wave function based methods and TD-DFT methods have been performed for the excitation energies and oscillator strengths in the equilibrium water monomer and dimer [63]. It was shown that in a water dimer, the lowest excited state is mostly associated with the hydrogen bond donor, while the higher energy second excited state mostly with the hydrogen bond acceptor [63]. It was also shown that most condensed phase water valence excitations involve more than one molecule due to pervasive delocalization and charge transfer.

A detailed computational study on excitation energies, oscillator strengths, and analysis of redistributions of electron density of quasi-tetrahedral water pentamer in its C_{2v} geometry has been performed using high level wave function based EOM-CCSD methods and TD-DFT methods [64]. The effect of hydrogen bonding on the lowest excited state associated with the central water molecule was studied by adding acceptor or donor hydrogen atoms to trimer and tetramer substructures of the C_{2v} pentamer. The focus was on the excitations associated with the central water molecule where the interior liquid water molecule is in an environment similar to the first solvation shell in bulk. It was shown that the number of acceptor hydrogen atoms mainly determines the

magnitude of blue shifts of the excitation energies upon condensation, whereas donor hydrogen atoms do not induce significant shifts in excitation energies [64].

In this chapter, to get further insight into the nature of the transitions associated with the lowest energy excited states of small water clusters $(H_2O)_n$, n=1-5, and to investigate the effect of electron correlation on such excited states, we have performed a detailed benchmark computations to study vertical excitation energies and oscillator strengths using range of high level electron structure methods including hierarchy of linear response coupled cluster CCS, CC2, CCSD and CC3 methods and related EOM-CCSD method. The TD-DFT method is also applied for comparison. The effect of the basis set on the excitation energies and oscillator strengths is also investigated using the augmented-correlation consistent polarized valence basis set series.

Properties such as ground and excited state dipole moments and second moment of charge distribution are also investigated using coupled cluster methods to get a better understanding of the nature of transitions and the Rydberg character associated with a low lying excited states of small water clusters. Furthermore, the solvation or aggregation effect on the water monomer with C_{2v} symmetry is investigated by considering the lowest energy excitations associated with the central water molecule in the water trimer (C_{2v}) and water pentamer (C_{2v}) relative to those in isolated water monomer.

3.2 Computational Details

3.2.1 Computational Model

The initial structures for water monomer, water dimer, and water pentamer (C_1) optimized at the RI-MP2/aug-cc-pVDZ theory level were taken from Temelso *et al*. [207]. We have also studied the water trimer and pentamer of C_{2v} symmetry, and initial structures optimized at the B3LYP/6-31+G* theory level for each, were taken from Chipman *et al*. [62]. The water monomer of C_{2v} symmetry, dimer of C_s symmetry, trimer of C_{2v} symmetry, tetramer of S_4 symmetry and pentamer of C_1 and C_{2v} symmetry were chosen for our study.

3.2.2 Computational Methods

All ground state geometry optimizations were performed using second order Møller-Plesset perturbation theory (MP2) [109] with the augmented correlation-consistent polarized-valence double zeta basis set (aug-cc-pVDZ). Frequency calculations were carried out to check the nature of stationary points, and confirmed as minima for all ground state structures except the quasi-tetrahedral C_{2v} water pentamer structure which is a stationary point on the MP2/aug-cc-pVDZ potential energy surface but is not a minimum.

The lowest electronic singlet excited states of water monomer (C_{2v}), dimer (C_s), trimer (C_{2v}), pentamer (C_1) and pentamer (C_{2v}) were studied by using hierarchy of linear response coupled cluster models such as coupled cluster singles (CCS), CC2 [118], the coupled cluster singles-and-doubles (CCSD) [116], and the CC3 [119, 120] on the optimized geometries. Details of all these coupled cluster methods have already been discussed in Section 2.2.1.9 and 2.5.1 in Chapter 2. Excitation energies, oscillator strengths to lowest singlet excited states were obtained using the augmented correlation-consistent polarized-valence basis set family aug-cc-pVXZ with X = D, T, Q [105, 106] for the water monomer and dimer, while for the trimer (C_{2v}) basis set employed were in the series of aug-cc-pVXZ with X = D, T. For the pentamer (C_1) and pentamer (C_{2v}), we have used aug-cc-pVDZ basis set.

The wavefunction-based equation of motion coupled cluster EOM-CCSD method [208, 209] was used to obtain excitation energies and oscillator strengths to singlet lowest excited states of the water monomer, dimer, trimer (C_{2v}), water tetramer, water pentamer (C_1), and pentamer (C_{2v}). The aug-cc-pVDZ and aug-cc-pVTZ basis sets were employed for tetramer, while we used the aug-cc-pVDZ basis set for pentamer (C_1) and pentamer (C_{2v}). For the water tetramer with S_4 symmetry, the excitation energies were also obtained by using linear response (LR) configuration interaction singles CIS [210, 211] and CIS(D)[212].

Ground state and excited state properties such as dipole moments and second moment of charge for water monomer, dimer and trimer were calculated using linear response coupled cluster methods such as CCS, CC2, CCSD method with aug-cc-pVXZ with X = D, T basis sets.

We have also used time-dependent density functional theory (TD-DFT) [184-187] to obtain excitation energies and oscillator strengths for $(H_2O)_{n=1-5}$, using the Truhlar's meta hybrid M06-2X functional [129] with a range of basis sets. The augmented aug-

cc-pVXZ basis set with X = D, T, Q, 5, 6 was used for the water monomer, while for the dimer and trimer (C_{2v}) basis sets aug-cc-pVXZ with X= D, T, Q, 5 were employed. We have used the aug-cc-pVDZ and aug-cc-pVTZ basis sets for the tetramer, pentamer (C_1), and pentamer (C_{2v}).

We have used the Dalton 2.0 program [213] for all coupled cluster computations, while MP2 ground states and CIS, CIS(D), EOM-CCSD and TD-DFT excited state computations were performed using the Gaussian09 program [214].

3.3 Results and Discussion

3.3.1 Ground State Geometries

MP2/aug-cc-pVDZ optimized geometries of small water clusters from the monomer up to the pentamer i.e. $(H_2O)_{n=1-5,}$ are shown in Figure 3.1. The total optimized ground state energies and structural parameters of water $(H_2O)_{n=1-5}$ are listed in Table 3.1. The $r_{O\text{-}H}$ bond lengths are represented as $O_{(i)}H_{(ij)}$ where i denotes the i^{th} oxygen atom in the water cluster and j =1,2 denotes the j^{th} hydrogen atom bonded to that oxygen atom. Similarly, intramolecular HOH bond angles (θ_{HOH}) are represented as $H_{(i1)}O_{(i)}H_{(i2)}$.

The experimental geometry of water monomer with C_{2v} symmetry has a OH bond length $r_{O\text{-}H}$ of 0.9572 ± 0.0003 Å and bond angle θ_{HOH} of 104.52 ± 0.05° [215]. We have calculated the bond length $r_{O\text{-}H}$ of 0.966 Å, which is slightly longer by about 0.009 Å at the MP2/aug-cc-pVDZ level of theory than the experimental geometry. The calculated bond angle θ_{HOH} is 103.9° is slightly smaller by about 0.6° compared to the experimental value. Thus our results are generally in good agreement with the experiment and give a satisfactory representation of the water equilibrium geometry.

For the water dimer, the available experimental data does not allow for a complete structure determination. However, the microwave measurements has determined the vibrationally averaged O-O bond distance to be about 2.976 Å [216]. After an estimated correction, the experimental geometry of water dimer of C_s symmetry has shown the equilibrium value R_e for r_{OO} bond distance of about 2.946 Å, under the assumption that each monomer retains the equilibrium geometry of isolated water molecule [216]. Our results calculate the r_{OO} bond distance to be slightly short by 0.03 Å. Previous computational studies [217] have calculated the r_{OO} bond distance of about 2.90 Å at the CCSD(T)/aug-cc-pVTZ level of theory, which is in good agreement with our results. It is noticed that in the dimer formation most of the intramolecular geometrical

parameters are slightly changed with respect to isolated water geometry except the hydrogen-bound r_{OH} bond length which is elongated by 0.006 Å, and in good agreement with previous computational studies [62, 218]. Therefore, our calculations also give a good representation of the water dimer equilibrium geometry. To check the basis set superposition error (BBSE), the water dimer geometry is also optimized using the counterpoise method. BSSE error is found to be very small, and very similar geometrical parameters are obtained for the optimized water dimer geometry after the counterpoise correction.

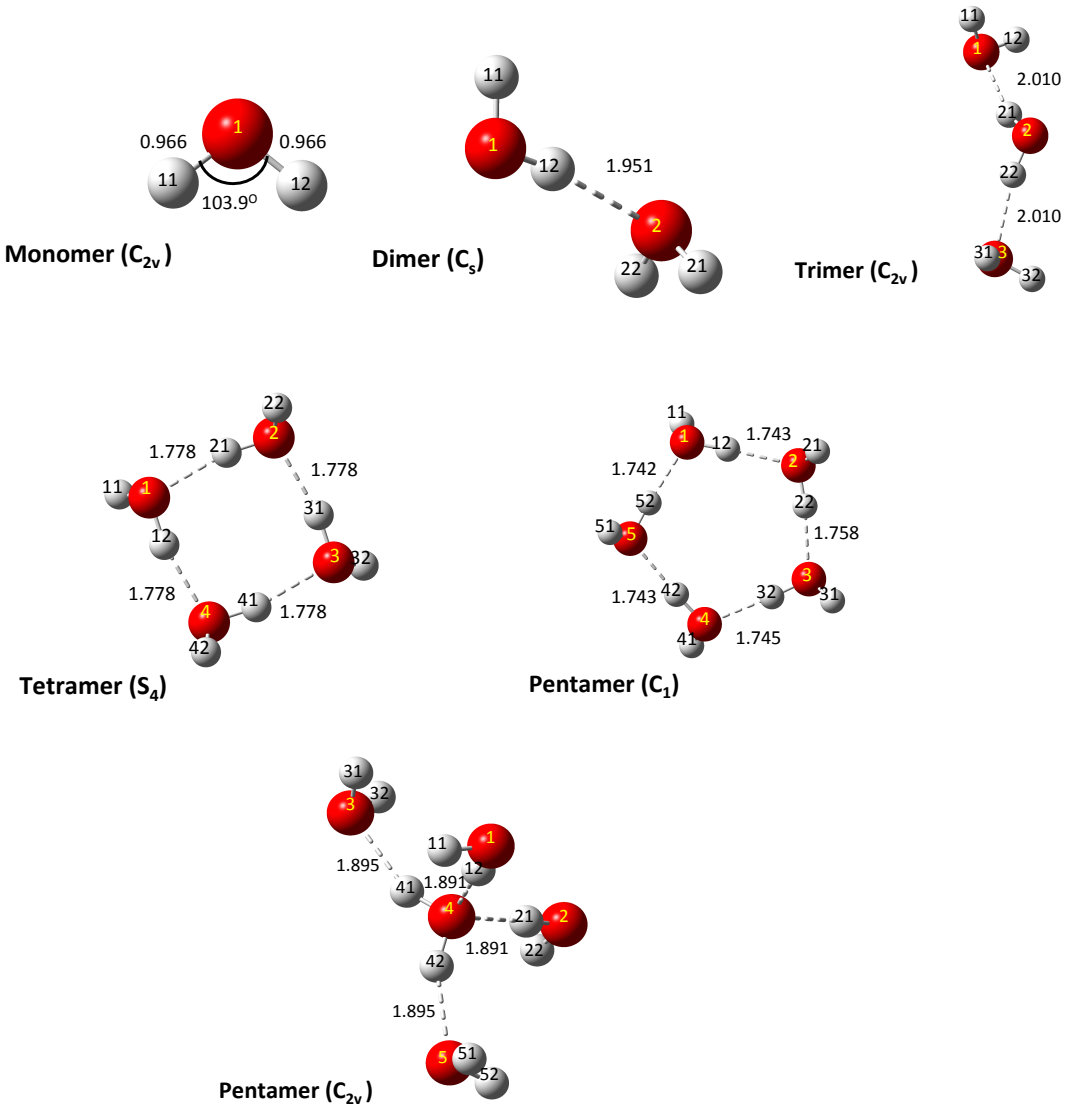

Figure 3.1 MP2/aug-cc-pVDZ optimized geometries of small water clusters. Hydrogen bonding distances are given in angstroms (Å).

Table 3.1 MP2/aug-cc-pVDZ optimized ground state energies and structural parameters of water clusters. O-H bond lengths (r) are given in angstroms (Å) and angles (θ) in degrees.

Model	**Ground state Energy (a.u.)**	r_{OH} **(Å)**	θ_{HOH} **(degrees)**
Monomer (C_{2v})	-76.2609	$O_{(1)}H_{(11)} = 0.966$ $O_{(1)}H_{(12)} = 0.966$	$H_{(11)}O_{(1)}H_{(12)} = 103.9$
Dimer (C_s)	-152.5302	$O_{(1)}H_{(11)} = 0.965$ $O_{(1)}H_{(12)} = 0.973$ $O_{(2)}H_{(21)} = 0.967$ $O_{(2)}H_{(22)} = 0.967$	$H_{(11)}O_{(1)}H_{(12)} = 104.3$ $H_{(21)}O_{(2)}H_{(22)} = 104.2$
Trimer (C_{2v})	-228.7978	$O_{(1)}H_{(11)} = 0.967$ $O_{(1)}H_{(12)} = 0.967$ $O_{(2)}H_{(21)} = 0.971$ $O_{(2)}H_{(22)} = 0.971$ $O_{(3)}H_{(31)} = 0.967$ $O_{(3)}H_{(32)} = 0.967$	$H_{(11)}O_{(1)}H_{(12)} = 103.9$ $H_{(21)}O_{(2)}H_{(22)} = 105.2$ $H_{(31)}O_{(3)}H_{(32)} = 103.9$
Tetramer (S_4)	-305.0894	$O_{(1)}H_{(11)} = 0.965$ $O_{(1)}H_{(12)} = 0.985$ $O_{(2)}H_{(21)} = 0.985$ $O_{(2)}H_{(22)} = 0.965$ $O_{(3)}H_{(31)} = 0.985$ $O_{(3)}H_{(32)} = 0.965$ $O_{(4)}H_{(41)} = 0.985$ $O_{(4)}H_{(41)} = 0.965$	$H_{(11)}O_{(1)}H_{(12)} = 104.9$ $H_{(21)}O_{(2)}H_{(22)} = 104.9$ $H_{(31)}O_{(3)}H_{(32)} = 104.9$ $H_{(41)}O_{(4)}H_{(42)} = 105.0$
Pentamer (C_1)	-381.3647	$O_{(1)}H_{(11)} = 0.965$ $O_{(1)}H_{(12)} = 0.987$ $O_{(2)}H_{(21)} = 0.965$ $O_{(2)}H_{(22)} = 0.986$ $O_{(3)}H_{(31)} = 0.965$ $O_{(3)}H_{(32)} = 0.987$ $O_{(4)}H_{(41)} = 0.965$ $O_{(4)}H_{(42)} = 0.987$ $O_{(5)}H_{(51)} = 0.965$ $O_{(5)}H_{(52)} = 0.987$	$H_{(11)}O_{(1)}H_{(12)} = 104.8$ $H_{(21)}O_{(2)}H_{(22)} = 105.0$ $H_{(31)}O_{(3)}H_{(32)} = 104.8$ $H_{(41)}O_{(4)}H_{(42)} = 104.5$ $H_{(51)}O_{(5)}H_{(52)} = 104.9$

Pentamer (C_{2v})	-381.34202	$O_{(1)}H_{(11)}$ = 0.965 $O_{(1)}H_{(12)}$ = 0.976 $O_{(2)}H_{(21)}$ = 0.976 $O_{(2)}H_{(22)}$ = 0.965 $O_{(3)}H_{(31)}$ = 0.968 $O_{(3)}H_{(32)}$ = 0.968 $O_{(4)}H_{(41)}$ = 0.975 $O_{(4)}H_{(42)}$= 0.975 $O_{(5)}H_{(51)}$ = 0.968 $O_{(5)}H_{(52)}$ = 0.968	$H_{(11)}O_{(1)}H_{(12)}$ = 104.2 $H_{(21)}O_{(2)}H_{(22)}$ = 104.2 $H_{(31)}O_{(3)}H_{(32)}$ = 103.8 $H_{(41)}O_{(4)}H_{(42)}$ = 108.3 $H_{(51)}O_{(5)}H_{(52)}$ = 103.8

There is no experimental data to compare structures of larger water clusters. The isolated water trimer, tetramer and pentamer favor cyclic ring structures as global minima and have been established previously [219, 220]. However, in this chapter, we have considered the water trimer and pentamer with C_{2v} symmetry to replicate the environment where the central water molecule is in an environment similar to the first solvation shell in bulk, as shown in Figure 3.1.

The O···H hydrogen bonding interactions exist in these water clusters, and calculated hydrogen bonding distances are shown in Figure 3.1. The number of hydrogen bonds found in dimer (C_s), trimer (C_{2v}), tetramer (S_4), pentamer (C_1), and pentamer (C_{2v}) are 1, 2, 4, 5, and 4, respectively. In the C_{2V} trimer arrangement, a central water molecule donates a hydrogen bond to each of two equivalent first-shell acceptor molecules and the two peripheral water molecules have oxygen atoms lying in the same plane as the central water. In the quasitetrahedral C_{2v} pentamer arrangement, two equivalent first-shell water molecules are added to the C_{2v} trimer and from each of which the central water accepts a hydrogen bond, and the final two peripheral water molecules have oxygen atoms out of the plane of the central water [62]. The water pentamer C_1 with cyclic structure has five hydrogen bonding interactions, and is more stable and lower in energy by 0.023 a.u. than the quasitetrahedral C_{2v} water pentamer with four hydrogen bonding interactions.

3.3.2 Electronic excitations in water clusters $(H_2O)_{n=1-5}$

3.3.2.1 Water Monomer (C_{2v})

Considering the water molecule, oriented in the *yz* plane with C_{2v} symmetry, the ground state molecular orbital configuration can be written as $(1a_1)^2(2a_1)^2(1b_2)^2(3a_1)^2(1b_1)^2$ ($\tilde{X}\ ^1A_1$), where a_1, b_2, b_1 corresponds to MO's symmetries. The highest energy occupied molecular orbital $1b_1$ (HOMO) corresponds to the nonbonding O $2p_x$ atomic orbital, while $3a_1$ (HOMO-1) and $1b_2$ (HOMO-2) are the bonding MO's result from the linear combination of O $2p_z$ and O $2p_y$ atomic orbitals with H 1*s* orbital, respectively. The lowest energy unoccupied orbital $4a_1$ (LUMO) is the admixture of the O 3*s* Rydberg character with the anti-bonding counterpart of the valence $3a_1$ orbital. Similarly, $2b_2$ (LUMO +1) orbital corresponds to the anti-bonding counterpart of the valence $1b_2$ orbital, along with admixture of Rydberg character. The MO's density plots are shown in Figure 3.2.

Vertical excitation energies and Oscillator Strengths

The vertical excitation energies and oscillator strengths obtained using hierarchy of linear response coupled cluster CCS, CC2, CCSD and CC3 methods along with the related EOM-CCSD, together with TD-DFT methods for the lowest singlet valence excited states of water monomer at its equilibrium geometry are presented in Table 3.2. The experimental results for the lowest lying excited states are also presented in Table 3.2. The basis set dependence of these excitation energies and oscillator strengths using range of aug-cc-pVXZ with X = D, T, Q, 5, 6 basis sets is also listed in Table 3.2. (Note: All excited states discussed below are singlets).

The effect of electron correlation in the calculation of excitation energies using linear response (LR) coupled cluster hierarchy of models for the first five excited states of water have been investigated. The $1B_1$ state is found to be the first lowest energy singlet excited state followed by $1A_2$, $1A_1$, $2B_1$ and $1B_2$ states in order of increasing excitation energy. We have shown the coupled cluster convergence of excitation energies in the aug-cc-pVXZ basis set series, with X = D, T, Q (See Figures. 3.3(a)-(c)). For a given basis set, it is seen that the lowest cost CCS largely overestimates the excitation energies of these states; CC2 underestimates while CCSD and CC3 converge monotonically to a similar result. We will therefore limit our discussion to the CCSD

and CC3 methods as noticed to produce results at the desired accuracy rather than CCS or CC2.

Considering the basis set effect on these excitation energies at the CC3 level, the excitation energies increase by about 0.09 eV going from the augmented aug-cc-pVDZ to the aug-cc-pVTZ basis set for the first two low lying $1B_1$ and $1A_2$ states, while the energy difference is small i.e. about 0.04 eV going from the aug-cc-pVTZ to the aug-cc-pVQZ basis set. For the $1A_1$ and $1B_2$ states, increasing the basis set size from aug-cc-pVDZ to aug-cc-pVQZ does not change the results substantially, i.e. energy difference is within 0.04 eV. Thus excitation energies at aug-cc-pVQZ level can be considered as the converged values for CC3 calculations. (See Figure 3.3(d)). We find that the basis set effect at the CCSD level is very much similar to the CC3 level and produces results within 0.01-0.03 eV with each other for both aug-cc-pVTZ and aug-cc-pVQZ basis set.

For the first lowest singlet excited state $1B_1$ of water, the experimental estimate was taken as the position of the first maximum in the photoabsorption cross section at around 7.4-7.5 eV [61, 189]. Wave-packet calculations of the photo-absorption spectrum have further provided a semi-experimental estimate of vertical excitation energy with an average value of 7.78 eV, using a series of potentials after small empirical adjustments [191]. We find that CCSD and CC3 methods give the vertical excitation energies of about 7.40 and 7.47 eV, respectively, for the $1B_1$ state using aug-cc-pVDZ basis set that is in accuracy of 0.06 eV with the experimental value. Using the aug-cc-pVQZ basis set, both CCSD and CC3 methods give the vertical excitation energy of about 7.60 eV for the $1B_1$ state, which is in good agreement with the experimental as well as semi-experimental estimate.

The second singlet excited state $1A_2$ with an excitation energy of 9.17 eV at the CCSD/aug-cc-pVDZ level is calculated with a good accuracy of about 0.07 eV with the experimental values [221-223], while it is calculated with an accuracy of about 0.14 eV at the CC3/aug-cc-pVDZ level. The calculated excitation energy of about 9.98 eV for the third singlet excited state $1A_1$ at both CCSD and CC3 level using aug-cc-pVQZ basis set is in excellent agreement with the experimental result [61] within 0.01 eV. The excited state $1B_2$ with excitation energy of 11.59 eV at the CCSD/aug-cc-pVDZ level is calculated with a good accuracy of about 0.2 eV with the experimental result [223, 224]. It is noted that EOM-CCSD and LR-CCSD results are equivalent for all excited states.

Also for the TD-DFT results using the M06-2X functional, we have seen the convergence of excitation energies in the aug-cc-pVXZ basis set series, with X = D, T, Q, 5, 6 (See Figure 3.4 and Table 3.2). The excitation energies show convergence at aug-cc-pVTZ basis set with nearly similar excitation energies with increase in basis set cardinality from X = T to Q, 5, 6 for lowest singlet $1B_1$, $1A_2$, $1A_1$ and $1B_2$ states. For the lowest singlet excited state $1B_1$, the excitation energy is in good agreement with the experimental result [61, 189] within 0.04 eV at the aug-cc-pVTZ basis set level. The discrepancies are now larger for $1A_2$, $1A_1$ and $1B_2$ states, the TD-DFT excitation energies being 0.3-0.4 eV too low. Compared to the best available coupled cluster CCSD and CC3 results, TD-DFT excitation energies are too low by 0.2-0.6 eV depending on the state.

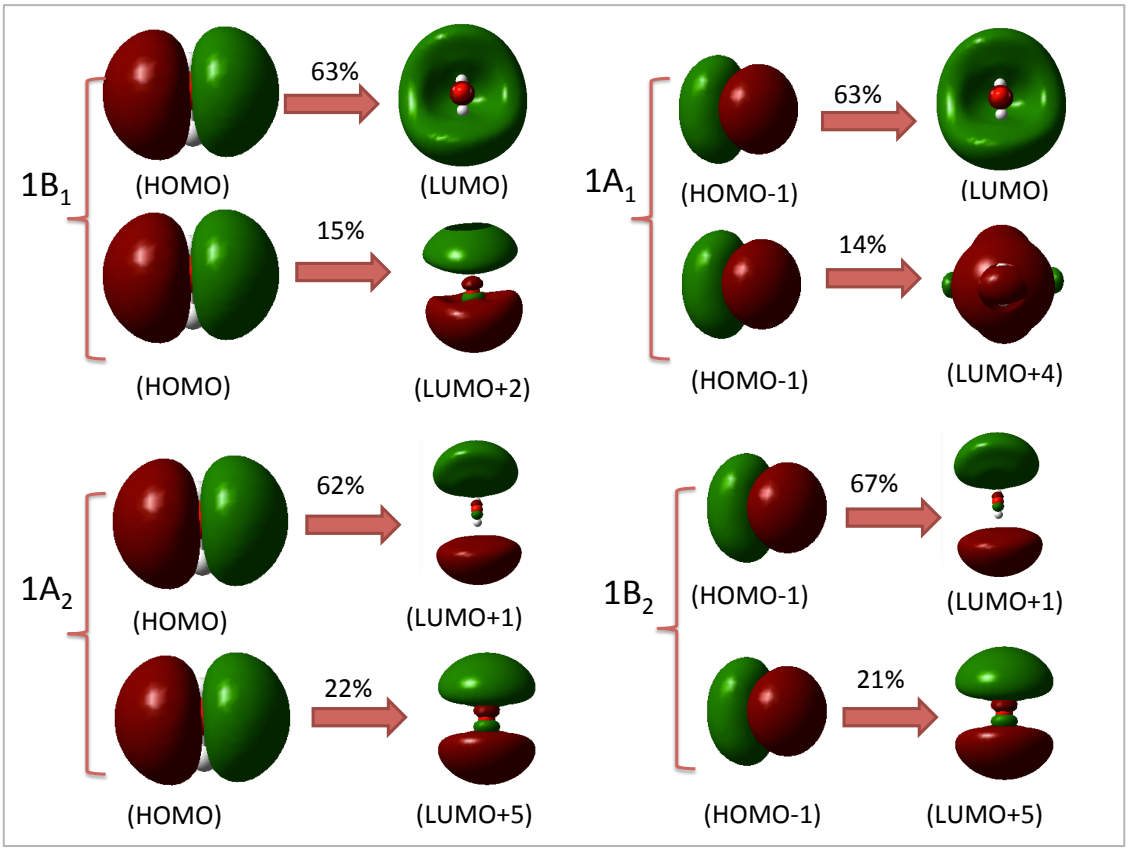

Figure 3.2 Water monomer (C_{2V} symmetry): Molecular orbitals involved in the electronic transitions for lowest energy singlet electronic excited states of different symmetry i.e. one excited state of each symmetry computed at the EOM-CCSD level. Isovalue used is 0.02 for the density plots.

Table 3.2 Water monomer (C_{2v}): Excitations energies in eV and oscillator strengths *f* (in parenthesis) of the lowest energy singlet electronic excited states using the hierarchy of correlated coupled cluster such as CCS, CC2, CCSD, CC3 methods, EOM-CCSD, and TD-DFT methods ([a]Exptl/Taken from Ref. [61], [a]Exptl/Taken from Ref. [61], [b]Exptl/Taken from Ref. [223, 224], [c]Exptl/Taken from Ref. [221-223]).

Water monomer (C_{2v})	**Excited States**				
	$1B_1$	**$1A_2$**	**$1A_1$**	**$2B_1$**	**$1B_2$**
Experimental					
	7.464[a]	9.1[c]	9.991[a]		11.4[b]
LR-CCS					
aug-cc-pVDZ	8.62	10.31	10.97	12.12	12.63
	(0.0499)	(0.0000)	(0.1061)	(0.0054)	(0.0304)
aug-cc-pVTZ	8.64	10.31	10.93	11.78	12.59
	(0.0476)	(0.0000)	(0.1007)	(0.007)	(0.0278)
aug-cc-pVQZ	8.64	10.31	10.92	11.59	12.58
	(0.0466)	(0.0000)	(0.0967)	(0.0088)	(0.0262)
LR-CC2					
aug-cc-pVDZ	7.04	8.70	9.47	10.68	11.09
	(0.0598)	(0.0000)	(0.1042)	(0.0001)	(0.0170)
aug-cc-pVTZ	7.19	8.85	9.56	10.33	11.19
	(0.0568)	(0.0000)	(0.1012)	(0.0007)	(0.0149)
aug-cc-pVQZ	7.25	9.38	9.61	10.14	11.73
	(0.0553)	(0.0000)	(0.0985)	(0.0022)	(0.0132)
LR-CCSD					
aug-cc-pVDZ	7.40	9.17	9.84	11.06	11.59
	(0.0565)	(0.0000)	(0.1039)	(0.0009)	(0.0201)
aug-cc-pVTZ	7.55	9.32	9.94	10.78	11.68
	(0.0527)	(0.0000)	(0.0993)	(0.0027)	(0.0181)
aug-cc-pVQZ	7.61	9.38	9.98	10.61	11.73
	(0.0512)	(0.0000)	(0.0959)	(0.0044)	(0.0162)
LR-CC3					
aug-cc-pVDZ	7.47	9.25	9.90	11.15	11.67
	(0.0574)	(0.0000)	(0.1060)	(0.0012)	(0.0220)
aug-cc-pVTZ	7.56	9.34	9.94	10.81	11.71
	(0.0538)	(0.0000)	(0.1016)	(0.003)	(0.0198)
aug-cc-pVQZ	7.60	9.38	9.97	10.63	11.74
	(0.0524)	(0.0000)	(0.0985)	(0.0047)	(0.0179)
EOM-CCSD					
aug-cc-pVDZ	7.40	9.17	9.84	11.06	11.59
	(0.0566)	(0.0000)	(0.1046)	(0.0009)	(0.0202)
aug-cc-pVTZ	7.55	9.32	9.94	10.78	11.68
	(0.0527)	(0.0000)	(0.0999)	(0.0027)	(0.0183)
aug-cc-pVQZ	7.61	9.38	9.98	10.61	11.73
	(0.0512)	(0.0000)	(0.0964)	(0.0044)	(0.0164)
TD-M06-2X					
aug-cc-pVDZ	7.35	8.80	9.62	10.60	11.01
	(0.0445)	(0.0000)	(0.0828)	(0.0007)	(0.0120)
aug-cc-pVTZ	7.42	8.90	9.62	10.28	11.06
	(0.0420)	(0.0000)	(0.0811)	(0.0022)	(0.0122)
aug-cc-pVQZ	7.41	8.91	9.61	10.07	11.07
	(0.0431)	(0.0000)	(0.0816)	(0.0037)	(0.0121)
aug-cc-pV5Z	7.42	8.91	9.61	9.83	11.07
	(0.0408)	(0.0000)	(0.0754)	(0.0051)	(0.0106)
aug-cc-pV6Z	7.41	8.89	9.57	9.65	11.06
	(0.0405)	(0.0000)	(0.0659)	(0.0065)	(0.0096)

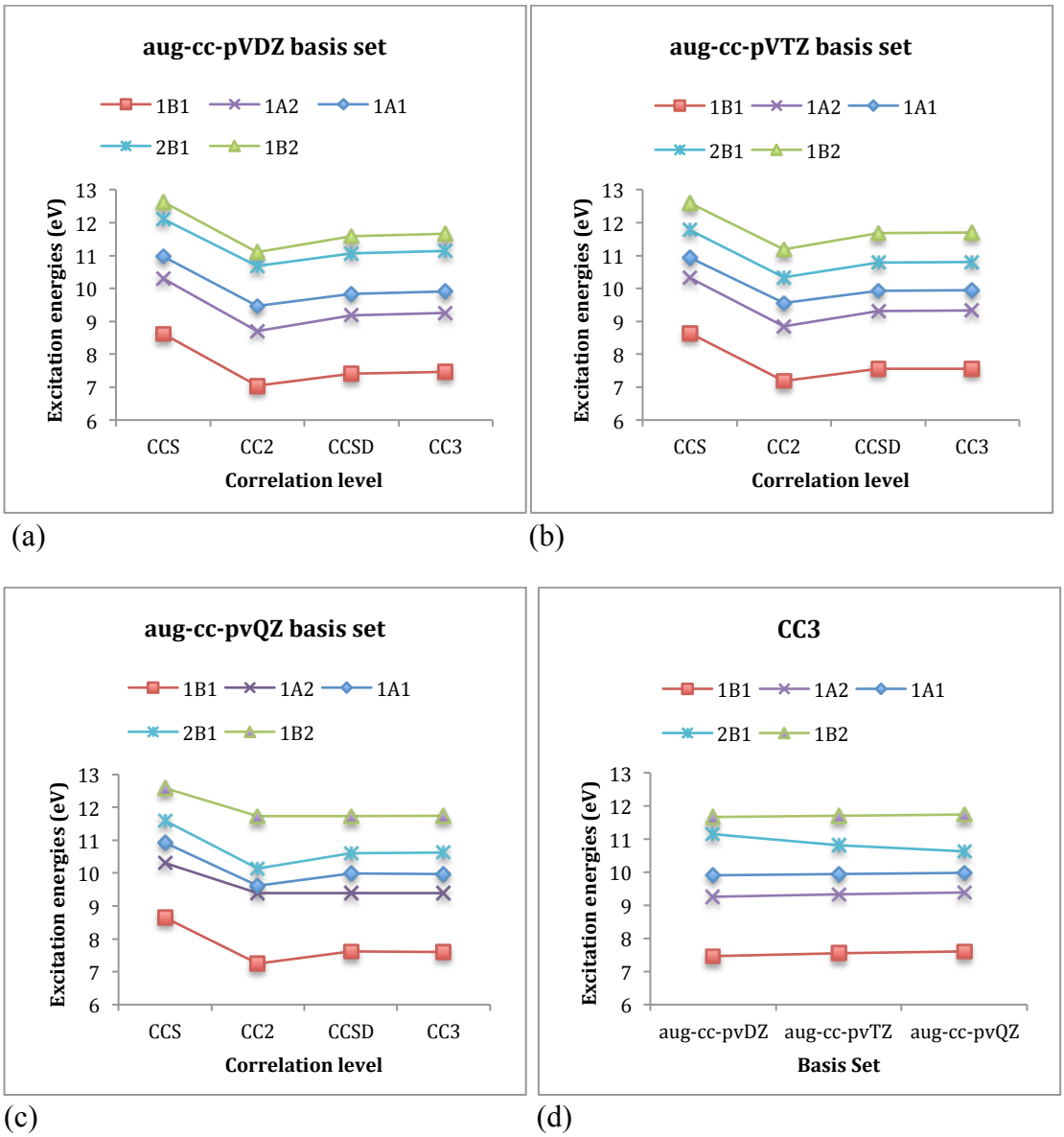

Figure 3.3 Excitations energies (in eV) of lowest singlet electronic excited states of water monomer of C_{2V} symmetry using the hierarchy of correlated coupled cluster (CC) methods with the (a) aug-cc-pVDZ basis set, (b) aug-cc-pVTZ basis set and (c) aug-cc-pVQZ basis set. (d) Basis set effect on the excitation energies using the coupled cluster CC3 method.

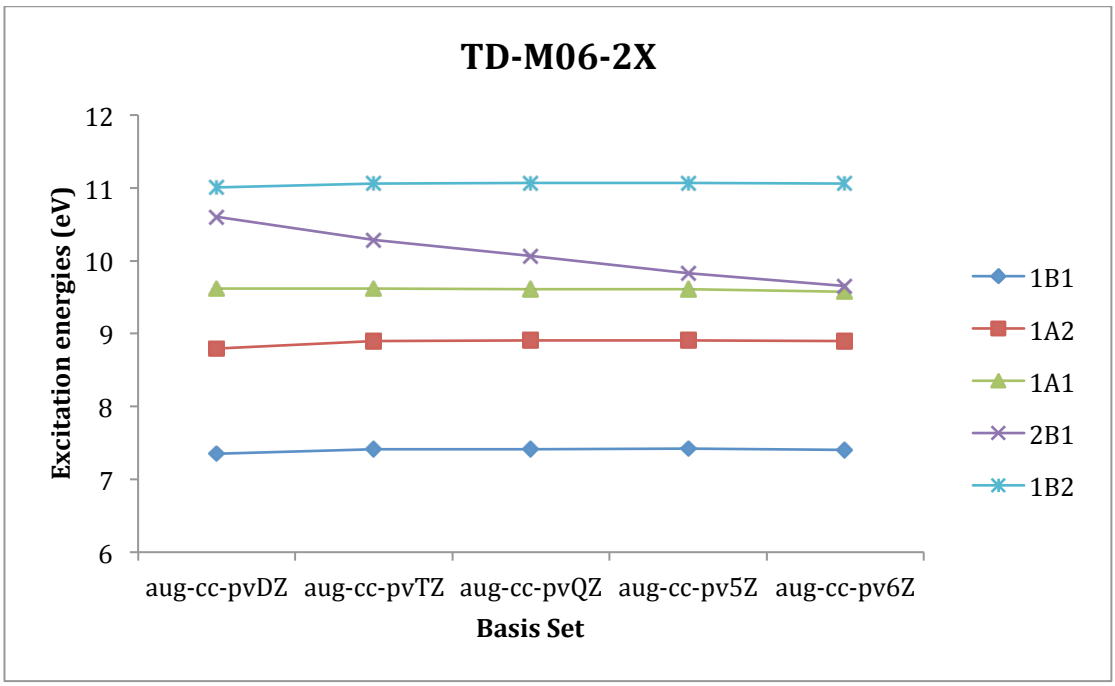

Figure 3.4 Excitations energies (in eV) of lowest singlet electronic excited states of water monomer of C_{2V} symmetry using TD-DFT theory with the MO6-2X functional and the aug-cc-pVXZ basis set with X = D, T, Q, 5, 6.

The oscillator strengths *f* calculated by LR-coupled cluster CCS, CC2, CCSD, CC3 methods for these lowest singlet excited states has also shown convergence in the aug-cc-pVXZ basis set series, with X = D, T, Q (See Figures 3.5(a)-(c)). CCS underestimates oscillator strength for the first lowest singlet excited state $1B_1$ while overestimates for $1B_2$ state. In contrast, CC2 overestimates oscillator strength for $1B_1$ state while underestimate for $1B_2$ state. For a given basis set, CCSD and CC3 results converge to similar oscillator strengths, with CC3 values marginally higher. It was found that $1B_1$ state is the lowest bright state with $f \approx 0.0524$, while $1A_1$ is the brightest state with highest oscillator strength $f \approx 0.0985$, calculated at the CC3/aug-cc-pVQZ level. It is also noticed that $1A_2$ is the lowest dark state with zero oscillator strength for all coupled cluster calculations.

The basis set effect on the oscillator strengths shows that the *f* values are lowered with increase in basis set size from aug-cc-pVDZ to aug-cc-pVQZ at each CC level of calculation. However the deviation noticed is small for all methods. Such basis set effect at the CC3 level is shown in Figure 3.5(d).

For the TD-DFT results, we have seen the basis set effect on the oscillator strengths in the aug-cc-pVXZ basis set series, with X = D, T, Q, 5, 6 (See Figure 3.6 and Table 3.2). The oscillator strengths are nearly similar for aug-cc-pVTZ and aug-cc-pVQZ

basis set while values are lowered slightly in going from aug-cc-pVQZ to higher aug-cc-pV5Z, aug-cc-pV6Z basis sets. It is also seen that oscillator strengths calculated by TD-DFT are too low in comparison to coupled cluster results and discrepancies are much more significant.

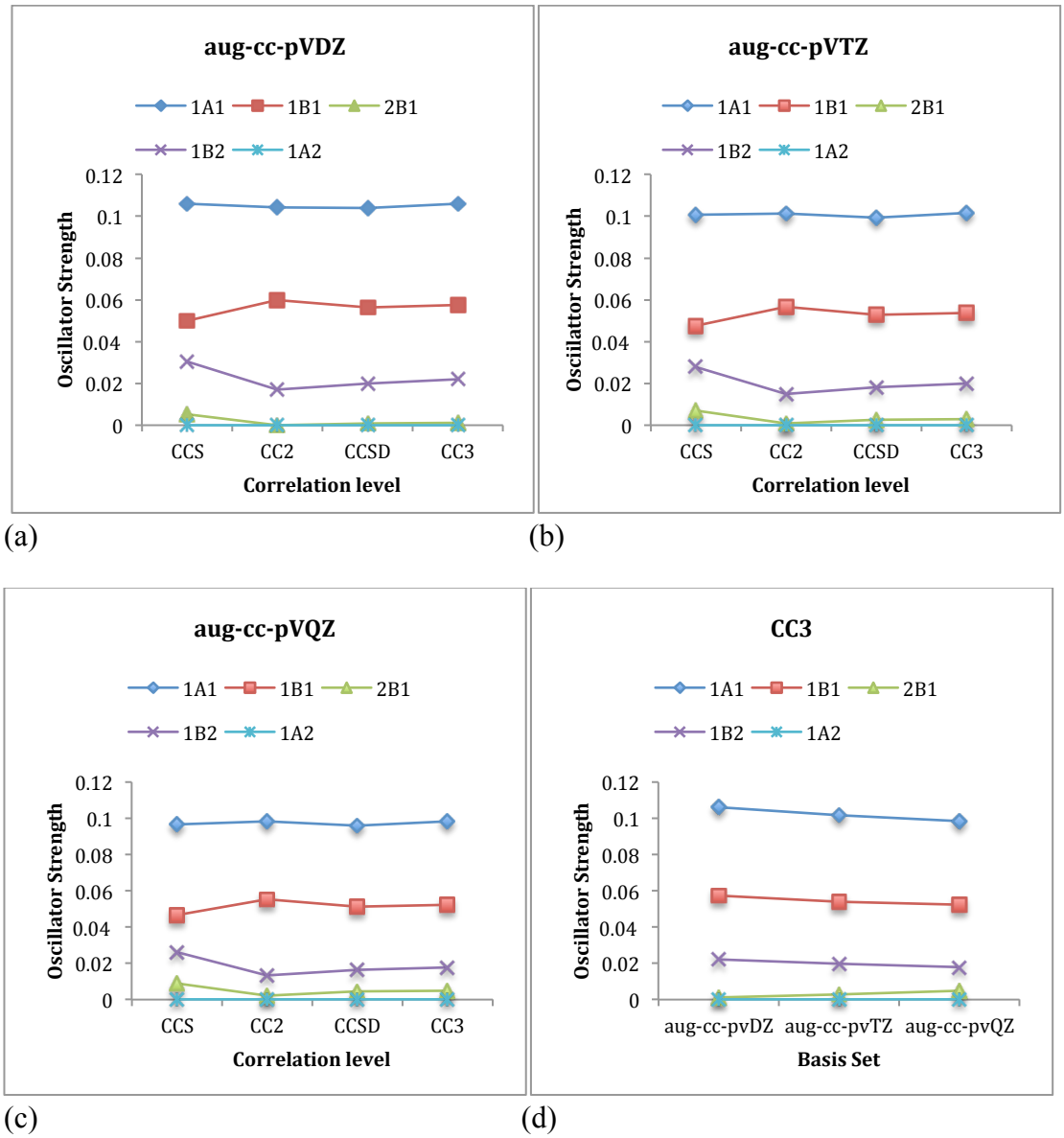

Figure 3.5 Oscillator strengths of lowest singlet electronic excited states of water monomer of C_{2V} symmetry using the hierarchy of correlated coupled cluster (CC) methods with the (a) aug-cc-pVDZ basis set, (b) aug-cc-pVTZ basis set and (c) aug-cc-pVQZ basis set. (d) Basis set effect on the oscillator strengths using the coupled cluster CC3 method.

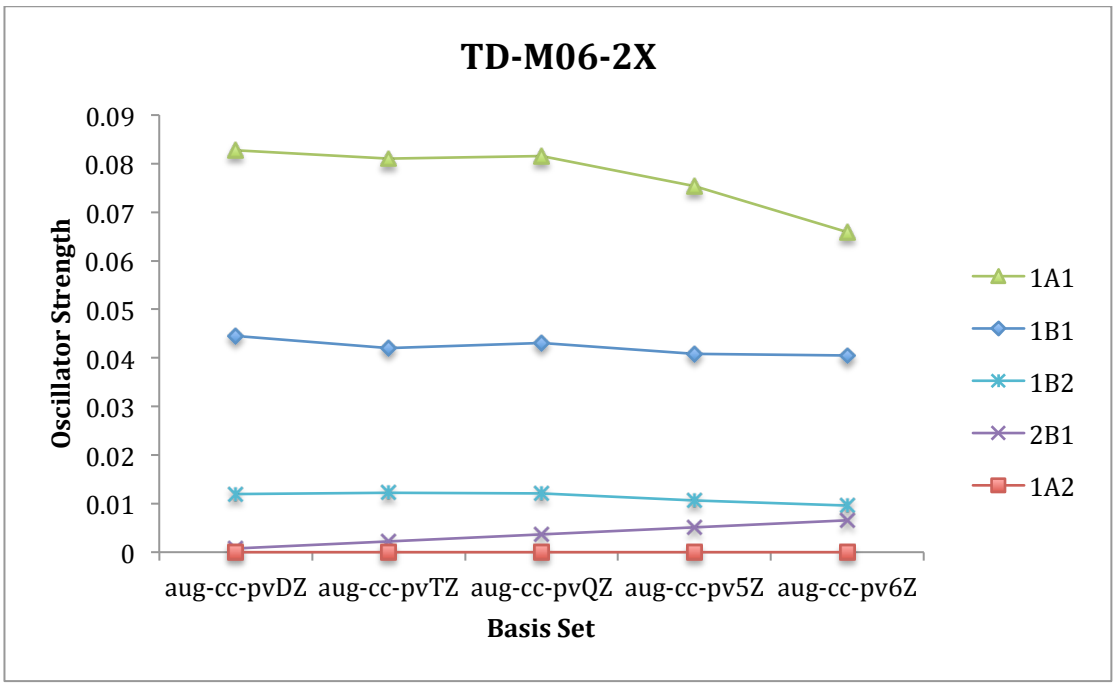

Figure 3.6 Oscillator strengths of lowest singlet electronic excited states of water monomer of C_{2V} symmetry using TD-DFT theory with the MO6-2X functional and the aug-cc-pVXZ basis set with X = D, T, Q, 5, 6.

The molecular orbital (MO) analysis has been done to understand the nature of electronic transitions and to characterize the excited states in the water monomer at both TD-DFT and EOM-CCSD level of calculations.

The calculated lowest energy singlet excited state $1B_1$ (first bright state) is described by the electronic transition from $1b_1$ (HOMO) to $4a_1$ (LUMO) i.e. from the nonbonding O $2p_x$ atomic orbital to the orbital that is an admixture of the O $3s$ Rydberg character with the anti-bonding b^* OH character (or anti-bonding counterpart of the valence $3a_1$ orbital). The second bright state $1A_1$ with high oscillator strength is assigned as the electronic transition from $3a_1$ (HOMO-1) to $4a_1$ (LUMO) orbital. The excited state $1A_2$ arises due to the electronic transition from $1b_1$ (HOMO) to $2b_2$ (LUMO+1) orbital and is the first dark state with zero oscillator strength. The excited state $1B_2$ corresponds to the electronic transition from $3a_1$ (HOMO-1) to $2b_2$ (LUMO+1) orbital.

Thus diffuse Rydberg character is noticed in the excited states of the water monomer as shown in Figure 3.2, which plays an important role and therefore makes it such a challenging system to study.

The excited-state second-moments of the charge distributions give useful information about the Rydberg character involved in the excited states and have been used as a main tool to investigate such states in the past [225]. The size of the isotropic

invariant $\langle r_{iso}^2 \rangle$ of the excited state second-moment tensor relative to the $\tilde{X}$ ground state $\langle r_{iso}^2 \rangle$ is of particular relevance to the parameterization of excited state Rydberg character. The average of the trace of the second moment tensor gives the $\langle r_{iso}^2 \rangle$ values for each state using the relation

$$\langle r_{iso}^2 \rangle = \frac{1}{3}(\langle x^2 \rangle + \langle y^2 \rangle + \langle z^2 \rangle) \tag{3.1}$$

It has been discussed previously by Reisler and Kryov [225] that $\Delta\langle r_{iso}^2 \rangle$ values for valence states are close to 1 $Å^2$, whereas for 3s Rydberg states this value may be in the region of 12 $Å^2$.

The isotropic invariant $\langle r_{iso}^2 \rangle$ (in $Å^2$) of the lowest singlet electronic excited states of water monomer of C_{2v} symmetry obtained using LR-CCSD method and the ground state using CCSD method with the aug-cc-pVDZ and the aug-cc-pVTZ basis set are presented in Table 3.3. For both $1A_1$ and $1B_1$ excited states, $\Delta\langle r_{iso}^2 \rangle$ values are close to 6 $Å^2$, that suggests that these states are mixed states which exhibit both valence and Rydberg character. However, $\Delta\langle r_{iso}^2 \rangle$ values increase considerably for $1B_2$ and $1A_2$ excited states to about 10-11 $Å^2$, which suggests strong Rydberg character of these states.

Table 3.3 The isotropic invariant $\langle r_{iso}^2 \rangle$ (in $Å^2$) of the ground state and lowest singlet electronic excited states of water monomer of C_{2v} symmetry using coupled cluster CCSD method with the aug-cc-pVDZ and the aug-cc-pVTZ basis set.

Method: CCSD	**Isotropic property $\langle r_{iso}^2 \rangle$ (in $Å^2$)**	
States	**aug-cc-pVDZ**	**aug-cc-pVTZ**
$\tilde{X}A_1$ (Ground)	6.7258	6.6531
$1A_1$ (Excited)	12.597	12.462
$1B_1$ (Excited)	12.389	12.212
$1B_2$ (Excited)	17.094	17.228
$1A_2$ (Excited)	16.512	16.424

Dipole Moment

The total electric dipole moment values obtained for the first four lowest energy excited states of different symmetry i.e. one of each symmetry using the hierarchy of linear response (LR) coupled cluster CCS, CC2 and CCSD methods are listed in Table 3.4. For comparison, the ground state dipole moment is also calculated using CCS, CC2 and CCSD method. The basis set aug-cc-pVXZ with X = D, T were employed for these calculations. The total electric dipole moment values calculated for ground and excited states are shown in Figures 3.7(a) and 3.7(b) using the aug-cc-pVDZ and aug-cc-pVTZ basis set, respectively.

The CCS calculations overestimate the ground state dipole moments compared to the experimental value of about 1.855 D, with the deviations from experiment being 0.162 D with the aug-cc-pVDZ basis set while slightly smaller deviation of about 0.146 D with the aug-cc-pVTZ basis set. The CC2 calculations underestimate the ground state dipole moments, with the deviations from experiment being 0.162 D with the aug-cc-pVDZ basis set while slightly smaller deviation of about 0.146 D with the aug-cc-pVTZ basis set. CCSD results are in good agreement with the experiments within the accuracy of 0.01D for both aug-cc-pVDZ and aug-cc-pVTZ basis set.

For the excited states, it is seen that dipole moment is directed in the opposite direction to the ground state dipole moment. Total electric dipole moment is dependent on the level of correlation and choosing LR-CCSD as the best reference correlated method, we see that CC2 results clearly overestimate dipole moments for excited states under study. CCS overestimates for $1B_1$ state, while underestimates for $1A_1$, $1B_2$, $1A_2$ excited states. Similar effect is noticed for both the aug-cc-pVDZ and aug-cc-pVTZ basis set, although calculated excited state dipole moments are slightly smaller using the aug-cc-pVDZ basis set (See Table 3.4 and Figures 3.7(a)-3.7(b)).

Comparing excited state dipole moments with the ground state, it is seen that the total dipole moment for the lowest energy $1B_1$ state is reduced by about 13% with respect to the ground state, while reduction is about 32-37% for $1A_1$, $1B_2$, $1A_2$ excited states at the CCSD/aug-cc-pVTZ level. Thus the significant change in charge density is noticed for $1A_1$, $1B_2$, $1A_2$ excited states with respect to ground state, while smaller change for $1B_1$ state.

Table 3.4 The total electric dipole moment (in D) of the ground state and lowest singlet electronic excited states of water monomer of C_{2V} symmetry using the coupled cluster methods with the aug-cc-pVDZ and the aug-cc-pVTZ basis set. The value in parenthesis corresponds to experimental ground state dipole moment of water monomer ([a]Taken from Ref. [226]).

Electric dipole moment (Debye) Basis Set: aug-cc-pVDZ		**Excited states**			
Method	**(Ground) $\tilde{X}A_1$**	**$1A_1$**	**$1B_1$**	**$1B_2$**	**$1A_2$**
CCS	2.016 (1.855[a])	-1.031	-1.566	-0.941	-0.839
CC2	1.831 (1.855[a])	-1.456	-1.665	-1.402	-1.176
CCSD	1.864 (1.855[a])	-1.166	-1.470	-1.197	-1.042
Electric dipole moment (Debye) Basis Set: aug-cc-pVTZ		**Excited states**			
Method	**(Ground) $\tilde{X}A1$**	**$1A_1$**	**$1B_1$**	**$1B_2$**	**$1A_2$**
CCS	2.000 (1.855[a])	-1.080	-1.698	-0.989	-0.943
CC2	1.820 (1.855[a])	-1.575	-1.850	-1.476	-1.294
CCSD	1.861(1.855[a])	-1.232	-1.614	-1.264	-1.164

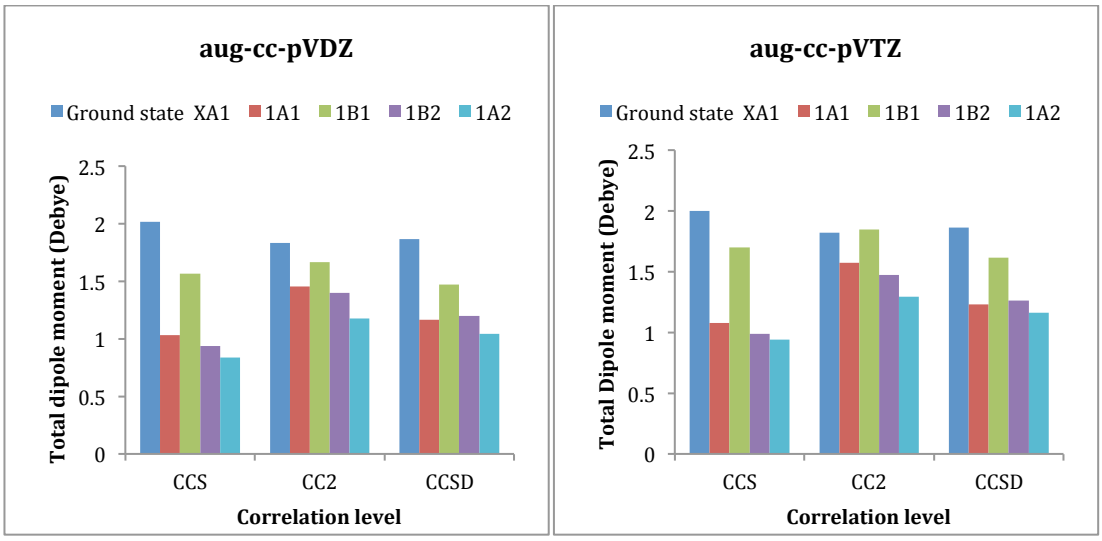

(a) (b)

Figure 3.7 The total electric dipole moment (in Debye) of the ground state and lowest singlet electronic excited states of water monomer of C_{2V} symmetry using the hierarchy of correlated coupled cluster (CC) methods such as CCS, CC2 and CCSD with the (a) aug-cc-pVDZ basis set and (b) aug-cc-pVTZ basis set.

3.3.2.2 Water Dimer (C_s)

The ground state molecular orbital configuration of the water dimer molecule having C_s symmetry, can be written as

$(1a')^2(2a')^2(3a')^2(4a')^2(1a'')^2(5a')^2(6a')^2(7a')^2(8a')^2(2a'')^2(\tilde{X}^1A')$,

where a' and a'' corresponds to MO's symmetries. The highest energy occupied molecular orbital 2a'' (HOMO) corresponds to the nonbonding O $2p_z$ atomic orbital of water monomer within dimer, while 8a' (HOMO-1) orbital corresponds to the bonding MO result from the linear combination of O $2p_x$ and O $2p_y$ atomic orbitals with H $1s$ orbital, respectively for each monomer within dimer. The lowest energy unoccupied orbital 9a' (LUMO) is the admixture of the peak contribution from the O $3s$ Rydberg character along with some contribution from with the anti-bonding counterpart of the valence 8a' orbital of a water monomer within dimer. The 10a' (LUMO +1) orbital is similar to 9a' (LUMO), primarily dominated by O $3s$ Rydberg character, however this MO is occupied by another water monomer. The MO's density plots are shown in Figure 3.8.

Vertical excitation energies and Oscillator Strengths

Table 3.5 presents the linear response coupled cluster CCS, CC2, CCSD and CC3 results as well as related EOM-CCSD results, together with TD-DFT results for the vertical excitation energies and oscillator strengths for the four lowest energy singlet excited states i.e. two states of each symmetry A' and A'' of water dimer of C_s symmetry. (Note: All excited states discussed below are singlets).

The investigation of electron correlation effects on the excitation energies of the states obtained using linear response (LR) coupled cluster hierarchy of models has shown a significant overestimation of excitation energies by the CCS method with respect to highly correlated wave function CCSD and CC3 methods, which both converge monotonically to the similar results within a difference of 0.06 eV. CC2 underestimates the excitation energies compared to CCSD and CC3 results. The 1A'' state is found to be the first lowest energy singlet excited state followed by 1A', 2A'' and 2A' states in order of increasing excitation energy. We choose CCSD and CC3 as the best reference methods to compare results with the other methods as well as for detailed discussion.

The basis set dependence of these excitation energies using aug-cc-pVXZ split valence series with X = D, T, Q is also listed in Table 3.5 and the coupled cluster

convergence of excitation energies in the aug-cc-pVXZ basis set series, with X = D, T is also shown in Figures 3.9(a)-(b). At CCSD level of theory, the excitation energies increase by about 0.15 eV going from augmented aug-cc-pVDZ to aug-cc-pVTZ basis set for first three low lying 1A", 1A', 2A" excited states, while a small difference of about 0.07 eV in going from aug-cc-pVTZ to aug-cc-pVQZ basis set is noticed. Similarly at the CC3 level, the excitation energies increase by about 0.1 eV in going from augmented aug-cc-pVDZ to aug-cc-pVTZ basis set for the first three low lying 1A", 1A', 2A" excited states, while a very small increase of about 0.03 eV is noticed for the 2A' state. It is seen that the basis size effect at the CC3 level is consistent to the CCSD level and produces results within 0.02-0.07 eV with each other for both aug-cc-pVDZ and aug-cc-pVTZ basis set.

For the first lowest singlet excited state 1A" of water dimer, both the CCSD and CC3 method with the aug-cc-pVTZ basis set give consistent vertical excitation energies of about 7.53 and 7.51 eV, respectively, whereas with the aug-cc-pVQZ basis set, the CCSD method gives a vertical excitation energy of about 7.60 eV for the 1A" state. The second singlet excited state 1A' with excitation energy of 7.96 eV at the CCSD/aug-cc-pVTZ level is in excellent agreement with the CC3/aug-cc-pVTZ results within about 0.01 eV. The calculated excitation energy of about 8.88 eV for the third singlet excited state 2A" at the CCSD level using aug-cc-pVTZ basis set is slightly larger by 0.07 eV with the CC3 level, thus in satisfactory agreement with each other. The excited state 2A' with excitation energy of about 9.60 eV is obtained at the CCSD/aug-cc-pVTZ level with an excellent agreement with the CC3/aug-cc-pVTZ results within about 0.01 eV.

Similar to the water monomer results, we have seen the convergence of excitation energies in the aug-cc-pVXZ basis set series, with X = D, T, Q, 5 for the TD-M06-2X results for the water dimer (See Figure 3.10 and Table 3.5). The excitation energies show convergence at the aug-cc-pVQZ basis set with nearly similar excitation energies with increase in basis set cardinality from X = T to 5 for lowest singlet 1A" and 1A' states, while within 0.04 eV difference for 2A" and 2A' excited states. For the lowest lying singlet excited states 1A" and 1A', the TD-M06-2X excitation energies are too low by about 0.24 eV and 0.13 eV, respectively, as compared to results at both CCSD and CC3 levels using aug-cc-pVTZ level, while discrepancies are much larger for 2A" and 2A' states, the TD-DFT excitation energies being about 0.6-0.8 eV too low.

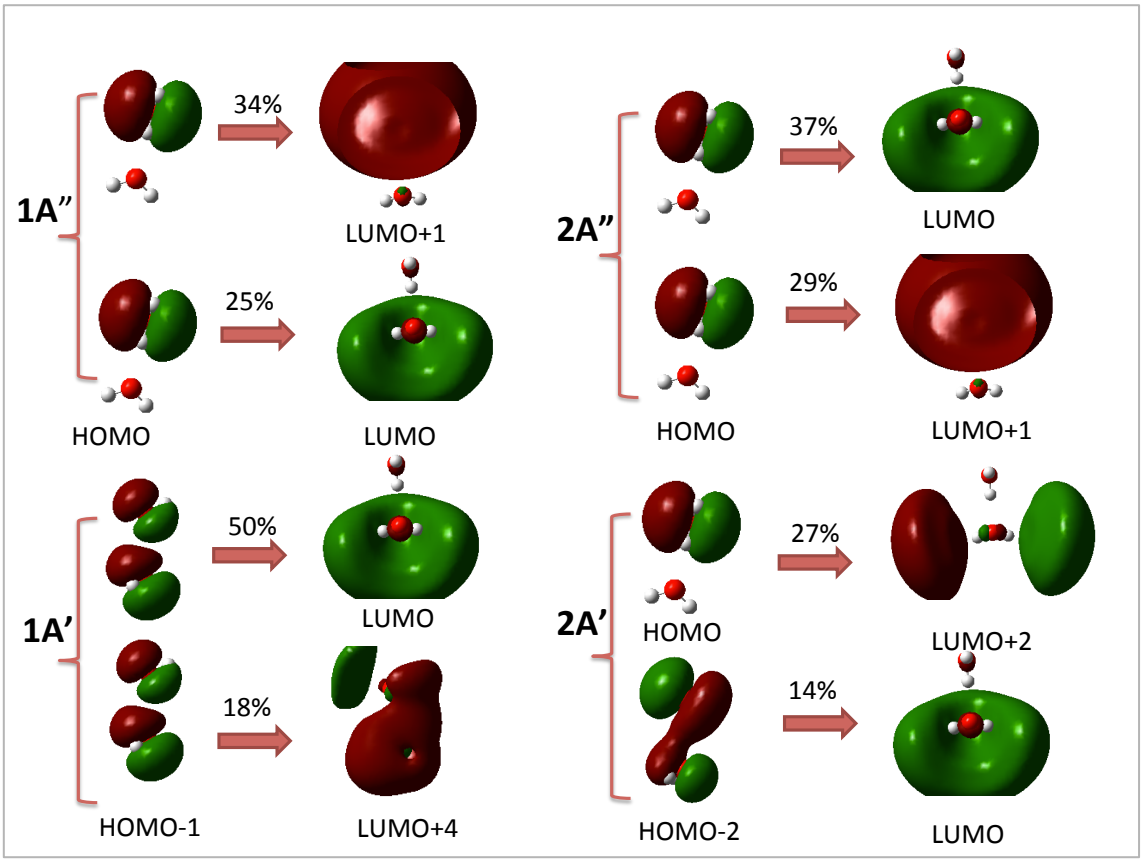

Figure 3.8 Water dimer (C_s symmetry): Molecular orbitals involved in the electronic transitions for lowest energy singlet electronic excited states of different symmetry i.e. two excited states of each symmetry computed at the EOM-CCSD level. Isovalue = 0.02 for the density plots.

Table 3.5 Water dimer (C_s): Excitations energies in eV and oscillator strengths (in parenthesis) of the lowest energy singlet electronic excited states using the hierarchy of correlated coupled cluster such as CCS, CC2, CCSD, CC3 methods, EOM-CCSD, and TD-DFT methods.

Water Dimer (C_s)	**Excitation energies E (eV)**			
	Excited States			
	1A"	**1A'**	**2A"**	**2A'**
LR-CCS				
aug-cc-pVDZ	8.69	9.06	10.35	10.78
	(0.0494)	(0.0564)	(0.0037)	(0.0586)
aug-cc-pVTZ	8.71	9.08	10.33	10.74
	(0.0475)	(0.0550)	(0.0042)	(0.0528)
aug-cc-pVQZ	8.71	9.09	10.31	10.72
	(0.0468)	(0.0543)	(0.0048)	(0.0476)
LR-CC2				
aug-cc-pVDZ	6.97	7.47	8.16	9.00
	(0.0562)	(0.0674)	(0.0001)	(0.0067)
aug-cc-pVTZ	7.11	7.62	8.30	9.04
	(0.0543)	(0.0653)	(0.0000)	(0.0038)
aug-cc-pVQZ	7.18	7.68	8.35	9.05
	(0.0535)	(0.0642)	(0.0000)	(0.0025)
LR-CCSD				
aug-cc-pVDZ	7.37	7.81	8.73	9.52
	(0.0546)	(0.0640)	(0.0000)	(0.0410)
aug-cc-pVTZ	7.53	7.96	8.88	9.60
	(0.0518)	(0.0614)	(0.0001)	(0.0311)
aug-cc-pVQZ	7.60	8.03	8.95	9.63
	(0.0508)	(0.0602)	(0.0003)	(0.0224)
LR-CC3				
aug-cc-pVDZ	7.41	7.86	8.71	9.56
	(0.0547)	(0.0659)	(0.0000)	(0.0400)
aug-cc-pVTZ	7.51	7.95	8.81	9.59
	(0.052)	(0.0634)	(0.0000)	(0.0293)
EOM-CCSD				
aug-cc-pVDZ	7.37	7.81	8.73	9.52
	(0.0549)	(0.0640)	(0.0000)	(0.0410)
aug-cc-pVTZ	7.53	7.96	8.88	9.60
	(0.0521)	(0.0613)	(0.0002)	(0.0311)
aug-cc-pVQZ	7.60	8.03	8.95	9.63
	(0.0511)	(0.0602)	(0.0003)	(0.0224)
TD-M06-2X				
aug-cc-pVDZ	7.22	7.75	8.03	8.93
	(0.0370)	(0.0517)	(0.0030)	(0.0012)
aug-cc-pVTZ	7.29	7.83	8.12	8.97
	(0.0366)	(0.0513)	(0.0023)	(0.0015)
aug-cc-pVQZ	7.30	7.84	8.15	8.96
	(0.0385)	(0.0527)	(0.0018)	(0.0016)
aug-cc-pV5Z	7.30	7.84	8.14	8.93
	(0.0367)	(0.0508)	(0.0017)	(0.0012)

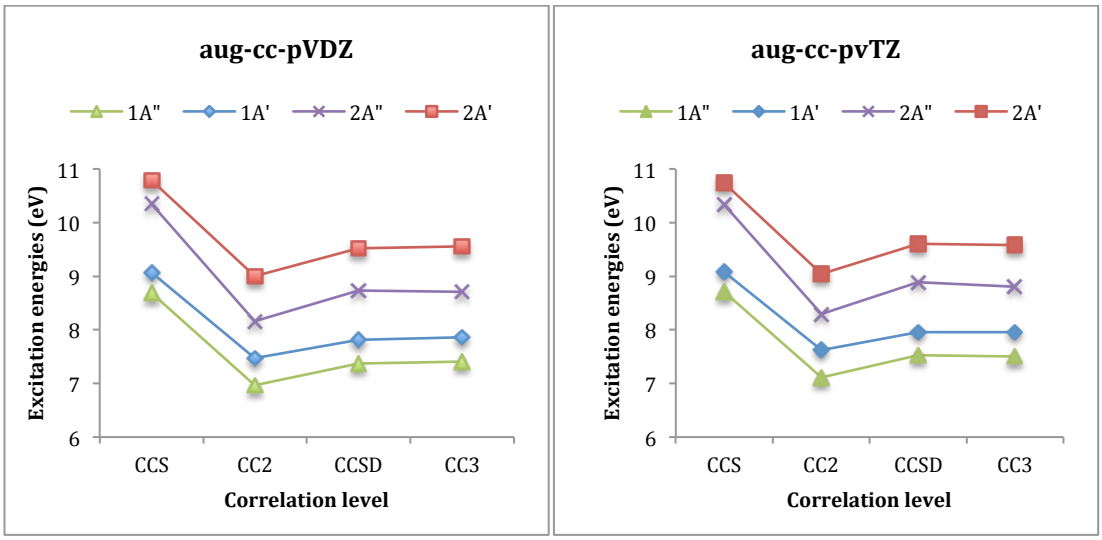

(a) (b)

Figure 3.9 Excitation energies (in eV) of lowest singlet electronic excited states of water dimer of C_s symmetry using the hierarchy of correlated coupled cluster (CC) methods with the (a) aug-cc-pVDZ basis set, (b) aug-cc-pVTZ basis set.

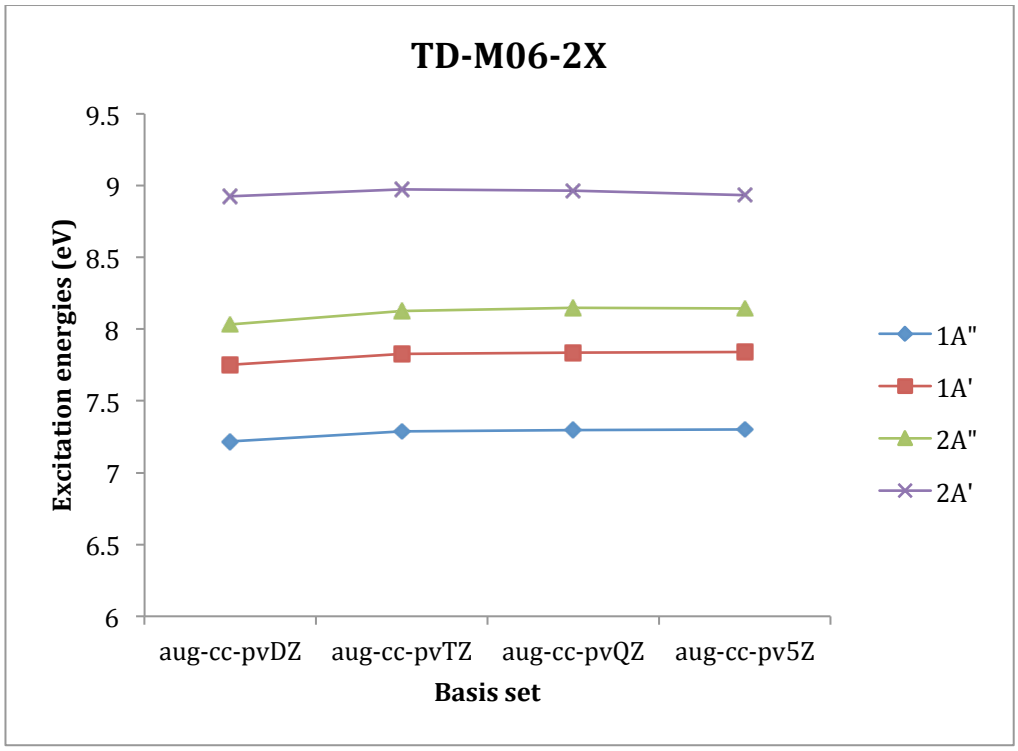

Figure 3.10 Excitation energies (in eV) of lowest singlet electronic excited states of water dimer of C_s symmetry using TD-DFT theory with the MO6-2X functional and the aug-cc-pVXZ basis sets with X = D, T, Q, 5.

The oscillator strengths *f* calculated by LR-coupled cluster CCS, CC2, CCSD, CC3 methods for these lowest singlet excited states have also shown convergence in the aug-cc-pVXZ basis set series, with X = D, T, Q (See Table 3.5 and Figures 3.11(a)-(b)). CCS underestimates oscillator strengths for the lowest singlet excited states 1A" and 1A', while overestimates for 2A" and 2A' states. CC2 slightly overestimates oscillator strengths for 1A" and 1A' excited states, while underestimates for 2A' state. For a given basis set, CCSD and CC3 results converge to similar oscillator strengths, with CC3 values marginally higher for 1A" and 1A' excited states. We observe 1A" state as the lowest bright state with $f \approx 0.0508$, while 1A' is the brightest state with highest oscillator strength $f \approx 0.0602$, calculated at the CCSD/aug-cc-pVQZ level. It is also noticed that 2A" is a dark state with nearly zero oscillator strength for all coupled cluster CC2, CCSD and CC3 calculations, while 2A' state shows larger discrepancies with oscillator strength ranges from $f \approx 0.003$-0.04, depending on the CC method. It is also seen that that the *f* values decrease with increase in basis set size from aug-cc-pVDZ to aug-cc-pVQZ at each CC level of calculation, however deviations noticed are very small for all methods.

Figure 3.12 shows the basis set effect on the oscillator strengths calculated by TD-M06-2X method in the aug-cc-pVXZ basis set series, with X = D, T, Q, 5 (Also see Table 3.5). The oscillator strengths are quite similar for all aug-cc-pVXZ basis set series, with X = D, T, 5 basis set except for X = Q where values are slightly higher for the brighter 1A" and 1A' excited states. The dim (dark) states 2A" and 2A' have nearly similar zero oscillator strengths. It is also noticed that TD-M06-2X oscillator strengths are too low compared to those obtained by coupled cluster CC2, CCSD and CC3 methods.

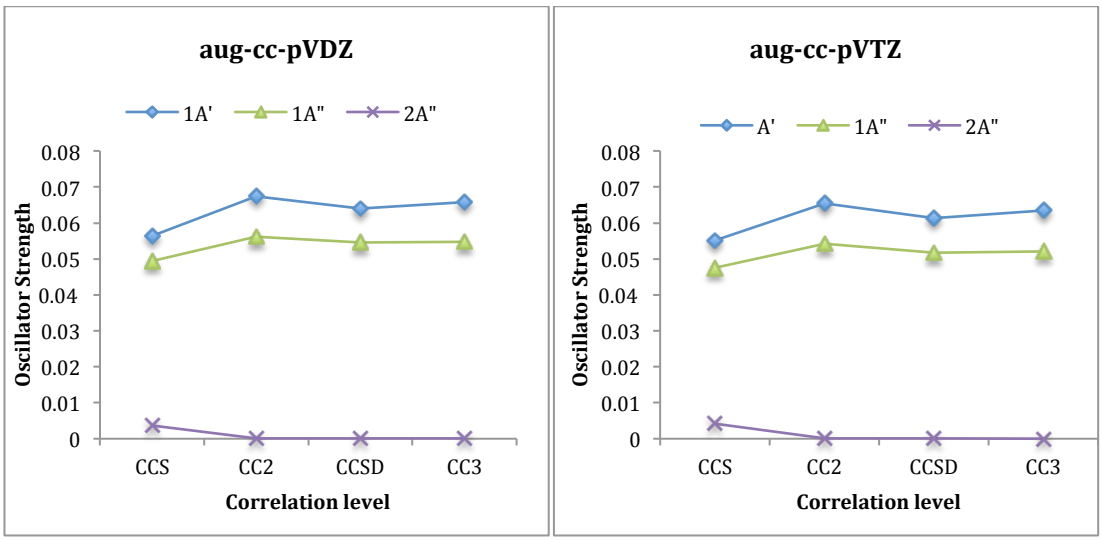

(a) (b)

Figure 3.11 Oscillator strengths of lowest singlet electronic excited states of water dimer of C_s symmetry using the hierarchy of correlated coupled cluster (CC) methods with the (a) aug-cc-pVDZ basis set and (b) aug-cc-pVTZ basis set.

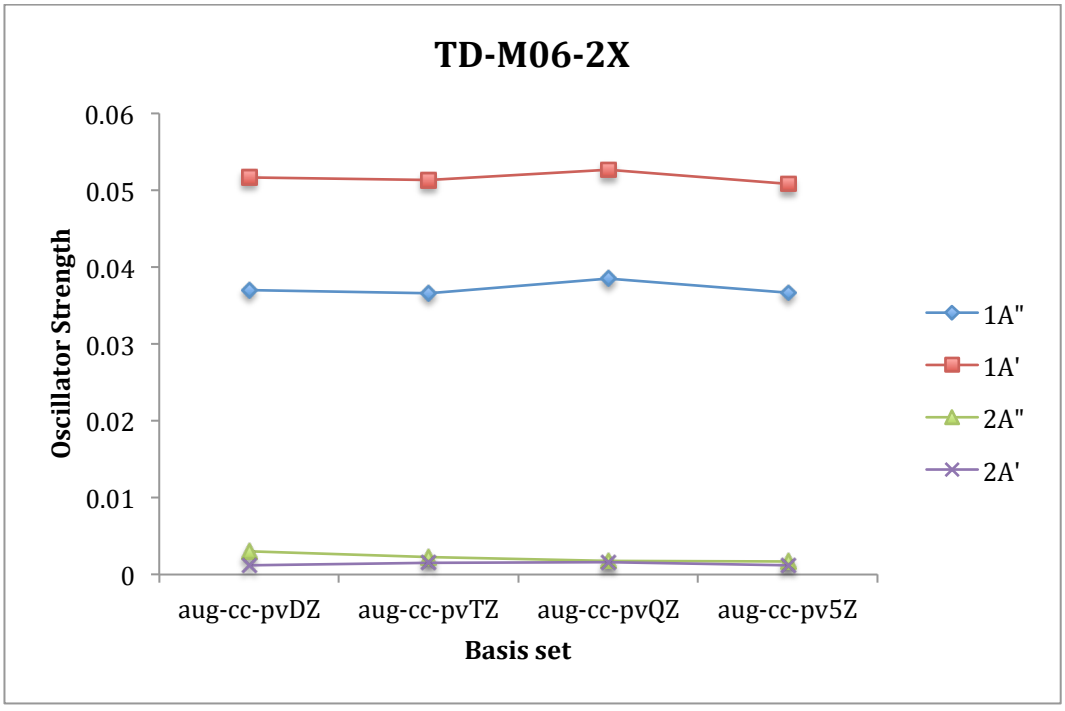

Figure 3.12 Oscillator strengths of lowest singlet electronic excited states of water dimer of C_s symmetry using TD-DFT theory with the M06-2X functional and the aug-cc-pVXZ basis sets with X = D, T, Q, 5.

It is seen from the molecular orbital (MO) analysis that the calculated lowest energy singlet excited state 1A" (first bright state) is described by the electronic transition from 2a" (HOMO) to 9a' (LUMO) in combination with the electronic transition from 2a" (HOMO) to 10a' (LUMO+1) orbitals i.e. from the nonbonding O $2p_z$ atomic orbital to the orbital that is an admixture of the O 3*s* Rydberg character with the anti-bonding b^* OH character (See Figure 3.8). Similarly, the excited state 2A" with nearly zero oscillator strength arise due to combined contribution from the electronic transition from 2a" (HOMO) to 10a' (LUMO+1) orbital as well as the electronic transition from 2a" (HOMO) to 9a' (LUMO) orbital. These excited states involving orbitals are localized within one or the other monomer. The second bright state 1A' also with highest oscillator strength is assigned as the electronic transition from 8a'(HOMO-1) to 9a' (LUMO) orbital with some contribution from electronic transition from 8a'(HOMO-1) to 12a' (LUMO+4) orbital. The excited state 2A' corresponds to the electronic transition from 2a"(HOMO) to 3a" (LUMO+2) orbital as well as some contribution from the electronic transition from 7a'(HOMO-2) to 9a' (LUMO) orbital. The nature of molecular orbitals involved in the electronic transitions for each excited state is shown in Figure 3.8. The diffuse Rydberg character dominates in the excited states of the water dimer, which can be further analysed by calculating the moment of charge distribution for each excited state and comparing it with the ground state.

Table 3.6 presents the isotropic invariant $\langle r_{iso}^2 \rangle$ (in $Å^2$) of the lowest singlet electronic excited states of water dimer obtained using linear response CCSD method along with the ground state value obtained using CCSD method. Both aug-cc-pVDZ and aug-cc-pVTZ basis sets were employed. We have calculated $\Delta\langle r_{iso}^2 \rangle$ for each excited state, as the size of the isotropic invariant $\langle r_{iso}^2 \rangle$ of the excited state second-moment tensor relative to the $\tilde{X}$ ground state $\langle r_{iso}^2 \rangle$ is important to analyze the nature of the excited states as mentioned above for the water monomer. For both lowest energy excited states 1A" and 1A', $\Delta\langle r_{iso}^2 \rangle$ values are close to 7 $Å^2$, that indicates mixed states which exhibit both valence and Rydberg character. However, for 2A" and 2A' excited states with higher excitation energies, $\Delta\langle r_{iso}^2 \rangle$ values increases considerably to about 10-11 $Å^2$, which suggest strong Rydberg character of these states. The results obtained are consistent for both aug-cc-pVDZ and aug-cc-pVTZ basis sets within 1 $Å^2$.

Table 3.6 The isotropic invariant $\langle r_{iso}^2 \rangle$ (in Å^2) of the ground state and lowest singlet electronic excited states of water dimer of C_s symmetry using coupled cluster CCSD method with the aug-cc-pVDZ and aug-cc-pVTZ basis sets.

Method: CCSD	**Isotropic property $\langle r_{iso}^2 \rangle$ (in Å^2)**	
States	**aug-cc-pVDZ**	**aug-cc-pVTZ**
$\widetilde{X}$A' (Ground)	64.216	64.063
1A' (Excited)	71.095	70.817
2A' (Excited)	72.608	73.705
1A" (Excited)	71.544	71.349
2A" (Excited)	75.053	75.429

Dipole Moment

For the water dimer, the total electric dipole moment values obtained for the first four lowest energy excited states of different symmetry (i.e. two of each symmetry) using the hierarchy of linear response (LR) coupled cluster CCS, CC2 and CCSD methods with the basis set aug-cc-pVXZ with X = D, T, along with ground state dipole moments obtained using CCS, CC2 and CCSD method are listed in Table 3.7. Figures 3.13 (a) and 3.13(b) show the total electric dipole moment values calculated for ground and excited states using aug-cc-pVDZ and aug-cc-pVTZ basis set, respectively.

The CCS calculations slightly overestimate the total ground state dipole moment of water dimer by about 0.1 D with respect to the experimental value of about 2.608 D [227]. Both CC2 results and CCSD results are in good agreement with the experiment within an accuracy of about 0.05 D and 0.02 D, respectively. The results are quite consistent for both the aug-cc-pVDZ and the aug-cc-pVTZ basis set.

For the excited states, choosing LR-CCSD as the best reference correlated method to compare results, we see that CCS overestimate total dipole moments for 1A', 1A" excited states by about 1.0 D, overestimates largely by about 3.0 D for the for 2A' state, and underestimates by 0.9 D for the 2A" excited state. CC2 slightly overestimates for 1A', 2A" excited states, overestimates largely for 2A' state with maximum deviation of about 8.0 D, and slightly underestimates for the 1A" excited state. Similar effect is noticed for both the aug-cc-pVDZ and the aug-cc-pVTZ basis set (See Table 3.7 and Figures 3.13(a)-3.13(b)).

Now, by comparing excited state total dipole moments with the ground one at the CCSD/aug-cc-pVTZ level, it is seen that the total dipole moment for the lowest energy 1A" state is increased by about 82% with respect to the ground state, while small increment of about 7% is noticed for 1A' state. The significant change in charge density is noticed for 2A' state where total dipole moment changes by about 120% with respect to ground state, whereas 2A" excited state gives a increment of about 45% with respect to ground state.

Table 3.7 The total electric dipole moment (in Debye) of the ground state and lowest singlet electronic excited states of water dimer of C_s symmetry using coupled cluster methods with the aug-cc-pVDZ and aug-cc-pVTZ basis sets. The value in parenthesis corresponds to experimental ground state dipole moment of water monomer ([a] Taken from Ref. [227]).

Electric dipole moment (Debye) Basis Set: aug-cc-pVDZ		**Excited states**			
Method	**Ground state $\tilde{X}$A'**	**1A'**	**1A"**	**2A'**	**2A"**
CCS	2.714 (2.608[a])	2.929	5.863	4.195	4.744
CC2	2.575 (2.608[a])	2.895	4.367	9.107	5.875
CCSD	2.593 (2.608[a])	2.722	4.639	1.596	5.583
Electric dipole moment (Debye) Basis Set: aug-cc-pVTZ		**Excited states**			
Method	**Ground state $\tilde{X}$A'**	**1A'**	**1A"**	**2A'**	**2A"**
CCS	2.702 (2.608[a])	2.955	5.899	3.786	4.937
CC2	2.563 (2.608[a])	2.960	4.407	8.834	5.886
CCSD	2.588 (2.608[a])	2.762	4.702	1.401	5.610

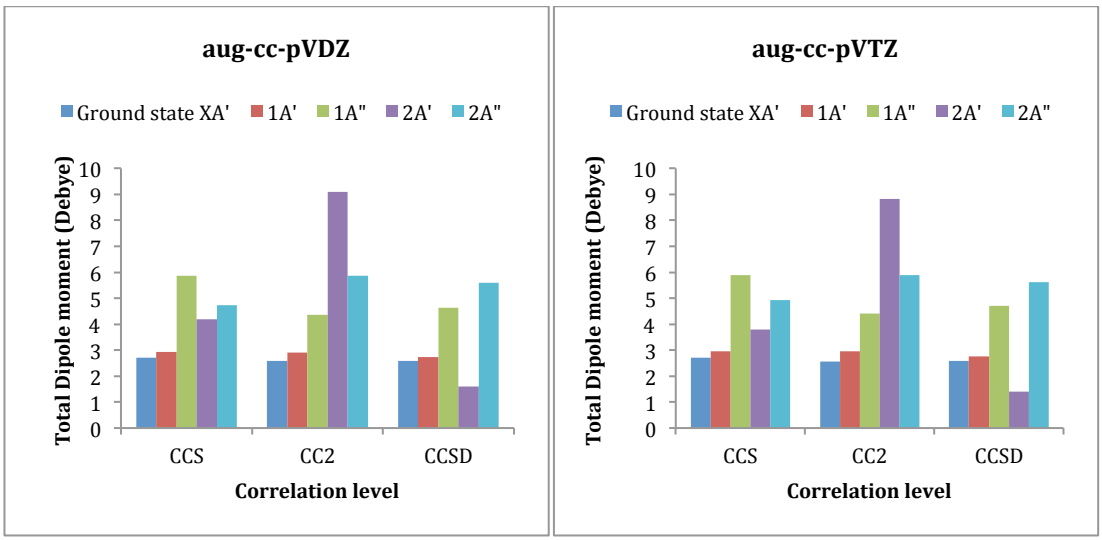

(a) (b)

Figure 3.13 The total electric dipole moment (in Debye) of the ground state and lowest singlet electronic excited states of water dimer of C_s symmetry using the hierarchy of correlated coupled cluster (CC) methods such as CCS, CC2 and CCSD with the (a) aug-cc-pVDZ basis set and (b) aug-cc-pVTZ basis set.

3.3.2.3 Water Trimer (C_{2v})

Vertical excitation energies and Oscillator Strengths

For the water trimer with C_{2v} symmetry, the effect of electron correlation on the excitation energies have been investigated using linear response (LR) coupled cluster hierarchy of models CCS, CC2, CCSD and CC3 methods along with the related EOM-CCSD for first four excited states (i.e. one state of each symmetry) are presented in Table 3.8. The results obtained using both aug-cc-pVDZ and aug-cc-pVTZ basis set are also listed in Table 3.8. (Note: All excited states discussed below are singlets).

For all coupled cluster calculations, it is found that $1B_1$ state is the first lowest energy singlet excited state in water trimer. $1B_2$ is the second lowest energy excited state followed by energetically very close lying $1A_1$ excited state and then energetically slightly higher $1A_2$ excited state. For a given basis set, it is seen that CCS largely overestimates the excitation energies of these states; CC2 underestimates, while CCSD excitation energies are slightly higher (for larger basis set) with respect to those obtained by CC3 method, as also shown in Figures 3.14(a) and 3.14(b) for aug-cc-pVDZ and aug-cc-pVTZ basis sets, respectively.

Now investigating the basis set effect on these excitation energies, we find that there is no substantial difference in results obtained by using aug-cc-pVDZ or aug-cc-pVTZ basis set at the CCS level, while at both CC2 and CCSD levels, excitation energies

increases within 0.15 eV going from the aug-cc-pVDZ to the aug-cc-pVTZ basis set. At the CC3 level, the excitation energies increase by about 0.10 eV in going from augmented aug-cc-pVDZ to aug-cc-pVTZ basis set for all excited states under study.

For the first lowest singlet excited state $1B_1$, both CCSD and CC3 methods using aug-cc-pVDZ basis set give consistent vertical excitation energy of about 7.47 and 7.45 eV, respectively, whereas using the aug-cc-pVTZ basis set, CCSD excitation energy is slightly higher by about 0.07 eV compared to CC3. For both close lying second and third excited states $1B_2$ and $1A_1$, the calculated excitation energies are about 7.91 eV and 7.94 eV respectively, at the CCSD/aug-cc-pVTZ level, which are in excellent agreement with the CC3/ aug-cc-pVTZ result within 0.01 eV. The calculated excitation energy of about 8.42 eV for the $1A_2$ excited state at the CCSD level is slightly larger by 0.07 eV with the CC3 level using aug-cc-pVDZ basis set, while difference is about 0.13 eV using aug-cc-pVTZ basis set, thus in satisfactory agreement with each other. It is noted that EOM-CCSD and LR-CCSD excitation energies results are equivalent for all excited states.

Also for the TD-M06-2X results, we have seen the convergence of excitation energies in the aug-cc-pVXZ basis set series, with X = D, T, Q, 5 (See Figure 3.15 and Table 3.8). The excitation energies are underestimated by smaller aug-cc-pVDZ basis set compared to larger aug-cc-pVXZ basis set, with X = T, Q, 5. For all excited states under study, excitation energies don't change substantially and similar values are noticed with increase in basis set cardinality from X = T to Q, 5. Some discrepancies are observed in energetic ordering of states with respect to the coupled cluster results, as states are closely spaced within 1 eV. $1B_1$ state is the first lowest excited state followed by $1A_2$ $1B_2$ and $1A_1$ excited states in increasing order of energy. For the lowest lying singlet excited state $1B_1$, the TD-M06-2X excitation energy is too low by about 0.44 eV and 0.37 eV, respectively, as compared to results at both CCSD and CC3 levels using aug-cc-pVTZ level, while discrepancies are much larger for $1A_2$ state, the TD-DFT excitation energies being about 0.9-0.7 eV too low. For $1B_2$ and $1A_1$ excited states, TD-M06-2X excitation energies are in satisfactory agreement with both CCSD and CC3 results using aug-cc-pVTZ basis set, with energies being low by about 0.15 eV.

Table 3.8 Water trimer (C_{2v}): Excitations energies (in eV) of the lowest energy singlet electronic excited states using the hierarchy of correlated coupled cluster such as CCS, CC2, CCSD, CC3 methods, EOM-CCSD, and TD-DFT methods.

Water trimer (C_{2v})	**Excitation energies E (eV)**			
	Excited States			
	$1B_1$	**$1B_2$**	**$1A_1$**	**$1A_2$**
LR-CCS				
aug-cc-pVDZ	9.02	9.01	9.04	10.21
	(0.0577)	(0.0611)	(0.0548)	(0.0000)
aug-cc-pVTZ	9.03	9.03	9.06	10.19
	(0.0565)	(0.0614)	(0.0527)	(0.0000)
LR-CC2				
aug-cc-pVDZ	7.00	7.42	7.45	7.84
	(0.0518)	(0.0725)	(0.0637)	(0.0000)
aug-cc-pVTZ	7.14	7.57	7.59	7.97
	(0.0511)	(0.0725)	(0.061)	(0.0000)
LR-CCSD				
aug-cc-pVDZ	7.47	7.76	7.78	8.42
	(0.0527)	(0.0700)	(0.0604)	(0.0000)
aug-cc-pVTZ	7.62	7.91	7.94	8.58
	(0.0516)	(0.0695)	(0.0572)	(0.0000)
LR-CC3				
aug-cc-pVDZ	7.45	7.80	7.83	8.35
	(0.0505)	(0.0739)	(0.0616)	(0.0000)
aug-cc-pVTZ	7.55	7.90	7.93	8.45
	(0.0497)	(0.0735)	(0.0585)	(0.0000)
EOM-CCSD				
aug-cc-pVDZ	7.47	7.76	7.78	8.42
	(0.0534)	(0.0697)	(0.0605)	(0.0000)
aug-cc-pVTZ	7.62	7.91	7.94	8.58
	(0.0523)	(0.0690)	(0.0573)	(0.0000)
TD-M06-2X				
aug-cc-pVDZ	7.10	7.68	7.71	7.63
	(0.0285)	(0.0582)	(0.0473)	(0.0000)
aug-cc-pVTZ	7.18	7.77	7.79	7.73
	(0.0297)	(0.0586)	(0.0471)	(0.0000)
aug-cc-pVQZ	7.19	7.77	7.80	7.76
	(0.0324)	(0.0610)	(0.0484)	(0.0000)
aug-cc-pV5Z	7.19	7.78	7.80	7.75
	(0.0311)	(0.0593)	(0.0464)	(0.0000)

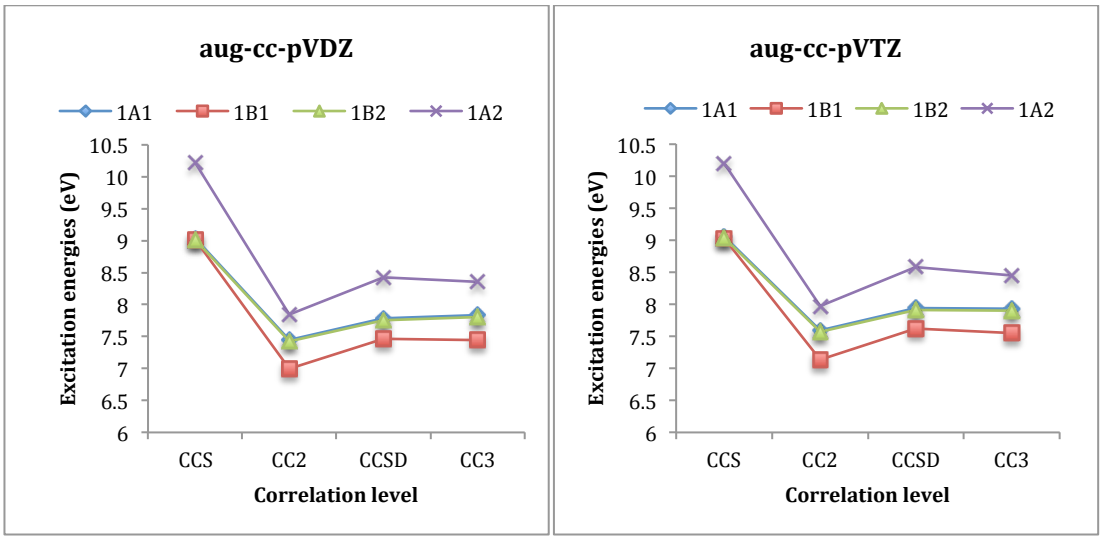

(a) (b)

Figure 3.14 Excitations energies (in eV) of lowest singlet electronic excited states of water trimer of C_{2v} symmetry using the hierarchy of correlated coupled cluster (CC) methods with the (a) aug-cc-pVDZ basis set and (b) aug-cc-pVTZ basis set.

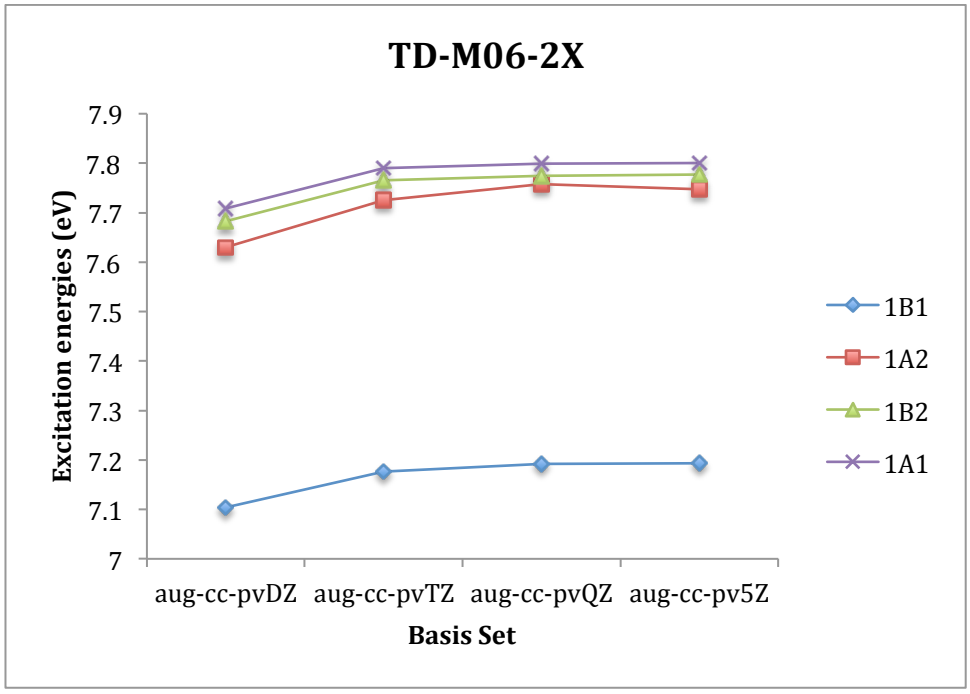

Figure 3.15 Excitations energies (in eV) of lowest singlet electronic excited states of water trimer of C_{2v} symmetry using TD-DFT theory with the MO6-2X functional and the aug-cc-pVXZ basis sets with X = D, T, Q, 5.

The oscillator strengths *f* calculated by using LR-coupled cluster CCS, CC2, CCSD, CC3 methods for these lowest singlet excited states are shown in Figure 3.16(a) and Figure 3.16(b), using aug-cc-pVDZ and aug-cc-pVTZ basis set, respectively (Also See Table 3.8). CCS underestimates oscillator strengths for the excited states $1A_1$ and $1B_2$ while overestimates for $1B_1$ state. For a given basis set, CC2, CCSD and CC3 results generally are in good agreement, with CC3 oscillator strength values slightly lower for the $1B_1$ state, and slightly higher for the $1B_2$ state with respect to CC2 and CCSD values. At the CC3/aug-cc-pVDZ level, oscillator strengths calculated for the lowest bright state $1B_1$ is $f \approx 0.0505$, while $1B_2$ is calculated as the brightest state with highest oscillator strength $f \approx 0.0739$. Similar to water monomer results, $1A_2$ is calculated as the lowest dark excited state with zero oscillator strength by all coupled cluster calculations. The basis set effect on the oscillator strengths shows that the *f* values decrease slightly with increase in basis set size from aug-cc-pVDZ to aug-cc-pVTZ and is true for all coupled cluster methods used above.

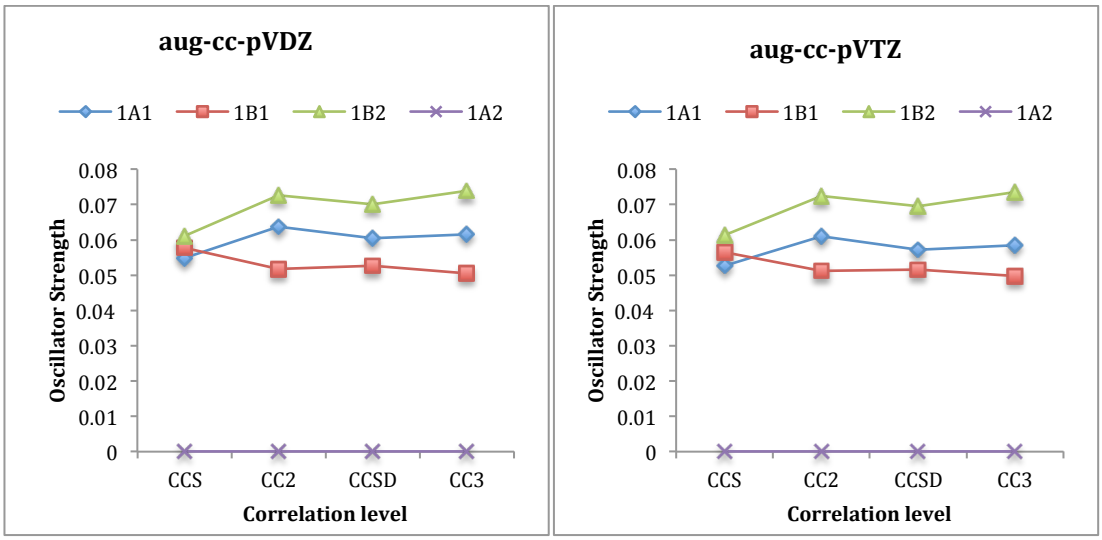

(a) (b)

Figure 3.16 Oscillator strengths of lowest singlet electronic excited states of water trimer of C_{2v} symmetry using the hierarchy of correlated coupled cluster (CC) methods with the (a) aug-cc-pVDZ basis set and (b) aug-cc-pVTZ basis set .

For the TD-M06-2X results, the basis set effect on the oscillator strengths in the aug-cc-pVXZ basis set series, with X = D, T, Q, 5 is shown in Figure 3.17. The oscillator strengths obtained are quite similar for all aug-cc-pVXZ basis sets, X= D, T, Q, 5. The *f* values slightly increases with increase in basis set cardinality from X = D to Q, but then decreases slightly at X = 5, however no substantial effect of basis set on oscillator strengths are observed. It is also seen that TD-DFT oscillator strengths are too low in comparison to coupled cluster results and large discrepancies are noticed.

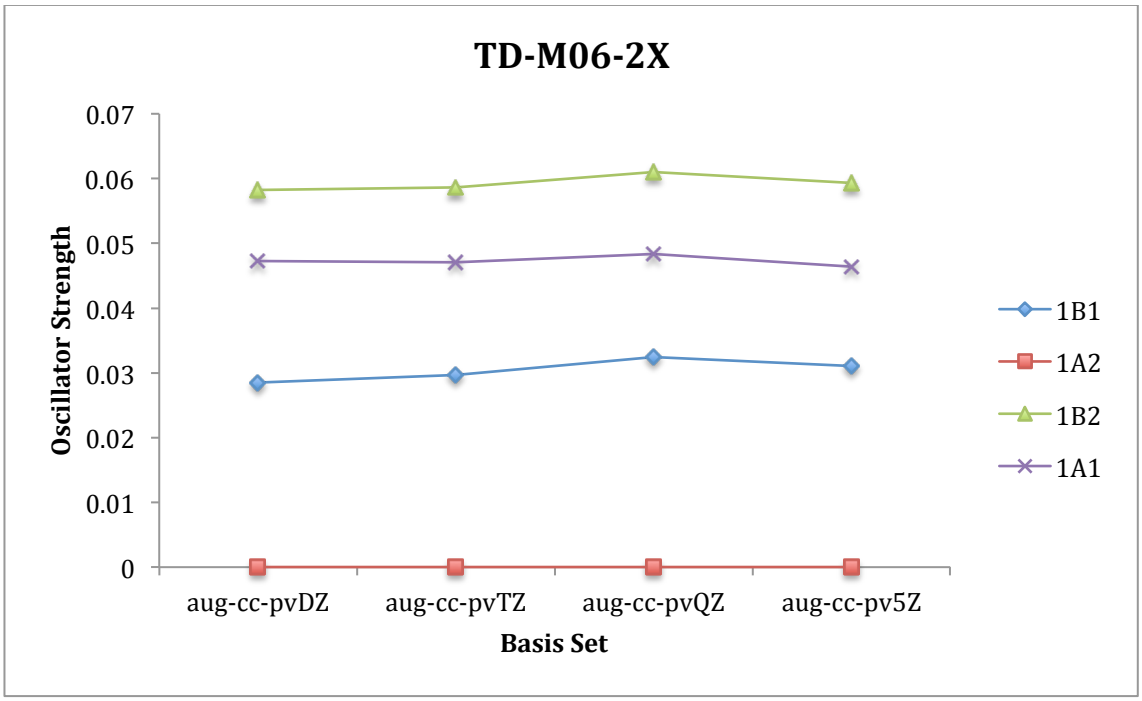

Figure 3.17 Oscillator strengths of lowest singlet electronic excited states of water trimer of C_{2v} symmetry using TD-DFT theory with the MO6-2X functional and the aug-cc-pVXZ basis sets with X = D, T, Q, 5.

The molecular orbital (MO) analysis has investigated the nature of electronic transitions for $1A_1$, $1B_1$, $1B_2$ and $1A_2$ excited states and diffuse Rydberg character is observed in the excited states of the water trimer as shown in Figure 3.18.

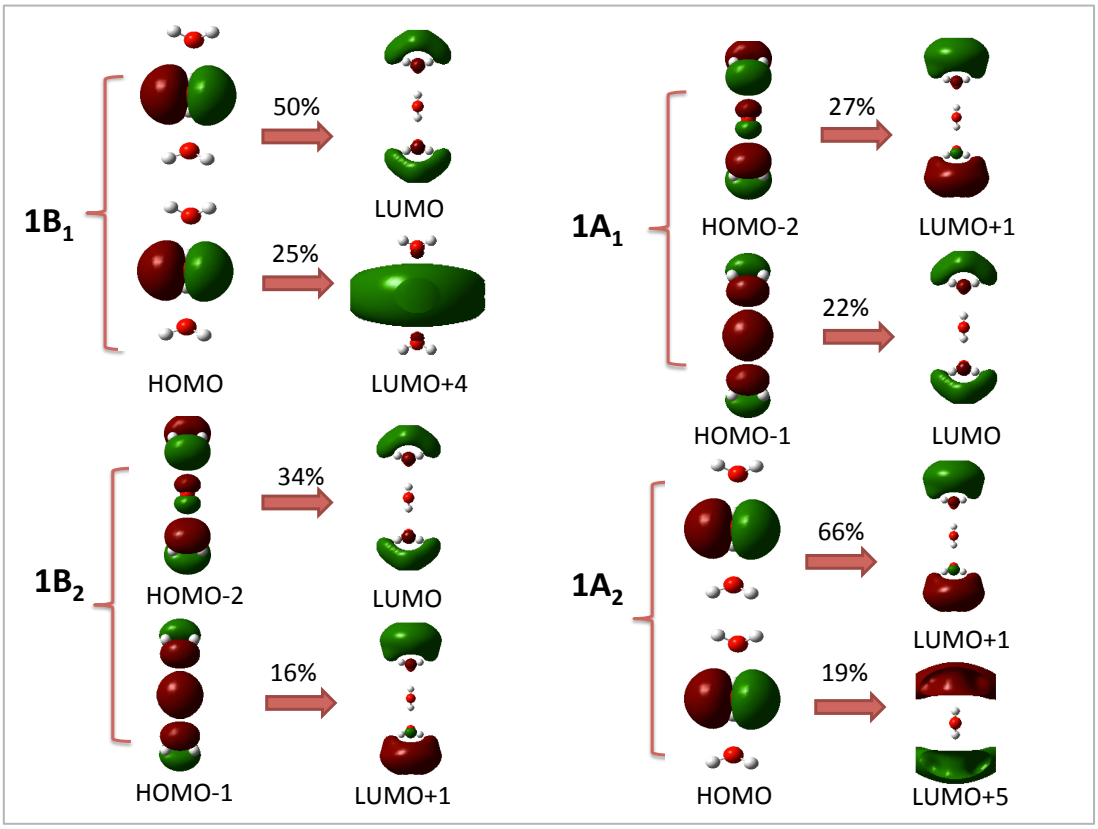

Figure 3.18 Water trimer (C_{2v} symmetry): Molecular orbitals involved in the electronic transitions for four lowest energy singlet electronic excited states of different symmetry i.e. one excited state of each symmetry computed at the EOM-CCSD level. Isovalue = 0.02 for the density plots.

Table 3.9 shows the isotropic invariant $\langle r_{iso}^2 \rangle$ (in Å^2) for the lowest singlet electronic excited states of water trimer of C_{2v} symmetry using coupled cluster CCSD method obtained using the coupled cluster LR-CCSD method with aug-cc-pVXZ basis set for X = D, T, along with ground state values obtained by CCSD method. We have calculated $\Delta\langle r_{iso}^2 \rangle$ for each excited state, which gives the difference of the size of the isotropic invariant $\langle r_{iso}^2 \rangle$ of the excited state second-moment tensor relative to the $\tilde{X}$ ground state $\langle r_{iso}^2 \rangle$. For singlet excited states $1A_1$, $1B_1$, and $1B_2$, $\Delta\langle r_{iso}^2 \rangle$ values are close to 9 Å^2, which suggests that these states exhibit Rydberg character with some mixing of valence character. However, $\Delta\langle r_{iso}^2 \rangle$ values are considerably large for $1A_2$ excited state of about 18 Å^2, which suggest strong Rydberg character of these states.

Table 3.9 The isotropic invariant $\langle r_{iso}^2 \rangle$ (in Å^2) for the ground state and lowest singlet electronic excited states of water trimer of C_{2v} symmetry using coupled cluster CCSD method with the aug-cc-pVDZ and aug-cc-pVTZ basis sets.

Method: CCSD	**Isotropic property $\langle r_{iso}^2 \rangle$ (in Å^2)**	
States	**aug-cc-pVDZ**	**aug-cc-pVTZ**
$\tilde{X}A_1$ (Ground)	206.282	206.054
$1A_1$ (Excited)	215.347	214.988
$1B_1$ (Excited)	215.600	215.628
$1B_2$ (Excited)	215.226	214.870
$1A_2$ (Excited)	224.199	224.735

Dipole Moment

The total electric dipole moment values for first four lowest energy excited states of different symmetry (i.e. one of each symmetry) of water trimer (C_{2v} symmetry), obtained using the hierarchy of linear response (LR) coupled cluster CCS, CC2 and CCSD methods with the basis set aug-cc-pVXZ for X = D, T are listed in Table 3.10. For comparison, the ground state dipole moment is also calculated using CCS, CC2 and CCSD method. The total electric dipole moment values calculated for ground and excited states are shown in Figures 3.19 (a) and 3.19 (b) using aug-cc-pVDZ and aug-cc-pVTZ basis sets, respectively.

The CCS calculations overestimate the ground state dipole moments slightly with respect to the best reference value of 0.44 D calculated by correlated CCSD method, with the deviations being 0.081 D with the aug-cc-pVDZ basis set, and a slightly smaller deviation of about 0.072 D with the aug-cc-pVTZ basis set. The CC2 calculations underestimate the ground state dipole moments, which are within 0.022 D of the values calculated by CCSD using both aug-cc-pVDZ as well as aug-cc-pVTZ basis set. The CCSD total dipole moment value calculated using aug-cc-pVDZ basis set is in good agreement with the aug-cc-pVTZ basis set within the accuracy of 0.01D.

For the excited states, choosing LR-CCSD as the best reference correlated method, we see that the total dipole moments calculated by CCS and CC2 methods are generally in good agreement with the CCSD results (See Table 3.10 and Figures 3.19(a)-(b)). CCS overestimates total dipole moments slightly for $1A_1$ and $1B_2$ excited states by

about 0.2 D, while underestimates by about 0.3 D for the $1A_2$ state with respect to CCSD results. CC2 results clearly overestimate dipole moments for all excited states under study, however maximum deviation is within 0.3 D of the values calculated by CCSD. The calculated excited state dipole moments are slightly smaller using aug-cc-pVDZ basis set for $1A_1$ and $1B_2$ states, while values are slightly higher for $1B_1$ and $1A_2$ states, with respect to those calculated by aug-cc-pVTZ basis set.

Table 3.10 The total electric dipole moment (in Debye) of the ground state and lowest singlet electronic excited states of water trimer of C_{2v} symmetry using coupled cluster methods with the aug-cc-pVDZ and aug-cc-pVTZ basis sets.

Electric dipole moment (Debye) Basis Set: aug-cc-pVDZ		**Excited states**			
Method	**Ground state** $\tilde{X}A_1$	**$1A_1$**	**$1B_1$**	**$1B_2$**	**$1A_2$**
CCS	0.515	-1.545	2.042	-1.517	1.246
CC2	0.413	-1.410	2.315	-1.403	1.819
CCSD	0.434	-1.3460	2.098	-1.323	1.583
Electric dipole moment (Debye) Basis Set: aug-cc-pVTZ		**Excited states**			
Method	**Ground state** $\tilde{X}A_1$	**$1A_1$**	**$1B_1$**	**$1B_2$**	**$1A_2$**
CCS	0.515	-1.573	1.660	-1.538	0.612
CC2	0.421	-1.481	2.052	-1.464	1.354
CCSD	0.443	-1.394	1.836	-1.363	1.094

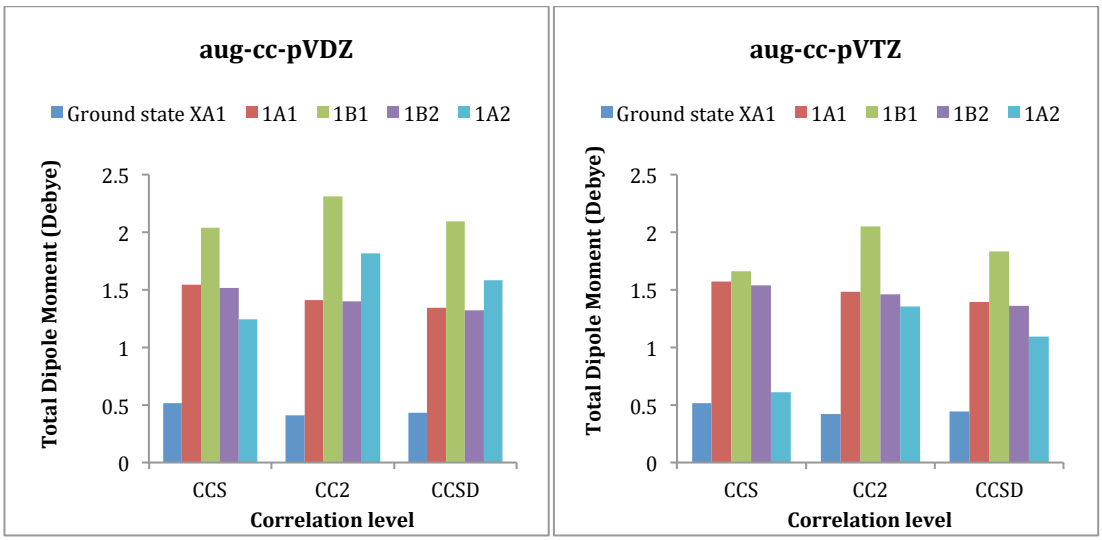

(a) (b)

Figure 3.19 The total electric dipole moment (in Debye) of the ground state and lowest singlet electronic excited states of water trimer of C_{2v} symmetry using hierarchy of correlated coupled cluster (CC) methods such as CCS, CC2 and CCSD with the (a) aug-cc-pVDZ basis set and (b) aug-cc-pVTZ basis set.

Comparing excited state dipole moments with the ground one, it is seen that the total dipole moment for the lowest energy $1B_1$ excited state is increased largely and becomes about five times the ground state dipole moment. Similarly, a large increment is also for seen for $1A_1$, $1B_2$, and $1A_2$ excited states and total excited state dipole moments is about three times the ground state dipole moment. Thus the significant change in charge density is noticed in all excited states with respect to ground state.

Evolution of $\Delta\langle r_{iso}^2\rangle$ with size of water cluster

The evolution of $\Delta\langle r_{iso}^2\rangle$ for the first lowest energy singlet electronic excited state of water cluster with increase in cluster size from the monomer up to the trimer is also investigated using the linear response coupled cluster CCSD method with the aug-cc-pVDZ and aug-cc-pVTZ basis set and shown in Figure 3.20. It is clearly seen that value of $\Delta\langle r_{iso}^2\rangle$ increases with increase in size of cluster from the monomer ($\approx$ 6 Å^2) to the trimer C_{2v} ($\approx$ 10 Å^2), illustrating the increase in Rydberg character of the lowest energy excited state with increase in cluster size. It is also noticed that results are consistent for both aug-cc-pVDZ and aug-cc-pVTZ basis sets.

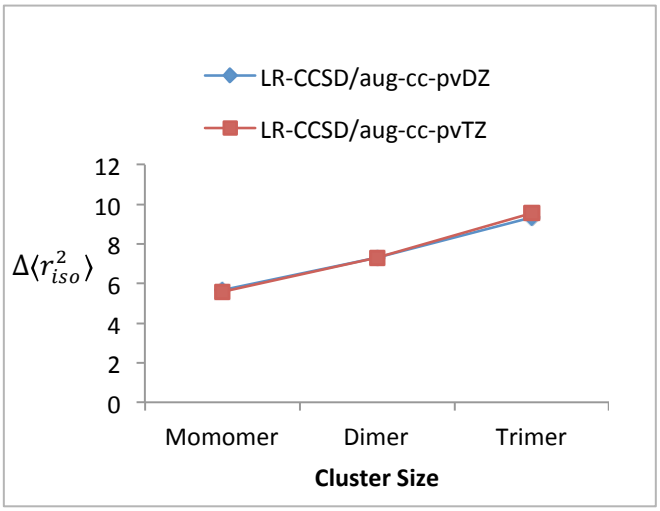

Figure 3.20 The evolution of $\Delta\langle r_{iso}^2 \rangle$ for the first lowest singlet electronic excited state of water cluster with increase in cluster size from monomer up to trimer using coupled cluster LR-CCSD method with aug-cc-pVDZ and aug-cc-pVTZ basis set.

3.3.2.4 Water Tetramer (S_4)

Vertical excitation energies and Oscillator Strengths

For the water tetramer of S_4 symmetry, the excitation energies obtained using linear response (LR) configuration interaction singles CIS, CIS(D), EOM-CCSD method along with the TD-DFT method using M06-2X functional for the first four excited states (i.e. one state of each symmetry), and with both aug-cc-pVDZ and aug-cc-pVTZ basis sets are presented in Table 3.11 and Figures 3.21(a)-(b). (Note: All excited states discussed below are singlets).

For all methods, it is found that 1E is the first lowest energy singlet excited state in the water tetramer, which is doubly degenerate state with two E states having the same energy. 1B and 1A are energetically very close lying excited states with 1A state marginally higher in energy than 1B excited state by ≤ 0.02 eV. All excited states under study are very close lying in energy i.e. within 0.03 eV difference to each other. It is calculated that the excitation energies of these states are largely overestimated by CIS method while CIS(D) underestimates with respect to those obtained by highly correlated EOM-CCSD method (See Figure 3.21).

At the CIS level, the increase in size of basis set from aug-cc-pVDZ to aug-cc-pVTZ doesn't produce substantial difference in excitation energies, while for both CIS(D) and EOM-CCSD level of calculations, excitation energies increases by about ≤ 0.20 eV going from aug-cc-pVDZ to aug-cc-pVTZ basis set, depending on the excited state. For

the first lowest doubly degenerate excited state 1E, the vertical excitation energy of about 7.95 is calculated by EOM-CCSD/aug-cc-pVDZ level of theory, whereas for the close lying excited states 1B and 1A, the calculated excitation energies are about 7.96 eV and 7.97 eV, respectively. The EOM-CCSD excitation energies increase slightly by about 0.15 eV using the aug-cc-pVTZ basis set for these excited states.

Table 3.11 Water tetramer (S_4): Excitations energies in eV and oscillator strengths (in parenthesis) of the lowest energy singlet electronic excited states using LR-CIS, EOM-CCSD, and TD-DFT using M06-2X functional.

	1E	**1B**	**1A**
LR-CIS			
aug-cc-pVDZ	9.27	9.28	9.29
	(0.0739)	(0.0634)	(0.0000)
aug-cc-pVTZ	9.29	9.30	9.31
	(0.0726)	(0.0604)	(0.0000)
LR-CIS(D)			
aug-cc-pVDZ	7.47	7.48	7.50
aug-cc-pVTZ	7.68	7.69	7.71
EOM-CCSD			
aug-cc-pVDZ	7.95	7.96	7.97
	(0.0856)	(0.0692)	(0.0000)
aug-cc-pVTZ	8.10	8.11	8.13
	(0.0834)	(0.0653)	(0.0000)
TD-M06-2X			
aug-cc-pVDZ	7.85	7.87	7.87
	(0.0699)	(0.0485)	(0.0000)
aug-cc-pVTZ	7.92	7.94	7.95
	(0.0701)	(0.0490)	(0.0000)
aug-cc-pVQZ	7.94	7.95	7.96
	(0.0724)	(0.0509)	(0.0000)
aug-cc-pV5Z	7.94	7.95	7.96
	(0.0707)	(0.0490)	(0.0000)

For the TD-M06-2X results, the basis set effect on excitation energies in the aug-cc-pVXZ basis set series, with X = D, T, Q, 5 is studied (See Table 3.11). The excitation energies calculated by aug-cc-pVDZ basis set are slightly low by < 0.1 eV as compared to larger aug-cc-pVXZ basis set, with X = T, Q, 5. For all the excited states under study, the excitation energies don't change substantially with an increase in basis set cardinality from X = T to Q, 5. Consistent with the EOM-CCSD results, the doubly degenerate 1E is again the lowest energy excited state, which is followed close lying nearly iso-energetic 1B and 1A excited states. For excited states 1E, 1B and 1A, TD-M06-2X excitation energies are in satisfactory agreement with EOM-CCSD results using aug-cc-pVDZ basis set, with energies being low by about 0.10 eV, while

deviation is slightly more by about ≤ 0.20 eV using aug-cc-pVTZ basis set (Also See Figure 3.21).

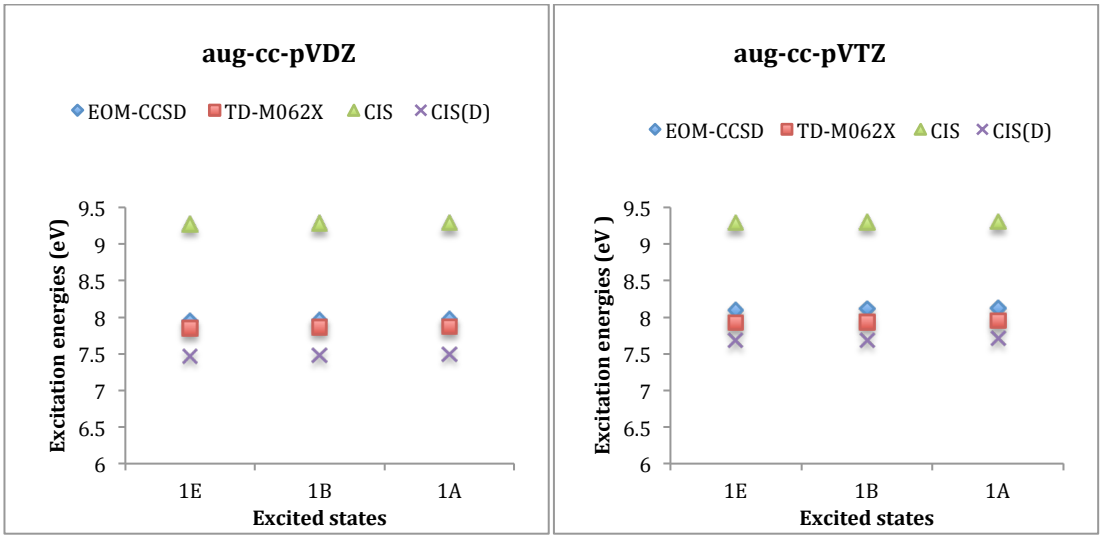

(a) (b)

Figure 3.21 Excitation energies (eV) of lowest singlet electronic excited states of water tetramer of S_4 symmetry using CIS, CIS(D), EOM-CCSD and TD-M06-2X methods with (a) aug-cc-pVDZ basis set (b) aug-cc-pVTZ basis set.

The oscillator strengths *f* calculated by using LR-configuration interaction CIS, EOM-CCSD, and TD-DFT using the M06-2X functional for these lowest singlet excited states are shown in Figure 3.22(a) and Figure 3.22(b), and employing the aug-cc-pVDZ and aug-cc-pVTZ basis sets, respectively (Also See Table 3.11). CIS underestimates oscillator strengths with respect to EOM-CCSD values for all excited states under study. At the EOM-CCSD/aug-cc-pVDZ level, oscillator strengths calculated for the lowest bright state 1E is $f \approx 0.0856$, while $f \approx 0.0692$ for 1B excited state. The excited state 1A is calculated as a lowest dark excited state with zero oscillator strength by all above used methods. For both CIS and EOM-CCSD methods, the *f* values decrease slightly with increase in basis set size from aug-cc-pVDZ to aug-cc-pVTZ.

For the TD-DFT results using M06-2X functional results, the basis set effect on the oscillator strengths is investigated using aug-cc-pVXZ basis set series, with X = D, T, Q, 5. The oscillator strengths obtained are quite consistent for all aug-cc-pVXZ basis set, with X= D, T, Q, 5, indicating very minor effect on oscillator strengths as we increase cardinality of basis set from X = D to 5 (See Table 3.11). Comparing with EOM-CCSD results, it is noticed that the TD-DFT oscillator strengths are too low with respect to those generated by EOM-CCSD method, as shown in Figure 3.22.

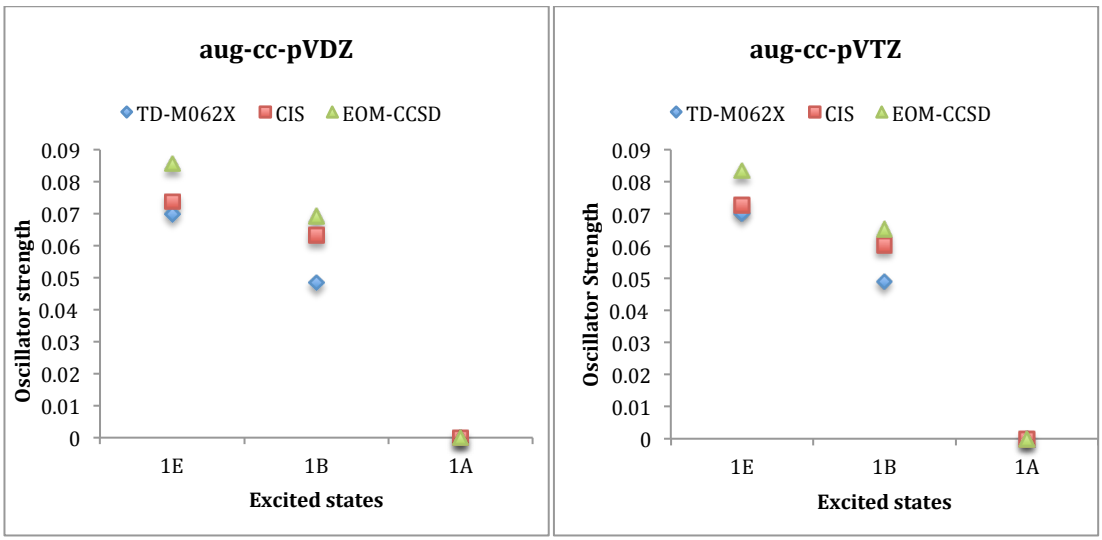

(a) (b)

Figure 3.22 Oscillator strengths of lowest singlet electronic excited states of water tetramer of S_4 symmetry using CIS, EOM-CCSD and TD-M06-2X methods with (a) aug-cc-pVDZ basis set (b) aug-cc-pVTZ basis set.

The localized valence character with mixing of some diffuse Rydberg character is observed in the excited states of the water tetramer by checking the nature of the molecular orbital (MO) involved in the electronic transitions for 1E, 1B and 1A excited states, as shown in Figure 3.23.

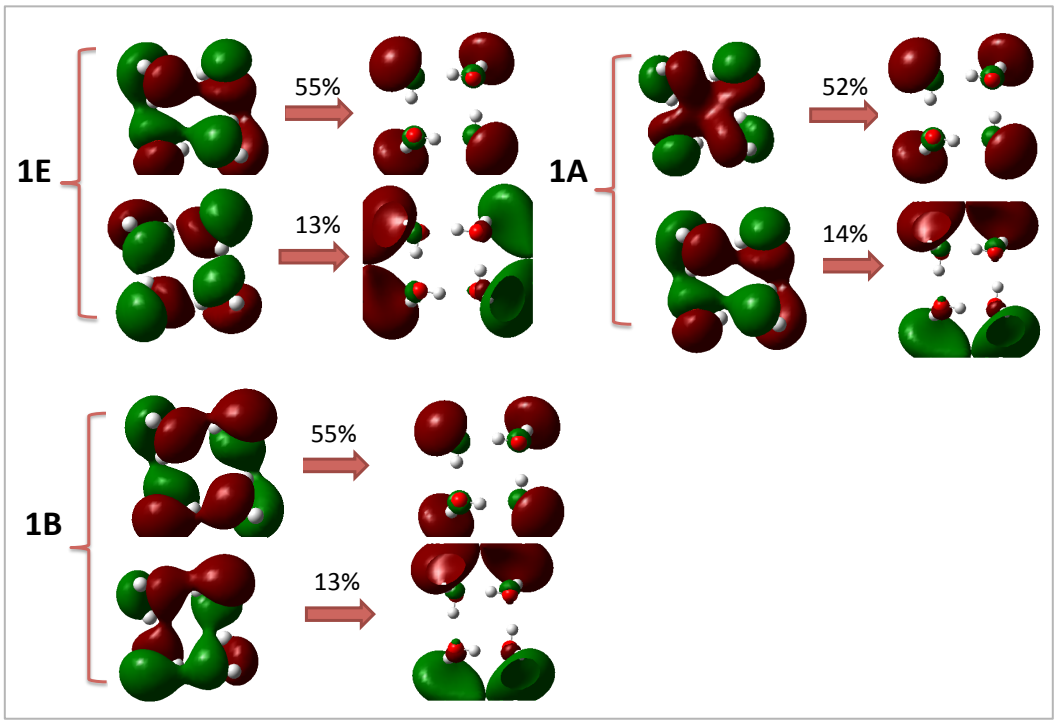

Figure 3.23 Water tetramer (S_4 symmetry): Molecular orbitals involved in the electronic transitions for lowest energy singlet electronic excited states of different symmetry i.e. one excited state of each symmetry computed at the EOM-CCSD level. Isovalue = 0.02 for the density plots.

3.3.2.5 Water Pentamer (C_1)

Vertical excitation energies and Oscillator Strengths

For the cyclic water pentamer with C_1 symmetry, Table 3.12 depicts the excitation energies and oscillator strengths obtained using linear response (LR) coupled cluster hierarchy of models CCS, CC2 and CCSD methods along with the related CIS, EOM-CCSD methods for the first three excited states. We employ the aug-cc-pVDZ basis set for our calculations. All excited states discussed below are singlets.

For all coupled cluster calculations, it is seen that 1A, the lowest energy excited state is followed by very close lying 2A and 3A excited states within 0.02 eV with each other. As compared to CCSD results, CCS largely overestimates while CC2 underestimates the excitation energies of these states.

The LR-CIS excitation energies are equivalent to LR-CCS results, whereas EOM-CCSD results are equivalent to LR-CCSD results. We find that there is no substantial difference in excitation energies by increasing basis set size from aug-cc-pVDZ to aug-cc-pVTZ at the CIS level i.e. within 0.02 eV, for all excited states under study, as also shown in Figure 3.24.

For the lowest singlet excited state 1A, the EOM-CCSD/aug-cc-pVDZ calculations give vertical excitation energy of about 7.72 eV, whereas 2A and 3A excited states give slightly higher excitation energies of about 7.87 eV and 7.89 eV, respectively.

For TD-M06-2X results, we have seen the convergence of excitation energies in the aug-cc-pVXZ basis set series, with X = D, T, Q, 5 (See Table 3.12). The aug-cc-pVDZ basis set gives slightly lower excitation energies as compared to larger aug-cc-pVXZ basis set, with X = T, Q, 5. For all excited states under study, similar excitation energies are noticed as we increase the basis set cardinality from X = T to Q, 5. For all singlet excited states under study, the TD-M06-2X excitation energies obtained using aug-cc-pVXZ basis set series with X = T, Q, 5 are in good agreement with the results obtained at the EOM-CCSD/aug-cc-pVDZ level.

Now for oscillator strengths, we find that CCS underestimates oscillator strengths for 1A and 3A excited states, while overestimates for 2A excited state as compared to CCSD results. In contrast, CC2 overestimates oscillator strengths for all excited states under study. The oscillator strengths obtained using LR-CCS and LR-CCSD methods are consistent with the CIS and EOM-CCSD results, respectively. At the EOM-CCSD/aug-cc-pVDZ level, oscillator strengths calculated for the lowest bright state 1A is $f \approx 0.0296$, while 4A is the brightest state with highest oscillator strength of $f \approx$

0.0726. The oscillator strengths observed for excited states 2A and 3A are $f \approx 0.0458$ and $f \approx 0.0512$, respectively.

For the TD-M06-2X results, oscillator strengths obtained are quite consistent for all aug-cc-pVXZ basis set, X= D, T, Q, 5. However, very small deviations i.e. slightly higher *f* values are obtained by using aug-cc-pVQZ basis set. The oscillator strengths obtained by TD-M06-2X are too low in comparison to CIS and EOM-CCSD results for all excited states, as also shown in Figure 3.25. Also, we observe that for TD-M06-2X results, 4A is the brightest excited state, while lowest oscillator strength is noticed for 2A excited state.

The molecular orbital analysis shows that all excited states of the cyclic water pentamer (C_1) exhibit diffuse Rydberg character, as shown in Figure 3.26.

Table 3.12 Water pentamer (C_1): Excitation energies in eV and oscillator strengths (in parenthesis) of the lowest energy singlet electronic excited states using hierarchy of correlated coupled cluster such as CCS, CC2, CCSD methods, CIS, EOM-CCSD, and TD-DFT methods.

Water pentamer (C_1)	**Excitation energies E (eV)**			
	Excited States			
	1A	**2A**	**3A**	
LR-CCS				
aug-cc-pVDZ	9.10	9.21	9.23	
	(0.0263)	(0.0535)	(0.0461)	
LR-CC2				
aug-cc-pVDZ	7.33	7.49	7.50	
	(0.0298)	(0.0491)	(0.0532)	
LR-CCSD				
aug-cc-pVDZ	7.72	7.87	7.89	
	(0.0295)	(0.0456)	(0.0507)	
	1A	**2A**	**3A**	**4A**
LR-CIS				
aug-cc-pVDZ	9.10	9.21	9.23	9.25
	(0.0262)	(0.0536)	(0.047)	(0.0827)
aug-cc-pVTZ	9.12	9.23	9.25	9.27
	(0.0260)	(0.0508)	(0.0458)	(0.0803)
EOM-CCSD				
aug-cc-pVDZ	7.72	7.87	7.89	7.91
	(0.0296)	(0.0458)	(0.0512)	(0.0726)
TD-M06-2X				
aug-cc-pVDZ	7.65	7.79	7.81	7.83
	(0.0246)	(0.0192)	(0.0436)	(0.0554)
aug-cc-pVTZ	7.72	7.86	7.88	7.90
	(0.0245)	(0.0192)	(0.0431)	(0.0569)
aug-cc-pVQZ	7.73	7.87	7.89	7.91
	(0.0252)	(0.0203)	(0.0445)	(0.0604)
aug-cc-pV5Z	7.73	7.87	7.89	7.91
	(0.0245)	(0.0191)	(0.0434)	(0.0589)

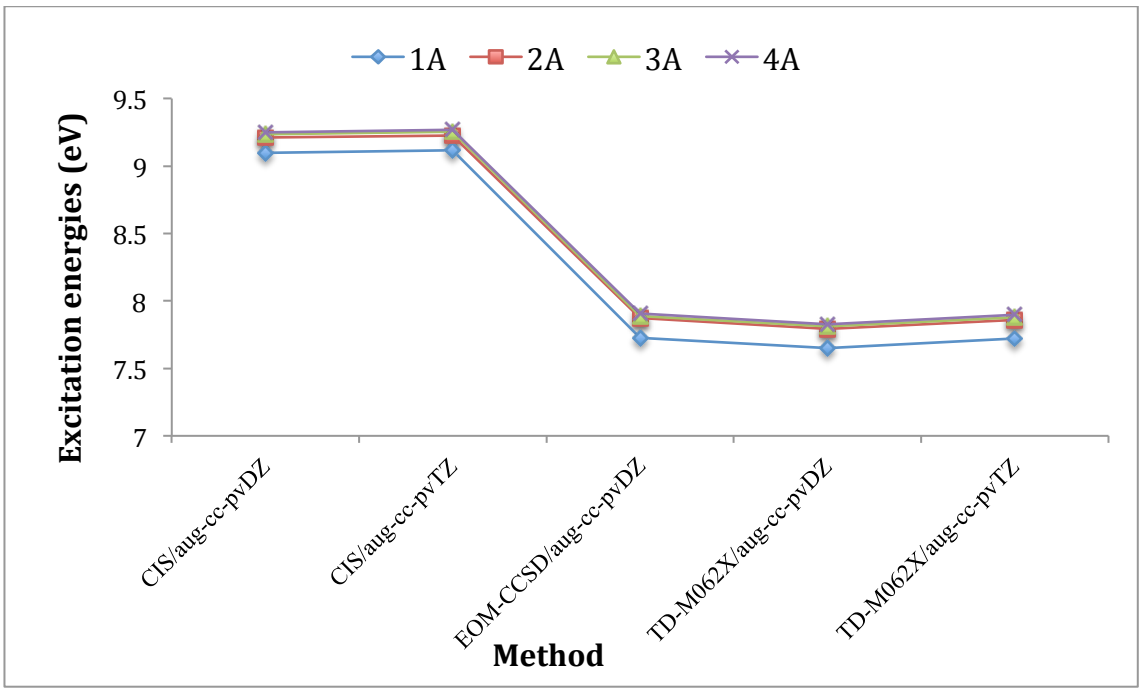

Figure 3.24 Excitation energies (eV) of lowest singlet electronic excited states of water pentamer of C_1 symmetry using CIS, EOM-CCSD and TD-M06-2X methods with the aug-cc-pVXZ basis sets with X = D, T.

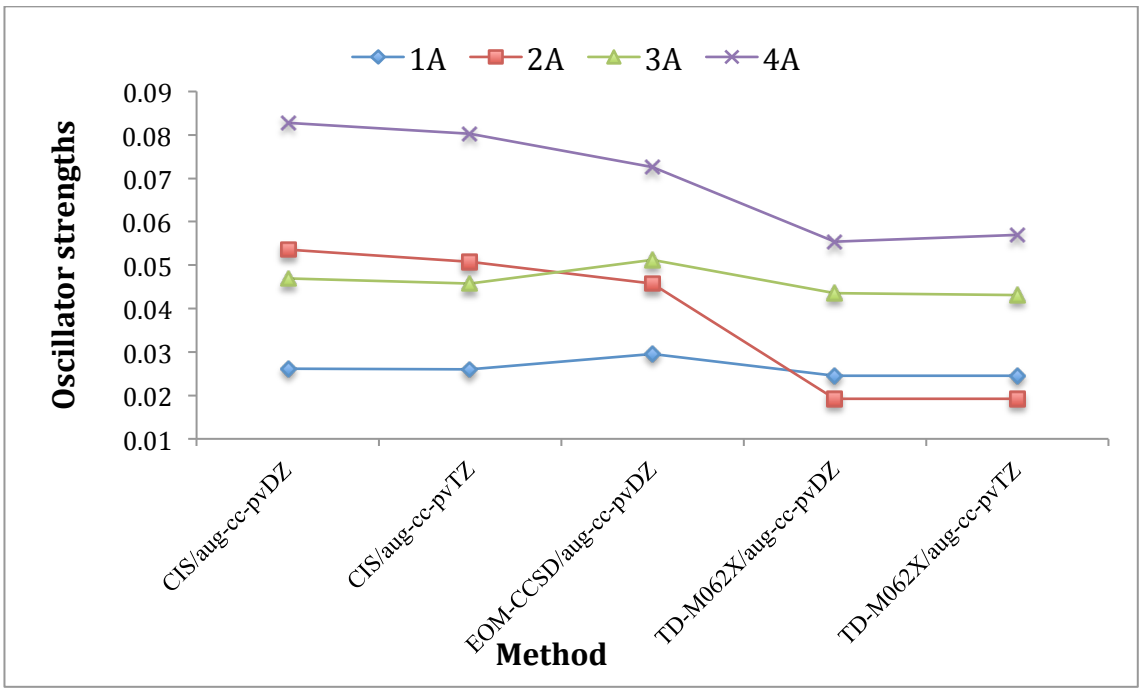

Figure 3.25 Oscillator strengths of lowest singlet electronic excited states of water pentamer of C_1 symmetry using CIS, EOM-CCSD and TD-M06-2X methods with the aug-cc-pVXZ basis sets with X = D, T.

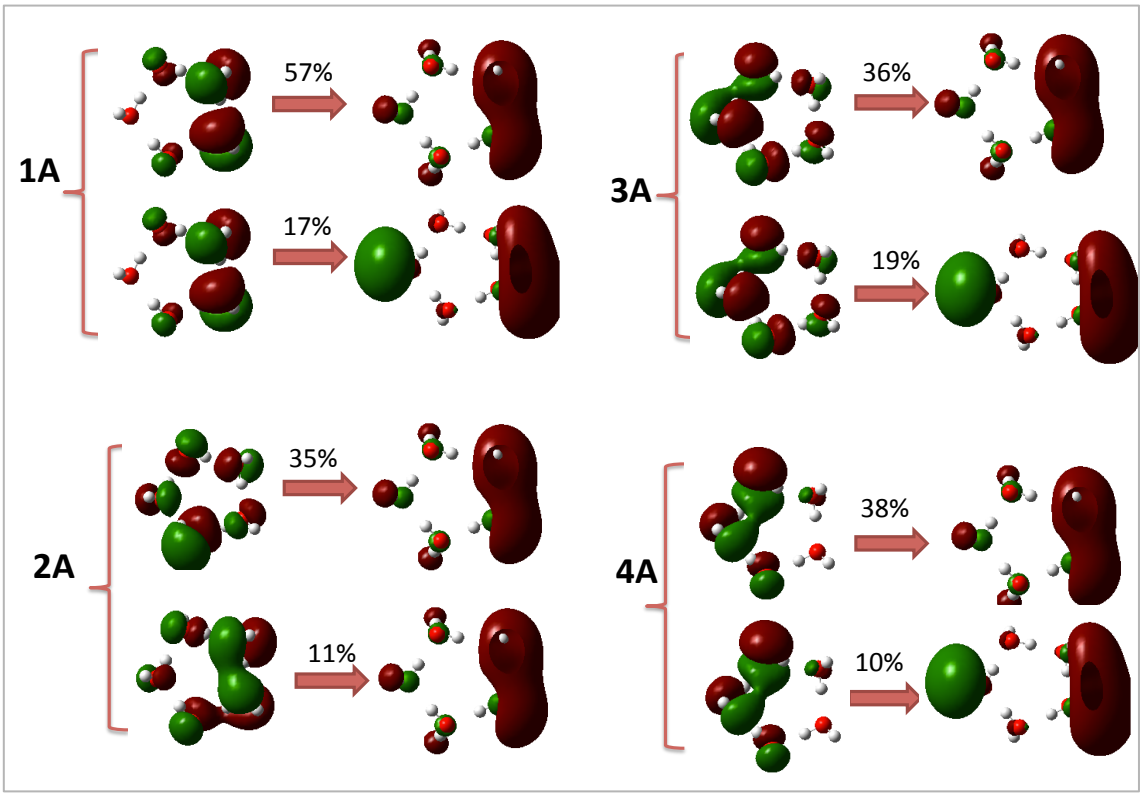

Figure 3.26 Water pentamer (C_1 symmetry): Molecular orbitals involved in the electronic transitions for four lowest energy singlet electronic excited states of different symmetry i.e. one excited state of each symmetry computed at the EOM-CCSD level. Isovalue = 0.02 for the density plots.

3.3.2.6 Water Pentamer (C_{2v})

Vertical excitation energies and Oscillator Strengths

For the water pentamer with C_{2v} symmetry, the excitation energies obtained using linear response (LR) coupled cluster hierarchy of models CCS, CC2 and CCSD methods along with the related CIS, EOM-CCSD methods with the aug-cc-pVDZ basis set for the first four excited states (i.e. one state of each symmetry) are presented in Table 3.13. (Note: All excited states discussed below are singlets).

For all coupled cluster calculations, it is found that the $1A_2$ and $1B_1$ excited states are the lowest energy excited states that lie very closely to each other within 0.01 eV energy difference, followed by $1A_1$ and $1B_2$ excited states. CCS largely overestimates while CC2 underestimates the excitation energies of these states with respect to CCSD results. The excitation energies obtained using the uncorrelated wavefunction CIS method are consistent to LR-CCS results; whereas EOM-CCSD results are consistent to LR-CCSD results. Now investigating the basis set effect on these excitation energies, we find that there is no substantial difference in results by increasing basis set size from aug-cc-

pVDZ to aug-cc-pVTZ at the CIS level, while at the EOM-CCSD level, excitation energies increases by about 0.15 eV in going from aug-cc-pVDZ to aug-cc-pVTZ basis set for all excited states under study, as also shown in Figure 3.27.

For the lowest close lying singlet excited states $1A_2$ and $1B_1$, the EOM-CCSD/aug-cc-pVDZ calculations give consistent vertical excitation energies of about 7.28 and 7.29 eV, respectively, whereas for excited states $1A_1$ and $1B_2$, the calculated excitation energies are about 8.03 eV and 8.14 eV, respectively. The excitation energies are slightly higher by about 0.15 eV using aug-cc-pVTZ basis set with respect to those calculated by aug-cc-pVDZ basis set for all excited states.

For TD-M06-2X results, we have seen the convergence of excitation energies in the aug-cc-pVXZ basis set series, with X = D, T, Q, 5 (See Table 3.13). The excitation energies calculated by aug-cc-pVDZ basis set are slightly low as compared to the larger aug-cc-pVXZ basis set, with X = T, Q, 5. For all excited states under study, excitation energies don't change substantially with increase in basis set cardinality from X = T to Q, 5. $1A_2$ and $1B_1$ states are again close lying lowest energy excited states followed by $1B_2$ and $1A_1$ excited states in increasing order of energy, however some discrepancies are observed in energetic ordering of $1B_2$ and $1A_1$ excited states with respect to the coupled cluster results. For the lowest lying singlet excited states $1B_1$ and $1A_2$, the TD-M06-2X excitation energy is too low by about 0.27 eV and 0.23 eV, respectively, as compared to results at EOM-CCSD level using aug-cc-pVTZ level, while discrepancies are much larger for $1B_2$ state, the TD-DFT excitation energies being about 0.40 eV too low. For $1A_1$ excited state, TD-M06-2X excitation energies are in satisfactory agreement with CCSD results using aug-cc-pVTZ basis set, with energies being low by about 0.15 eV.

The oscillator strengths *f* calculated by using LR-coupled cluster CCS, CC2, CCSD, along with the related CIS and EOM-CCSD methods for these lowest singlet excited states are listed in Table 3.13. Considering CCSD as a reference method, CCS underestimates oscillator strengths for all excited states under study. In contrast, CC2 overestimates oscillator strengths for the $1A_1$ and $1B_1$ excited states while underestimates for the $1B_2$ excited state. For a given basis set, oscillator strengths obtained using LR-CCS method are consistent with the CIS results, whereas EOM-CCSD results are equivalent to the LR-CCSD results. It is seen that the lowest excited state $1A_2$ is a dark excited state with zero oscillator strength calculated by all coupled cluster calculations. At the EOM-CCSD/aug-cc-pVDZ level, oscillator strengths

calculated for the lowest bright state $1B_1$ is $f \approx 0.1110$, which is also the brightest state with highest oscillator strength. Similar oscillator strengths are observed for excited states $1A_1$ and $1B_2$ with $f \approx 0.0665$ and $f \approx 0.0657$, respectively. It is noticed that that the f values decrease slightly with increase in basis set size from aug-cc-pVDZ to aug-cc-pVTZ and holds for all methods used above (See Figure 3.28).

For the TD-M06-2X results, oscillator strengths obtained are quite consistent for all aug-cc-pVXZ basis set, X= D, T, Q, 5, therefore very minor deviations in oscillator strengths f are noticed with increase in basis set size. TD-DFT gives lower oscillator strengths in comparison to EOM-CCSD results, as also shown in Figure 3.28.

Table 3.13 Water pentamer (C_{2v}): Excitation energies E in eV and oscillator strengths (in parenthesis) of the lowest energy singlet electronic excited states using hierarchy of correlated coupled cluster such as CCS, CC2, CCSD methods, EOM-CCSD, and TD-DFT methods.

Water pentamer (C_{2v})	**Excitation energies E (eV)**			
	Excited States			
LR-CCS	**$1A_1$**	**$1B_1$**	**$1B_2$**	**$1A_2$**
aug-cc-pVDZ	9.30 (0.0590)	8.61 (0.0966)	9.84 (0.0644)	8.60 (0.0000)
LR-CC2				
aug-cc-pVDZ	7.71 (0.0708)	6.88 (0.1153)	7.68 (0.0625)	6.87 (0.0000)
LR-CCSD				
aug-cc-pVDZ	8.03 (0.0664)	7.29 (0.1101)	8.14 (0.0655)	7.28 (0.0000)
LR-CIS				
aug-cc-pVDZ	9.30 (0.0585)	8.61 (0.0983)	9.84 (0.0637)	8.60 (0.0000)
aug-cc-pVTZ	9.32 (0.0565)	8.63 (0.0951)	9.85 (0.0619)	8.62 (0.0000)
EOM-CCSD				
aug-cc-pVDZ	8.03 (0.0665)	7.29 (0.1110)	8.14 (0.0657)	7.28 (0.0000)
aug-cc-pVTZ	8.18 (0.0634)	7.44 (0.1058)	8.30 (0.0655)	7.43 (0.0000)
TD-M06-2X				
aug-cc-pVDZ	7.94 (0.0530)	7.10 (0.0809)	7.82 (0.0429)	7.09 (0.0000)
aug-cc-pVTZ	8.02 (0.0536)	7.17 (0.0794)	7.89 (0.0440)	7.20 (0.0000)
aug-cc-pVQZ	8.03 (0.0550)	7.17 (0.0832)	7.91 (0.0464)	7.16 (0.0000)
aug-cc-pV5Z	8.03 (0.0531)	7.17 (0.0800)	7.91 (0.0456)	7.16 (0.0000)

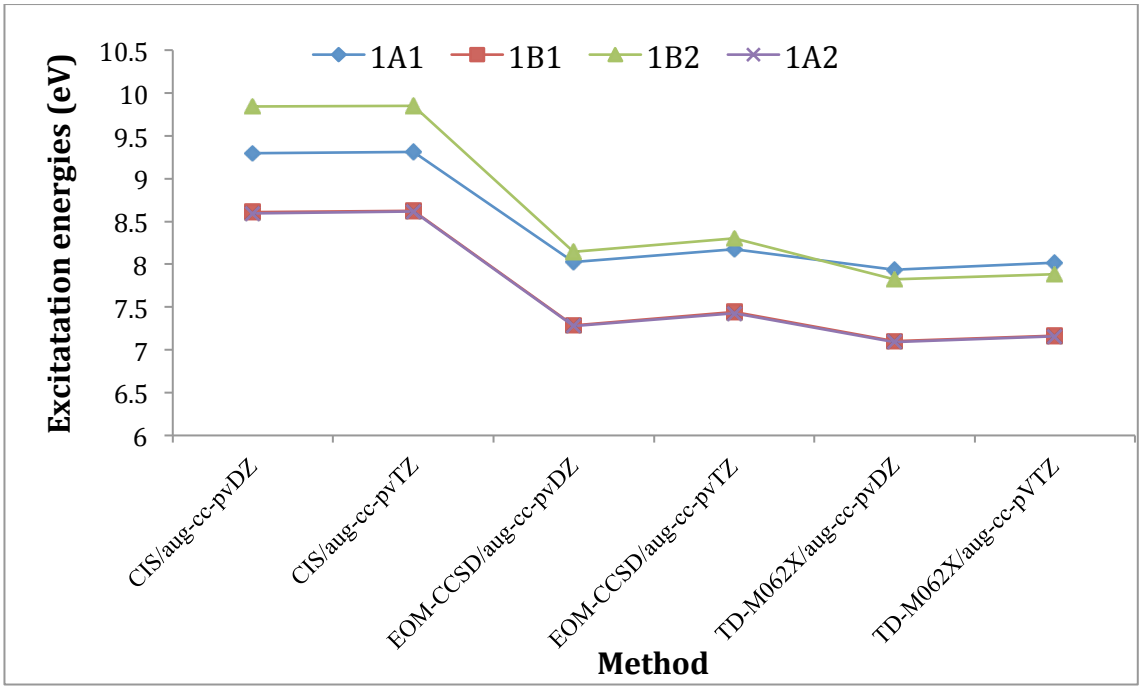

Figure 3.27 Excitation energies (eV) of lowest singlet electronic excited states of water pentamer of C_{2v} symmetry using CIS, EOM-CCSD and TD-M06-2X methods with the aug-cc-pVXZ basis sets with X = D, T.

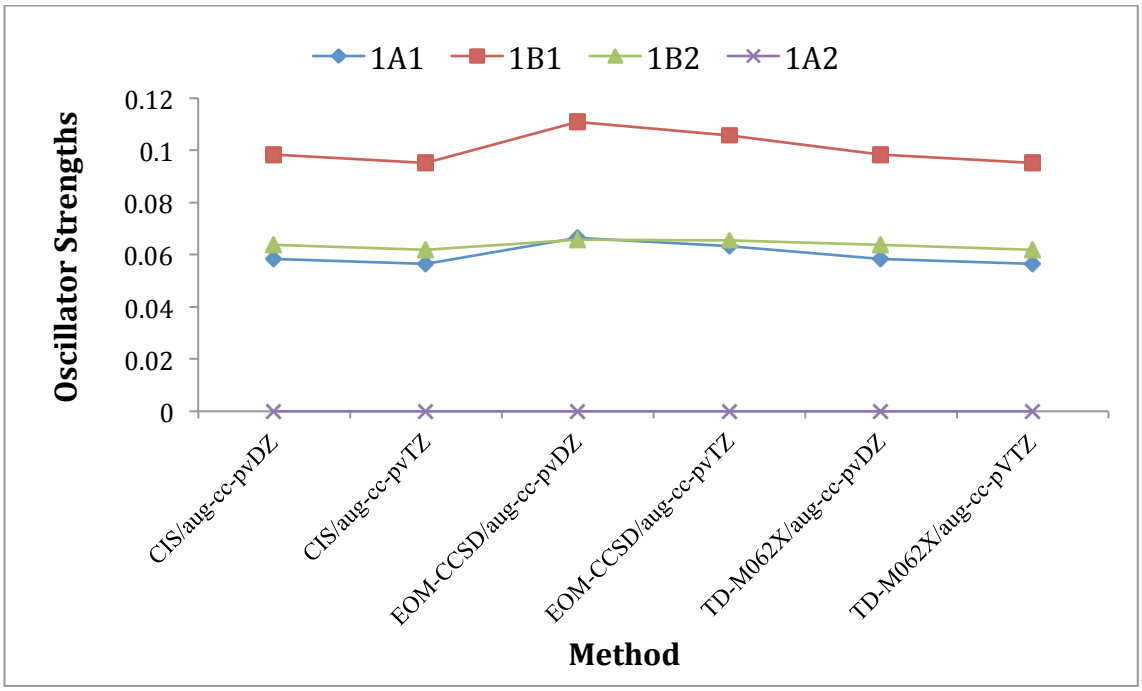

Figure 3.28 Oscillator strengths of lowest singlet electronic excited states of water pentamer of C_{2v} symmetry using CIS, EOM-CCSD and TD-M06-2X methods with the aug-cc-pVXZ basis sets with X = D, T.

It is also noticed that diffuse Rydberg character is involved in the electronic transitions of $1A_2$, $1B_1$, $1A_1$ and $1B_2$ excited states of the water pentamer (C_{2v}), as shown in Figure 3.29. The $1A_1$ excited state is associated with the excitation from the central water molecule, which we are more interested so as to check the effect of aggregation on excitation energies of the water monomer as discussed below.

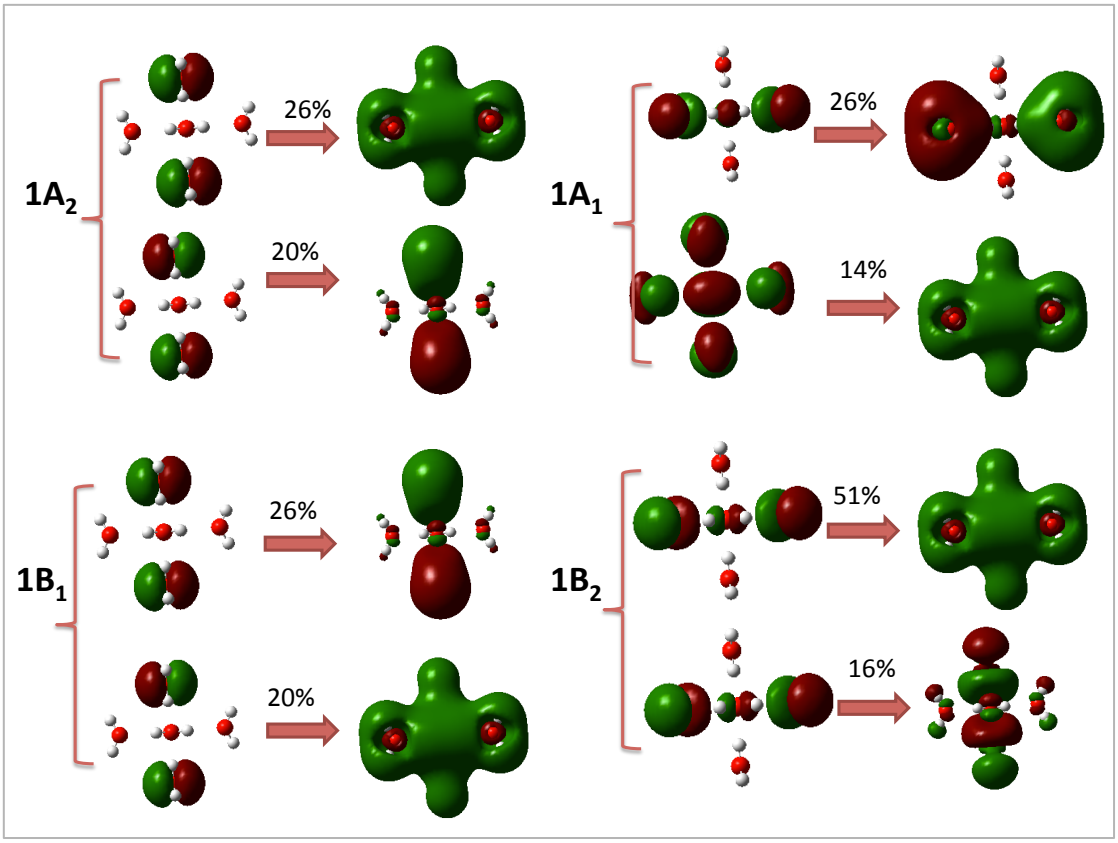

Figure 3.29 Water pentamer (C_{2v} symmetry): Molecular orbitals involved in the electronic transitions for four lowest energy singlet electronic excited states of different symmetry i.e. one excited state of each symmetry computed at the EOM-CCSD level. Isovalue = 0.02 for the density plots.

Effect of aggregation

Finally, we consider the effect of aggregation on the water monomer. It is found experimentally that condensation produces a blue shift of ~1 eV in the absorption maximum found at 7.4-7.5 eV in the water vapour spectrum [60, 228, 229]. Comparing monomer (C_{2v}) to trimer (C_{2v}), our coupled cluster CCSD and related EOM-CCSD calculations show a very small blue shift of ~ 0.07 eV in lowest excitation energy associated with the excitation of the central water in water trimer relative to water monomer, while CCS calculations give a slightly larger singlet blue shift of up to 0.4

eV. TD-DFT calculations show discrepancies and a small red shift of about 0.2 eV is noticed, while CC2 and CC3 calculations give unnoticeable singlet red shift of ~ 0.04 eV relative to water monomer. Comparing the monomer (C_{2v}) to the pentamer (C_{2v}), the substantial blue shift of ~ 0.7 eV relative to water monomer is calculated by CCS, CC2, CCSD and EOM-CCSD methods, which are comparable to the experimental blue shifts of ~ 1 eV found in condensed phases. TD-M06-2X calculations also show a blue shift of about ~ 0.6 eV.

3.4 Conclusions

We have performed benchmark computations to examine the vertical excitation energies and oscillator strengths of small water clusters from the monomer up to the pentamer using a wide range of electronic structure methods including the linear response coupled cluster hierarchy of CCS, CC2, CCSD, and CC3 methods and related EOM-CCSD method. The configuration interaction method CIS (D) is also used for the water tetramer and the pentamer. Our results show that electron correlation effects are very important to examine carefully in such systems. In general, CCS method often calculates excitation energies that are too high by about ≤ 2 eV, while CC2 underestimates excitation energies as compared to best-coupled cluster results obtained by CCSD and CC3 methods. Similarly, large discrepancies in oscillator strengths *f* are noticed by CCS calculations with respect to CCSD and CC3 methods, mainly CCS underestimates the *f* values for low lying excited states. The large error in CCS calculations clearly shows the significant contribution of double and triple excitations in excitation energies and strong correlation effects dominating these small water clusters.

Furthermore, for all coupled cluster results, basis set dependence of these excitation energies and oscillator strengths has shown the convergence of excitation energies and oscillator strengths in the aug-cc-pVXZ basis set series, with X = D, T, Q depending on the size of water cluster. For these water clusters, the excitation energies don't change substantially with increase in basis set cardinality X, and deviations noticed are within 0.15 eV. We also show the minor effect of size of basis set on the oscillator strengths *f* in the aug-cc-pVXZ basis set series, where *f* values decrease slightly with increase in size of basis set size and is true for all coupled cluster methods.

We have also compared the best benchmark coupled cluster results with the TD-DFT using the M06-2X functional. Compared to the best available coupled cluster

CCSD and CC3 results, TD-DFT excitation energies are often too low by few eV (about 0.1-0.8 eV) depending on the excited state and the size of the water cluster. In general, TD-M06-2X results are in better agreement with the EOM-CCSD and coupled cluster CCSD and CC3 results than the CCS and CIS results. We find that oscillator strengths calculated by TD-DFT are too low in comparison to coupled cluster results and discrepancies are significant.

For TD-M06-2X results, we have seen the convergence of excitation energies in the aug-cc-pVXZ basis set series, with X = D, T, Q, 5. In general, excitation energies calculated by aug-cc-pVDZ basis set are slightly low and underestimated by about < 0.1 eV as compared to larger aug-cc-pVXZ basis set, with X = T, Q, 5. However, excitation energies are generally in good agreement with nearly similar excitation energies within 0.05 eV difference with increase in basis set cardinality from X = T to Q, 5. It is also seen that oscillator strengths obtained are quite consistent for all aug-cc-pVXZ basis set, with X= D, T, Q, 5, showing quite small deviations as we increase cardinality of basis set from X = D to 5.

Further, coupled cluster calculations for ground state dipole moment has shown excellent performance of the CCSD method, where results are in good agreement with experiment within the accuracy of about < 0.01 D for both water monomer and about < 0.02 D for water dimer, while CCS calculations generally overestimate the ground state dipole moments. The excited state dipole moment obtained using the hierarchy of linear response (LR) coupled cluster CCS, CC2 and CCSD methods for lowest excited states has shown a reduction in dipole moment with respect to ground state in the water monomer, while in both dimer and trimer, a very large increment in total dipole moment is noticed in all excited states with respect to the ground state dipole moment. Thus significant change in charge density is observed in water dimer and the trimer.

It is also evident that excited states of water clusters exhibit a diffuse Rydberg type character, which make it a challenging system to study. From our second moment of charge distribution calculations, it is observed that diffuse Rydberg character involved in the first lowest excited state increases with increase in size of water cluster $(H_2O)_n$ from the water monomer (n=1) to the water trimer (n=3).

The effect of aggregation on lowest excited state of water monomer is also investigated using coupled cluster and TD-DFT methods. We show that the CCSD and TD-M06-2X calculations give a blue shift of ~ 0.7 eV and ~ 0.6 eV, respectively, in the lowest energy excitation associated with the central water molecule in water pentamer

(C_{2V}) relative to water monomer (C_{2v}), and are in good agreement with blue shift of ~ 1 eV in condensed phase as observed experimentally [60, 229]. However, such effect is unnoticeable in the comparatively smaller water trimer (C_{2v}) cluster.

Chapter 4 - The Structure and UV Spectroscopy of Benzene-Water ($Bz\text{-}W_6$) Clusters using Time-Dependent Density Functional Theory*

4.1 Introduction

Water clusters are of fundamental importance in many areas of chemistry, and are also a useful model system to understand the relation of the properties of the gas phase clusters to the condensed phase, ice, and liquid water. The structures and properties of water W_n clusters have been studied extensively both theoretically and experimentally because of their importance in many physical, chemical and biological fields, such as in the understanding of cloud and ice formation, bio-chemical processes, *etc* [230-240]. The interactions of aromatic molecules with water solvents, and the role of these weak interactions to determine the physical and chemical properties of such systems is an area of particular interest for many theoretical and experimental studies. In this context, the simplest system of this type, benzene-water complexes, considering benzene as a prototype of intermolecular interactions involving aromatic systems, has been studied extensively [65, 67, 230, 241-250]. The study of complexes of benzene (Bz) with water clusters is also of considerable astrophysical importance and can replicate polycyclic aromatics-ice systems to gain better understanding on the interactions of polycyclic aromatic hydrocarbons (PAHs), which may account for up to 20 % of galactic carbon [25, 251], with water being the most abundant molecule in icy grain mantles [11]. Benzene has been detected in the proto-planetary nebula CRL 618 [33, 252] and is amongst the list of known interstellar molecules. Benzene may be thought of as a prototypical PAH compound that plays an important role as an intermediate in the formation of PAHs from acetylene [252-255], and water clusters can be a good representation of interstellar ice surfaces. It has been observed that UV irradiation of water ice containing PAHs may play an important role in the formation of complex organic species such as alcohols, quinones and ethers [58].

Photo-desorption is an important process to account for the high gas phase abundances of water under astrophysically relevant conditions [23, 256]. Benzene and its derivatives, also being environmental pollutants [257, 258] and the constituents of

* D. Sharma and M. J. Paterson, *Photochem. Photobiol. Sci*., 2014, **13**, 1549-1560

many organic products, e.g. solvents, perfumes, etc. can be efficiently excited electronically by UV radiation present in the environment. Therefore, the computational study of the ground and excited states of the complexes of benzene with water clusters is of possible environmental as well as astrophysical relevance.

Numerous theoretical and experimental studies have been performed on the ground state properties such as binding energies and IR spectra of Bz-W_n clusters, and also on non-covalent interactions such as hydrogen bonding interactions that dominate such systems [65, 66, 230, 235, 240, 245-247, 259-262]. Zwier and their co-workers [65-67, 246, 247, 249, 250] have undertaken detailed experimental studies on Bz-W_n clusters using resonant ion-dip spectroscopy (RIDIRS) and resonant two-photon ionization (R2PI) techniques. It was observed that the water O-H stretch spectra depends on the size of cluster and is sensitive to the number, strength and the type of hydrogen bonds in which it participates while C-H stretch in benzene was found insensitive to the size of water cluster with $n \leq 7$ [65]. For n = 3-5, the water cluster was considered to bind to benzene primarily through single water molecule on or near benzene six-fold axis and the O-H spectra was consist of free O-H stretches, π H-bonded O-H stretches and the single donor O-H stretches. The significant spectral signature was observed at $n \geq 6$ in O-H stretch spectra, showing new transitions that are associated with the double-donor O-H stretches, which exist, in the more compact large Bz-W_n clusters. Experimental evidence predicted the change in shape of cluster from cyclic to non-cyclic at n = 6 such that Bz-W_6 cluster was found likely to exist as a cage shaped arrangement of six water molecules giving the lowest energy structure.

A detailed computational study on geometries, binding energies and infrared (IR) spectra of Bz-W_n (n = 1-10) clusters has been carried out by Prakash *et al*. [245] using hybrid meta DFT based M05-2X method with the 6-31+G** basis set. Using Bader's theory of atoms in molecule (AIM) approach, it is found that the nonconventional H-bonding interactions, such as O-H$^{\cdots}\pi$ interactions are present in all these clusters with additional contributions from C-H$^{\cdots}$O and lone pair $(lp)^{\cdots}\pi$ interactions, leads to overall stability of these clusters. It is also noted that π H-bonded O-H stretching vibrational frequencies are red shifted in all the clusters. The inverted book conformer of water hexamer is found to have highest binding energy in compared to all other water clusters [245].

Slipchenko *et al*. [263] investigated the structures and bonding in water W_n (n = 1-8)-Bz_n (n = 1-2) complexes computationally using an effective fragment potential (EFP)

method. It is predicted that benzene can act both as an H-bond donor and acceptor in the water-benzene complexes and all of the larger water-benzene complexes are dominated by H-bonding interactions i.e. O-H$^{\cdots}\pi$ and C-H$^{\cdots}$O interactions. The interactions between such systems are considered complicated due to the existence of various possible structures that depend on the number and type of hydrogen bonds involved in these complexes as the benzene-water interactions are weaker than the water-water interactions and the very small energy differences between different isomers are involved in such complexes.

Excited state properties of such systems have received very little attention as of yet. Computational studies on low lying excited states of Bz-W_n (n=1-6) complexes have been performed by Upadhyay *et al*. [75] using configuration interaction method involving all the singly excited configurations (CIS). The binding energies of these clusters were also calculated and complex of water dimer with benzene (Bz-W_2) is found to be the most stable among various complexes, with a high stability of Bz-W_6 complex as well. It is found that the whole Bz-W_n complex as well as the water cluster W_n undergoes an expansion in size following excitation to lowest singlet excited states. The small blue shifts in the excitation energies are observed in the electronic absorption spectra in going from Bz to higher complexes (Bz-W_n, (n = 4-6)). Photon-stimulated desorption in an astrophysical context has not been studied extensively until recently. A few experiments have been performed on photo processing of laboratory models of Bz-ice complexes by UV radiation [70-72]. Experimental study [72] on photo-processes in model interstellar ices by modelling multilayer films of benzene & water deposited on a sapphire substrate at a temperature of around 80 K has investigated three distinct photo-desorption mechanisms in such systems: (i) Direct adsorbate-mediated desorption of benzene; (ii) Indirect adsorbate–mediated desorption of water; (iii) Substrate-mediated desorption of both benzene and water. The translational temperature of both desorbed species i.e. benzene and water molecule is found to be more than the ambient temperature of the complex system. Recent experimental study on photon- and electron- induced desorption from laboratory models of interstellar ice grains by mimicking the conditions found in dense interstellar clouds has been performed by Thrower *et al.* [70]. The desorption cross sections and first order rate coefficients for the desorption processes in benzene-water (Bz-W_n) complexes have been obtained. It is observed that photon absorption by benzene can make H_2O desorption possible at wavelengths where photon-absorption cross-section for H_2O is negligible.

The electronically excited states play an important role in the photochemistry and electronic spectroscopy and are the subject of our investigations detailed below. The main aim of the work presented in this chapter is to investigate the spectroscopy and photochemistry of interstellar ice analogs i.e. Bz-W_6 cluster quantum mechanically to provide insight into elementary process involved in their processing, and to study important electronic transitions involved in such systems using time dependent DFT with a range of well developed DFT functionals for response theory.

4.2 Computational Details

4.2.1 Computational Model

Since it has been observed from earlier studies that the water hexamer $(H_2O)_6$ cluster is the smallest water cluster that allows non-cyclic structures and a more three dimensional structure, it can be considered as the building block of many ice forms [230, 232]. So, to make the choice of water cluster to start with, we have chosen a water hexamer (W_6) clusters and are also taken as a benchmark system for many computational chemistry studies [207, 230-232, 264, 265]. The hydrogen-bond arrangements of these six water molecules in the cluster determine the shape and stability of the cluster. A few low-lying iso-energetic conformers of the water hexamer cluster are ring, book, cage and prism with 6, 7, 8 and 9 number of hydrogen bonds, respectively (Figure 4.1).

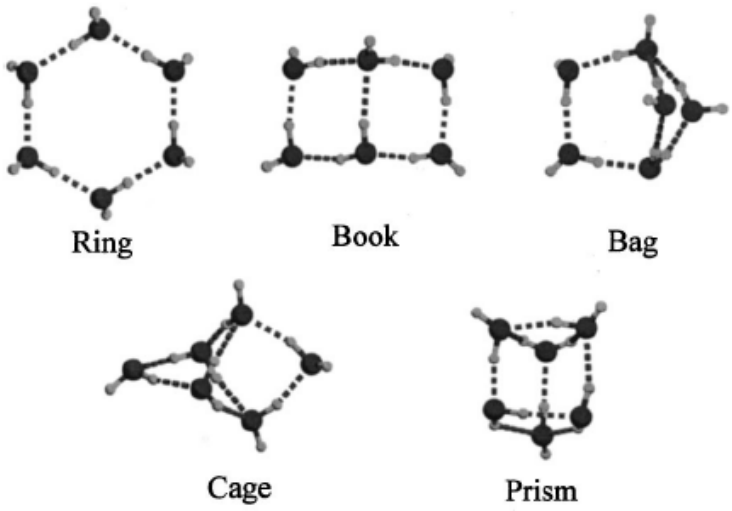

Figure 4.1 Lowest energy conformers of the water hexamer [266].

There have been uncertainties in the literature on predicting the exact order in energetics of very close lying water hexamer conformers. Previous theoretical investigations have found the cage shaped water W_6 cluster, with four dangling hydrogen atoms (non-hydrogen bonded atoms) and eight hydrogen bonds, to be the most stable one giving the minimum energy, among the other low lying conformers i.e. prism, book, ring and chair forms [231, 234, 240, 265]. DFT-D calculations on the water hexamer has predicted the energetic order Prism < Cage < Book < Chair [267, 268]. Most recent computational studies have predicted prism, cage and book conformers as the three lowest energy conformers with ZPE correction, with prism as the lowest energy structure, and cage conformer is found to be very closer to prism in energy [207, 238]. A very recent theoretical study on the water hexamer using full dimensional Diffusion Quantum Monte-Carlo simulations has predicted the presence of cage and prism conformers at low temperatures [239], in agreement with the experimental measurements of broadband rotational spectra of the water hexamer formed in supersonic expansion [264]. Experimental study by Pate *et al*. has also established the cage conformer of water hexamer as the global minimum energy structure [264]. Taking account of both theoretical [238] and experimental [264] evidences of existence of cage and prism conformers at low temperatures, that are relevant to astrophysical interstellar conditions, and are also established as lowest energy conformers of water hexamer by very recent studies [207, 238, 264], we have chosen both the cage and prism structures as model systems in our present study. We have used flexible water W_6 cluster i.e. all the water molecules of the water W_6 cluster are moving.

The benzene (Bz) molecule is then brought closer to the water W_6 cluster and it binds to the water cluster through hydrogen-bonded interactions and thus form Bz-W_6 complex system. The benzene molecule binds to the water cluster mainly through O-H$\cdots\pi$ hydrogen bonds where one of the free dangling hydrogen atom of the water cluster points toward the π electron cloud of the benzene ring [245, 261, 263]. Small contributions from C-H…O and lone pair $(lp)\cdots\pi$ hydrogen bonded interactions also stabilize the Bz-$(H_2O)_6$ cluster [245]. Both cage and prism geometries of water W_6 cluster interact with Bz to give Bz-W_6 cluster and are predicted to retain their cage and prism structures in Bz-W_6 cluster too.

4.2.2 Computational Methods

The ground state geometries of both the cage and prism conformers of W_6 clusters and Bz-W_6 clusters were optimized using density functional theory with Truhlar's meta hybrid functional M05-2X functional and the 6-31+G(d,p) basis set. M05-2X and M06-2X are non-local functionals with double the amount of non-local (Hartree-Fock) exchange with respect to M05 and M06 functionals, respectively. They are found to perform better than standard hybrid functionals for systems involving non-covalent interactions, and modelling electronic excitation energies to both valence and Rydberg states [128, 129].

In order to properly investigate any long range correction due to dispersion effects in such complex systems, the obtained optimized ground state geometries were further re-optimized using the following range of hybrid functionals LC-wPBE, wB97X, wB97XD, B2PLYP, B2PLYPD, in addition to second order Møller-Plesset perturbation theory (MP2), and employing the augmented correlation-consistent polarized-valence double zeta basis set (aug-cc-pvDZ). Long range corrected functionals such as LC-wPBE, CAM-B3LYP, wB97X, wB97XD functionals account the non-Coulomb part of exchange functionals, which typically dies off too rapidly and gives inaccurate results at large distances, where wB97XD functional also includes an empirical atom-atom dispersion corrections [130-132]. Harmonic vibrational frequency calculations were carried out to check the nature of stationary points, and confirmed as minima for all ground state structures.

We then used TD-DFT linear response theory [184-187], one of the most popular and widely used electronic structure methods to calculate electronic excitation energies and oscillator strengths by performing time-dependent DFT calculations on both MP2/aug-cc-pVDZ and wB97XD/aug-cc-pVDZ optimized ground state geometries of Bz, W_6 and Bz-W_6 clusters using three different functionals i.e. B3LYP, CAM-B3LYP and M06-2X. The 6-31++G(d,p) as well with aug-cc-pVTZ basis set were used for computations.

The Gaussian09 program [214] was used for all computations.

4.3 Results and Discussion

4.3.1 Ground State Structures

MP2/aug-cc-pVDZ optimized geometries of cage and prism form of Bz-W_6 cluster are shown in Figure 4.2(a) and Figure 4.2(b), respectively. We have studied different orientations of benzene with respect to the cage and prism conformers of water W_6 clusters. We have chosen the most stable cage and prism Bz-W_6 complexes out of many fully optimized Bz-W_6 complexes.

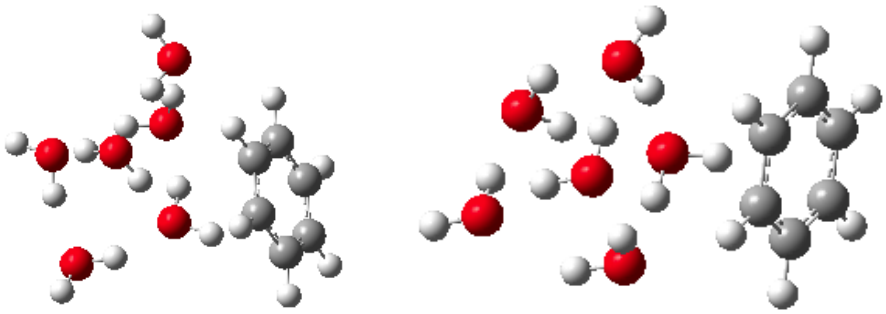

(a) (b)

Figure 4.2 MP2/aug-cc-pVDZ optimized geometries of C_6H_6-$(H_2O)_6$ clusters, (a) cage form (b) prism form.

The binding energy (BE) of the Bz-W_6 cluster is calculated using

$$|BE| = (E_{Bz-W_6} - (E_{W_6} + E_{Bz})) \quad (4.1)$$

where E_{Bz-W_6}, E_{W_6} *and* E_{Bz} denote the total energy of Bz-W_6 cluster, W_6 cluster and benzene, respectively. Table 4.1 shows the optimized total energies of the W_6 clusters, Bz-W_6 clusters, benzene (Bz) and absolute values of binding energies (BE's) of Bz-W_6 clusters (with and without zero point energy (ZPE) correction). It is seen that BE's of the Bz-W_6 cluster (with ZPE) ranges from 2.91-8.73 kcal mol^{-1} for cage conformer and 2.69-8.08 kcal mol^{-1} for the prism conformer.

In order to get correct energetics of both the cage and prism forms of Bz-W_6 clusters, basis set superposition error (BSSE) is also calculated using the counterpoise (CP)

method and corrected binding energies are also listed in Table 4.1. Here BSSE or counterpoise correction is for single-point (SP) energy calculation on optimized Bz-W_6 clusters. Bindings energies are reduced noticeably after applying BSSE correction and it ranges from 2.67-6.14 kcal mol^{-1} for the cage conformer and 2.47-5.65 kcal mol^{-1} for the prism conformer.

Table 4.1 depicts the variation of BE's of the prism and cage forms of Bz-W_6 clusters versus different DFT hybrid functionals and MP2 with ZPE and BSSE correction, respectively. It is clearly seen from these results that the cage conformer is more stable than the prism conformer, for all of the various functionals employed, as the cage form is found to have higher binding energy (BE) than the prism form, which is also consistent with previous computational studies [245, 261, 265]. The magnitude of BE's of Bz-W_6 cluster (with ZPE correction) for both the cage and prism forms with different computational methods vary in the following order: LC-wPBE < B2PLYP < wB97X < wB97XD < B2PLYPD < MP2. With ZPE correction, Bz-W_6 cluster is found to be most stable at the MP2 level with the highest BE, and least stable at the LC-wPBE level of calculation. However with BSSE correction, the 'wB97XD' functional gives higher binding energies than MP2, that clearly indicates that BSSE error is higher for wavefunction methods and energies are overestimated by MP2 level of calculations for both prism and cage conformers, respectively.

Since MP2 method is used extensively in computational chemistry and is considered reliable for ground state geometry optimizations and to estimate the energies of the loosely bound hydrogen bonded and dispersion bound complexes by accounting the electron-correlation effects including dispersion[112]. Taking into account the reliability and success of MP2 method in the past, and highest BE values with ZPE correction for our Bz-W_6 clusters, we have used MP2 optimized ground state geometries for main discussion on TD-DFT studies.

Table 4.1 Optimized total energies of the W_6 clusters, Bz-W_6 clusters, benzene (Bz) and calculated absolute values of binding energies (BEs) of Bz-W_6 clusters for both cage and prism geometries (with and without zero point energy (ZPE) correction) at different levels of theory with aug-cc-pVDZ basis set. (Value in the parenthesis corresponds to BSSE corrected binding energy).

PRISM	**LC-wPBE**	**wB97X**	**wB97XD**	**MP2**	**B2PLYP**	**B2PLYPD**
$E_{Bz\text{-}W6}$ (au)	-690.5773	-690.8295	-690.7965	-689.197	-690.377	-690.3948
E_{W6} (au)	-458.4780	-458.6150	-458.5969	-457.6430	-458.351	-458.3600
E_{Bz} (au)	-232.0941	-232.2051	-232.1888	-231.540	-232.019	-232.0236
BE (kcal mol^{-1})	3.24 (2.47)	5.84(4.76)	6.80 (5.65)	9.04 (4.35)	3.93 (2.54)	7.03 (4.79)
ZPE corrected						
$E_{Bz\text{-}W6}$ (au)	-690.3237	-690.5751	-690.5415	-688.946	-690.126	-690.1432
E_{W6} (au)	-458.3271	-458.4630	-458.4445	-457.492	-458.201	-458.2097
E_{Bz} (au)	-231.9923	232.10382	-232.0878	-231.440	-231.919	-231.9237
BE (kcal mol^{-1})	2.69	5.20	5.76	8.08	3.20	6.12
BE (kcal mol^{-1}) from Previous Computational Studies: 4.63 [a], 4.70 [b], 5 .0 [d]						
CAGE	**LC-wPBE**	**wB97X**	**wB97XD**	**MP2**	**B2PLYP**	**B2PLYPD**
$E_{Bz\text{-}W6}$ (au)	-690.578	-690.830	-690.797	-689.198	-690.378	-690.396
E_{W6} (au)	-458.478	-458.614	-458.597	-457.642	-458.351	-458.359
E_{Bz} (au)	-232.094	-232.205	-232.189	-231.540	-232.019	-232.024
BE (kcal mol^{-1})	3.69 (2.67)	6.41(5.41)	7.35 (6.14)	9.91 (5.18)	4.68 (2.94)	7.88 (5.58)
ZPE Corrected						
$E_{Bz\text{-}W6}$ (au)	-690.325	-690.575	-690.541	-688.947	-690.127	-690.144
E_{W6} (au)	-458.328	-458.463	-458.444	-457.492	-458.201	-458.209
E_{Bz} (au)	-231.992	232.104	-232.087	-231.440	-231.919	-231.923
BE (kcal mol^{-1})	2.91	5.66	6.19	8.73	3.74	6.76
BE (kcal mol^{-1}) from Previous Computational Studies: 5.65 [a], 4.94 [b], 5.69 [c], 6.62 [d]						

[a]Taken from Ref. [245] , [a]Method: M05-2X/6-31+G** and ZPE correction;
[b]Taken from Ref. [265] ,[b]Method: MP2/6-31+G** with 50% BSSE correction;
[c]Taken from Ref. [75] , [c]Method: B3LYP/6-31+G** and MP2 single point;
[d]Taken from Ref. [245], [d]Method: M05-2X/6-31+G** and BSSE correction.

4.3.2 Electronic excitations in Bz-W_6 clusters

In recent years, TD-DFT linear response theory [184-187] has become the most widely used electronic structure method for calculating vertical electronic excitation energies. These TD-DFT calculations provide the Ultraviolet (UV) absorption spectra giving the information about the excitation wavelength and oscillator strength *(f)* of each excited state.

The oscillator strength can be written as [269]:

$$f = \frac{2}{3}\omega_{ij}\,|\langle i|\bar{\mu}|j\rangle|^2 \tag{4.2}$$

where ω_{ij} is the frequency of transition from i^{th} to j^{th} quantum state and $|\langle i|\bar{\mu}|j\rangle|^2$ is the associated transition dipole moment.

UV spectrum of benzene shows three well-known absorption bands at 4.9, 6.20, and 6.94 eV related to three electronic excitations from the ground state to the excited states with symmetries $^1B_{2U,}$ $^1B_{1U,}$ and $^1E_{1U}$, respectively [37]. The calculated valence $\pi \rightarrow \pi^*$ excitation energies (experimental values in parenthesis) using M06-2X functional are $^1B_{2U}$: 5.47(4.9 [37, 38]), $^1B_{1U}$: 6.17(6.20 [37], 6.19 [38]), and $^1E_{1U}$: 6.98(6.94 [37], 6.96 [38]) eV, respectively. Our results show good agreement with the experiments. $^1B_{1U}$ and $^1E_{1U}$ excited states are computed with an accuracy of about 0.03 eV, while overestimated by about 0.5 eV for $^1B_{2U}$. CAM-B3LYP with long-range correction and B3LYP functional also compare well with the experiments and values are listed in Tables 4.2 and 4.3.

For Bz-W_6 prism shaped geometry, the UV spectra results obtained from TD-DFT calculations on MP2 optimized ground state Bz-W_6 prism shaped cluster, using all three functionals are presented in Figure 4.3(a). Figure 4.3(a) shows the diverse spectra for three different functionals where B3LYP functional generates the strongest peak at around 182 nm, with other less intense peaks within the range 174-190 nm, while CAM-B3LYP functional predicts transitions over the spectral range 157-180 nm, with strongest one centred around 180 nm and less intense peaks at around 157 nm and 175 nm. M06-2X and CAM-B3LYP functionals are consistent to generate the strongest intensity peak at 180 nm. It is also noted that B3LYP predicts few less intense peaks above 180 nm. In order to investigate the effect of Bz interaction with isolated water cluster W_6 and also to investigate how it affects excitation features in Bz-W_6 cluster, it

is important to compare the UV spectra of Bz-W_6 cluster with UV spectra of isolated water cluster W_6 and benzene Bz. The performances of all three functionals i.e. B3LYP, CAM-B3LYP and M06-2X are also tested on prism-shaped W_6 & Bz-W_6 clusters and Bz molecule (See Figures 4.3(b)-(d)).

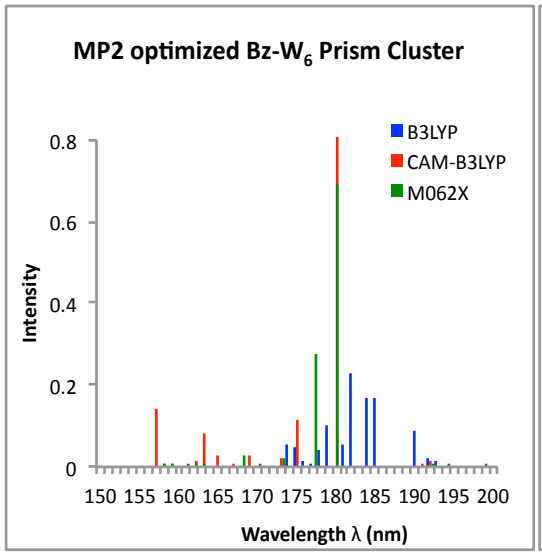

(a)

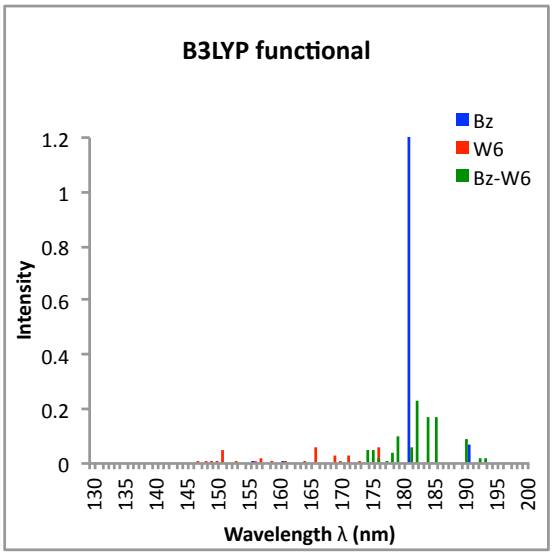

(b)

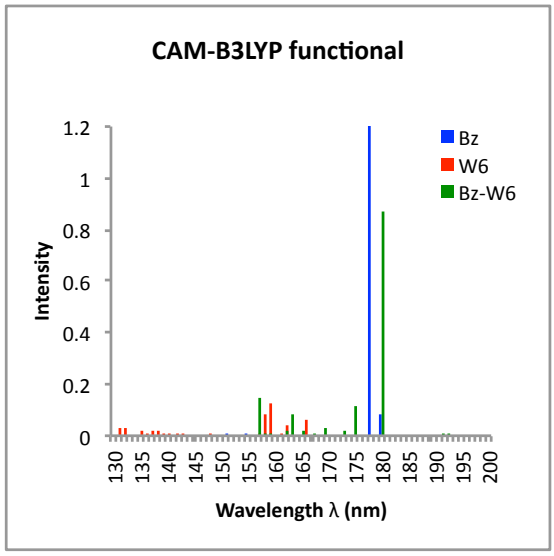

(c)

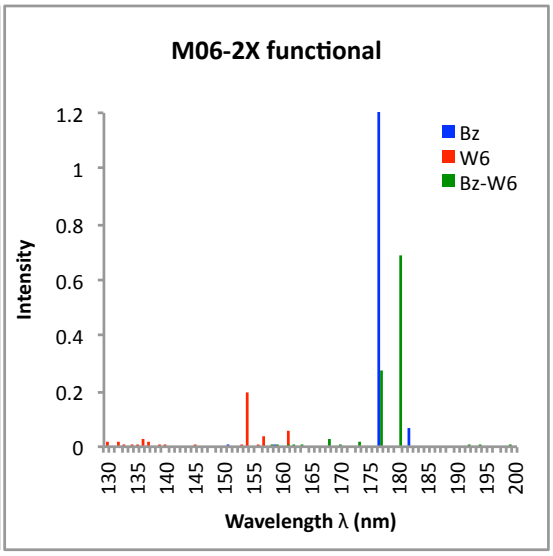

(d)

Figure 4.3 Simulated UV spectra obtained from TD-DFT calculations on MP2 optimized ground state geometries of prism shaped water W_6 cluster, Bz-W_6 cluster and Bz. (a) Comparison of B3LYP, CAM-B3LYP and M06-2X functionals performance on Bz-W_6 prism cluster (b) Performance of B3LYP functional (c) Performance of CAM-B3LYP functional (d) Performance of M06-2X functional.

It is also important to investigate the nature of these transitions and to understand whether Bz or W_6 cluster excitations, plays the dominant role in Bz-W_6 clusters. So, we have also analyzed the orbital transformations for those excitations that are associated with the high oscillator strengths or high intensity peaks found in the prism Bz-W_6 spectra for all three functionals, and are presented in Table 4.2.

Figure 4.3(b) clearly indicates different excitation features in Bz-W_6 prism cluster with respect to excitation features in isolated W_6 prism cluster and Bz molecule given by B3LYP functional. The excitations in Bz-W_6 cluster are shifted towards longer wavelengths (above 174 nm extended up to 193 nm) with respect to W_6 cluster where electronic excitations are dominant only in shorter wavelength region i.e. below 176 nm. The Bz excitation feature at around 181 nm is of very high intensity, with another less intense peak at 190 nm. In Bz-W_6 prism cluster, it is interesting to see that one of the strong intensity peak at around 182 nm is due to a charge transfer feature of the W_6 cluster to Bz system. Another strong peaks at around 184 nm and 185 nm is identified as the $\pi \rightarrow \pi^*$ electronic transition of benzene. Few weak excitations showing partial charge transfer from benzene to W_6 moiety and Bz locally diffuse excitations are also seen at wavelengths around 179 nm and 190 nm, respectively. It is interesting to note that presence of Bz enhances the excitations in W_6 cluster towards longer wavelengths above 176 nm, not present in isolated W_6 cluster. The intensity of peaks associated with water excitations in Bz-W_6 prism cluster are also found to be higher than in isolated water W_6 cluster.

Figure 4.3(c) shows that the CAM-B3LYP functional predicts a few excitations below 170 nm region in Bz-W_6 cluster which are in close proximity to excitations in W_6 cluster. Similarly peaks observed at longer wavelengths at around 175 nm and 180 nm in the Bz-W_6 cluster (completely absent in W_6 cluster) are found to be closer to Bz excitation feature at 178 nm. Using the CAM-B3LYP functional, it is found that the strongest peak at around 180 nm is the $\pi \rightarrow \pi^*$ electronic transition of benzene. A second intense peak at 157 nm is predicted due to the combined influence of $\sigma \rightarrow \pi^*$ transition from σ bonding orbital to π anti-bonding orbital of the benzene at 157.1 nm and the benzene charge transfer (CT) state at 157.4 nm, while third peak at around 175 nm corresponds to locally diffuse charge state associated with Bz excitation. We can also see that Bz excitations in Bz-W_6 prism cluster are red-shifted as compared to isolated Bz spectra. Thus, it is realized that Bz excitations are also influenced by presence of W_6 cluster around it.

Table 4.2 List of lowest energy $\pi \rightarrow \pi^*$ singlet electronic transitions and important electronic transitions corresponding to highest peak intensities (or oscillator strengths) obtained using B3LYP, CAM-B3LYP and M06-2X hybrid functional on MP2 optimized Bz-W_6 prism shaped clusters. (Value in parenthesis correspond to singlet $\pi \rightarrow \pi^*$ transitions of an isolated benzene molecule).

DFT functional	E (eV)	λ (nm)	Oscillator strength *(f)*	Electronic transition
M06-2X	5.45	227.6	0.0001	$\pi \rightarrow \pi^*$
	(5.47, 4.9[a,b])	(226.8)	(0.0000)	
	6.24	198.6	0.00014	$\pi \rightarrow \pi^*$
	(6.27, 6.20[a,c], 6.19[b])	(197.5)	(0.0000)	
	6.88	180.2	0.3967	$\pi \rightarrow \pi^*$
	(6.99, 6.94[a], 6.96[b])	(177.3)	(0.6084, 1.25[d])	
	6.87	180.4	0.2920	$\pi \rightarrow \pi^*$
	6.99	177.4	0.1871	$\pi \rightarrow \pi^*$
	7.02	176.6	0.0882	Bz CT state
CAM-B3LYP	5.38	230.3	0.0002	$\pi \rightarrow \pi^*$
	(5.40, 4.9[a,c])	(229.8)	(0.0000)	
	6.08	204.0	0.0006	$\pi \rightarrow \pi^*$
	(6.10, 6.20[a,c], 6.19[b])	(203.3)	(0.0000)	
	6.88	180.2	0.4353	$\pi \rightarrow \pi^*$
	(6.98, 6.94[a], 6.96[b])	(177.7)	(0.6301,1.25[d])	
	6.90	179.7	0.4323	$\pi \rightarrow \pi^*$
	7.09	174.9	0.1133	Bz Diffuse state
	7.89	157.1	0.0851	$\sigma \rightarrow \pi^*$
	7.88	157.4	0.0312	Bz CT state
B3LYP	5.28	234.7	0.0002	$\pi \rightarrow \pi^*$
	(5.30, 4.9[a,b])	(233.9)	(0.0000)	
	5.96	208.1	0.0003	$\pi \rightarrow \pi^*$
	(5.98, 6.20[a,c], 6.19[b])	(207.4)	(0.0000)	
	6.71	184.7	0.1747	$\pi \rightarrow \pi^*$
	(6.86, 6.94[a], 6.96[b])	(180.7)	(0.6064, 1.25[d])	
	6.75	183.6	0.1719	$\pi \rightarrow \pi^*$
	6.80	182.4	0.1622	W-CT state
	6.94	178.7	0.1056	Bz CT state
	7.13	174.0	0.0527	W-CT state
	6.51	190.4	0.0489	Bz Diffuse state

Previous work: [a]Exptl/Taken from Ref. [37], [b]Exptl/Taken from Ref. [38], [c]Exptl/Taken from Ref. [270], [d]Exptl/Taken from Ref. [271]

It is seen from Figure 4.3(d) that Bz-W_6 spectra are red shifted with respect to W_6 spectra, using M06-2X functional. Since, excitations observed in Bz system are above 175 nm wavelength region and therefore more likely to influence excitations at longer wavelengths in Bz-W_6 cluster rather than W_6 cluster. The M06-2X functional predicts the $\pi \rightarrow \pi^*$ transition feature of benzene at around 180 nm for the strongest peak, while another strong peak at around 177 nm is due to combined effect of $\pi \rightarrow \pi^*$ transition feature of benzene at 177.36 nm, and benzene charge transfer (CT) state at 176.56 nm, in which charge from Bz ring is transferred to W_6 cluster in prism shaped Bz-W_6 complex system.

It is found that most of the peak excitations in Bz-W_6 prism cluster are influenced by Bz excitations as compared to water W_6 excitations. It is also noted that intensity of the strongest peak is much higher in Bz and Bz-W_6 cluster than those in W_6 cluster, which hold for all three functionals.

Among various long range corrected functionals, wB97XD functional is found to be one of the most promising DFT functional used for systems involving general non-covalent interactions [272]. It is already mentioned above that wB97XD provides highest binding energies among all DFT functionals on Bz-W_6 clusters with BSSE correction, and it is same for both cage and prism conformers (See Table 4.1). Therefore, TD-DFT calculations on wB97XD-optimized ground state geometries of Bz-W_6 clusters with three functionals i.e. B3LYP, CAM-B3LYP and M06-2X are also performed.

Similar UV spectral characteristics are obtained from TD-DFT calculations on the wB97XD optimized ground state Bz-W_6 prism shaped cluster, where UV spectra undergo a red shift in going from the CAM-B3LYP to the B3LYP functional. Again we clearly see that the strongest intensity peak associated with the benzene $\pi \rightarrow \pi^*$ transition undergoes a small red shift in going from Bz to Bz-W_6 cluster for both CAM-B3LYP and M06-2X functionals, and the magnitude of shift is slightly larger for MP2 optimized geometries than wB97XD optimized geometries. The intensities are also found to be much stronger in Bz-W_6 cluster than those in W_6 cluster. It is again noted that presence of Bz enhances the excitations in W_6 cluster towards wavelengths above 170 nm. The strong intensity $\pi \rightarrow \pi^*$ transition features of Bz has shown small blue shift of order of around 2-3 nm in wB97XD optimized ground state geometries of Bz-W_6 cluster with respect to MP2 geometries.

Now, focusing on cage form of Bz-W_6 geometry, UV spectra results obtained from TD-DFT calculations on the MP2 optimized Bz-W_6 cage cluster using all three B3LYP, CAM-B3LYP and M06-2X functional are shown in Figure 4.4(a). The important electronic transitions corresponding to high oscillator strengths or strong intensity peaks in UV spectra of cage shaped Bz-W_6 cluster for all three functionals, are presented in Table 4.3.

Figure 4.4(a) shows that in Bz-W_6 cage cluster, electronic excitations predicted by B3LYP functional are red shifted with respect to excitations in M06-2X and CAM-B3LYP level of calculations. Both CAM-B3LYP and M06-2X functionals are consistent to find strong intensity peaks very close to each other at wavelength around 179-180 nm. However, a few less intense peaks at shorter wavelengths below 174 nm are also observed in CAM-B3LYP level of calculations.

Figure 4.4(b) shows that excitations in Bz-W_6 cage cluster are shifted towards longer wavelengths (region above 180 nm) with respect to W_6 cluster using B3LYP functional. It is interesting to notice that excitations in isolated water W_6 cluster above 170 nm wavelength range are rarely observed, however the B3LYP functional generates some weaker transitions at around 180-181 nm. It is found that strongest peaks generated at around 183 nm in UV spectra corresponds to contributions from $\pi \rightarrow \pi^*$ transition of benzene, and from a locally diffuse state due to Bz excitation. The another strong peak at around 182 nm is associated with $\pi \rightarrow \pi^*$ transition of benzene while other peaks at around 180 nm and 181nm correspond to Bz charge transfer excitation and to local Rydberg type state associated with W_6 cluster excitation, respectively. It is also again evident from spectra that intensity of water excitations increases in Bz-W_6 cluster as compared to the isolated water W_6 cluster.

Figure 4.4(c) indicates that excitations found in Bz-W_6 cage cluster do not overlap with the peaks found in isolated W_6 cage cluster for CAM-B3LYP functional. However, some weak excitation peaks at shorter wavelengths below 170 nm lie close to the W_6 cluster excitation region and some of the strong peaks at longer wavelengths (above 170 nm) lie close to Bz strongest intensity peak centred at around 178 nm. The analysis of these excitations has shown that with CAM-B3LYP, two close lying peaks with strong intensities at around 179 nm and 180 nm are associated with $\pi \rightarrow \pi^*$ transition of benzene. The third peak at around 161 nm corresponds to locally diffuse Rydberg state due to W_6 cluster excitation while another peak at around 174 nm seems like Bz charge transfer state. The molecular orbital plots are shown in Figure 4.5, which

illustrates the nature of the molecular orbitals involved in the electronic transitions for some of the electronic excited states computed at the TD-DFT level for both cage and prism conformers of benzene-W_6 clusters.

From Figure 4.4(d) we see that peaks in Bz-W_6 cluster are red shifted (above 170 nm) with respect to W_6 cluster with W_6 excitations lies below 161 nm as given by M06-2X functional. The M06-2X functional accounts for the $\pi \rightarrow \pi^*$ transition of benzene at around 180 nm and 179 nm which corresponds to strong intensities too, while another weak excitation at around 178 nm seems to be due to a benzene charge transfer excitation.

Benzene is found to dominate all the excitations in the Bz-W_6 cage cluster with M06-2X. It is again noted that once again the intensities of peaks are much stronger in Bz-W_6 cage cluster than isolated water cage W_6 cluster.

The UV spectra results obtained from TD-DFT calculations on the wB97XD optimized ground state Bz-W_6 cage shaped cluster, using all three functionals are generally consistent with the one obtained on MP2 optimized geometries. Most of the strong intensity peaks are found around the wavelength range 175-180 nm for all three hybrid functionals. UV spectra obtained by M06-2X is quite similar to those predicted by CAM-B3LYP functional. B3LYP again shows transitions towards longer wavelengths with respect to transitions given by CAM-B3LYP and M06-2X functionals.

It is interesting to see that the peaks are slighly red-shifted for TD-DFT calculations on MP2 optimized geometries as compared to wB97XD optimized ground state geometries for both prism and cage Bz-W_6 clusters, which is true for all three functionals. The nature of the transitions in UV spectra for both MP2 and wB97XD optimized geometries are generally quite consistent.

We again note that water excitations are observed in Bz-W_6 cage cluster at longer wavelengths, which are completely absent in isolated cage W_6 system. The intensities of water excitations are also stronger in Bz-W_6 cluster as compared to isolated W_6 cluster. Again we clearly see that the benzene $\pi \rightarrow \pi^*$ transition undergoes a small red shift in Bz-W_6 cluster with respect to isolated Bz. The intensities are also found to be much stronger in Bz-W_6 cluster than those in W_6 cluster.

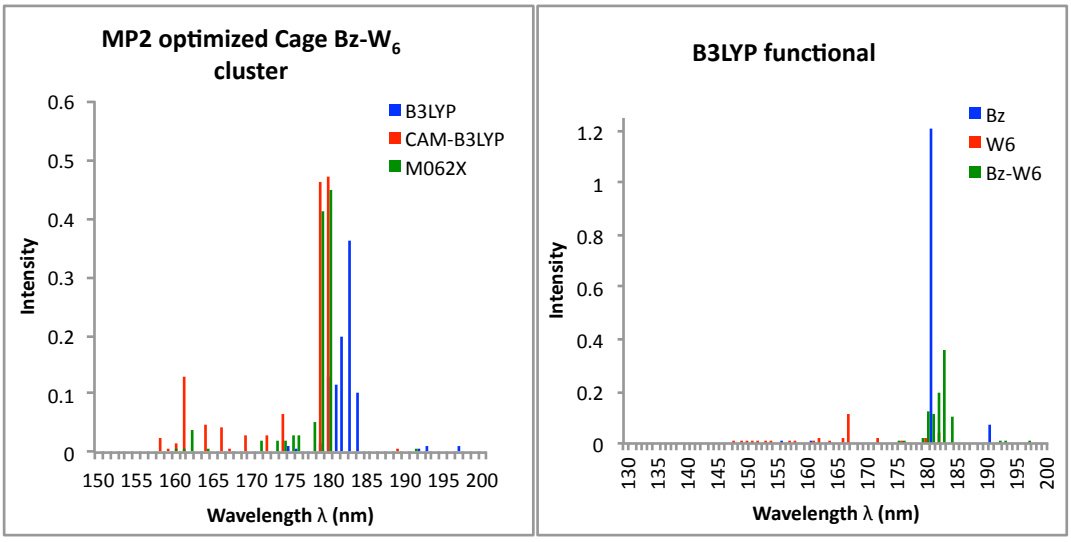

(a) (b)

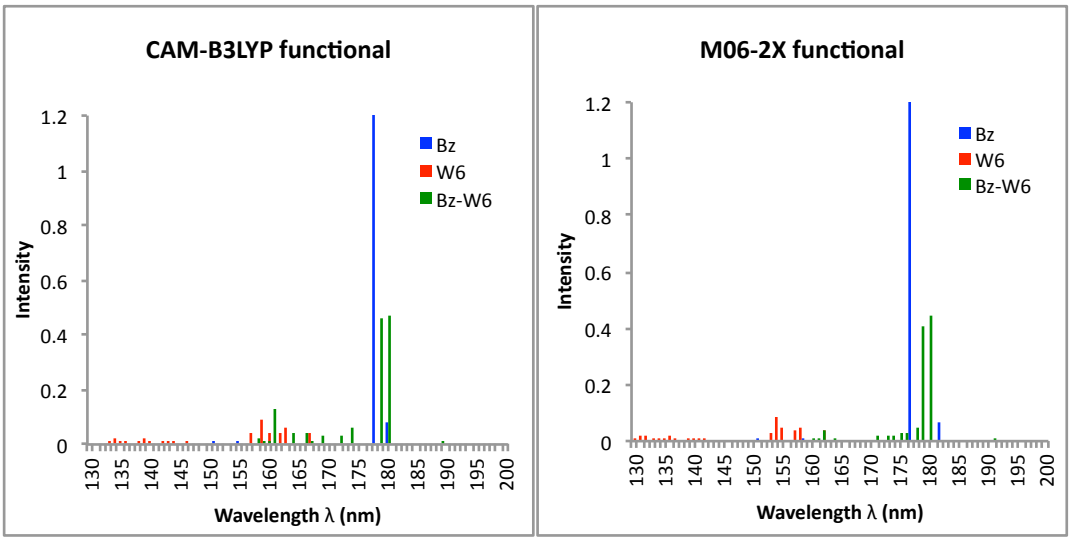

(c) (d)

Figure 4.4 Simulated UV spectra obtained from TD-DFT calculations on MP2 optimized ground state geometries of cage shaped water W_6 cluster, Bz-W_6 cluster and Bz. (a) Comparison of B3LYP, CAM-B3LYP and M06-2X functional performance on Bz-W_6 prism cluster (b) Performance of B3LYP functional (c) Performance of CAM-B3LYP functional (d) Performance of M06-2X functional.

Table 4.3 List of lowest energy $\pi \rightarrow \pi^*$ singlet electronic transitions and important electronic transitions corresponding to highest peak intensities (or oscillator strengths) obtained using B3LYP, CAM-B3LYP and M06-2X hybrid functionals on MP2 optimized Bz-W_6 cage shaped clusters. (Value in parenthesis correspond to singlet $\pi \rightarrow \pi^*$ transition of an isolated benzene molecule).

DFT functional	E (eV)	λ (nm)	Oscillator strength *(f)*	Electronic transition
M06-2X	5.46	226.9	0.0000	$\pi \rightarrow \pi^*$
	(5.47, 4.9[a,b])	(226.8)	(0.0000)	
	6.26	198.0	0.0000	$\pi \rightarrow \pi^*$
	(6.27, 6.20[a,c], 6.19[b])	(197.5)	(0.0000)	
	6.90	179.7	0.4475	$\pi \rightarrow \pi^*$
	(6.99, 6.94[a], 6.96[b])	(177.3)	(0.6084,1.25[d])	
	6.93	178.9	0.4107	$\pi \rightarrow \pi^*$
	6.99	177.5	0.052	Bz CT state
CAM-B3LYP	5.40	229.6	0.0000	$\pi \rightarrow \pi^*$
	(5.40, 4.9[a,c])	(229.8)	(0.0000)	
	6.10	203.4	0.0000	$\pi \rightarrow \pi^*$
	(6.10, 6.20[a,c], 6.19[b])	(203.3)	(0.0000)	
	6.90	179.6	0.4723	$\pi \rightarrow \pi^*$
	(6.98, 6.94[a], 6.96[b])	(177.7)	(0.6301,1.25[d])	
	6.94	178.7	0.4633	$\pi \rightarrow \pi^*$
	7.71	160.7	0.0807	W-Rydberg state
	7.12	174.1	0.0636	Bz CT State
B3LYP	5.30	233.8	0.0000	$\pi \rightarrow \pi^*$
	(5.30, 4.9[a,c])	(233.9)	(0.0000)	
	5.97	207.7	0.0000	$\pi \rightarrow \pi^*$
	(5.98, 6.20[a,c], 6.19[b])	(207.4)	(0.0000)	
	6.80	182.2	0.1980	$\pi \rightarrow \pi^*$
	(6.86, 6.94[a], 6.96[b])	(180.7)	(0.6064, 1.25[d])	
	6.77	183.2	0.1917	$\pi \rightarrow \pi^*$
	6.76	183.4	0.1701	Bz Diffuse state
	6.86	180.7	0.1157	W-Rydberg state
	6.89	180.0	0.1101	Bz CT state
	6.72	184.5	0.1039	Bz-Diffuse state

Previous work:

[a]Exptl/Taken from Ref. [37] , [b]Exptl/Taken from Ref. [38], [c]Exptl/Taken from Ref. [270], [d]Exptl/Taken from Ref. [271] ; Lowest $\pi \rightarrow \pi^*$ singlet vertical excitation energy (eV) in Bz-W_6 cage cluster = 6.17 [e] and f=0.004[e] , [e] CIS/Taken from Ref. [75].

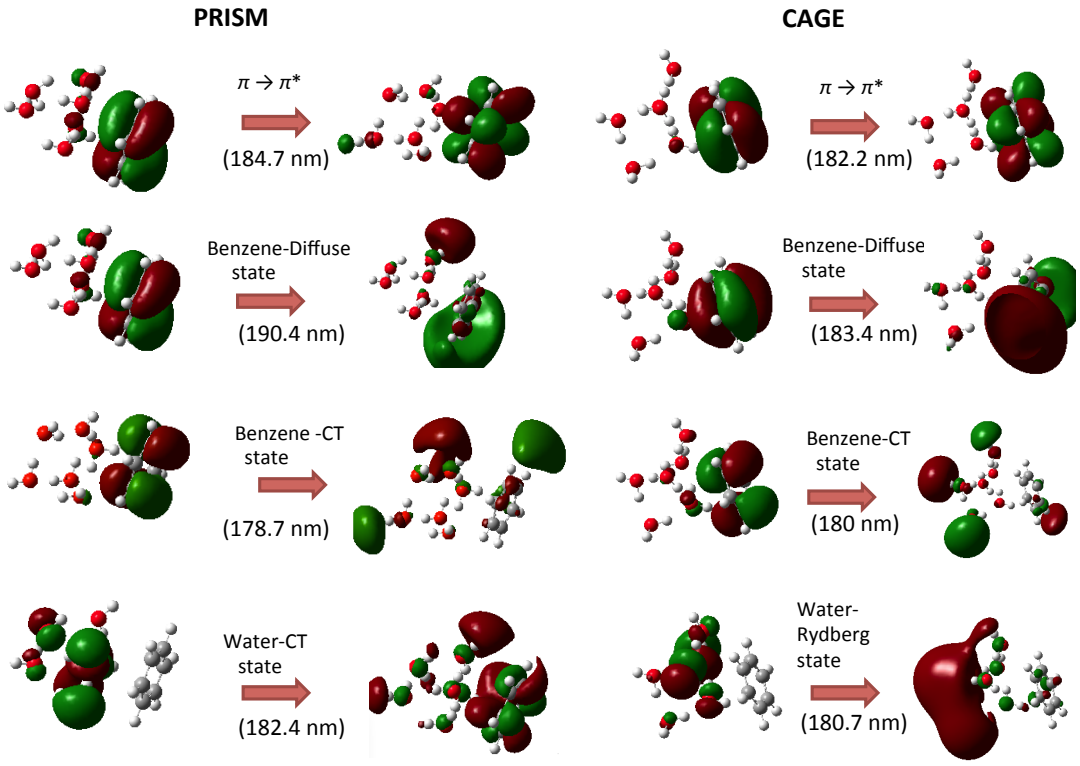

Figure 4.5 Molecular orbitals involved in the electronic transitions for few electronic excited states computed at the TD-DFT level for both prism and cage conformers of Bz-W_6 cluster.

It is worth mentioning that the lowest valence transitions of Bz from ground to excited states 1^1B_{2U} and 1^1B_{1U} are strictly dipole forbidden on symmetry grounds. The low lying vertical $\pi \rightarrow \pi^*$ excited states in Bz-W_6 prism clusters show small red shift of about 1 nm in excitation wavelengths, and oscillator strengths are slightly increased as compared to dipole forbidden 1^1B_{2U} and 1^1B_{1U} excited states in Bz, indicating slight allowed character in restricted lowest energy $\pi \rightarrow \pi^*$ electronic transitions due to the presence of prism W_6 conformer around Bz. However, no such difference has been noticed in cage conformer of Bz-W_6 cluster.

In UV spectra of both Bz-W_6 prism and cage clusters, the strong intensity $\pi \rightarrow \pi^*$ electronic transitions (bright states) with high oscillator strengths are red-shifted towards longer wavelengths with respect to corresponding dipole allowed degenerate $^1E_{1U}$ excited states of isolated Bz. The magnitude of red-shifts are about 3-4 nm in Bz-W_6 prism clusters, while Bz-W_6 cage clusters give red-shifts of about 2-3 nm. The degeneracies of these states are slightly broken by magnitude of about 0.8-1.0 nm in Bz-W_6 cage clusters, while it ranges from 0.2-1.0 nm for Bz-W_6 prism clusters. It is seen that cage Bz-W_6 cluster shows higher individual transition oscillator strengths than

prism Bz-W_6 cluster (See Table 4.2 and Table 4.3). However due to overlapping of very close lying peaks in prism Bz-W_6 cluster, the intensity of the strongest peak is larger in prism case than in cage one for CAM-B3LYP and M06-2X functionals, as degeneracy of strongest intensity $\pi \rightarrow \pi^*$ electronic transitions is broken slightly lesser in prism cluster than in cage cluster. The oscillator strengths of these bright $\pi \rightarrow \pi^*$ electronic states are decreased in Bz-W_6 clusters as compared to isolated Bz, illustrating the effect of water cluster around Bz, and existence of other close lying new Bz charge transfer and diffuse states, which also increase the intensities of water excitations and shift the excitations towards longer wavelengths as also seen in recent experimental studies [70-72]. It is clear from above results and discussion that the benzene interaction with W_6 cluster plays a significant role in giving new excitation features in UV spectra of Bz-W_6 clusters.

4.4 Conclusions

TD-DFT calculations have been performed on both MP2 and wB97XD optimized geometries for Bz, W_6 and Bz-W_6 clusters. The results obtained are noticeably different for both cage and prism conformers of W_6 and Bz-W_6 clusters giving different UV spectral characteristics. Our results and discussions also show that TD-DFT calculations are functional-dependent, with CAM-B3LYP and M06-2X generally showing good agreement. We have calculated some interesting features for water W_6 cluster excitations at longer wavelengths above 170 nm in both Bz-W_6 cage and prism geometries which are absent in isolated water W_6 cluster, indicating benzene-mediated excitations in the W_6 cluster as observed in recent experimental studies [70-72]. The intensities of W_6 excitations are also found to increase in Bz-W_6 cluster relative to those in isolated W_6 clusters. It is predicted that for both MP2 and wB97XD optimized geometries, benzene $\pi \rightarrow \pi^*$ transition undergoes small red shift in Bz-W_6 cluster with respect to isolated benzene, for both cage and prism geometries and that the degeneracy of this transition is very slightly broken compared to the isolated gas-phase benzene. Our results also predict that charge transfer (CT) states and locally excited diffuse states play an important role in such systems due to complicated nature of benzene-water ($\pi \cdots$HO) hydrogen bonding interactions prevailing in such systems, including conventional $\pi \rightarrow \pi^*$ type interactions between benzene and electrostatic interactions between hydrogen bonded water W_6 cluster.

Chapter 5 - Ground and excited states of Naphthalene-Water (Naphtha-W_6) Clusters: A Computational Study[†]

5.1 Introduction

The properties of water clusters (W_n) have been the subject of interest in many theoretical and experimental studies due to their interesting features, and their fundamental importance in many areas of Science such as Physics, Chemistry, Biology, *etc.* have been well established in the past [232-240]. Many theoretical and experimental research groups have carried out extensive research to study the interactions of water clusters with aromatic molecules. The weak hydrogen bonding interactions in such systems play an important role in determining its physical and chemical properties. Considering one of the simplest systems to replicate such aromatic-water interactions, benzene-water (Bz-W_n) complexes has been chosen extensively and studied in detail [65-67, 241-250, 261, 262, 265]. Numerous theoretical and experimental studies have been performed on the ground state properties such as binding energies and IR spectra of Bz-W_n clusters, and also on non-covalent interactions such as hydrogen bonding interactions that dominate such systems [65, 66, 230, 235, 240, 245-247, 259-262]. Such aromatic-water interactions are also very important in interstellar ices where polycyclic aromatic hydrocarbons (PAHs) interact with water as the most abundant molecule in icy mantles [11].

Polycyclic aromatic hydrocarbons (PAHs) as a reservoir of cosmic carbon are regarded as key molecules in the astrochemical evolution of the interstellar medium.[25, 251] The photo-processing of interstellar ices containing PAHs by UV light has been studied and it is observed to play an important role in the formation of many complex organic species [58]. Experiments [72] have been performed to study photo-processes in interstellar ice analogs i.e. PAH-ice model systems under interstellar icy conditions that corresponds to diffuse regions of molecular clouds in the interstellar medium. In this experiment [72], benzene was chosen as a prototypical PAH compound and photo-processes in model interstellar ices was studied by modelling multilayer films of benzene & water deposited on a sapphire substrate at a temperature of around 80 K. Three distinct photo-desorption mechanisms were investigated in such systems:

[†] D. Sharma and M. J. Paterson, *R. Soc. Chem. Adv.*, 2015, **5**, 28281- 28291

(i) Direct adsorbate-mediated desorption of benzene; (ii) Indirect adsorbate–mediated desorption of water; (iii) Substrate-mediated desorption of both benzene and water. It is also observed by recent experimental study [70] on photon- and electron- induced desorption from laboratory models of interstellar ice grains that photon absorption by benzene can make H_2O desorption possible at wavelengths where the photon-absorption cross-section for H_2O is negligible.

Recently, we have performed a detailed computational study on ground and excited states of the benzene-water hexamer (Bz-W_6) system [273]. UV spectral characteristics and vertical excitation energies were calculated to analyze and characterize electronic excitations in this astrophysical and environmentally relevant system. In this present paper we extend this work to truly polycyclic aromatics via naphthalene ($C_{10}H_8$), consisting of linearly fused two benzene rings. Naphthalene has been identified in the interstellar medium (ISM)[34-36] and is considered as a complex molecule in the ISM. However, the formation mechanism of naphthalene in the interstellar medium and its derivatives has always been a subject of debate and interest due to ubiquitous presence of PAHs in the ISM. A recent experimental and theoretical study [274] has proposed the formation mechanism of naphthalene in the gas phase via a barrierless and exoergic reaction between the phenyl radical (C_6H_5) and vinylacetylene involving a van-der-Waals complex and submerged barrier in the entrance channel. It is also suggested that PAH-formation in the interstellar medium can also occur at low temperatures, and more complex PAHs like phenanthrene and anthracene at temperatures down to 10 K can also be formed in cold molecular clouds [274].

We have chosen naphthalene as a representative of PAH family, and water clusters to represent the basic features of an interstellar ice surface. Naphthalene and its derivatives are also used in the production of dyes, resin, plastics, lubricants, fuels, *etc*., and are also considered environmental pollutants [275]. Therefore, study of complexes of naphthalene with water clusters is of both astrophysical and environmental relevance.

Many theoretical [40-43] and experimental studies [44-47] have been performed to study excited state properties of isolated naphthalene. Naphthalene is of lower symmetry than benzene, which allows many transitions that are forbidden in benzene.

Excited state properties of naphthalene-water complex systems have not received much attention so far. In this chapter, the main aim is to study both ground and excited states of the naphtha-W_6 cluster using quantum chemical methods. The linear response

time-dependent DFT [184-187] with a range of well-developed DFT functionals is used to study photochemistry and UV spectroscopy of naphtha-W_6 clusters to investigate and characterize important electronic transitions in this system.

We have chosen the water hexamer $(H_2O)_6$ cluster for our study, the smallest water cluster which allows non-cyclic structures and more three dimensional structures, and also as this is considered as a benchmark system for many computational chemistry studies on water clusters and their effects [207, 230-232, 264, 265]. There have been extensive computational and experimental studies on the ground state properties and hydrogen bonding interactions present in the different conformers of the water hexamer [207, 230-232, 234, 236, 238, 264]. Many theoretical studies have established the cage conformer as the minimum energy structure among all other close lying conformers such as prism, book, ring, chair, *etc*. [231, 234, 240, 265]. An experimental study by Pate *et al*. has also established the cage conformer of water hexamer as the global minimum energy structure [264]. However, the most recent computational studies have shown the prism as the lowest energy structure, although nearly iso-energetic to the cage structure [207, 238]. It has been predicted by both theoretical [238] and experimental observations [264] that cage and prism conformers exist at low temperatures, which are relevant to interstellar conditions. Thus, we choose these two conformers for the water hexamer for our present study i.e. the cage and the prism conformers of the water hexamer $(H_2O)_6$ consisting of eight and nine hydrogen bonds, respectively. We have used flexible water W_6 cluster i.e. all the water molecules of the water W_6 cluster are moving. This also allows direct comparison of our previous computational study of benzene-W_6 clusters [273].

5.2 Computational Details

The ground state geometries of both the cage and prism conformers of W_6 clusters and their respective naphthalene bound W_6 clusters i.e. naphtha-W_6 clusters were fully optimized using second order Møller-Plesset perturbation theory (MP2), in addition to density functional theory (DFT) with the long range corrected wB97XD functional. MP2 is considered reliable for ground state geometry optimizations by accounting for dynamic electron-correlation effects including dispersion and has been used extensively to study loosely bound hydrogen bonded and dispersion bound complexes [112]. wB97XD is one of the most promising long range corrected DFT functionals, i.e. one

that also includes an empirical atom-atom dispersion correction to treat systems involving general non-covalent interactions [130, 272]. The augmented correlation-consistent polarized-valence double zeta basis set (aug-cc-pVDZ) was employed for geometry optimization. Harmonic vibrational frequency calculations were carried out to check the nature of stationary points, and confirmed as minima for all ground state structures except the MP2/aug-cc-pvDZ optimized naphtha-W_6 cage structure which is a stationary point on the MP2/aug-cc-pVDZ potential energy surface but has a very small imaginary frequency. The surface is very flat for this geometry and we have taken this stationary point as it is matches the corresponding DFT stationary point which is a minimum.

We have used TD-DFT linear response theory [184-187] to calculate electronic excitation energies. TD-DFT calculations are performed on both MP2/aug-cc-pVDZ and wB97XD/aug-cc-pVDZ optimized ground state geometries of naphthalene, W_6 and naphtha-W_6 clusters using three different functionals i.e. B3LYP [127], CAM-B3LYP [131], and M06-2X [129] with the aug-cc-pVDZ basis set. We have also calibrated the TD-DFT calculations on MP2 optimized geometries using the larger TZ basis set. M06-2X is a non-local functional with 52% Hartree-Fock exchange, and are often found to perform better than standard hybrid functionals (such as the popular B3LYP) for systems involving non-covalent interactions, and modelling electronic excitation energies to both valence and Rydberg states [128, 129]. CAM-B3LYP has been specifically designed to model charge-transfer excitations in TD-DFT by "switching on" Hartree-Fock exchange as a function of distance. Thus, the three functionals chosen represent a reasonable variation in characteristics to better understand the transitions in these naphtha-W_6 clusters.

CIS(D) [212] calculations were also performed with the aug-cc-pVDZ basis set at the MP2 optimized ground state geometries of naphthalene, W_6 and naphtha-W_6 clusters, in order to compare TD-DFT with a basic wavefunction approach accounting for some correlation effects on excitation energies. The Gaussian09 program [214] was used for all computations.

5.3 Results and discussion

5.3.1 Ground State Geometries and Energetics

MP2/aug-cc-pVDZ optimized ground state geometries of the prism and cage form of the naphtha-W_6 cluster are shown in Figure 5.1(a) and Figure 5.1(b), respectively. Many different orientations of naphthalene with respect to the cage and prism conformers of water clusters were studied. More than 10 different fully optimized naphtha-W_6 complexes were found. Of these, we have selected the most stable cage and prism naphtha-W_6 complexes.

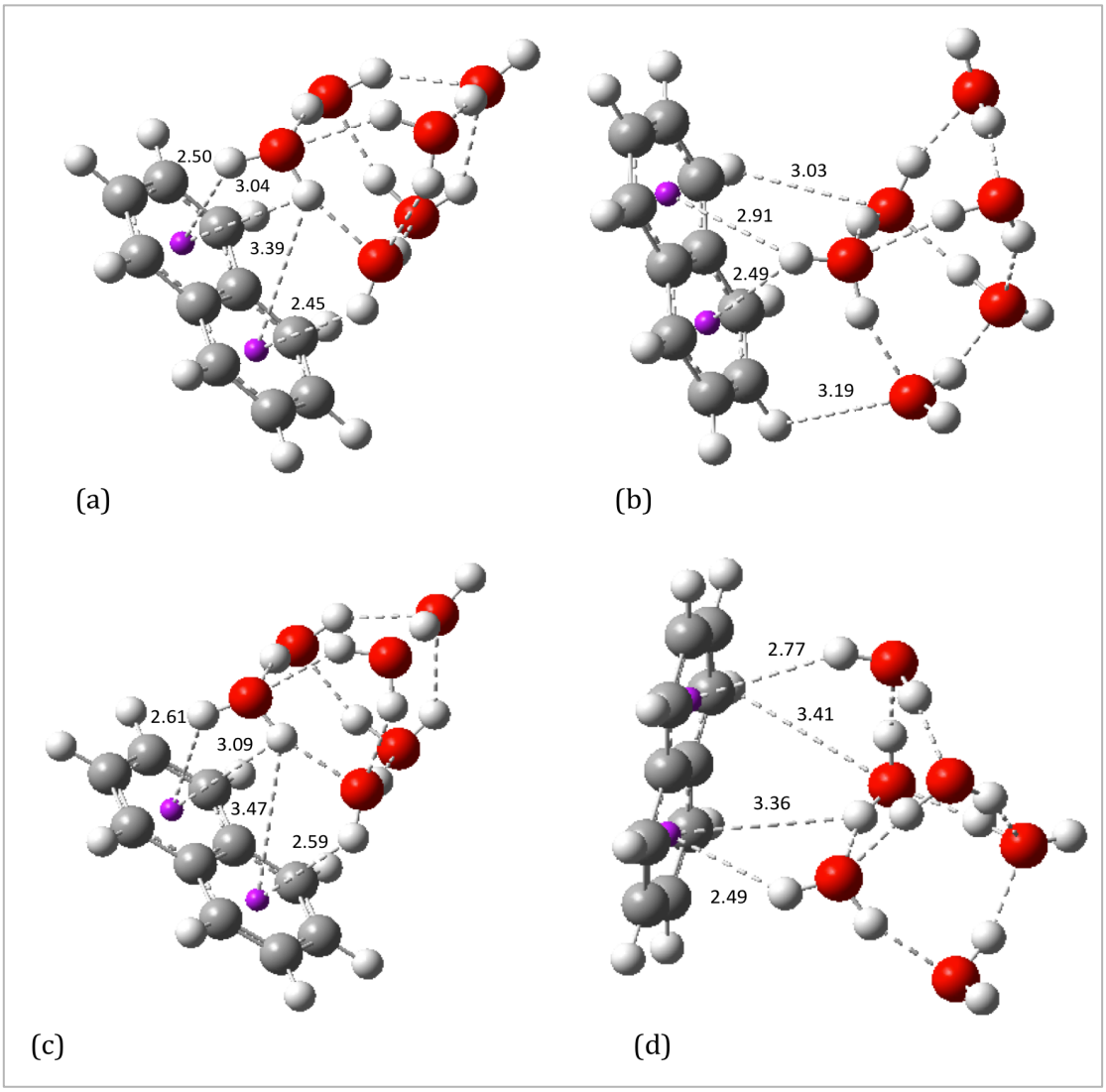

Figure 5.1 MP2/aug-cc-pVDZ optimized geometries of naphtha-W_6 clusters (a) prism conformer (b) cage conformer. wB97XD/aug-cc-pVDZ optimized geometries of naphtha-W_6 clusters (c) prism conformer (d) cage conformer. Aromatic centre of both aromatic rings are shown as purple circle.

The binding energy (BE) of the naphtha-W_6 cluster was calculated using

$$|BE| = E_{Naphthalene-W_6} - (E_{W_6} + E_{Naphthalene}) \quad (5.1)$$

where $E_{Naphthalene-W_6}$, E_{W_6}, and $E_{Naphthalene}$ denote the total energy of naphtha-W_6 cluster, W_6 cluster, and naphthalene, respectively. The optimized total energies of the W_6 clusters, naphtha-W_6 clusters, naphthalene, with the calculated absolute values of binding energies (BE's) of naphtha-W_6 clusters are given in Table 5.1.

It is noticed that BE's of the naphtha-W_6 cluster (with zero point energy (ZPE) correction) ranges from 9.11-14.29 kcal mol^{-1} for the prism conformer between DFT and MP2, whilst this varies between 7.24-10.82 kcal mol^{-1} for the cage conformer. In both systems it is observed that MP2 calculations give higher binding energies (after ZPE) than wB97XD calculations. It is seen that both cage and prism conformers of the water hexamer cluster essentially retain their shape after interacting with the naphthalene.

Table 5.1 Optimized total energies of the W_6 clusters, Naphthalene-W_6 clusters, Naphthalene and calculated absolute values of binding energies (BEs) of Naphtha-W_6 clusters for both cage and prism geometries with and without zero point energy ZPE correction at different levels of theory with aug-cc-pVDZ basis set. Value in the parenthesis corresponds to BSSE corrected binding energy.

PRISM	**MP2 (Without ZPE)**	**MP2 (With ZPE)**	**wB97XD (Without ZPE)**	**wB97XD (With ZPE)**
$E_{Naphtha-W6}$ (au)	-842.4050	-842.1090	-844.4083	-844.1052
E_{W6} (au)	-457.6430	-457.4930	-458.5969	-458.4445
$E_{Naphthalene}$ (au)	-384.7391	-384.5932	-385.7946	-385.6462
BE (kcal mol^{-1})	14.33 (7.57)	14.29	10.51 (8.91)	9.11
CAGE				
$E_{Naphtha-W6}$ (au)	-842.3982	-842.10332	-844.4045	-844.1019
E_{W6} (au)	-457.6426	-457.4929	-458.5966	-458.4442
$E_{Naphthalene}$ (au)	-384.7391	-384.5932	-385.7946	-385.6462
BE (kcal mol^{-1})	10.31 (4.97)	10.82	8.33 (7.01)	7.24

At the MP2 optimized geometries, it is found that naphthalene binds to the water hexamer cluster via hydrogen bonding interactions. In the prism conformer, four O-H$^{\cdots}$ π hydrogen bonding type interactions are noticed where dangling hydrogen atoms of the water cluster point toward the π electron cloud of the naphthalene ring (See Figure 5.1(a)). In the cage conformer, two O-H$^{\cdots}$ π hydrogen bonding interactions are noticed where one of the dangling hydrogen atom of the water cluster interacts with the π electron cloud of the naphthalene ring, including two C-H$^{\cdots}$O type hydrogen bonding interactions where H atom of the naphthalene ring interacts with the dangling oxygen of the water cluster, gives total of four hydrogen bonding interactions (Figure 5.1(b)).

Similarly, in the wB97XD optimized geometries, four O-H$^{\cdots}$ π hydrogen bonding type interactions are noticed in the prism conformer too (See Figure 5.1(c)), while in cage conformer, three O-H$^{\cdots}$ π hydrogen bonding type interactions and one C-H$^{\cdots}$O type hydrogen bonding interactions are seen (Figure 5.1(d)). However, shorter bond distances for these hydrogen-bonding interactions are noticed in MP2 optimized geometries as compared to wB97XD-optimized geometries. This may result in stronger binding and hence higher binding energies for naphtha-water clusters calculated by MP2 than by wB97XD.

Basis set superposition error (BSSE) was also estimated for both the cage and prism forms of naphtha-W_6 clusters using the counterpoise (CP) method and CP-corrected binding energies are also listed in Table 5.1. Here BSSE correction is for the single point energy calculation on the optimized naphtha-W_6 clusters. BSSE error is significantly larger for MP2 calculations than wB97XD, and binding energies are overestimated by MP2 of calculations for both prism and cage conformers. With BSSE correction, it is seen that binding energies are reduced noticeably for both conformers, varying from 7.57-8.91 kcal mol^{-1} for the prism conformer between DFT and MP2, while relatively lower binding energies with a wider MP2-DFT variation of 4.97-7.01 kcal mol^{-1} are observed for the cage conformer. Thus, the prism conformer is found to be more stable than the cage conformer for both MP2 and DFT levels of theory.

In order to check the effects of basis set on the binding energies of naphtha-W_6 cage and prism clusters, the ground state geometries of both the cage and prism conformers of W_6 clusters along with their respective naphthalene bound W_6 clusters and isolated naphthalene molecule were again fully optimized with DFT (wB97XD functional) using a larger basis set i.e. Dunning's correlation-consistent aug-cc-pVTZ basis set.

Without ZPE correction, it is noticed that binding energies of naphtha-W_6 cluster are 9.41 kcal mol^{-1} and 7.55 kcal mol^{-1} for prism and cage conformers, respectively, which differ by about 1 kcal mol^{-1} compared to respective binding energies calculated using the aug-cc-pVDZ basis set. After BSSE correction the binding energies of naphtha-W_6 cluster calculated using aug-cc-pVTZ basis set are 8.99 kcal mol^{-1} and 7.16 kcal mol^{-1} for prism and cage conformers, respectively, and are in good agreement with results obtained using aug-cc-pVDZ basis set i.e. within 0.15 kcal mol^{-1} difference, and hold for both prism and cage conformers. Thus, we can be confident that the smaller basis is accurately describing the binding in these systems.

5.3.2 Electronic excitations in Naphthalene-W_6 clusters

The UV spectral results obtained from TD-DFT calculations on MP2 optimized ground state of the naphtha-W_6 cluster, using all three functionals are presented in Figure 5.2(a) and Figure 5.3(a), for the prism and cage conformers respectively. For the prism conformer of the naphtha-W_6 cluster, it is noticed that the B3LYP functional generates the strongest peak at around 220-221 nm, while both M06-2X and CAM-B3LYP functionals give the consistent results, and generate the strongest intensity peak at around 212-213 nm (See Figure 5.2(a)). Similar trends are noticed for the cage conformer, with UV spectra generated using B3LYP being red-shifted towards compared to M06-2X and CAM-B3LYP functionals, as shown in Figure 5.3(a).

The effects of naphthalene interaction with the water cluster W_6 on the UV spectral characteristics are investigated by comparing to those of the isolated water cluster W_6, and the isolated naphthalene. The results obtained using all three functionals on the W_6 cluster, naphtha-W_6 clusters and naphthalene molecule are shown in Figures 5.2(b)-5.2(d) for the prism conformer, and Figures 5.3(b)-5.3(d) for cage conformer. The nature of the electronic transitions are analysed by looking at the orbitals involved in the response eigenvectors in those excitations that are associated with higher oscillator strengths or strong intensity peaks in naphtha-W_6 spectra, and the important electronic transitions assigned for those excitations are listed in Table 5.2 and Table 5.3 for prism and cage conformer, respectively.

Experimentally three absorption bands labeled as α, p, and β are observed for naphthalene, where the p band is polarized along the short axis of the naphthalene and the α and β bands are polarized along the long axis [44]. It is observed that the β band is

of the strongest intensity; followed by the *p* and *α* bands. It is observed that the state corresponding to the *α* band (polarization along the long axis) is the lowest lying excited state in the naphthalene. For our TD-DFT calculations, we find that the *α* and the *β* absorption bands are related to electronic excitations from the ground state to the excited states with symmetry 1^1B_{2U} and 2^1B_{2U}, respectively, while *p* band relates to the electronic excitation to the 1^1B_{1U} state. All three electronic transitions are assigned as the $\pi \rightarrow \pi^*$ transitions. The TD-DFT calculations on naphthalene give consistent results using CAM-B3LYP and M06-2X, and the two lowest lying singlet vertical excitations in naphthalene are of $^1B_{2U}$ symmetry and $^1B_{1U}$ symmetry. This energy ordering is reversed for B3LYP. Both CAM-B3LYP and M06-2X results are in good agreement with the experiment. For the M06-2X functional, the calculated valence $\pi \rightarrow \pi^*$ excitation energies of naphthalene (experimental values in the parenthesis) are 1^1B_{2U}: 4.52(4.13[46], 4.03[44], 4.0[47]), 1^1B_{1U}: 4.57(4.66[46], 4.38[44], 4.45[47]), and 2^1B_{2U}: 5.90(5.7[44], 5.89[47]) eV, respectively. The *α* excitation is over-estimated by 0.5 eV for the 1^1B_{2U} state with the experiments, while the *p* excitation is calculated with an accuracy of about 0.09 eV for the 1^1B_{1U} state. The *β* excitation (i.e. 2^1B_{2U} state) is described well and is computed with an accuracy of around 0.01 eV. We calculate that the lowest valence transition of naphthalene from ground to excited state 1^1B_{2U} is a dark state of zero oscillator strength, although not forbidden by symmetry. The naphthalene $\pi \rightarrow \pi^*$ electronic transition at around 210 nm (or about 5.9 eV) is of very high intensity i.e. a bright state and corresponds to *β* absorption band with electronic transition from ground to 2^1B_{2U} excited state. We have calculated the highest oscillator strength $f \approx 1.3$ for 2^1B_{2U} excited state, which is in good agreement with the experimental observations.

Different excitation features in naphtha-W_6 prism cluster are obtained with respect to excitation features in isolated W_6 prism cluster and naphthalene molecule by B3LYP calculations, as shown in Figure 5.2(b). The naphtha-W_6 spectra are red shifted with respect to W_6 spectra. The electronic transitions in naphtha-W_6 cluster are observed towards longer wavelengths i.e. in the spectral range of about 200-295 nm, whereas in W_6 cluster electronic transitions are seen at wavelengths below 176 nm. The naphthalene excitation feature at around 216 nm is of very high intensity, with other less intense peaks at around 208 nm and 294 nm. In the naphtha-W_6 prism cluster, the strongest intensity peak at around 220 nm is due to the $\pi \rightarrow \pi^*$ electronic transition of naphthalene. Another intense peaks at around 217 nm and 209 nm are also associated

with the naphthalene $\pi \rightarrow \pi^*$ electronic transition. Some weak electronic transitions at around 204-205 nm correspond to a naphthalene locally diffuse state and its charge transfer (CT) excitation to water the W_6 cluster. It is also interesting to observe a weak charge transfer transition caused by water excitations in naphtha-W_6 cluster at around 195 nm, which are completely absent in the isolated W_6 cluster.

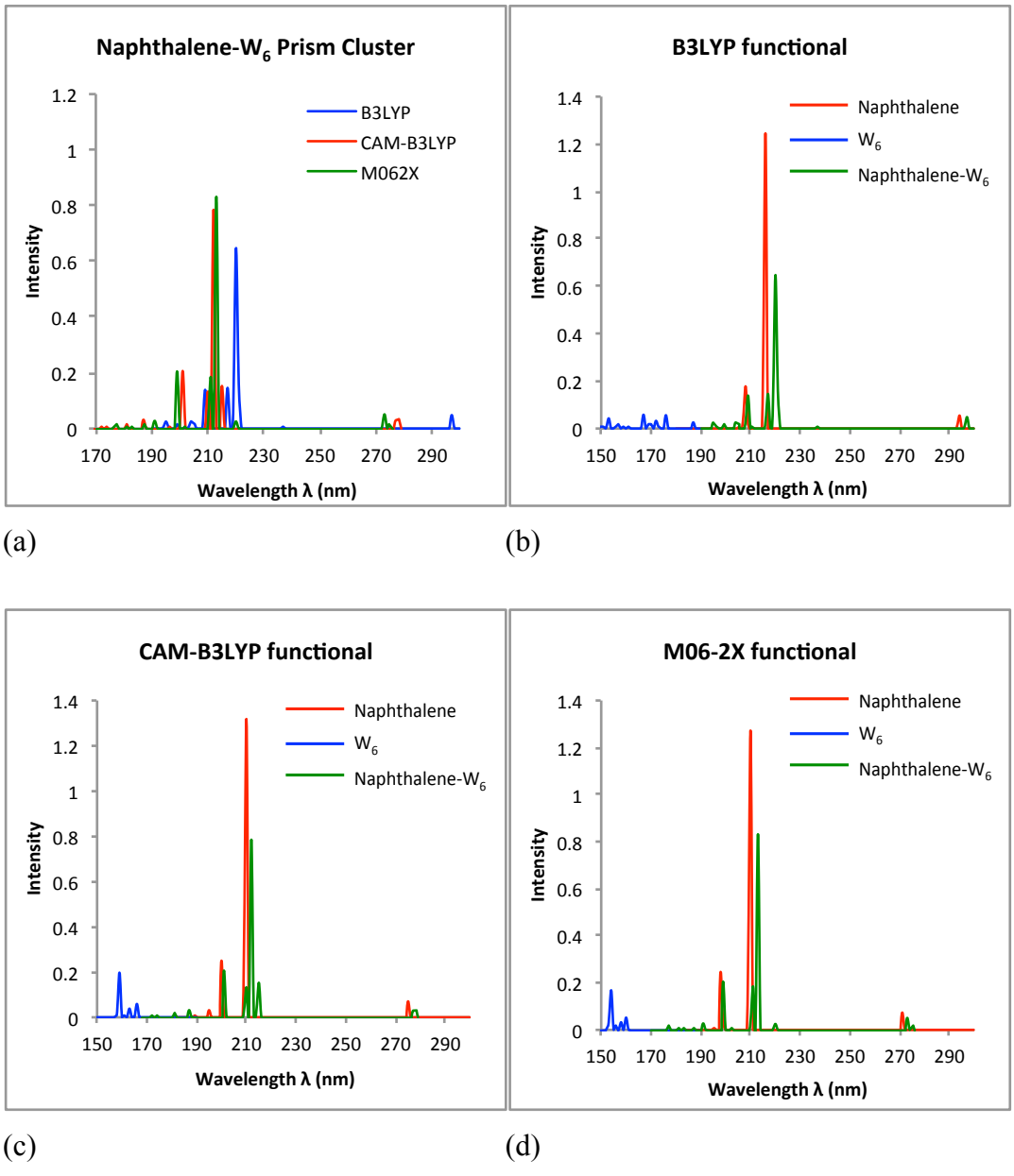

Figure 5.2 Simulated UV spectra obtained from TD-DFT calculations on MP2 optimized ground state geometries, (a) Comparison of B3LYP, CAM-B3LYP and M06-2X functionals on Naphtha-W_6 prism cluster. Performance of (b) B3LYP, (c) CAM-B3LYP, and (d) M06-2X on prism shaped water W_6 cluster, Naphtha-W_6 cluster and Naphthalene.

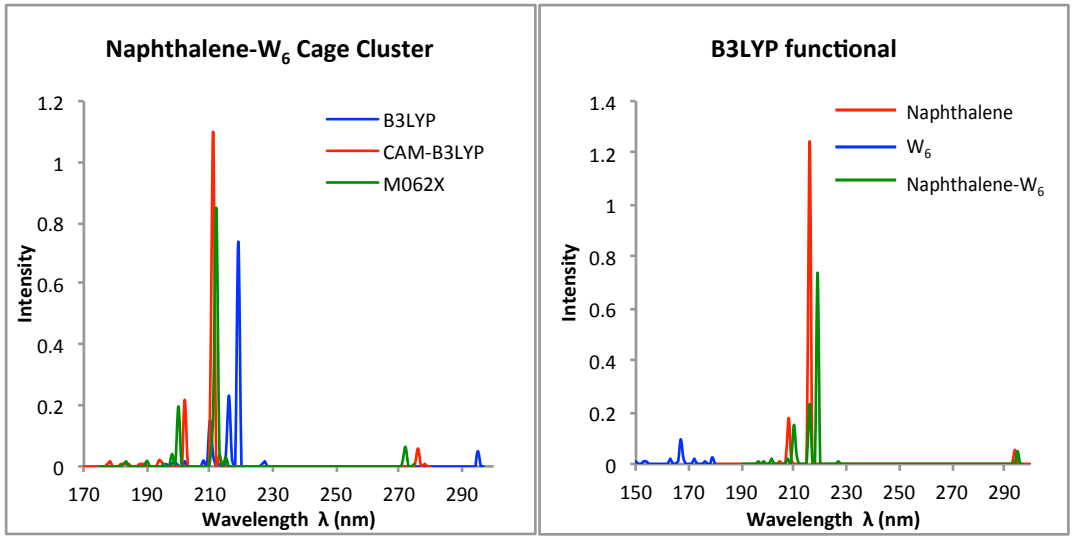

(a) (b)

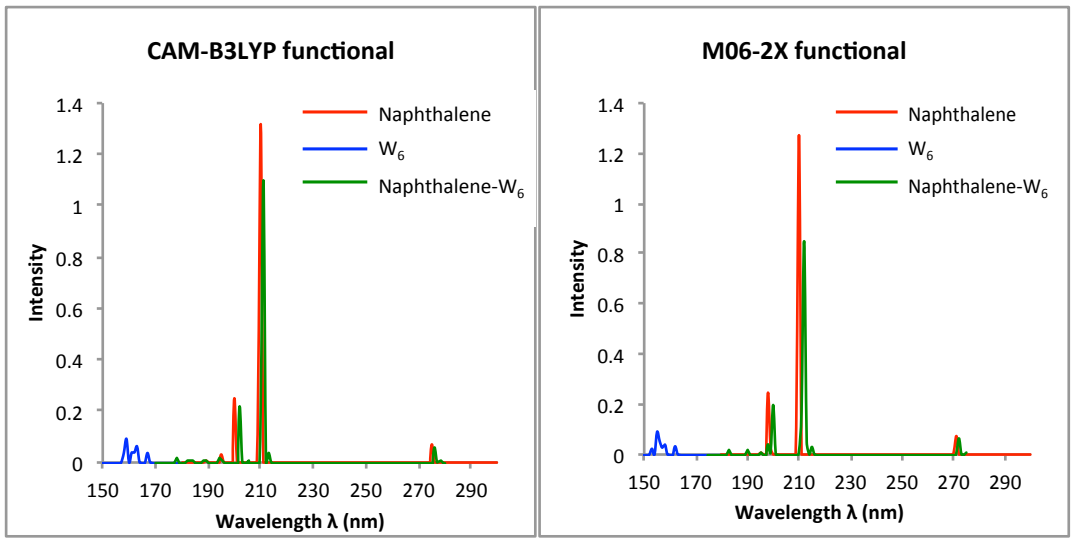

(c) (d)

Figure 5.3 Simulated UV spectra obtained from TD-DFT calculations on MP2 optimized ground state geometries, (a) Comparison of B3LYP, CAM-B3LYP and M06-2X functionals on Naphtha-W_6 cage cluster. Performance of (b) B3LYP, (c) CAM-B3LYP, and (d) M06-2X on cage shaped water W_6 cluster, Naphtha-W_6 cluster and Naphthalene.

Table 5.2 List of lowest energy singlet electronic transitions obtained using TD-B3LYP, TD-CAM-B3LYP and TD-M06-2X functionals on MP2 optimized naphtha-W_6 prism shaped clusters. (Value in parenthesis correspond to singlet $\pi \rightarrow \pi^*$ transitions of an isolated naphthalene molecule).

DFT functional	E (eV)	λ (nm)	Oscillator strength *(f)*	Electronic transition
B3LYP	4.18 (4.22, 4.66[a], 4.38[b], 4.45[c])	296.5 (294.2)	0.0483 (0.0547,0.109[c], 0.102[d])	$\pi \rightarrow \pi^*$
	4.32 (4.33, 4.13[a], 4.03[b], 4.0[c])	286.9 (286.5)	0.0007 (0.0000,0.002[d])	$\pi \rightarrow \pi^*$
	5.63 (5.73, 5.62[b], 5.89[c])	220.1 (216.3)	0.6459 (1.2450,1.3[c,d])	$\pi \rightarrow \pi^*$
	5.61	221.2	0.1590	$\pi \rightarrow \pi^*$ (Diffuse)
	5.73	216.5	0.1461	$\pi \rightarrow \pi^*$
	5.92	209.3	0.1391	$\pi \rightarrow \pi^*$
	6.04	205.2	0.0192	Naphtha-Diffuse State
	6.06	204.5	0.0191	Naphtha-CT state
	6.37	194.8	0.0123	Water-CT state
CAM-B3LYP	4.45 (4.48, 4.13[a], 4.03[b], 4.0[c])	278.4 (277.1)	0.0338 (0.0000,0.002[d])	$\pi \rightarrow \pi^*$
	4.48 (4.50, 4.66[a], 4.38[b], 4.45[c])	276.6 (275.5)	0.0295 (0.0708, 0.109[c], 0.102[d])	$\pi \rightarrow \pi^*$
	5.84 (5.91, 5.62[b], 5.89[c])	212.2 (209.8)	0.7849 (1.1319,1.3[c,d])	$\pi \rightarrow \pi^*$
	6.17	200.8	0.2066	$\pi \rightarrow \pi^*$
	5.76	215.3	0.1528	$\pi \rightarrow \pi^*$
	5.91	209.9	0.1328	$\pi \rightarrow \pi^*$ (Diffuse)
	6.62	187.2	0.0290	Naphtha-Diffuse State
	6.87	180.6	0.0157	Naphtha-CT state
	6.87	180.4	0.0012	Water-CT state
M06-2X	4.50 (4.52, 4.13[a], 4.03[b], 4.0[c])	275.3 (274.1)	0.0149 (0.0000,0.002[d])	$\pi \rightarrow \pi^*$
	4.54 (4.57, 4.66[a], 4.38[b], 4.45[c])	273.3 (271.3)	0.0510 (0.0737, 0.109[c], 0.102[d])	$\pi \rightarrow \pi^*$
	5.82 (5.90, 5.62[b], 5.89[c])	213.2 (210.2)	0.8315 (1.2728,1.3[c,d])	$\pi \rightarrow \pi^*$
	6.23	198.9	0.2052	$\pi \rightarrow \pi^*$
	5.87	211.2	0.1850	$\pi \rightarrow \pi^*$
	6.50	190.8	0.0205	Naphtha-Diffuse State
	6.65	186.5	0.0119	Naphtha-CT state
	6.68	185.6	0.0001	Water-CT state

Previous Work: [a]Exptl/Taken from Ref. [46], [b]Exptl/Taken from Ref. [44], [c]Exptl/Taken from Ref. [47], [d]Exptl/Taken from Ref. [45]

The CAM-B3LYP functional predicts a strongest intensity peak at around 212 nm in the naphtha-W_6 cluster which is in close proximity to the naphthalene excitation feature at 210 nm (See Figure 5.2(c)). The is the main $\pi \rightarrow \pi^*$ transition. All strong intensity peaks found at around 201 nm, 215 nm, and 210 nm are also assigned as $\pi \rightarrow \pi^*$ electronic transitions of naphthalene. Some weak transitions at around 278 nm and 187 nm are assigned as a $\pi \rightarrow \pi^*$ electronic transition of naphthalene and a locally diffuse state of naphthalene, respectively. A few very weak transitions due to water CT excitations and naphthalene CT excitations are observed at around 180 nm in naphtha-W_6 cluster.

Similar UV spectral characteristics are predicted by M06-2X functional, as shown in Figure 5.2(d). In naphtha-W_6 cluster, the strongest peak at around 213 nm is associated with the $\pi \rightarrow \pi^*$ transition feature of naphthalene, while other strong peaks at around 199 nm, and 211 nm are also due to $\pi \rightarrow \pi^*$ electronic transitions of naphthalene. A few weak intensity transitions at 273 nm and 191 nm correspond to a $\pi \rightarrow \pi^*$ electronic transition of naphthalene and naphthalene locally diffuse state, respectively. Naphthalene weak CT excitations to the water cluster are also observed around 180-185 nm, including small contributions from very weak charge transfer excitations of the water cluster to naphthalene too.

For all functionals we see that the strongest intensity naphthalene $\pi \rightarrow \pi^*$ electronic transition in naphtha-W_6 prism clusters are red-shifted as compared to that in isolated naphthalene. New weaker, non-addiative features such as inter-CT states appear at higher energies for all functionals. Given the nature of these the CAM-B3LYP results are probably the most accurate.

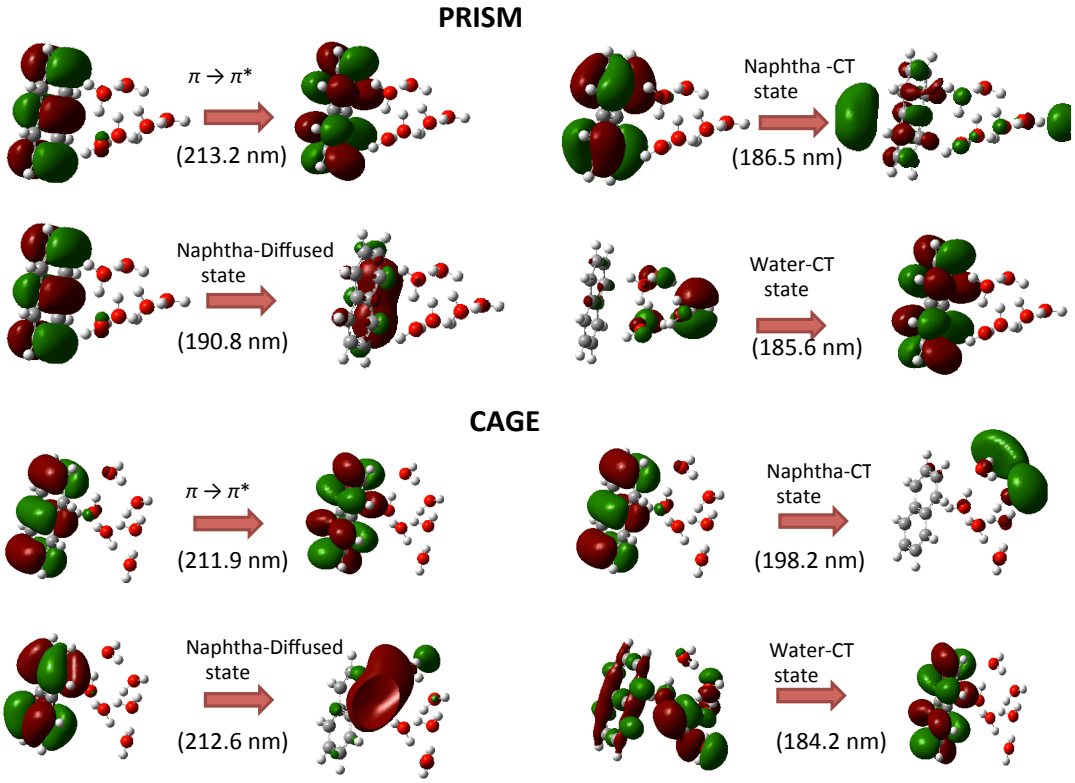

Figure 5.4 Molecular orbitals involved in the electronic transitions for few electronic excited states computed at the TD-M062X level for both prism and cage conformers of Naphtha-W_6 cluster.

Next, considering the cage conformer of the W_6 cluster interacting with naphthalene i.e. naphtha-W_6 cage shaped cluster, we have obtained results consistent with those presented above for the prism cluster one. The B3LYP functional predicts the $\pi \rightarrow \pi^*$ transition feature of naphthalene at around 219 nm as the strongest transition (See Figure 5.3(b)), while both CAM-B3LYP and M06-2X functionals generate this at around 211 nm (See Figure 5.3(c)-5.3(d)). All other important electronic transitions found in naphtha-W_6 cage shaped cluster are given in Table 5.3.

Table 5.3 List of lowest energy singlet electronic transitions obtained using TD-B3LYP, TD-CAM-B3LYP and TD-M06-2X functionals on MP2 optimized naphtha-W_6 cage shaped clusters. (Value in parenthesis correspond to singlet $\boldsymbol{\pi \rightarrow \pi^*}$ transitions of an isolated naphthalene molecule).

DFT functional	**E (eV)**	**λ (nm)**	**Oscillator strength *(f)***	**Electronic transition**
B3LYP	4.22 (4.22, 4.66[a], 4.38[b], 4.45[c])	294.7 (294.2)	0.0499 (0.0547, 0.109[c], 0.102[d])	$\pi \rightarrow \pi^*$
	4.32 (4.33, 4.13[a], 4.03[b], 4.0[c])	287.2 (286.5)	0.0008 (0.0000, 0.002[d])	$\pi \rightarrow \pi^*$
	5.66 (5.73, 5.62[b], 5.89[c])	219.2 (216.3)	0.7383 (1.2450,1.3[c,d])	$\pi \rightarrow \pi^*$
	5.75	215.7	0.2325	Naphtha-CT state
	5.91	209.9	0.1512	$\pi \rightarrow \pi^*$
	5.89	210.6	0.0377	Naphtha-Diffuse state
	5.72	216.9	0.0214	Naphtha-CT state
	6.13	202.2	0.0167	Naphtha-CT state
	6.26	198.2	0.0089	Water-CT state
CAM-B3LYP	4.46 (4.48, 4.13[a], 4.03[b], 4.0[c])	277.8 (277.1)	0.0067 (0.0000,0.002[d])	$\pi \rightarrow \pi^*$
	4.50 (4.50, 4.66[a], 4.38[b], 4.45[c])	275.6 (275.5)	0.0588 (0.0708, 0.109[c], 0.102[d])	$\pi \rightarrow \pi^*$
	5.87 (5.91, 5.62[b], 5.89[c])	211.2 (209.8)	1.0993 (1.1319, 1.3[c,d])	$\pi \rightarrow \pi^*$
	6.14	201.8	0.2189	$\pi \rightarrow \pi^*$
	5.82	212.9	0.0375	$\pi \rightarrow \pi^*$ (Diffuse)
	6.40	193.7	0.0216	Naphtha-CT state
	6.99	177.5	0.0131	Naphtha-CT state
	6.93	179.0	0.0010	Water-CT state
M06-2X	4.51 (4.52, 4.13[a], 4.03[b], 4.0[c])	274.9 (274.1)	0.0042 (0.0000,0.002[d])	$\pi \rightarrow \pi^*$
	4.56 (4.57, 4.66[a], 4.38[b], 4.45[c])	271.6 (271.3)	0.0645 (0.0737, 0.109[c], 0.102[d])	$\pi \rightarrow \pi^*$
	5.85 (5.90, 5.62[b], 5.89[c])	211.9 (210.2)	0.8498 (1.2728, 1.3[c,d])	$\pi \rightarrow \pi^*$
	5.88	210.9	0.1727	$\pi \rightarrow \pi^*$
	6.20	199.9	0.1974	$\pi \rightarrow \pi^*$
	5.83	212.6	0.0500	Naphtha-Diffuse state
	6.26	198.2	0.0407	Naphtha-CT state
	6.73	184.2	0.0002	Water-CT state

[a]Exptl/Taken from Ref. [46] , [b]Exptl/Taken from Ref. [44], [c]Exptl/Taken from Ref. [47] , [d]Exptl/Taken from Ref. [45]

It is found that most of the strong intensity electronic transitions in both naphtha-W_6 prism and cage clusters are influenced by naphthalene excitations as compared to water W_6 excitations. Similarly, naphthalene charge transfer states to cage-shaped water cluster are also observed, showing the effect of naphthalene to enhance water excitations towards longer wavelengths. The presence of weak water charge transfer excitations in these cage shaped naphtha-W_6 are also observed. It is also noted that oscillator strengths of the strongest transition are much higher in naphthalene and naphtha-W_6 cluster than those in W_6 cluster, which hold for all three functionals. It is also calculated that the cage naphtha-W_6 cluster shows higher individual transition oscillator strengths for bright states than the prism naphtha-W_6 cluster (See Table 5.2 and Table 5.3). Figure 5.4 illustrates the nature of the molecular orbitals involved in the electronic transitions for some of the electronic excited states computed at the TD-DFT level for both cage and prism conformers of naphtha-W_6 clusters.

In order to calibrate basis set effects on the UV spectra, we have also performed TD-DFT calculations using larger basis set at MP2 optimized ground state geometries of naphthalene, W_6 and naphtha-W_6 clusters. For all three functionals, it is noticed that electronic excitations show only a small red-shift < 0.04 eV for both isolated naphthalene and naphtha-W_6 clusters relative to those electronic excitations generated using aug-cc-pVDZ basis set, while a small blue shift of < 0.07 eV is seen in W_6 clusters for both prism and cage conformers. The nature of excitations associated with higher oscillator strengths in naphtha-W_6 clusters (for prism and cage conformers) is generally quite consistent for both aug-cc-pVDZ and aug-cc-pVTZ calculations.

We have also compared the TD-DFT excitations with a correlated approach by performing CIS(D) calculations i.e. configuration interaction with single excitations and added doubles (D) perturbation on those, in conjunction with the aug-cc-pVDZ basis set, on the MP2 optimized ground state geometries of naphthalene, W_6 and naphtha-W_6 clusters. It is noticed that the lowest dark excited state of naphthalene shows a red-shift of about 0.10-0.15 eV, while the brightest excited state shows a blue-shift of about 0.15 eV with respect to those in TD-CAM and TD-M062X results. We observe similar effects in the naphtha-W_6 cage and prism conformers, and the lowest excited state of very small oscillator strength gives a red-shift of about 0.15 eV, while the brightest state gives a blue-shift of about 0.30 eV with respect to those in TD-CAM and the TD-M06-2X results. The largest discrepancy seen is for a state where the CIS(D) is very

similar to the (uncorrelated) CIS and gives a blue-shift of about 0.5-0.6 eV with respect to those in TD-DFT results.

Finally, very similar UV spectral characteristics are observed for the wB97XD optimized naphtha-W_6 prism and cage shaped cluster, where UV spectra undergo a red shift in going from the CAM-B3LYP to the B3LYP functional. We observe stronger peak intensities in naphtha-W_6 cluster than those in the isolated W_6 cluster. It is again noted that the presence of naphthalene enhances the excitations in W_6 cluster towards wavelengths above 170 nm, therefore generating new naphthalene-CT and water-CT states too. Again for all three functionals, it is found that the strongest intensity peak (bright state) associated with the naphthalene $\pi \rightarrow \pi^*$ transition undergoes a small red shift in naphtha-W_6 cluster with respect to those in isolated naphthalene molecule. It is calculated that in naphtha-W_6 cluster, the strongest intensity transition (bright state) of the naphthalene shows a blue-shift of around 4-5 nm for wB97XD optimized geometries with respect to those in MP2 optimized geometries, and hold for both prism and cage conformers.

5.4 Conclusions

We have performed both DFT-wB97XD and MP2 calculations to obtain optimized ground state geometries of naphthalene, water hexamer W_6 and naphthalene bound W_6 clusters. We show that naphthalene binds more strongly to the prism conformer of the water hexamer cluster than the cage conformer as binding energies are calculated higher for the prism conformer than the cage conformer. In both naphthalene-bound prism and cage shaped W6 clusters, O-H$\cdots\pi$ type hydrogen bonding interactions are found to dominate and provide stability in these clusters, while some contribution from C-H$\cdots$O type hydrogen bonding interactions are also present in the cage conformer.

Further we have generated vertical excited states by performing linear response time-dependent DFT calculations on both MP2 and wB97XD optimized geometries of naphthalene, water hexamer W_6 and naphthalene-bound W_6 clusters. UV spectral characteristics are noticeably different for both cage and prism conformers of W_6 and naphtha-W_6 clusters. It is found that TD-DFT results obtained using CAM-B3LYP and M06-2X functionals are in good agreement. The $\pi \rightarrow \pi^*$ electronic transitions of naphthalene show a small red-shift in naphtha-W_6 cluster (for both cage and prism conformers) with respect to those in isolated naphthalene. The intensities of the $\pi \rightarrow$

π^* naphthalene excitations are found to be lower in naphtha-W_6 cluster relative to those in isolated naphthalene due to the presence of water cluster around it.

We have shown some interesting features of naphthalene-mediated water cluster excitations at wavelengths above 170 nm in both naphthalene-bound W_6 cage and prism water clusters which are not seen in isolated water W_6 clusters, indicating the effect of naphthalene on water excitations. Our results are in good agreement with the recent experimental [70-72] and computational studies [36], where it was shown that benzene as a prototypical PAH molecule can act as a mediator to excite water molecules and shift water excitations to lower energy, where the photon-absorption cross-section for water is negligible at such wavelengths. A similar effect is noticed in naphthalene-bound water hexamer clusters, and is more pronounced than benzene-bound water clusters. Our results also predict new naphthalene charge transfer (CT) states and locally excited diffuse states which also influence water excitations in such naphthalene-bound water complexes.

Chapter 6 - Computational study of the interactions between benzene and crystalline ice I_h: Ground and excited states

6.1 Introduction

Polycyclic aromatic hydrocarbons (PAHs) are considered to be one of the most important classes of carbon-bearing molecules [276]. They may account for up to 20 % of the carbon in our galaxy, and are now widely accepted as being ubiquitously present in many astrophysical environments [251, 277-279]. They have also been proposed as possible carriers of both the diffuse interstellar bands (DIBs) [280] and the unidentified infrared bands (UIRs) observed in a wide range of environments. Moreover, PAHs are likely to exist as either a component of water-rich icy mantles that are accreted on dust grains under cold conditions ($T \leq 20$ K) or as a part of the carbonaceous component of the dust grain itself [25, 251]. Infrared (IR) observations on icy mantles have revealed H_2O as the most abundant molecule, along with some other species such as CO, CO_2, and CH_3OH.[251] Several experiments have been performed to obtain IR absorption spectra of PAH/H_2O ice mixtures [281-283].

Chemical evolution of bulk ices during irradiation by UV light has been extensively studied [57, 58]. The photochemistry of H_2O ices containing PAHs upon irradiation by UV light has been studied experimentally using IR spectroscopy and mass spectrometry [58]. It has been observed that UV irradiation of water ice containing PAHs may play an important role in the formation of complex organic species such as alcohols, quinones and ethers including substituted PAH species [58]. Photon-stimulated desorption is an important process to account for the high gas phase abundances of water under astrophysically relevant conditions [23, 256]. Recently there has also been increased interest in the UV processing of laboratory models of interstellar ices [68-72].

Benzene (Bz) has been detected in the proto-planetary nebula CRL 618,[33] and is chosen as a representative of complex PAH molecules within ice mantles, while crystalline water ice (I_h) structures are chosen to model water-dominated interstellar icy mantles. Under ambient conditions, hexagonal crystal ice is the dominant solid form of H_2O. Experimental and computational studies have been performed to understand the effect of temperature on the crystalline ice surfaces that leads to the proton ordering-

disordering at the surface, which also affects the interactions between ice crystal surface and different adsorbates [284-286]. Computational studies by Buch *et al.* on the patterns of dangling H (*d*-H) and dangling O (*d*-O) atoms at the basal ice surface have shown a thermodynamic preference for the "striped phase", composed of ordered striped domains, with alternating rows of *d*-H and *d*-O atoms [286]. This finding is consistent with the Fletcher's striped phase at low temperatures [284] and experimental *ppp*-polarized sum frequency generation spectra [287, 288]. Computational studies by Pan *et al.* have shown that the energetics of proton ordering differ significantly at the surface compared to that in bulk due to more proton ordering at the surface than in the bulk, and the ice I_h surface will not become proton disordered at any temperature [285].

Numerous theoretical and experimental studies have been performed on the ground state properties such as geometries, binding energies, and infrared (IR) spectra of water W_n clusters [230-240] and Bz-W_n clusters [65, 245, 260, 263], with a detailed description of the non-covalent interactions, such as hydrogen bonding interactions prevailing in such complex systems [65, 235, 240, 245, 259, 260, 263]. Zwier and their co-workers have carried out extensive experimental studies on the Bz-W_n clusters and IR data have been presented [65-67]. Experimental studies on the interactions between Bz and amorphous ice surfaces have shown that the Bz interacts with the ice surface as proton acceptor and a strong down-shift of the dangling-H band in the IR spectra of the ice is noticed [289]. IR spectra characteristics of the ice-benzene system depend on the shape and position of the dangling-H band, which in turn depends on temperature.

The interaction of Bz with amorphous solid water adsorbed on polycrystalline Ag has been studied experimentally [290]. Detailed computational studies of Bz-W_n (n = 1-10) clusters using DFT method have shown the presence of nonconventional H-bonding interactions such as O-H$\cdots\pi$ interactions in all these clusters with additional contributions from C-H$\cdots$O and lone pair (lp)$\cdots\pi$ interactions, which lead to the overall stability of these clusters [245]. The computational investigations on the structures and bonding in water W_n(n=1-8)-Bz_n,(n=1-2) complexes using an effective fragment potential (EFP) method have predicted a dominant nature of H-bonding interactions i.e. O-H$\cdots\pi$ and C-H$\cdots$O interactions in all of the larger water-benzene complexes and benzene is shown to act both as an H-bond donor and acceptor in the water-benzene complexes [263]. The benzene-water interactions are found to be slightly weaker than the water-water interactions and the very small energy differences between different isomers are involved in the formation of such complexes [263].

The excited state properties of the systems discussed above have received very little attention [75, 273]. Recent computational studies on the UV spectroscopy of the cage and the prism conformers of the water hexamer (W_6), and the benzene-bound water hexamer (Bz-W_6) clusters have shown a small red shift in the main $\pi \rightarrow \pi^*$ electronic transition of benzene after interacting with the W_6 cluster [273]. It was noticed that benzene influences the water excitations by shifting it towards longer wavelengths in both the cage and the prism geometries of Bz–W_6 clusters. Furthermore, in these cluster models new charge transfer (CT) states are observed to occur. Experimental studies on photo processing of model interstellar ices have revealed three distinct photo-desorption mechanisms in such systems viz. (i) Direct adsorbate-mediated desorption of benzene (ii) Indirect adsorbate–mediated desorption of water (iii) Substrate-mediated desorption of both benzene and water [72]. The translational temperature of both desorbed species i.e. the benzene and the water molecules, is found to be higher than the ambient temperature of the complex system. It has been observed experimentally that photon absorption by benzene can make H_2O desorption possible at wavelengths where photon-absorption cross-section for H_2O is negligible [70]. A recent experimental study on the photodesorption of benzene from H_2O ice has shown a strong dependence of desorption of both Bz and water on the morphology of the ice [71].

In the experiments described above, the photon-simulated desorption of water from Bz-ice films have been studied at a specific wavelength around 250 nm to represent the interstellar radiation field (ISRF), that corresponds to diffuse regions of molecular clouds in the interstellar medium. However, a computational study of such interstellar ice models can provide deep insight into detailed spectroscopic transitions involved in these processes, and inform about new excited states available to the adsorbed benzene. It is evident that a more detailed understanding of the interactions between benzene and the underlying ice surfaces is required. There have been many experimental studies of the adsorption of benzene on both single and polycrystalline metal surfaces [291-293]. To the best of our knowledge, there have been no computational studies in the literature discussing the effects of dangling features of the ice surface on Bz adsorption and UV spectra of Bz-ice complexes.

Detailed studies on the ground and excited states of the complexes of Bz with crystalline ice are very important due to its astrophysical relevance. The purpose of the work presented in this chapter is two-fold. Firstly, we investigate the role of the

dangling atoms on Bz adsorption on crystalline water ice. Secondly, we investigate the UV spectroscopy and photochemistry of Bz-ice clusters.

6.2 Computational Details

6.2.1 Computational Model

ICE MODELS

We have considered two QM/MM crystalline ice I_h models A and B (Figure 6.1). In model A, three water layers are included with a total of 162 H_2O molecules, while model B consists of 156 H_2O molecules. In model A, the QM region consists of 12 H_2O molecules, and the remaining 150 H_2O molecules are in the MM region. In the case of model B, we have included 8 H_2O molecules in the QM region and 148 H_2O molecules are in the MM region. Depending on the number of *d*-H and *d*-O atoms present in the top layer of the QM region, a total of eight binding sites are possible (four binding sites from model A and another four from B). Moreover, four binding sites for models A and B have different dangling features; A1 and B1 (two *d*-H and and one *d*-O), A2 and B2 (one *d*-H and two *d*-O), A3 and B3 (three *d*-O), A4 and B4 (three *d*-H). The Bz molecule is then brought closer to each of these bindings sites to obtain the Bz-Ice system, where the Bz molecule is included in the QM region.

6.2.2 Computational Methods

The ONIOM (our own n-layered integrated molecular orbital and molecular mechanics) method [168, 171-173] is one of the most popular hybrid methods. In common practice, ONIOM can be applied to relatively large molecular systems. It produces results of good accuracy and also at limited computational cost. In a two-layer ONIOM calculation, the total ONIOM(QM:MM) energy of a real system is obtained as

$$E_{ONIOM(QM:MM)}(real) = E_{QM}(model) + E_{MM}(real) - E_{MM}(model) \quad (6.1)$$

where the model system is treated at the both QM and the MM level, while the real system is treated at the MM level only. Applications of ONIOM(QM:MM) are very well known and details are provided in the literature [175, 177, 294, 295]. However, the

ONIOM(QM:MM) method has not gained much attention in the field of astrochemistry. This is due to the fact that the commonly used ONIOM(QM:MM) implementations have limited access to the force fields that are suitable for modelling ices. In this direction, the ONIOM(QM:MM) implementation in the Shell interface for combining ONIOM with the Tinker (SICTWO) program is very useful [296] (W. M. C. Sameera, and F. Masersa (Submitted work)). SICTWO performs QM calculations with Gaussian09 and MM calculations with the Tinker [297, 298] program. This implementation supports suitable force fields for modelling ices, such as the AMOEBA (atomic multipole optimized energetics for bimolecular simulation) polarizable model. The AMOEBA polarizable force field has been explained in detail in the literature [143, 144, 146, 147, 299]. Successful applications of the AMOEBA force field to study a wide range of properties of gas-phase clusters, liquid water, and ice crystals have been given in several publications [144-146].

In the present work, the geometries of all ice models were optimized with the ONIOM(M06-2X:AMOEBA09) method as implemented in the SICTWO program. We have used a mechanical embedding scheme in our ONIOM calculations. The 6-31++G** basis set [100, 102, 103, 300] was used in the QM calculations. Final energies of the optimized structures were obtained by performing single-point energy calculations with ONIOM(LPNO-CCSD:AMOEBA09). The Dunning correlation-consistent cc-pVTZ and cc-pVTZ/C combination basis set was used for the QM calculations. The default cutoff parameters were employed in LPNO-CCSD calculations as implemented in the ORCA2.9 program [301].

Starting from the ONIOM(M06-2X:AMOEBA09) optimized structures, several model structures were generated, and performed TD-DFT [184-187] calculations with the M06-2X functional. Excellent performance of the M06-2X functional for the systems involving non-covalent interactions [302, 303], and also electronic excitation energies to valence and Rydberg states have been established previously [128, 129].

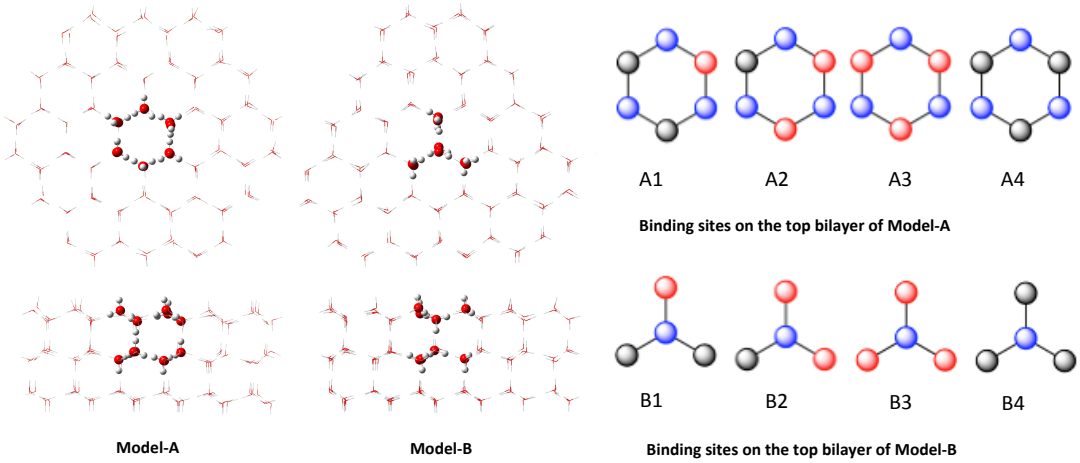

Figure 6.1 QM/MM structures of model A and B (Top and side view in the left side). Illustration of the dangling features at the binding sites in the right side. Dangling-hydrogen (*d*-H) and dangling-oxygen (*d*-O) are shown in black circles and red circles, respectively. O atoms in the bilayer immediately below are shown in blue circles.

6.3 Results and Discussion

6.3.1 Ground state Geometries and Energetics

The ground state geometries of all eight ice models and their respective Bz-ice complexes were fully optimized using the ONIOM(M06-2X:AMOEBA09) approach. More than 30 different fully optimized Bz-ice complexes were found. Of these, we have selected the most stable Bz-ice complexes from model A i.e. A1, A2, A3, and A4 binding sites (See Figure 6.2). Similarly most stable sites from B model i.e. B1, B2, B3, B4 are presented in Figure 6.3. Their key structural parameters are shown in Figure 6.4, and calculated binding energies are summarized in Table 6.1.

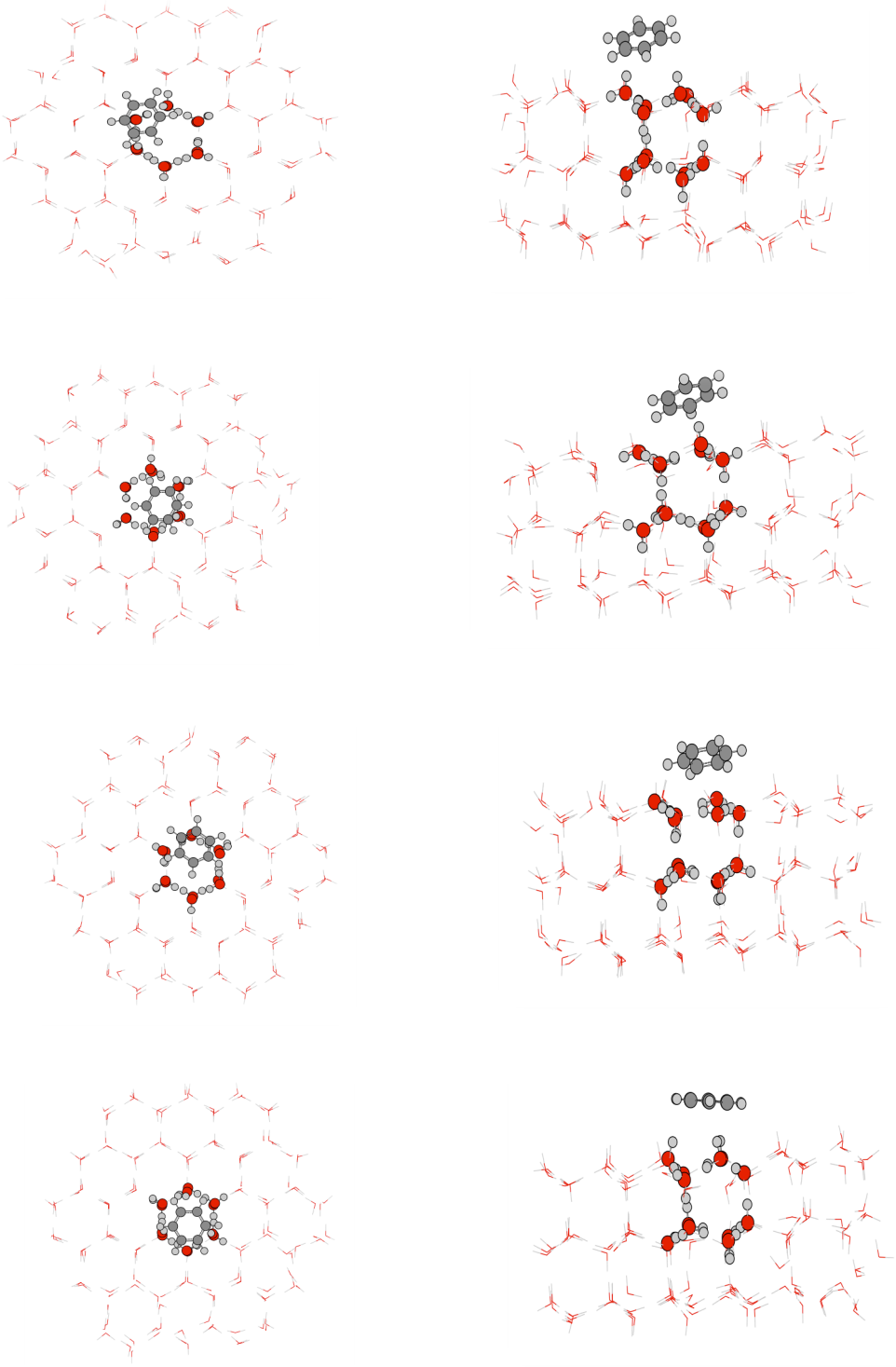

Figure 6.2 Top view (in the left) and the side view (in the right) of ONIOM(M06-2X:AMOEBA) optimized Bz-ice complexes for all four binding sites of model A i.e. A1, A2, A3, A4. QM region is shown in 'ball and stick ' and MM region in 'wireframe'.

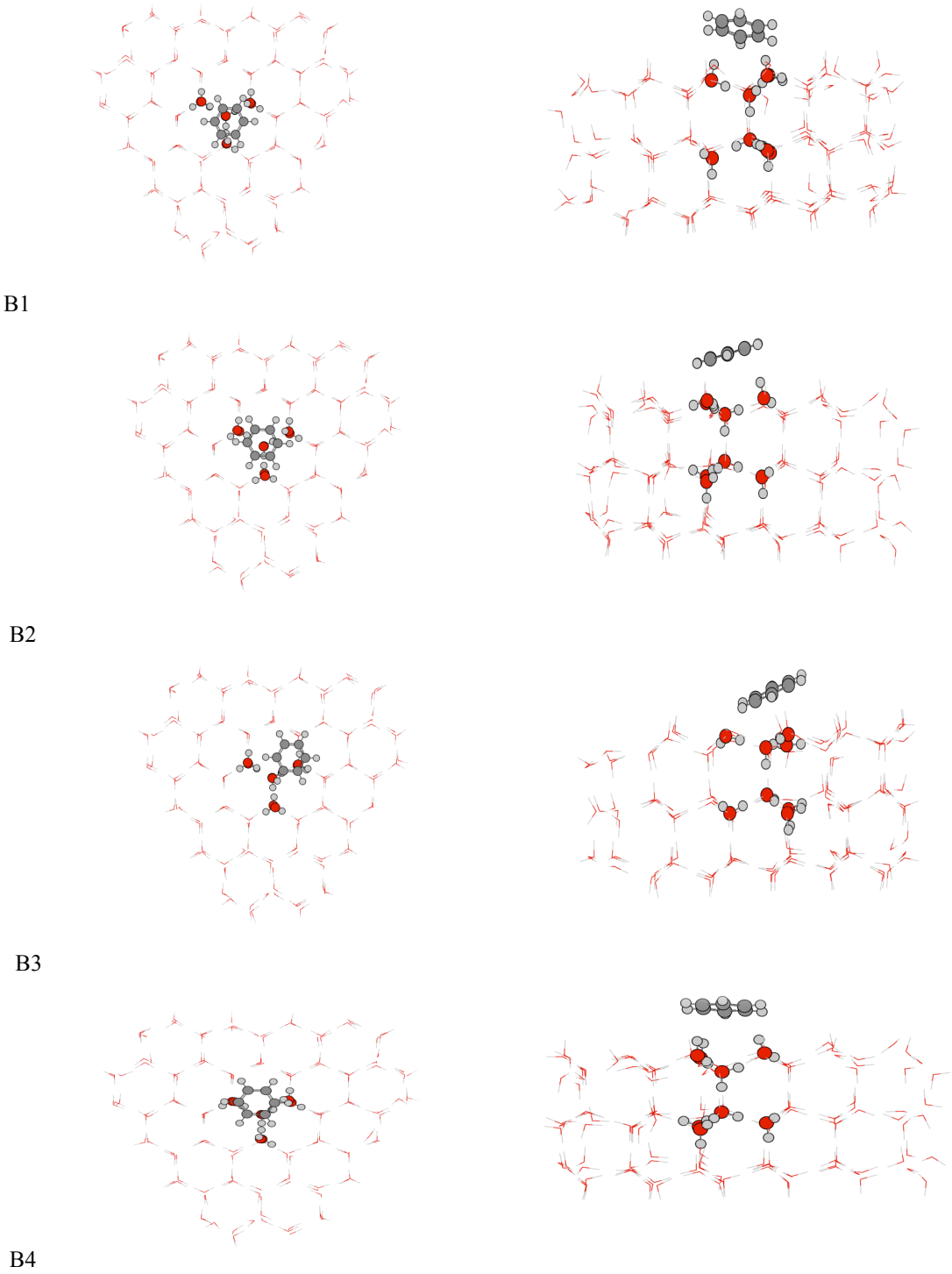

Figure 6.3 Top view (in the left) and the side view (in the right) of ONIOM(M06-2X:AMOEBA) optimized Bz-ice complexes for all four binding sites of model B i.e. B1, B2, B3, B4. QM region is shown in 'ball and stick ' and MM region in 'wireframe'.

Binding energies (BE) of the Bz-ice complexes were calculated using the following formula:

$$|\mathrm{BE}| = \mathrm{E_{Bz-ice}} - (\mathrm{E_{ice}} + \mathrm{E_{Bz}}) \quad (6.2)$$

where E_{Bz-ice}, E_{ice}, and E_{Bz} denote the total energy of the Bz-ice system, crystalline ice I_h and benzene, respectively.

According to our survey, the largest binding energies were observed for binding sites A1 (0.45 eV) and B1 (0.44 eV). The ONIOM(LPNO-CCSD:AMOEBA09) binding energies are consistent with those of the ONIOM(M06-2X:AMOEBA09) (See Figure. 6.5). Calculated binding energies of the Bz bound ice models range from 0.31 to 0.45 eV for all binding sites of model A, indicating that the dangling features have an effect on the binding preference. Binding of benzene is favoured at the A1 site, where the π electron cloud of the benzene interacts with the two *d*-H of the ice surface, which leads to two π···HO type hydrogen bonding interactions. There are two additional C-H···OH hydrogen bonding interactions present in this case, providing more stability thereby giving the highest binding energy for the A1 site. Two hydrogens of the benzene interact with two non-dangling oxygen atoms (See Figure 6.4). These oxygens are bonded to the dangling hydrogens of the ice surface. In the case of the A2 site, the binding energy is marginally different. Here two hydrogen atoms of benzene interacts with the two *d*-O of the surface and the π electron cloud of the benzene interacts with the *d*-H of the surface. This leads to two C-H···OH and one π···HO type hydrogen bonding interactions. Binding sites A3 has two C-H···OH and a lone pair (*lp*)···π interaction while site A4 has three π···HO hydrogen bonding interactions, giving them comparable binding energies.

We have performed a similar analysis as above for the B sites. The binding energies of these four sites are in the range 0.25–0.44 eV. The binding types are the same as for the A sites and consistent with the results for the A sites, binding site B1 gives the highest binding energy of the B sites. The π···HO and C-H···O type hydrogen bonding interactions dominate these systems, as also seen in previous computational studies [245, 263]. Surprisingly, A4 binding site having three π···HO hydrogen bonds gives lower binding energy, that suggest that the longer bond distances for these interactions as compared to those in A1 binding site may cause weaker binding in this complex.

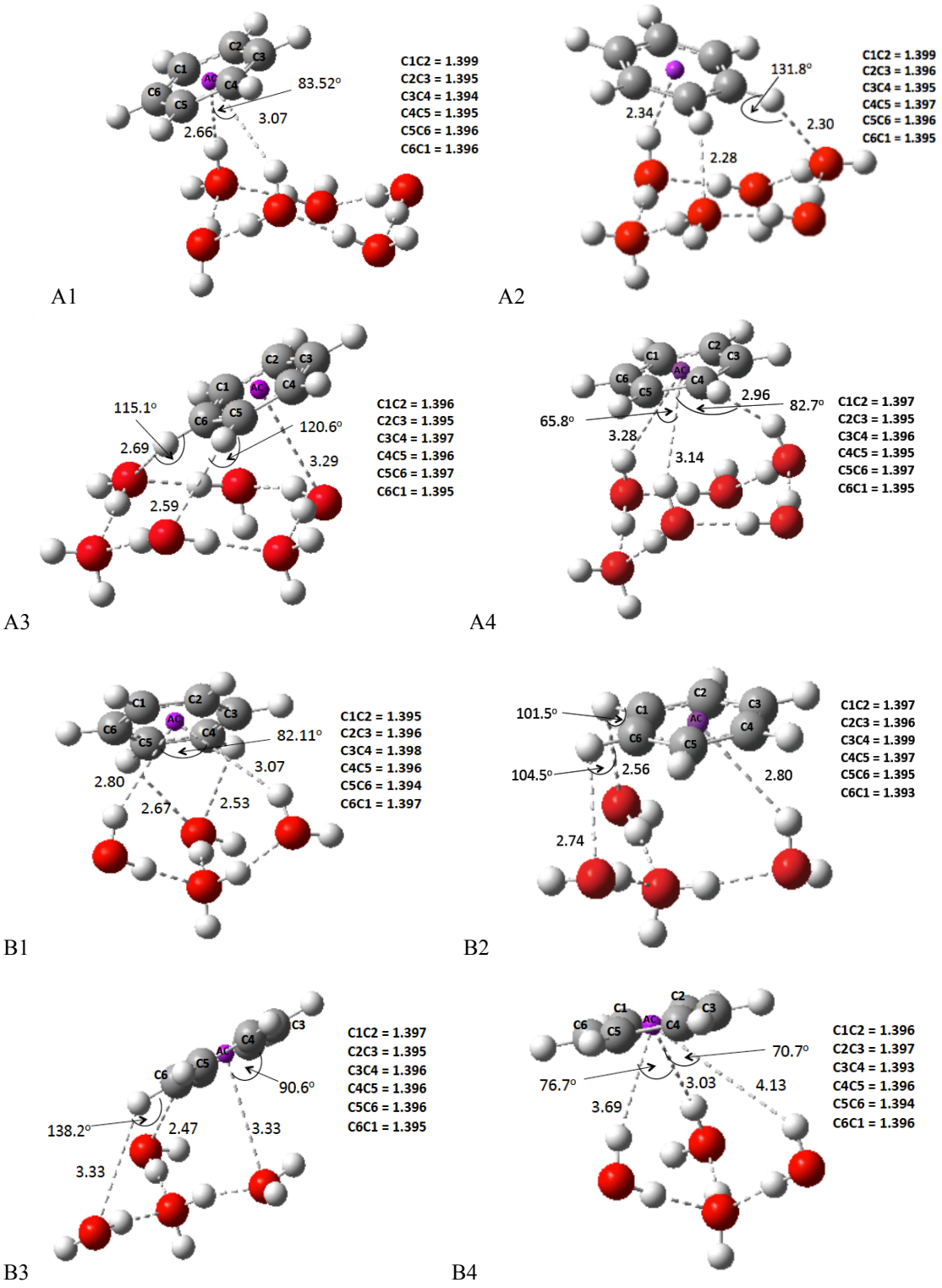

Figure 6.4 ONIOM(M06-2X:AMOEBA) optimized structures of all eight Bz bound binding sites for both ice models A and B. Carbon-Carbon bond lengths in Bz are also given for each binding site. All bond lengths are in Å and the aromatic centre of the benzene ring is labeled as AC.

Table 6.1 Binding energies (BEs) of Bz-ice complexes in units of eV for range of computational calculations.

Model	ONIOM (M06-2X:AMOEBA09)	ONIOM (LPNO-CCSD:AMOEBA09)	M06-2X
A1: 2*d*-H 1*d*-O	0.45	0.45	0.43
A2: 2*d*-O 1*d*-H	0.43	0.40	0.41
A3: 3*d*-O	0.33	0.30	0.37
A4: 3*d*-H	0.31	0.31	0.29
B1: 2*d*-H 1*d*-O	0.44	0.42	0.43
B2: 2*d*-O 1*d*-H	0.37	0.34	0.36
B3: 3*d*-O	0.25	0.25	0.22
B4: 3*d*-H	0.38	0.37	0.34

It is important to note that A1, A2, B1, and B2 binding sites consisting of both *d*-H and *d*-O, have the characteristics of the 'Striped phase' at low temperatures. It has been suggested that an ordered, striped dangling atom pattern is favoured by the ice basal surface as long as the surface remains solid and oxygen-ordered at $T \leq 180$ K [286]. Thus benzene can strongly adsorb to these sites of crystalline ices at low temperatures, which are more relevant to interstellar ice conditions where inside dense molecular clouds, gas species freeze out on the dust grains forming icy grain mantles at very low temperature ($T \leq 20$ K). However, binding sites A3, A4, and B3 with relatively weaker binding energies may exist at higher temperature due to proton ordering effects at higher temperature.

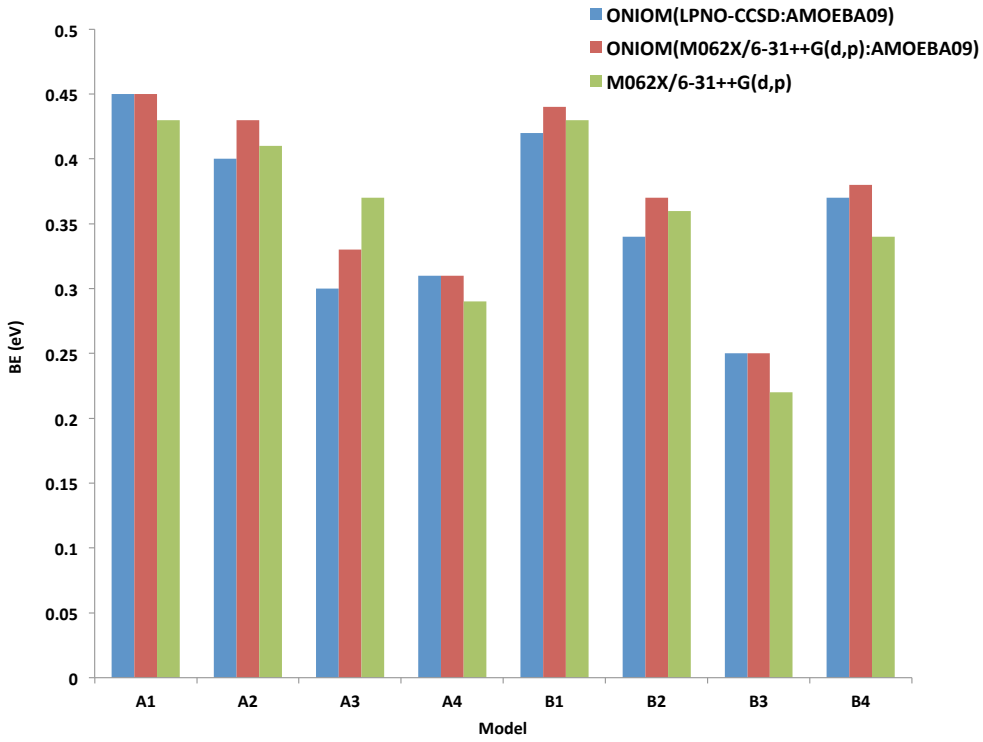

Figure 6.5 Variation of BE's (eV) of Bz-I_h complexes versus different level of theory for all four binding sites of model A i.e. A1, A2, A3, A4 and model B i.e. B1, B2, B3, B4.

In order to check the effect of size of QM region on the benzene binding energies and binding preference, M06-2X single-point calculations were carried out by including all H_2O molecules in the QM region. It is interesting to see that M06-2X binding energies and ONIOM(M06-2X:AMOEBA09) binding energies are in a good agreement (See Table 6.1 and Figure 6.5). Thus, it is evident that ONIOM(QM:AMOEBA09) method performs fairly well on these systems. In order to check whether structure optimization has an effect on the binding energies, we have fully optimized the A1, B1, and their benzene bound systems by increasing the size of QM region (48 H_2O molecules in the QM region and 114 H_2O in the MM region). ONIOM(M06-2X:AMOEBA09) optimized structures are shown in Figure 6.6. Calculated binding energies of both A1 and B1 are 0.40 eV each, and are in good agreement with M06-2X binding energies. Based on these results, we argue that our QM/MM model systems provided a good description for benzene binding on ices.

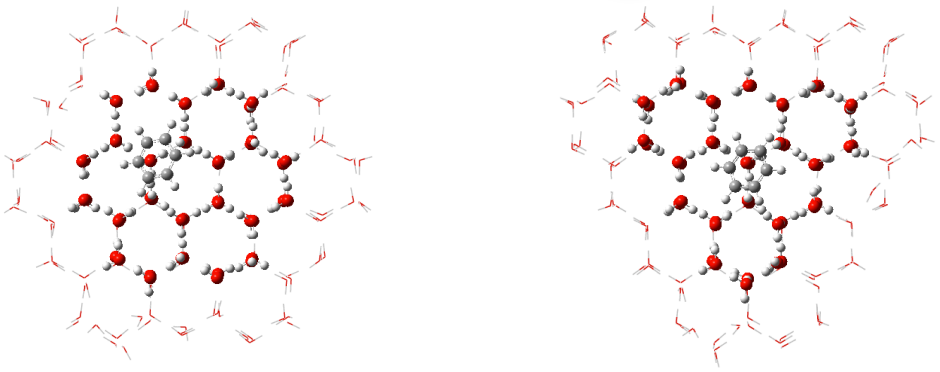

(a) (b)

Figure 6.6 ONIOM(M06-2X:AMOEBA) optimized Bz-ice complexes for (a) A1 binding site and (b) B1 binding site. QM region is shown in 'ball and stick ' and MM region in 'wireframe'.

6.3.2 Electronic excitations in benzene-bound ice cluster models

Ice cluster models of three different size for each binding site are taken into account to study the effect of cluster size on electronic excitations in Bz-ice clusters i.e. A1: Bz-$(H_2O)_{12}$; Bz-$(H_2O)_{48}$; Bz-$(H_2O)_{72}$ for binding site A1 and B1: Bz-$(H_2O)_8$; Bz-$(H_2O)_{32}$; Bz-$(H_2O)_{48}$ for binding site B1 (See Figure 6.7). Similar calculations are also performed on binding sites of cluster models A2, A3, A4, B2, B3 and B4. It is worth mentioning that for all binding sites of both cluster models A and B, all electronic transitions involved are singlet in nature.

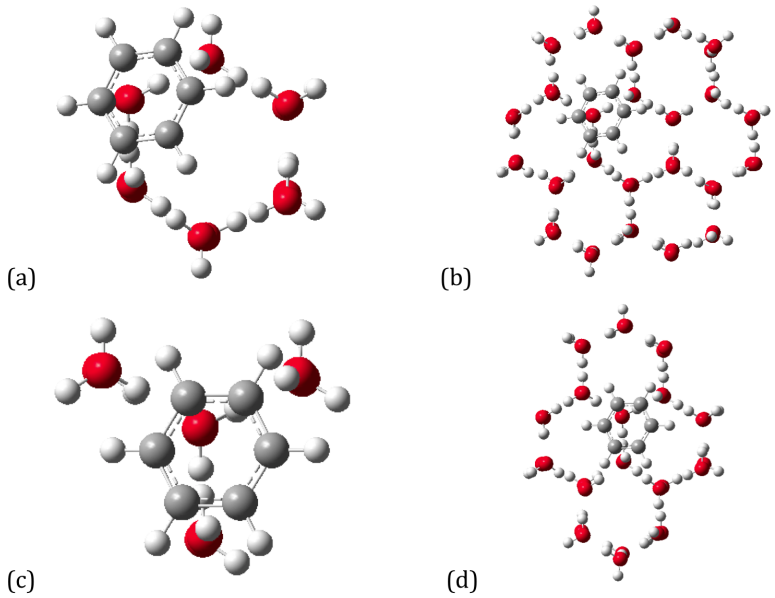

(a) (b)

(c) (d)

Figure 6.7 Structures for binding site A1: (a) Bz-$(H_2O)_{12}$; (b) Bz-$(H_2O)_{48}$,and for binding site B1: (c) Bz-$(H_2O)_8$; (d) Bz-$(H_2O)_{32}$.

ELECTRONIC EXCITATIONS IN MODEL A AND MODEL B

UV spectra results obtained by TD-DFT calculations for binding site A1 and B1 are presented in Figure 6.8 and Figure 6.9, respectively, and also see Figure 6.10 for A2, A3, and A4 binding sites, and Figure 6.11 for B2, B3, and B4 binding sites. It shows different excitation features in Bz-ice clusters with respect to excitation features in ice clusters and the Bz molecule. It has been observed experimentally that the UV spectrum of benzene shows three well-known absorption bands at 4.9, 6.20, and 6.94 eV related to three electronic excitations from the ground state to the excited states with symmetries $^1B_{2U,}$ $^1B_{1U,}$ and $^1E_{1U}$, respectively [37]. The calculated valence $\pi \rightarrow \pi^*$ excitation energies of Bz (experimental values in the parenthesis) are $^1B_{2U}$: 5.59(4.9[37, 38]), $^1B_{1U}$: 6.39(6.20[37],6.19[38]), and $^1E_{1U}$: 7.11(6.94[37],6.96[38]) eV, respectively. Our results compare well with the experiments. $^1B_{1U}$ and $^1E_{1U}$ excited states are computed with an accuracy of about 0.2 eV, while overestimated by about 0.6 eV for the $^1B_{2U}$ state. It is important to note that lowest valence transitions of Bz from ground to excited states 1^1B_{2U} and 1^1B_{1U} are strictly dipole forbidden on symmetry grounds. The Bz excitation feature at around 174 nm (or 7.11 eV) is of very high intensity, and corresponds to dipole allowed electronic transition from ground to 1^1E_{1U} excited state.

For Bz-ice complexes, most of the high intensity electronic transitions are dominant around 174-181 nm regions. In case of ice clusters, electronic excitations are dominant only in shorter wavelength region (i.e. below 174 nm). UV spectra are shown to be slightly dependent on the nature of the binding site i.e. small deviations in peak positions and peak intensities are noticed. For A1 binding site (See Figure 6.8), it is noticed that intensity of excitation peaks in Bz-ice clusters slightly increase with increase in size of the ice cluster i.e. as we move from Bz-$(H_2O)_{12}$ to Bz-$(H_2O)_{72}$, and it is more noticeable in binding sites A2 and A4 as compared to A1 and A3 binding sites. The position of strong intensity peaks shift by 1-2 nm shift with increase in cluster size. For binding sites A2 and A4, strong intensity peaks are centred around 177-178 nm with unnoticeable shift in peak positions with increase in cluster size, while for binding site A1, small red-shift in peak positions are noticed as the cluster size increase from Bz-$(H_2O)_{12}$ to Bz-$(H_2O)_{72}$ and excitations are seen at around 174-179 nm region. In the A3 binding site, strong intensity peaks are found over the spectral range 178-181 nm and are slightly red-shifted in Bz-(H_2O) cluster with respect to peak positions in Bz-

$(H_2O)_{48}$ and Bz-$(H_2O)_{72}$ clusters. Thus, it is seen that dangling features of the binding site play a minor role on the UV spectral characteristics.

Similar UV spectral characteristics are noticed for cluster model B, and results also show a slight dependence on the size and dangling feature of the binding site of ice cluster in Bz-ice complexes (See Figure 6.9). It is seen that intensities of electronic transitions in Bz-$(H_2O)_{32}$ and Bz-$(H_2O)_{48}$ clusters are slightly stronger than in Bz-$(H_2O)_8$ cluster. However, in all binding sites of B, very small shift in peak positions and their intensities are seen as we move from Bz-$(H_2O)_{32}$ to Bz-$(H_2O)_{48}$, indicating that increasing the size of ice cluster does not substantially affect the intensities and positions of electronic transitions, and holds for all binding sites.

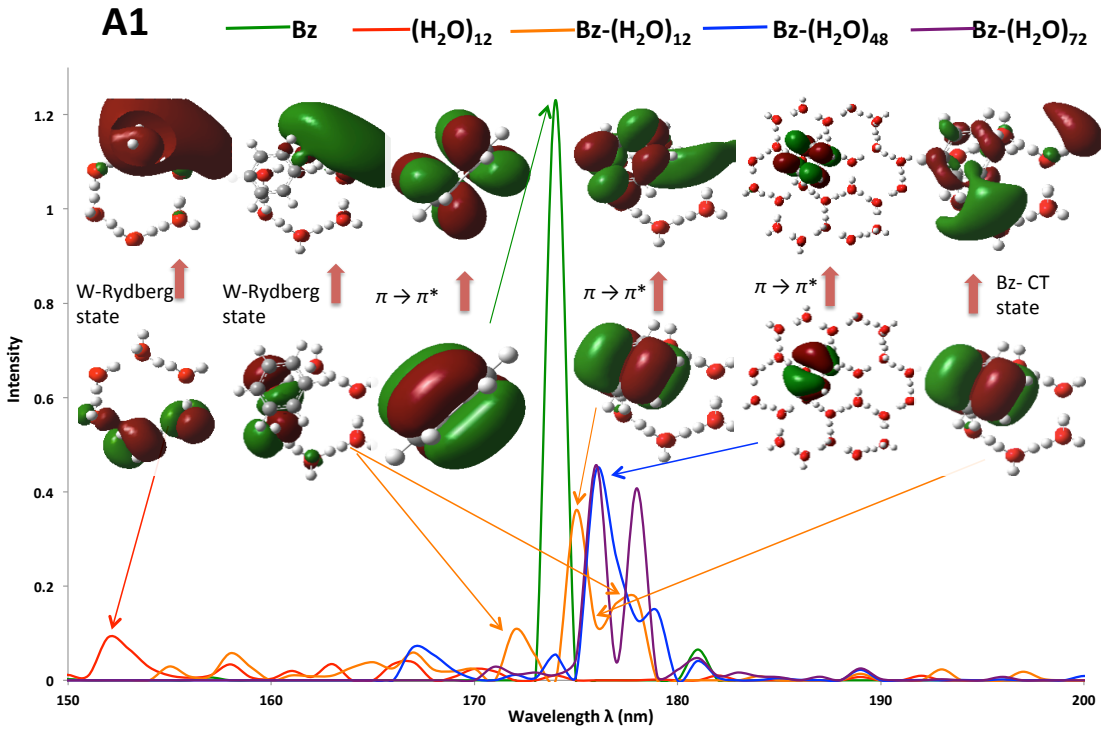

Figure 6.8 Simulated UV spectra obtained by TD-DFT calculations using M06-2X hybrid functional and 6-31++G(d,p) basis set on Bz molecule and on ONIOM optimized ground state geometries of cluster model A1. Some key orbitals involved in important electronic transitions are also presented.

The nature of these peak transitions are also investigated in Bz-ice clusters to understand the role of Bz and water (W) in generating these strong excitation peaks. Since binding energy of Bz bound ice cluster is found to be highest for A1 and B1 binding sites, as discussed above, we have performed detailed analysis on A1 and B1 binding sites to check the orbital transformations for those excitations that are

associated with high oscillator strengths *f* or strong intensity peaks in UV spectra (See Figure 6.8 & Table 6.2 for A1 binding site and Figure 6.9 & Table 6.3 for B1 binding site). However, some of the important electronic transitions found in Bz-$(H_2O)_{12}$ complexes for cluster models A2, A3, and A4 and Bz-$(H_2O)_8$ complexes for cluster models B2, B3, and B4 are also given in Table 6.4.

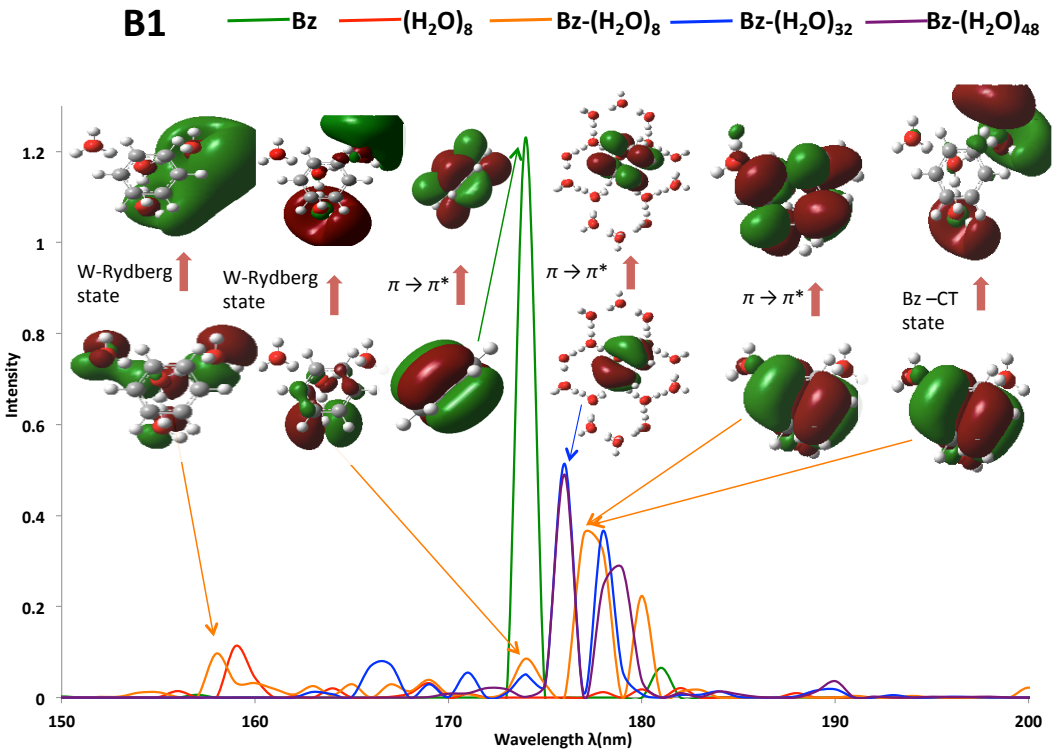

Figure 6.9 Simulated UV spectra obtained by TD-DFT calculations using M06-2X hybrid functional and 6-31++G(d,p) basis set on Bz molecule and on ONIOM optimized ground state geometries of cluster model B1. Some key orbitals involved in important electronic transitions are also present.

In UV spectra of both A1: Bz-$(H_2O)_{12}$ and B1: Bz-$(H_2O)_8$ clusters, the low lying vertical $\pi \rightarrow \pi^*$ excited states show a small red shift of about 2-3 nm in excitation wavelengths, and oscillator strengths become slightly allowed as compared to dipole forbidden 1^1B_{2U} and 1^1B_{1U} excited states in Bz i.e. $(\mathrm{Bz}\,(\mathrm{f}=0.000) \rightarrow \mathrm{A1{:}\,Bz}-(H_2O)_{12}(\mathrm{f}=0.004-0.018), \mathrm{B1{:}\,Bz}-(H_2O)_8(\mathrm{f}=0.001-0.005)$, indicating slight allowed character in restricted lowest energy $\pi \rightarrow \pi^*$ electronic transitions due to the presence of water ice around Bz. Similar spectral characteristics are noticed as we increase the size of the ice cluster, and low lying vertical $\pi \rightarrow \pi^*$ excitations become allowed with nearly same oscillator strengths for both A1 and B1 binding site. i.e.

$(\mathrm{Bz}\ (\mathrm{f} = 0.000) \rightarrow \mathrm{A1}: \mathrm{Bz} - (\mathrm{H_2O})_{72} (\mathrm{f} = 0.002 - 0.005), \mathrm{B1}: \mathrm{Bz} - (\mathrm{H_2O})_{32} (\mathrm{f} = 0.002 - 0.005)$.

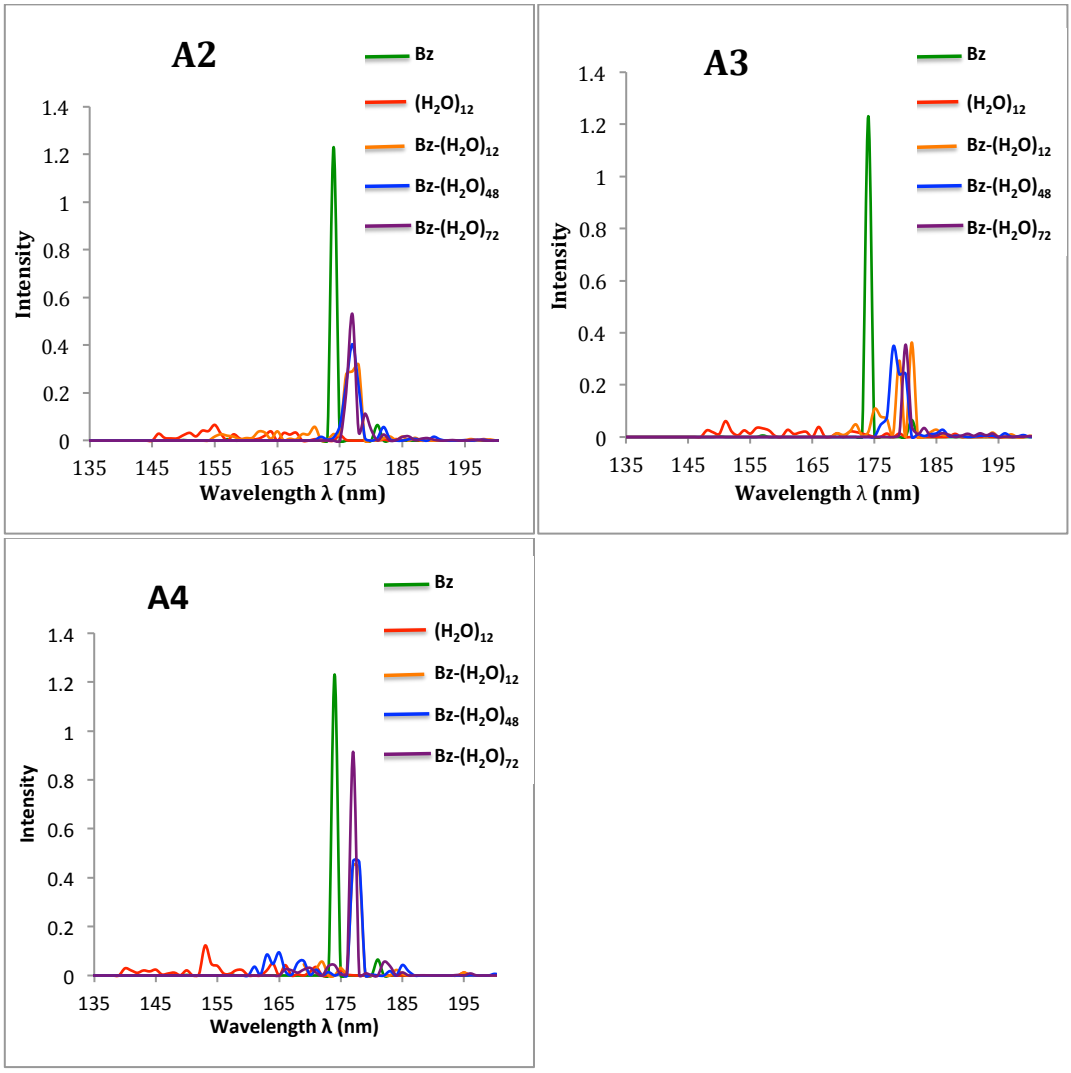

Figure 6.10 Simulated UV spectra obtained by TD-DFT calculations using M06-2X hybrid functional and 6-31++G(d,p) basis set on Bz molecule and on ONIOM optimized ground state geometries of cluster models A2, A3 and A4. Some key orbitals involved in important electronic transitions are also presented.

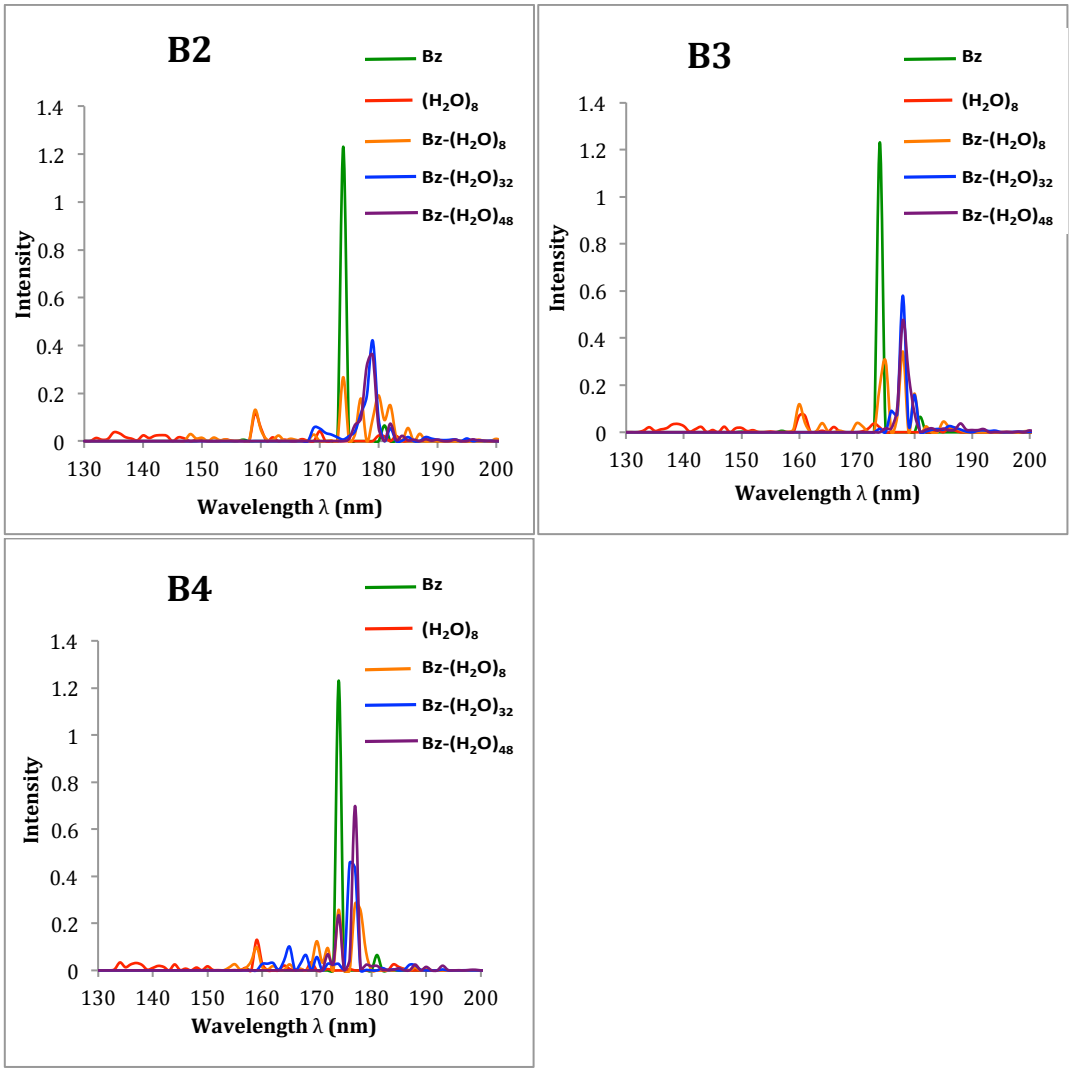

Figure 6.11 Simulated UV spectra obtained by TD-DFT calculations using M06-2X hybrid functional and 6-31++G(d,p) basis set on Bz molecule and on ONIOM optimized ground state geometries of cluster models B2, B3, and B4. Some key orbitals involved in important electronic transitions are also presented.

Table 6.2 List of lowest energy $\pi \rightarrow \pi^*$ singlet electronic transitions and important electronic transitions corresponding to highest peak intensities (or oscillator strengths) obtained by TD-DFT calculations on ONIOM optimized ground state geometries of Bz-ice complexes for cluster models A1: Bz-$(H_2O)_{12}$; Bz-$(H_2O)_{48}$ and Bz-$(H_2O)_{72}$ (Values in parenthesis correspond to singlet $\pi \rightarrow \pi^*$ transition of an isolated benzene molecule).

Model	E (eV)	λ(nm)	Oscillator strength *(f)*	Electronic Transition
A1: Bz-$(H_2O)_{12}$	5.54	223.9	0.0038	$\pi \rightarrow \pi^*$
	(5.59, 4.9[a,b])	(222.0)	(0.0000)	
	6.28	197.4	0.0182	$\pi \rightarrow \pi^*$
	6.39, 6.20[a,c], 6.19[b])	(194.1)	(0.0000)	
	7.07	175.4	0.3606	$\pi \rightarrow \pi^*$
	(7.11, 6.94[a], 6.96[b])	(174.3)	(0.6158,1.25[d])	
	6.97	177.9	0.1732	$\pi \rightarrow \pi^*$
	6.99	177.2	0.1415	W-Rydberg state
	7.03	176.4	0.1161	Bz CT state
	7.20	172.3	0.0692	W-Rydberg state
	7.43	166.8	0.0465	W-Rydberg state
A1: Bz-$(H_2O)_{48}$	5.53	224.4	0.0046	$\pi \rightarrow \pi^*$
	6.32	196.3	0.0019	$\pi \rightarrow \pi^*$
	7.05	175.9	0.2550	$\pi \rightarrow \pi^*$
	7.05	175.9	0.1610	W-Rydberg state
	6.99	177.2	0.2068	$\pi \rightarrow \pi^*$
	6.93	178.8	0.1471	Bz CT state
	6.95	178.3	0.1191	Bz CT state
	6.83	181.5	0.0281	$\pi \rightarrow \pi^*$
	7.44	166.7	0.0210	W-Rydberg state
	7.44	166.6	0.0172	$\pi \rightarrow \pi^*$
A1: Bz-$(H_2O)_{72}$	5.52	224.4	0.0051	$\pi \rightarrow \pi^*$
	6.31	196.4	0.0023	$\pi \rightarrow \pi^*$
	7.04	176.1	0.4515	$\pi \rightarrow \pi^*$
	6.97	177.9	0.3945	$\pi \rightarrow \pi^*$
	6.87	180.5	0.0449	Bz CT state
	6.89	180.1	0.0223	Bz CT state

[a]Exptl/Taken from Ref. [37]
[b]Exptl/Taken from Ref. [38]
[c]Exptl/Taken from Ref. [270]
[d]Exptl/Taken from Ref. [271]

Table 6.3 List of lowest energy $\pi \rightarrow \pi^*$ singlet electronic transitions and important electronic transitions corresponding to highest peak intensities (or oscillator strengths) obtained by TD-DFT calculations on ONIOM optimized ground state geometries of Bz-ice complexes for cluster models B1: Bz-$(H_2O)_8$ and Bz-$(H_2O)_{32}$ (Values in parenthesis correspond to singlet $\pi \rightarrow \pi^*$ transition of an isolated benzene molecule).

Model	E (eV)	λ(nm)	Oscillator strength *(f)*	Electronic Transition
B1: Bz-$(H_2O)_8$	5.51	224.9	0.0047	$\pi \rightarrow \pi^*$
	(5.59, 4.9[a,b])	(222.0)	(0.0000)	
	6.33	196.0	0.0005	$\pi \rightarrow \pi^*$
	(6.39,6.20[a,c],6.19[b])	(194.1)	(0.0000)	
	6.98	177.5	0.3203	$\pi \rightarrow \pi^*$
	(7.11, 6.94[a],6.96[b])	(174.3)	(0.6158, 1.25[d])	
	7.00	177.1	0.2350	$\pi \rightarrow \pi^*$
	6.87	180.4	0.2234	$\pi \rightarrow \pi^*$
	7.83	158.4	0.0965	W-Rydberg state
	7.14	173.6	0.0855	W CT state
	7.02	176.6	0.1232	Bz CT state
B1: Bz-$(H_2O)_{32}$	5.52	224.5	0.0053	$\pi \rightarrow \pi^*$
	6.32	196.2	0.0018	$\pi \rightarrow \pi^*$
	6.96	178.0	0.3665	$\pi \rightarrow \pi^*$
	7.04	176.3	0.3538	$\pi \rightarrow \pi^*$
	7.03	176.5	0.0656	BZ CT state
	7.04	176.2	0.0579	W-Rydberg state
	7.47	166.0	0.0420	W-CT state
	7.14	173.7	0.0459	Bz CT state
	6.92	179.3	0.0580	Bz CT state

[a]Exptl/Taken from Ref. [37]
[b]Exptl/Taken from Ref. [38]
[c]Exptl/Taken from Ref. [270]
[d]Exptl/Taken from Ref. [271]

In A1: Bz-$(H_2O)_{12}$ cluster, it is found that the strongest peak at around 175 nm is due to the $\pi \rightarrow \pi^*$ electronic transition of benzene i.e. from π bonding orbital to π^* anti-bonding orbital of benzene. The strong intensity $\pi \rightarrow \pi^*$ electronic transitions (bright states) with high oscillator strengths are small red-shifted towards longer wavelengths with respect to corresponding dipole allowed degenerate $^1E_{1U}$ excited states of isolated Bz. The magnitude of red-shifts are about 1-3 nm in A1:Bz-$(H_2O)_{12}$, while B1: Bz-$(H_2O)_8$ cluster give red-shifts of about 3 nm. The degeneracies of these states are broken by about 3 nm in A1:Bz-$(H_2O)_{12}$ while they are broken slightly lesser in B1:Bz-$(H_2O)_8$ cluster by about 1 nm. The oscillator strengths of these bright $\pi \rightarrow \pi^*$ electronic states are lower in Bz-ice clusters as compared to isolated Bz, illustrating the effect of

water cluster around Bz. Thus it is realized that the spectroscopy of benzene is influenced due to the presence of water cluster as the $\pi \rightarrow \pi^*$ electronic transition of benzene in Bz-ice clusters is small red-shifted as compared to isolated Bz, and also hold for all binding sites of cluster model A and B.

Table 6.4 List of important electronic transitions (bright states) obtained by TD-DFT calculations on optimized ground state geometries of Bz-ice complexes for cluster models A2, A3, A4, B2, B3 and B4.

Model	**E (eV)**	**λ(nm)**	**Oscillator strength *(f)***	**Electronic Transition**
A2:	7.01	176.9	0.2899	$\pi \rightarrow \pi^*$
Bz-$(H_2O)_{12}$	7.06	175.6	0.2768	$\pi \rightarrow \pi^*$
	6.97	178.0	0.2069	$\pi \rightarrow \pi^*$
	6.95	178.3	0.1102	Bz CT state
A3:	6.87	180.5	0.3628	$\pi \rightarrow \pi^*$
Bz-$(H_2O)_{12}$	6.91	179.5	0.2933	$\pi \rightarrow \pi^*$
	7.11	174.5	0.0909	Bz CT state
A4:	7.00	177.0	0.4495	$\pi \rightarrow \pi^*$
Bz-$(H_2O)_{12}$	6.97	177.8	0.4351	$\pi \rightarrow \pi^*$
	7.20	172.3	0.0566	$\pi \rightarrow \pi^*$
B2:	7.01	176.9	0.1781	$\pi \rightarrow \pi^*$
Bz-$(H_2O)_8$	6.83	181.6	0.1500	$\pi \rightarrow \pi^*$
	7.13	173.9	0.1454	$\pi \rightarrow \pi^*$
	7.11	174.4	0.1221	$\pi \rightarrow \pi^*$
B3:	6.96	178.0	0.3424	$\pi \rightarrow \pi^*$
Bz-$(H_2O)_8$	7.10	174.6	0.2425	$\pi \rightarrow \pi^*$
	7.13	173.8	0.1977	$\pi \rightarrow \pi^*$
	6.90	179.7	0.1345	Bz CT state
B4:	7.01	176.9	0.2824	$\pi \rightarrow \pi^*$
Bz-$(H_2O)_8$	7.11	174.5	0.1941	$\pi \rightarrow \pi^*$
	7.21	171.9	0.0950	$\pi \rightarrow \pi^*$
	6.97	177.9	0.0919	W CTstate

It is important to note that higher oscillator strengths are noticed for the $\pi \rightarrow \pi^*$ electronic transition (bright state) in Bz-$(H_2O)_{72}$ system as compared to that in Bz-$(H_2O)_{12}$ and Bz-$(H_2O)_{48}$ clusters. The electron density of the key orbitals involved in this main $\pi \rightarrow \pi^*$ electronic transition of Bz remain localized on benzene ring with increase in size of ice cluster, and are also consistent with the nature of orbitals involved in the $\pi \rightarrow \pi^*$ electronic transition of an isolated Bz molecule. Similar orbital features (i.e. localized electronic density) are observed in key transitions ($\pi \rightarrow \pi^*$) in both cluster models A and B. It is also evident from our results that both A and B cluster models are consistent with each other to predict important electronic transitions in such complex systems. The existence of other close lying Bz charge transfer (CT) states and diffuse states are also noticed in Bz-ice clusters (See Table 6.2 and Table 6.3), which may also influence the water Rydberg type excitations towards longer wavelengths above 170 nm, that are not present in isolated water $(H_2O)_{12}$ cluster, as also seen in recent experimental studies [70-72]. The intensities of water excitations in Bz-ice clusters are also found stronger as compared to those in isolated water ice clusters. It is clear from the above results and discussion that the benzene interaction with the ice cluster plays a significant role in giving new excitation features in UV spectra of Bz-ice clusters.

6.4 Conclusions

We have used ONIOM(QM:AMOEBA) to study benzene-ice complexes. This is one of the first applications of the ONIOM(QM:AMOEBA09) method. The trends in ordering of energetics of all eight ONIOM(M06-2X:AMOEBA09) optimized ground state structures of Bz-ice complexes are in good agreement with the ONIOM(LPNO-CCSD:AMOEBA09) level of calculations as well as with the fully-DFT calculations using the M06-2X functional, predicting good performance of the ONIOM(QM:AMOEBA09) method for modelling benzene-ice complex systems.

We show that the hydrogen bonding interactions play an important role in benzene-bound ice complex systems to provide stabilization, where benzene interacts with the ice clusters mainly via $\pi^{\cdots}$HO and C-H$^{\cdots}$OH type hydrogen bonding interactions. Binding energies of benzene-ice complexes are slightly dependent on the nature of the binding site of the ice surface, with binding sites consisting of both *d*-H and *d*-O atoms providing maximum stabilization to benzene-ice complexes as compared to binding

sites with only *d*-H or *d*-O atoms The binding energies of benzene on ice surfaces are estimated to be in the range of 0.25-0.45 eV.

Our results and discussions also show that the UV spectra of benzene-ice clusters show minor difference in peak positions and intensities, depending on the size and nature of the ice surface, and give slightly stronger intensities for excitations as the size of the ice cluster increases. Most of the important electronic excitations in benzene-ice complexes are dominated by benzene. We have also seen some interesting features of benzene-mediated excitations in ice cluster models indicating water excitations at longer wavelengths above 170 nm in benzene-ice clusters, predicting the possibility of photon absorption by water at wavelengths where photon absorption cross-sections are negligible, as observed in recent experimental studies [70-72]. The intensities of water excitations are also found to increase in benzene-ice cluster relative to those in isolated ice clusters. It is realized that the spectroscopy of benzene is also influenced due to the presence of an ice cluster, causing red–shift in the $\pi \rightarrow \pi^*$ electronic transition(s) of benzene in Bz-ice clusters as compared to those in isolated benzene, and the degeneracy of this transition is very slightly broken compared to the isolated gas-phase benzene. Charge transfer (CT) states and locally excited diffuse states are also important to describe electronic excitations in such systems.

6.5 Discussion

The work presented in this chapter and in previous result chapters describes the photochemistry and ultraviolet (UV) spectroscopy of cyclic aromatic hydrocarbons such as benzene and naphthalene, as well as small water clusters and crystalline ice clusters. Starting with the smaller water clusters (up to the water hexamer), the work was then extended to the larger crystalline ice cluster models. These were considered as astrophysically relevant systems to model polycyclic aromatic hydrocarbons (PAHs) interactions in interstellar ices, and to study their behaviour under UV field. Interactions of water clusters and crystalline ice clusters with cyclic aromatic hydrocarbons were modelled computationally using a range of computational chemistry techniques. These model systems were benchmarked with different computational methods to obtain binding energies of benzene and naphthalene with water complexes. Different orientations of benzene and naphthalene with respect to water clusters and ice clusters were studied and the structures with minimum energies were selected to study

UV spectroscopy and excited state of these complexes. Further primary focus was on the excited states of these complexes, which were generated following one-photon absorption. Characterization of these excited states was performed carefully by analysing the molecular orbitals involved in the electronic transitions.

For both benzene- and naphthalene-bound water W_6 clusters, it was found by both MP2 and DFT-wB97XD calculations that the cage conformer of the benzene-bound water hexamer cluster is more stable with slightly higher binding energy of about~ 1 kcal/mole than the prism conformer, in contrast to the results for the naphthalene-bound water hexamer cluster. In naphthalene-bound water hexamer cluster, we have calculated higher binding energy of about ~ 2-4 kcal/mole for the prism conformer than the cage conformer that indicates strong binding preference of naphthalene for the prism conformer of the water hexamer cluster. It was observed that the number and type of dangling sites i.e. dangling- hydrogen and/or dangling-oxygen present in the conformers of the water cluster determine the strength of hydrogen bonding interactions with benzene and naphthalene and hence the binding preference of benzene and naphthalene with different water conformers. Further comparison of binding energies of benzene and naphthalene with water hexamer cluster has predicted large binding energies for the naphthalene by about ≤ 6 kcal/mole than the benzene, indicating increase in stability and hydrogen bonding interactions in naphthalene-bound water cluster due to increase in size of the aromatic ring. However, using ONIOM(QM:MM) method with AMOEBA force field, binding energies of benzene were calculated slightly higher by about 2-3 kcal/mole when a crystalline ice replaces gas phase water W_6 cluster. For benzene-bound crystalline ice clusters, benzene binding was found to be favourable for the binding sites containing both dangling-hydrogen and dangling-oxygen.

From our ground state studies, we have found a good performance of MP2 and DFT-wB9XD methods for geometry optimization and binding energy calculations in benzene- and naphthalene-bound water clusters. For large benzene-bound crystalline ice models, binding energies obtained by using ONIOM(M06-2X:AMOEBA09) are in good agreement with the fully-quantum calculations obtained using the DFT-M06-2X. We have found a good performance of the ONIOM(M06-2X:AMOEBA09) method for modelling benzene-ice complex systems and therefore it could be used to model such larger PAHs-water model systems in future too.

Next discussing the UV spectral results obtained by TD-DFT calculations, the brightest $\pi \rightarrow \pi^*$ electronic transition of benzene and naphthalene in gas phase water hexamer W_6 cluster was calculated to be red-shifted in wavelength by about 2-4 nm with respect to that transition in isolated benzene and naphthalene. This red-shift is slightly more by about 1 nm in the prism conformer of water hexamer than the cage conformer, and holds for both benzene and naphthalene-bound water hexamer cluster. This $\pi \rightarrow \pi^*$ excitation was found to occur with lower intensity after interacting with the water W_6 and ice clusters. The degeneracy of this transition was also slightly broken in benzene. Similar UV spectral characteristics of benzene were observed when a crystalline ice cluster replaces gas phase water cluster. We observed new water excitations at longer wavelengths i.e. above 170 nm in both benzene- and naphthalene-bound water W_6 clusters. This finding is interesting as photon absorption cross section of water is negligible above 170 nm and these excitations were originally absent in the isolated water W_6 cluster. We have also calculated new electronic transition features such as charge transfer (CT), and locally diffuse Rydberg type excitation in these complexes, which are more pronounced in naphthalene-bound clusters than benzene-bound water clusters. The water CT excitations are observed at much longer wavelength range of about 180-200 nm in naphthalene-bound water clusters than in benzene-bound clusters at about ≤ 180 nm. Similar features were calculated for benzene-bound crystalline ice clusters, which also illustrate the effect of cyclic aromatic hydrocarbons on electronic excitations of ice clusters. Our results are showing good agreement with the recent experimental [70-72] and computational studies [36], where it was shown that benzene as a prototypical PAH molecule can act as a mediator to excite water molecules and shift water excitations to higher wavelengths or lower energies, where the photon-absorption cross-section for water is negligible at such wavelengths. Thrower *et al.* have done experimental studies on photo-processes in model interstellar ices by modelling multilayer films of benzene & water deposited on the sapphire substrate [72]. They investigated three distinct photo-desorption mechanisms occur in such systems: (i) Direct adsorbate-mediated desorption of benzene, (ii) Indirect adsorbate–mediated desorption of water, and (iii) Substrate-mediated desorption of both benzene and water. There are no experimental UV spectra available of these model systems of astrophysical relevance to compare results directly. However, we have computationally modelled UV electronic excitations by employing long-range corrected DFT functionals and observe direct excitations of benzene and

naphthalene, indirect benzene–mediated and naphthalene-mediated excitations of water, along with new CT and diffused states in our UV spectra. Thus our results suggest good qualitative comparison with the experimental results. It was also observed that the size of the ice cluster and dangling features show minor effect on the UV spectral characteristics. However, increasing the size of aromatic ring i.e., from benzene to naphthalene enhances the water excitations towards longer wavelengths and lower energies. Thus it is important to extend this work in future to model larger polycyclic aromatic hydrocarbons such as pyrene, coronene, *etc* that may further show similar trends in UV spectra which may be useful to extrapolate the results to real astrophysical model systems.

From our excited state studies, we have found a good performance of hybrid DFT functionals i.e. M06-2X and CAM-B3LYP in calculating vertical excitation energies of these complexes using time dependent density functional theory (TD-DFT). Both M06-2X and CAM-B3LYP functionals performed consistently with each other. Thus, these DFT hybrid functionals could be used in future for carrying out further excited state studies on larger PAHs and their interaction with gas phase water clusters as well as with ice surfaces.

Chapter 7 - Diffusion of deuterium (D) atom on crystalline and amorphous ice: A computational study

7.1 Introduction

Hydrogen is the most abundant molecule in the universe. It plays an important role in star formation and in the chemical evolution of interstellar clouds. The gas-phase formation of H_2 is inefficient to explain its observed high abundance in the interstellar medium (ISM), as the radiative association of two hydrogen atoms involves a spin-forbidden transition from the protomolecule to the ground state [304]. It was recognized that the H_2 formation most likely occurs predominantly through surface reactions on dust grains [15] (Gould & Saltpeter). The elementary processes associated with H_2 formation on dust grain surfaces are H-atom adsorption, diffusion, and recombination with another adsorbed H atom. In this H_2 formation process, H atoms first collide with a dust surface and get adsorbed. They move or diffuse on the surface in order to meet other H-atoms, and finally two H atoms meet on the surface and recombine to form an H_2 molecule [305]. Since H-H recombination is a radical-radical barrier-less reaction, the H_2 formation rate is limited by the diffusion of H atoms at low coverage on the surface. Hence, diffusion of an H atom on the grain surfaces is important to study to get a better understanding of the mechanism and rates of the H_2 formation on interstellar dust grain analogs. In cold dense molecular clouds, dust grains are covered with amorphous solid water (ASW). Therefore, it is particularly important to study diffusion on amorphous ice surfaces at very low temperatures [306].

Deuterium (D), a naturally occurring isotope of hydrogen, formed in the Big Bang event, is known to have abundance relative to hydrogen i.e. a cosmic D/H ratio of about 10^{-5}. Despite of this low abundance, deuterium enrichment in interstellar species has been detected by many observations [307-312]. It is proposed that chemical processes occurring both in the gas phase [308, 309] and the solid phase [311-313] may result in D enrichment. It is necessary to study diffusion of the D atom on ASW to understand the importance of the processes involved in the formation of interstellar deuterated species.

Several experimental groups have studied the H-atom and D-atom diffusion on amorphous water ice or ASW under conditions closely simulating those encountered in

astrophysical environments [314-319]. However, results are inconsistent and are somewhat contradictory. Some groups have observed slow diffusion [314, 316], while some other groups have observed fast diffusion [315, 317]. Manico *et al.* first proposed that the H-atom diffusion is very slow at a temperature of around 10 K, and higher temperatures are needed to achieve a production rate of H_2 that are needed to maintain a quasi-steady state in a molecular cloud [314]. In this experiment, H and D atoms were co-deposited on ASW at 10 K and then using the temperature-programmed desorption (TPD) method, the formation of HD molecules were detected resulting from H and D recombination on the ice surface. TPD spectra of HD molecules suggested that HD molecules were not formed during co-deposition of atoms but were observed to form during the increase in temperature of ASW at a very low coverage of hydrogen atoms. Perets *et al*. also proposed the slow diffusion for H atom and obtained the higher activation energy for diffusion in the range 41-55 meV using the TPD technique [316].

Hornekaer *et al.* also studied the formation of HD molecules and HD molecules were observed in TPD spectra only when H and D atoms were deposited simultaneously on ASW, while no HD formation was detected when H and D atoms were deposited sequentially [315]. They supported the fast diffusion of H and D atoms on ASW even at 10 K and observed the formation of HD molecules efficiently during exposure of ASW to H and D atoms. Mater *et al*. reported the lower activation energy of about 22 meV for the D-atom diffusion and observed the fast diffusion for the D-atom on porous ASW at 10 K [317].

The discrepancies in results observed by different experimental groups for fast and slow diffusion was explained by Pirronello *et al.* and was associated with the difference in the incident flux of atoms used for the experiments, resulting in difference in coverage of atoms on ASW [320]. At a very low coverage and temperatures, if only deep adsorption sites existed on ASW, then atoms would be so sparse and immobile on the surface that an event to encounter with an other atom would become difficult, and also not easy to encounter with the atoms coming from the gas phase during their search for adsorption sites to accommodate on the surface [320]. At the higher surface coverage, diffusion is fast and molecular hydrogen is readily formed even during the exposure.

All the experimental results discussed above have used the TPD method for their diffusion studies. To get a better understanding of the H-atom diffusion problem, Watanabe *et al.* studied hydrogen atom diffusion using new apparatus, Reaction

Apparatus for Surface Chemistry in Astrophysical environments with Laser Spectroscopy (RASCAL), and resonance enhanced multiphoton ionization (REMPI) [318]. The diffusion rate of H atom was measured at 8 K and they observed two type of potential sites i.e. shallow and deep potential sites with the energy depths of ~ 20 meV and > 50 meV, respectively. The fast diffusion was observed at shallow sites, which enables the H_2 formation on interstallar ice dust even at 8 K. The slow diffusion was associated with deeper potential sites, where atoms once trapped hardly migrated [318].

A recent experimental study by Hama *et al.* on diffusion of H and D atoms on ASW at temperatures of 8-15 K has shown the existence of various potential sites on ASW, and the potential sites were categorized in three groups: very shallow, middle-, and deep-potential sites [319]. The activation energies for diffusion (E_{diff}) reported were ≤ 18 meV for shallow sites, ≤ 22 meV (23 meV for D atoms) for middle sites, and ≥ 30 meV for deep potential sites. The very shallow potentials sites were observed to dominate the diffusion of H and D-atom on ASW. The little isotopic difference between H-and D-atom diffusion has been noticed on ASW, indicating that thermal hopping better explains the diffusion mechanism instead of quantum tunneling, at least at middle-potential sites, as significant isotope effect in the diffusion can be an indicator of quantum tunneling as it strongly depends on particle mass [319].

Theoretical studies have also been performed to investigate H_2 formation on ice surfaces [321, 322]. Buch & Zhang used the classical trajectory simulation technique to study H and D atom sticking on the amorphous surface with 115 water molecules [321]. They reported the binding energy of 8.8 meV for H atom and 17.2 meV for D atom. Computational studies have been performed by Masuda *et al.* to study diffusion and sticking of single H atom on amorphous ice surface using molecular dynamics (MD) simulations [322]. A periodic flat surface of 1000 water molecules was modelled using periodic boundary conditions. Several potential wells were observed, with the maximum energy depth of 22 meV [322].

Al-Halabi & van Dishoeck investigated the H atom adsorption and diffusion on amorphous solid water and crystalline ice at a surface temperature of 10 K using classical trajectory calculations [323]. The average binding energy (E_b) of the trapped H atoms was calculated to be higher for amorphous ice than crystalline ice, i.e. E_b = 36 meV for crystalline ice and E_b = 56 meV for amorphous ice. The residence time of H atoms adsorbed on the ASW was found to be longer as compared to that of H atoms adsorbed on the crystalline ice at the same surface temperature. At low temperatures,

the long values of residence time, and the high values of diffusion coefficient have suggested the higher formation yield of H_2 on ASW surfaces [323].

As discussed above, there have been many experimental studies on H and D atom diffusion on crystalline and amorphous ice surfaces. However, very few theoretical studies of the D atom diffusion on amorphous and crystalline ice surfaces have been performed. Interstellar H_2O ice is observed to be predominantly amorphous in nature [324]. However, it has been observed that in dense interstellar clouds, water ice can exist in both amorphous and crystalline forms [325-327]. Thus, in order to get better understanding of the D atom diffusion on interstellar ices, we have studied the D atom diffusion on both crystalline and amorphous ice surfaces i.e. the hopping of D atom between neighbouring local minima on both amorphous and crystalline ice surfaces at 10 K (See Figure 7.1). The main aim of the work presented in this chapter is to calculate binding energies, barrier heights, hopping rate constants, residence times, and diffusion coefficients. We have used quasi-quantum harmonic transition state theory (qq-HTST) for the rate constant calculations. The Adaptive Kinetic Monte Carlo (AKMC) method is used to obtain diffusion coefficients of the deuterium atom on both amorphous and crystalline ice surfaces at astronomically relevant temperatures (T=8-30 K) in the present study. All simulations are performed using the EON software package [90, 91].

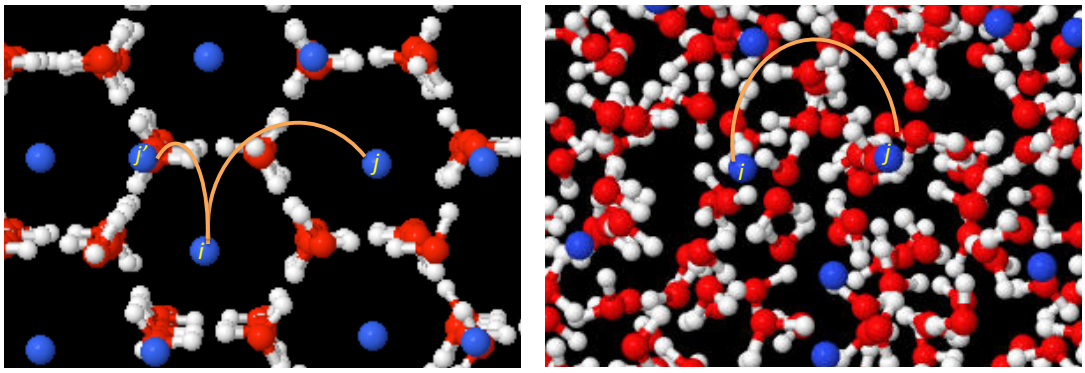

(a) (b)

Figure 7.1 Illustration of one hop of D atom. *i* and *j* (or *j'*) are the initial and final minimum of the hop on (a) crystalline surface (I_h) (b) amorphous surface (ASW). Local minima are represented in blue dots.

7.2 Computational Details

7.2.1 Ice models

The crystalline ice model is taken from Abascal *et al*.[164] The interactions between water (H_2O) molecules are described by the TIP4P-2005f potential. A smaller bond distance at equilibrium ($r_{eq}^{OH} = 0.9419$Å) and a larger angle (θ_{eq}^{HOH}=107°) than those of TIP4P/2005 was considered to incorporate flexibility by means of a Morse potential for the bond stretching and a harmonic term for the angle bending. More details on structural parameters and construction of crystalline water ice are given in Abascal *et al*. [164] and Cuppen *et al*. [328]. The amorphous solid water surface is taken from Andersson *et al* [52]. The ice surfaces are constructed using the TIP4P-2005f potential with all molecules kept rigid. The ice structures are snapshots obtained from molecular dynamics simulations.

The crystalline ice model is a hexagonal ice (I_h) that consists of a unit cell of 6 bilayers with a total of 360 H_2O molecules holding 60 H_2O molecules in each bilayer. The unit cell dimensions along the x, y and z directions are 23.164 Å, 22.464 Å, and 81.932 Å, respectively. For ASW, the unit cell consists of 480 H_2O molecules, with unit cell dimensions of 22.484 Å, 23.366 Å and 100 Å in x, y and z directions, respectively. To simulate an infinite ice surface, periodic boundary conditions are applied in x and y directions, keeping z direction as the surface normal. We have used completely frozen ice surfaces i.e. all the water molecules of the ice surfaces are kept fixed.

7.2.2 Potential for D-H_2O interaction

We have considered the interaction between a free D atom and each water (H_2O) molecule in the unit cell of the ice. The potential V_{D-H_2O} considered has the same form as the V_{H-H_2O} potential i.e. the potential due to interaction between a single H atom and a water molecule, which is taken from Andersson *et al*. [52] where it is discussed in detail. Since the potential V_{D-H_2O} is independent of the mass of the atom, we can use same potential for deuterium (D) atom as of H atom.

The potential V_{D-H_2O} can be illustrated as

$$V_{D-H_2O} = V_{disp}(R_{DH(1)}) + V_{disp}(R_{DH(2)}) + V_{disp}(R_{DO}) + \quad (7.1)$$

$$V_{rep}(R_{DH(1)}) + V_{rep}(R_{DH(2)}) + V_{rep}(R_{DO}) + V_{Morse}(R_{DO})$$

where each term in Equation (7.1) can be represented by mathematical equations as given below:

$$V_{disp}(R_{ij}) = -D(R_{ij})C_6^{ij}R_{ij}^{-6} \tag{7.2}$$

$$D(R_{ij}) = \begin{cases} 1.0, & R_{ij} \geq R_c^{ij} \\ e^{\left(-\left(\frac{R_c^{ij}}{R_{ij}}-1\right)^2\right)}, & R_{ij} \leq R_c^{ij} \end{cases} \tag{7.3}$$

$$V_{rep}(R_{ij}) = a_{ij}e^{(-b_{ij}R_{ij})} \tag{7.4}$$

$$V_{Morse}(R_{DO}) = D_{DO}\{e^{(-2\beta_{DO}(R_{DO}-R_{e,DO}))} - 2e^{(-\beta_{DO}(R_{DO}-R_{e,DO}))}\} \tag{7.5}$$

As given in Equation (7.1), the total potential of the D-H_2O interaction consists of the contribution due to the dispersion interactions between D-H and D-O, the repulsive interactions between D-H and D-O, and the D-O Morse potential. The Morse potential represents the partially bonding character of the D-H_2O interaction. Figure 7.2 illustrates the distances between the D atom and the corresponding atoms of the water molecule i.e. $R_{ij} = |\overrightarrow{R_i} - \overrightarrow{R_j}|$ where i = D atom and j = H(1), H(2) or an O atom. The values of all parameters used for this interaction potential are listed in Table 7.1.

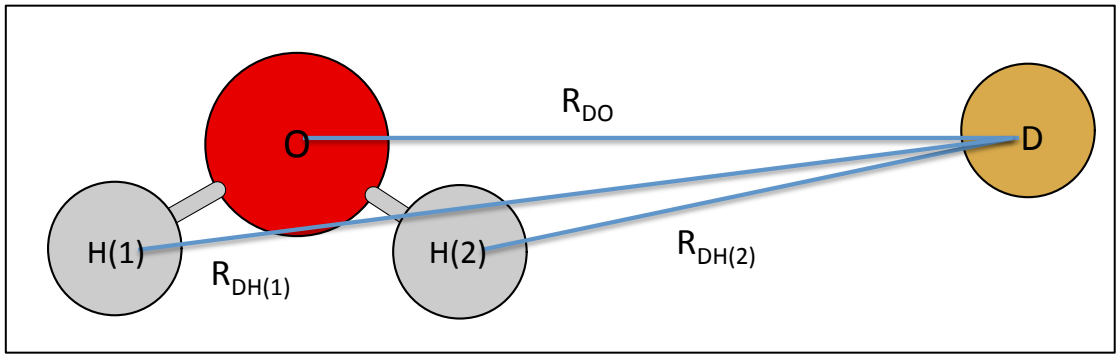

Figure 7.2 Illustration of distances between the single D atom and each atom of one H_2O molecule.

Table 7.1 Parameters for the D-H_2O potential.

Dispersion	
C_6^{DH}	30.2562 kJ mol^{-1} Å^6
R_c^{DH}	2.81541 Å
C_6^{DO}	2216.76 kJ mol^{-1} Å^6
R_c^{DO}	5.18068 Å
Repulsion	
a_{DH}	5563.57 kJ mol^{-1}
b_{DH}	4.27352 Å^{-1}
a_{DO}	4158.88 kJ mol^{-1}
b_{DO}	2.63805 Å^{-1}
Morse	
D_{DO}	287.598 kJ mol^{-1}
β_{DO}	4.73771 Å^{-1}
$R_{e,DO}$	0.816286 Å

7.3 Results and Discussion

7.3.1 Local minima and saddle points search of a D atom on an ice surface

We have used the conjugate gradient method [85] to perform energy minimization by optimizing the configuration along the steepest descent and then all the possible local minima of D atoms were located on the surface of the chosen unit cell of both crystalline and amorphous ice surfaces. The number of local minima obtained for crystalline ice is 56 per unit cell, while amorphous ice give 32 minima per unit cell. The ice maps showing all possible local minima on both crystalline and amorphous ice surfaces are shown in Figures 7.3 and 7.4, respectively. The local minima are numbered in decreasing order of classical binding energies i.e. a local minimum with index (1) has the maximum classical binding energy (or well depth), while the one with index (56) has the minimum classical binding energy (or well depth), for the crystalline ice. Similarly, in amorphous ice, local minimum with index (1) and (32) has the maximum and the minimum classical binding energy, respectively.

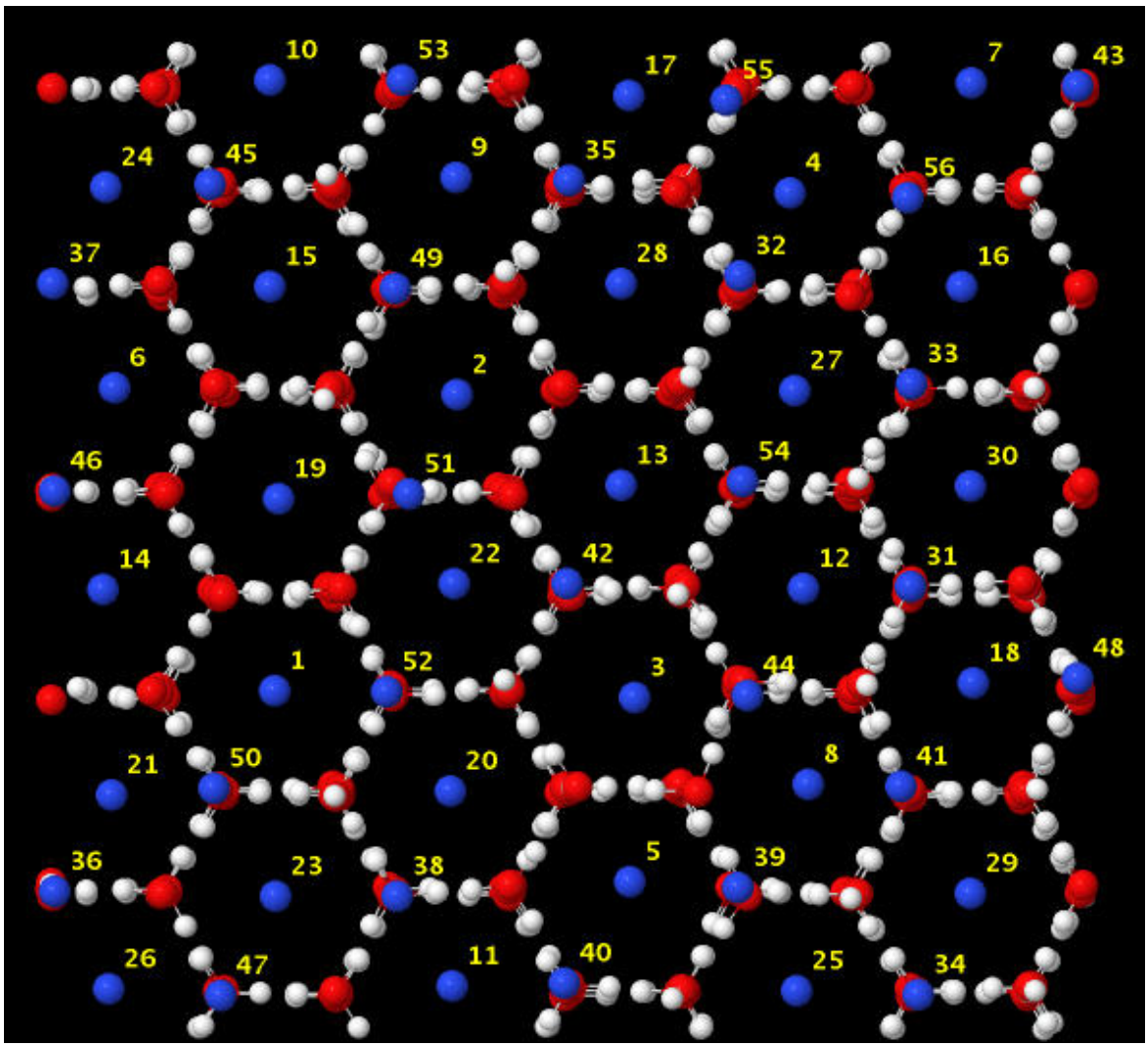

Figure 7.3 Ice map showing all possible local minima (blue dots) of the deuterium atom on the crystalline ice surface. The indexes on local minima are assigned according to maximum to minimum binding energy.

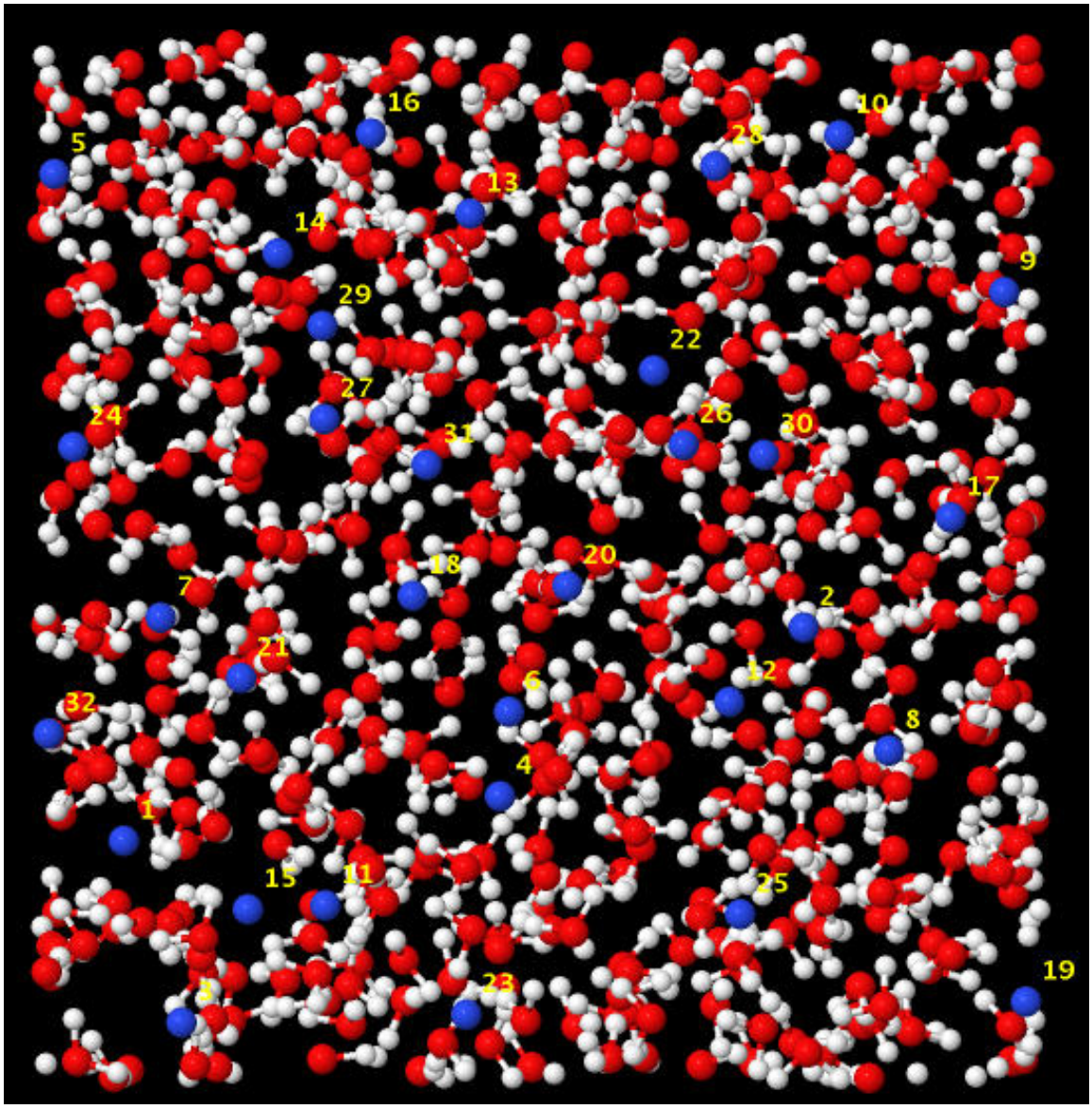

Figure 7.4 Ice map showing all possible local minima (blue dots) of the deuterium atom on the amorphous ice surface. The indexes on local minima are assigned according to maximum to minimum binding energy.

The saddle point search between two local energy minima is performed using the activation-relaxation technique nouveau (ART_n) with the Lanczos algorithm. ART technique has already been discussed in detail in Chapter 2, Section 2.1.3.1.

The maps of the configurations of saddle points obtained using ARTn and all possible local minima for crystalline and amorphous ice surfaces are shown in Figures 7.5 and 7.6, respectively. A thorough analysis has been done to check all the possible jumps (hops) of a D atom from given minimum to other neighbouring minima on a surface and trajectories are drawn to show all the saddle points connecting two neighbouring minima.

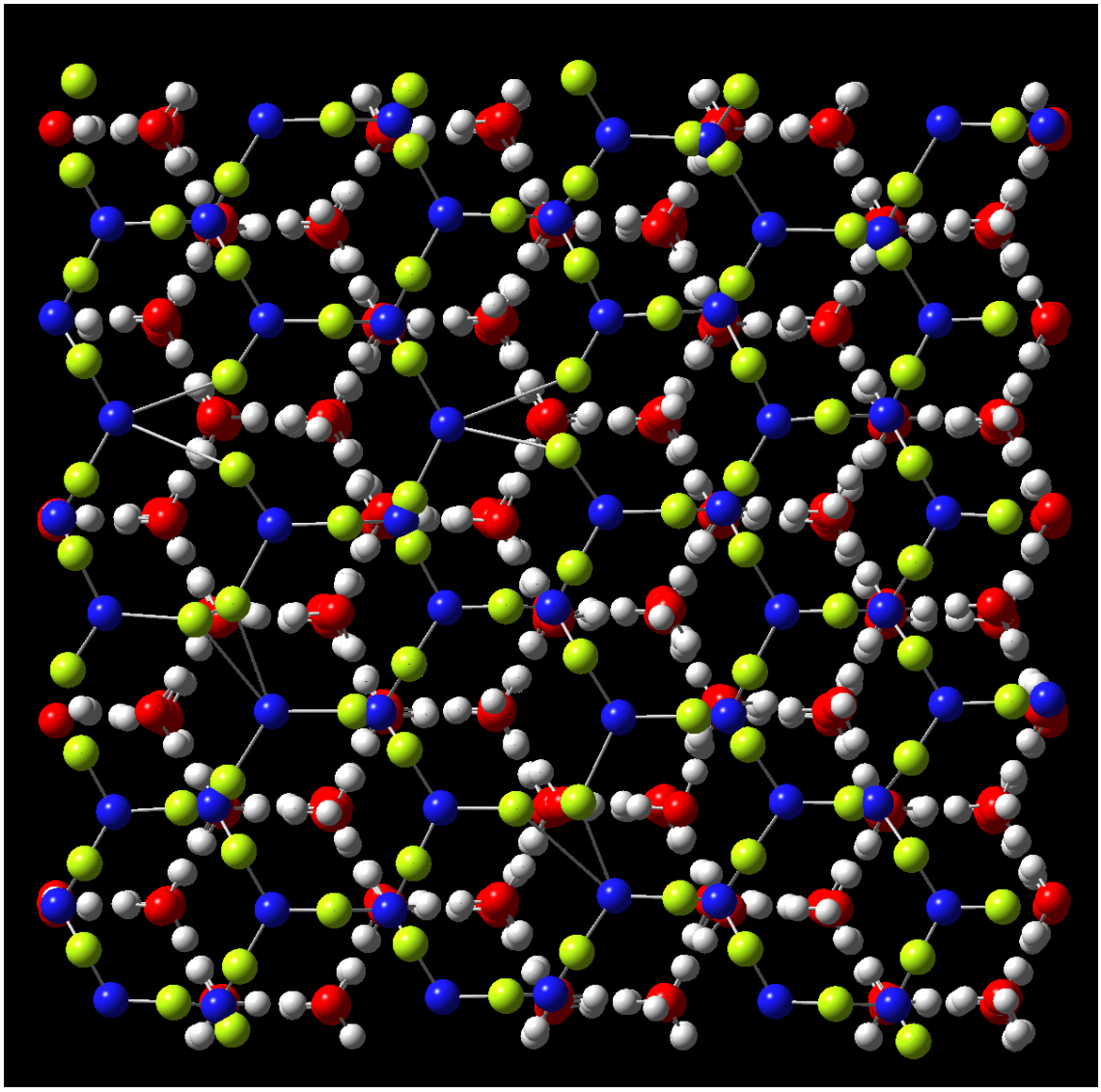

Figure 7.5 Ice map showing all possible local minima (blue dots) of the deuterium atom with corresponding saddle points (green dots) on the crystalline ice surface.

Figures 7.5 and 7.6 illustrate the ice maps for both ice surfaces showing the positions of local minima and the corresponding saddle points connecting them. The surface of I_h is much smoother and is found to have more local minima as compared to the complicated ASW surface. Deep potential wells with higher binding energies are noticed on the surface of ASW, where the D atom is found to be more stable. The morphology of the ice surface also plays an important role in the ASW surface. For the ASW surface, a higher binding energy of 79 meV is calculated when the D atom sits inside a deep cavity i.e. position 01 in Figure 7.4, as compared to when it sits on the flat surface with binding energy of 39 meV i.e. at position 32 in Figure 7.4. The hopping rate of the D

atom between two local minima depends on the position of the minima. A slow movement with a longer residence time is noticed if the D atom in the deep cavity i.e. residence time at position 01 is about 0.45 seconds, while a fast movement is noticed on a flat surface with a residence time of 1.03 picoseconds at position 32.

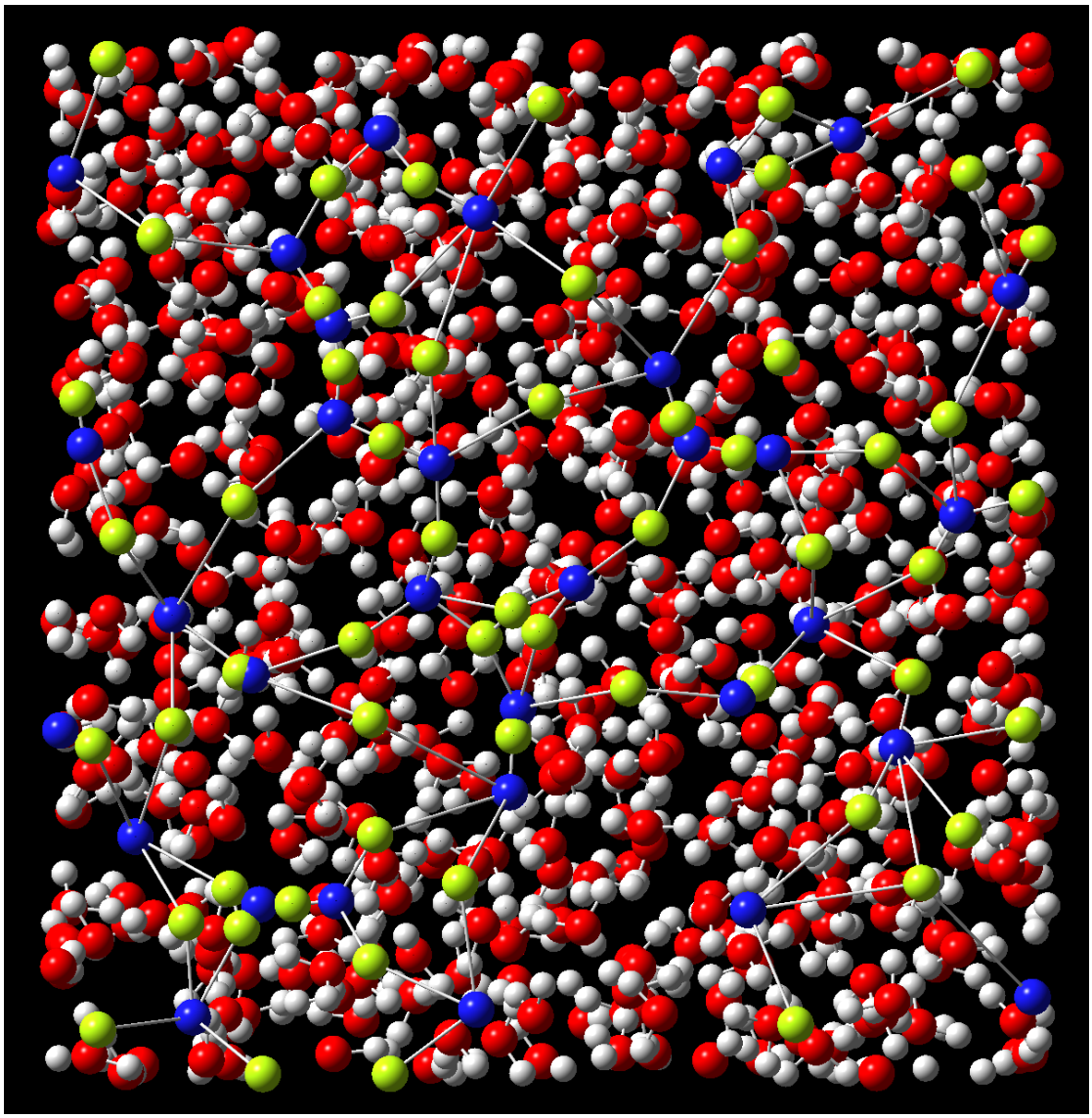

Figure 7.6 Ice map showing all possible local minima (blue dots) of the deuterium atom with corresponding saddle points (green dots) on the crystalline ice surface.

7.3.2 Binding Energies

On the crystalline ice surface I_h, we have observed two kinds of minima, deep minima at the middle of the each hexagon, and the shallow minima at the corners of the hexagons. There are 30 deep minima and 26 shallow minima on the I_h surface, as shown in Figure 7.3. A small gap can be seen in the distribution of classical binding

energies of local minima due to the existence of deep and shallow minima on the I_h surface (See Figure 7.7 (a)). This gives the cut-off between the well depths of deep minima (40.5-47.6 meV) situated at the middle of the hexagons and the shallow minima (34.8-38.5 meV) situated in the corner of the hexagons. The classical binding energies (E_b) are in a narrow range of about 34.8-47.6 meV due to regularity of I_h surface.

For the ASW surface, the distribution of classical binding energies is complex, as several cut-offs are noticed in the distribution (See Figure 7.7(b)). Due to the complex morphology of the ASW surface, classical binding energies (E_b) of local minima of D atom are in a broad range of about 39-79 meV and several discontinuities can be seen due to the existence of very deep and shallow minima. The results are consistent with the calculated binding energy range of about 34-86 meV for local minima of H atom on the ASW surface by Al-Halabi & van Dishoeck (2007) [323], using the same H-H_2O interaction potential [52].

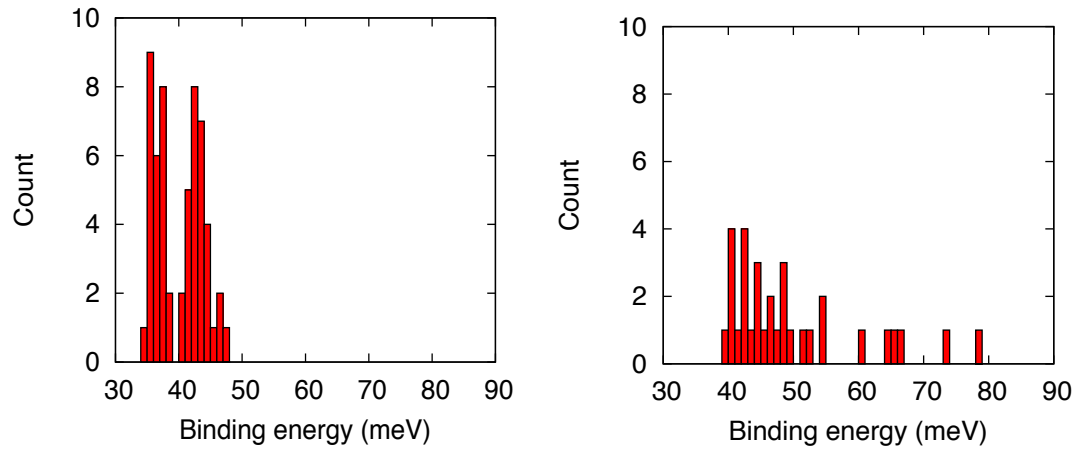

(a) (b)

Figure 7.7 The distribution of classical binding energies of local minima of D atom on (a) crystalline I_h surface (b) amorphous ASW surface.

7.3.3 Barrier Heights

The classical barrier heights (ΔE) for all possible hops of the single D atom on I_h and ASW surfaces are shown in Figures 7.8(a) and 7.8(b), respectively. We have calculated 172 hops of D atom, i.e. jumps from *i* to *j* (or *j'*) or *j* (or *j'*) to *i* on crystalline I_h surface as shown in Figure 7.1(a). In Figure 7.1(a), jump from *i* to *j* illustrates a jump between a deep minimum to a neighbouring deep minimum. The jump *i* to *j'* represents a jump between a deep minimum to a shallow minimum. The barrier height ranges are $\Delta E \leq 4.97$ meV (78 hops ≈ 45%) and $\Delta E > 5$ meV (94 hops ≈ 55%) for I_h surface, as

shown in Figure 7.8(a). The maximum barrier height for I_h is calculated to be $\Delta E_{max}^{I_h} = 13.9$ meV.

Figure 7.8(b) clearly shows that the barrier heights of D atom hops on ASW are in broader range as compared to that in crystalline ice. We have found 116 hops of D atom on the surface of ASW (See Figure 7.1(b)). The maximum barrier height for ASW is calculated to be $\Delta E_{max}^{ASW} = 48$ meV, which is much higher as compared to that for crystalline I_h surface. It is clear from the distribution of barrier heights (See Figure 7.8(b)) that different types of potential sites exist on the ASW surface. The ASW surface shows several energy ranges, where barrier heights are in range $\Delta E \leq 21$ meV (92 hops ≈ 79 %), 26 meV (7 hops ≈ 6 %), 30 meV (5 hops ≈ 4.5%), and $\Delta E \geq 32$ meV (12 hops ≈ 10.5 %).

It is noticed that most of the hops have barrier heights in the range $\Delta E \leq 21$ meV that corresponds to very shallow potential sites. Recently, Hama *et al*. have observed several potential sites on the porous ASW surface experimentally[319]. The activation energies for diffusion (E_{diff}) reported are ≤ 18 meV (for very shallow sites), 22 meV (23 meV for D atoms for middle sites), and ≥ 30 meV (for deep potential sites).[319] The very shallow potentials sites are observed to dominate the diffusion of H and D-atom on ASW, which is in agreement with our results for deuterium diffusion on ASW. The barrier heights for D-atom diffusion are in good agreement with the experimental results, with a barrier heights differences of about 2-3 meV are calculated with respect to experimental results.

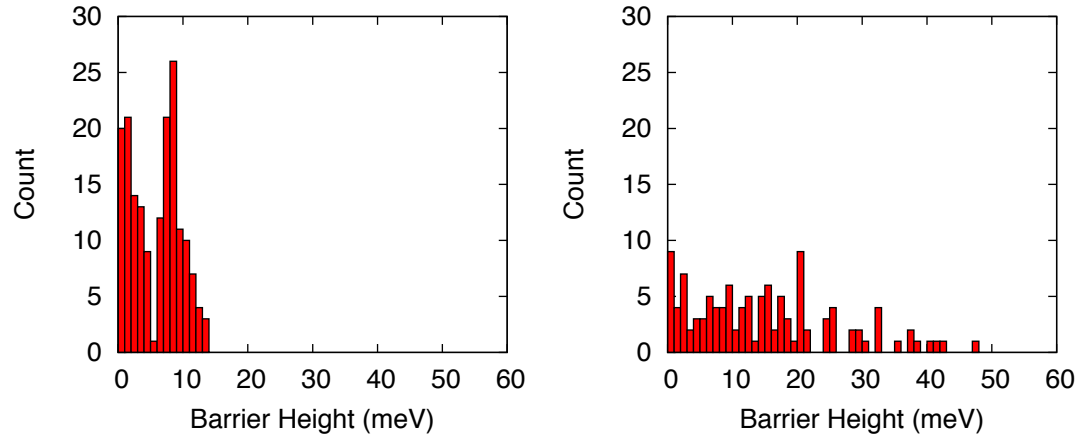

(a) (b)

Figure 7.8 The distribution of classical barrier heights of local minima of D atom on (a) crystalline I_h surface (b) amorphous ASW surface.

7.3.4 Rate Constants

We have also calculated rate constants for D atom hops between potential minima, and hopping rate constants (k) are obtained for each hop.

For the present work, the quasi-quantum harmonic transition state theory (qq-HTST) is applied for calculating rate constants [87, 88], and the vibrational motion of the physisorbed D atom is considered only.

It is already mentioned in Chapter 2, Section 2.1.4, that for $\Delta E^{VAG} > 0$, where VAG stands for vibrational adiabatic ground state, qq-HTST provides reasonable hopping rates k for each hop and behaves properly. But for $\Delta E^{VAG} < 0$, qq-HTST doesn't provide accurate values for k, as the Boltzmann factor becomes very large for negative VAG, and leads to improper behaviour. Thus for the hops with $\Delta E^{VAG} < 0$, k values were calculated using different technique, considering whether the hop is exoergic or endoergic. More details on transition state theory and rate equations used for calculating rate constants are given in Chapter 2, Section 2.1.4.

7.3.5 Residence Time

The residence time t_i i.e. an average time the D atom remains in a certain local minimum i, was calculated using Equation (7.6), where k_{ij} gives the transition rate constant of D atom from an initial minimum (i) to an adjacent minimum (j), as illustrated in Figure 7.9.

$$t_i = \frac{1}{\sum_j k_{ij}} \tag{7.6}$$

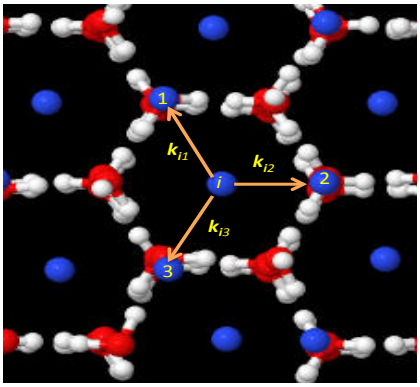

Figure 7.9 Rate constant k_{ij} for transition from an initial local minimum i to an adjacent minimum [j=(1,2,3)]. Local minima are represented in blue dots.

We have obtained the residence time values for hopping of D atom for each local minima at temperature T=10 K using Equation (7.6). For both I_h and ASW, the hops with VAG > 0, the residence values were calculated using the qq-HTST while for the hops with VAG < 0, values were calculated using different technique, considering whether the hop is exoergic or endoergic and the corresponding residence times values obtained are shown in Figure 7.10. The residence times in the case of I_h is in a narrow range and all the hops are very fast at 10 K, which are in the picoseconds to nanoseconds range, as shown in Figure 7.10(a).

The ASW surface gives a much broader range of residence times from picoseconds to seconds (See Figure 7.10(b)). It is also noticed that residence time are not always larger for the local minima with higher binding energies (more stable sites), and vice versa (See Figure 7.11).

We have analyzed the correlation between rate constant ($\log_{10}(k)$) of hop and the corresponding classical barrier height for both I_h and ASW, as shown in Figure 7.12. It is seen that $\log_{10}(k)$ values are higher at lower barrier heights and vice versa. Thus, fast hopping of D atom is observed around potential area with low barrier heights while slow hopping is observed when D atom hops around potential sites with high barrier heights. There could be a possibility of D atom getting trapped in such deep potential sites.

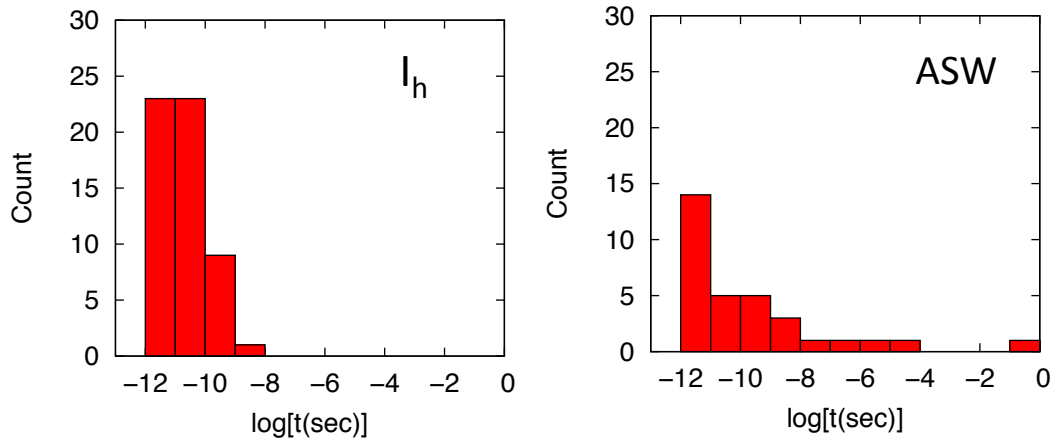

(a) (b)

Figure 7.10 Illustration of the residence time (t) of local minima of D atom on (a) crystalline I_h surface (b) amorphous ASW surface. The residence times are calculated using qq-HTST theory including exoergic and endoergic corrections at 10 K.

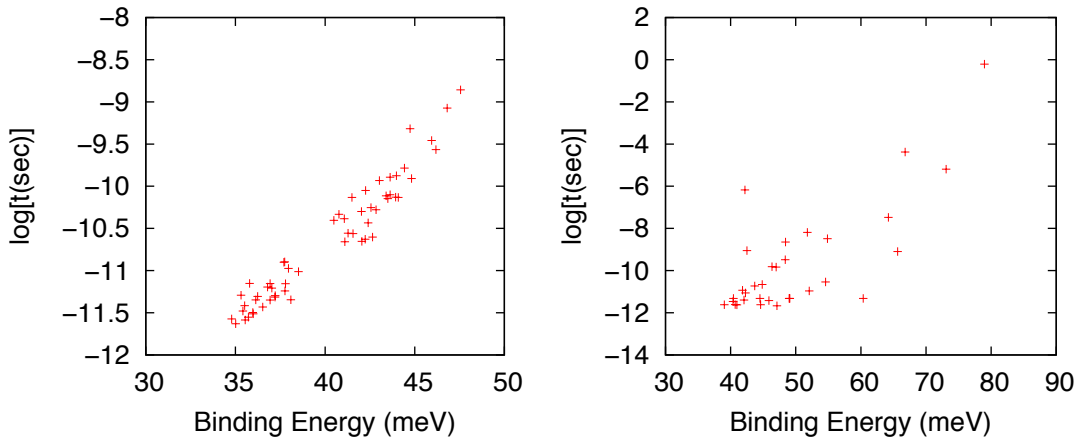

(a) (b)

Figure 7.11 Correlation of the residence time (t) of the local minima of D atom with the corresponding classical binding energy on (a) crystalline I_h surface (b) amorphous ASW surface. The residence times are calculated using qq-HTST theory including exoergic and endoergic corrections at 10 K.

Further analysis is done to study correlation between rate constant and the corresponding VAG barrier height of D atom hops at 10 K. It is found that the hopping rate constant strongly depends on the corresponding value of VAG barrier height (See Figure 7.13). For positive values of the VAG barrier height i.e. when $\Delta E^{VAG} > 0$, the rate constant $\log_{10}(k)$ decreases with an increase in VAG. Thus fast hopping is observed for lower values of VAG barrier heights, and hopping seems to slow down at higher VAG barrier heights. When $\Delta E^{VAG} < 0$ and the transition is exoergic, the rate constant $\log_{10}(k)$ becomes constant as $k = min\left[\frac{k_B T}{h}, v^R_{min}\right]$ in this case, as also seen in Figure 7.13(a)-(b). It is clearly seen that ZPEs of reactants and saddle points influence the rate constants. Thus it is important to properly account the ZPEs of reactants and saddle points to get results with better accuracy. It is concluded from our results that the diffusion of D atom can be slower for the hops with higher VAG barrier heights and vice versa.

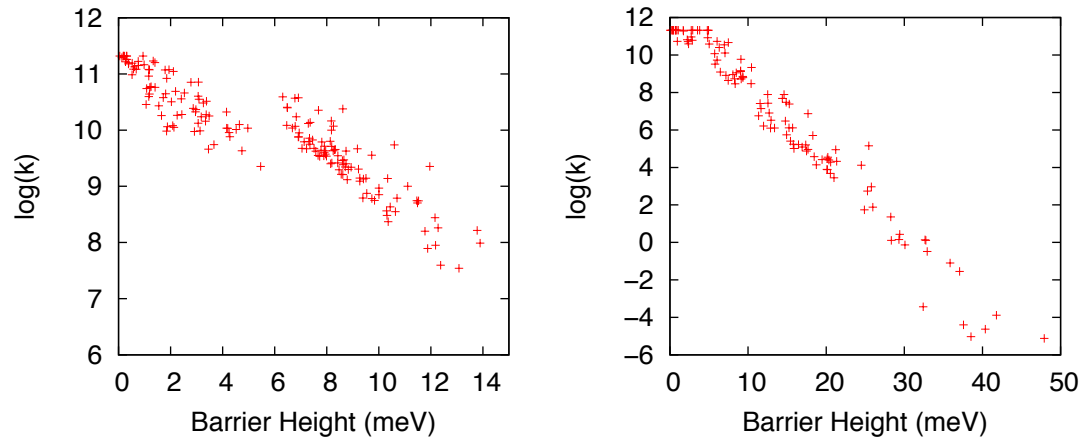

(a) (b)

Figure 7.12 Correlation of the hopping rate constant (k) of the local minima of D atom with the corresponding classical barrier height on (a) crystalline I_h surface (b) amorphous ASW surface. The hopping rate constants are calculated using qq-HTST theory including exoergic and endoergic corrections at 10 K.

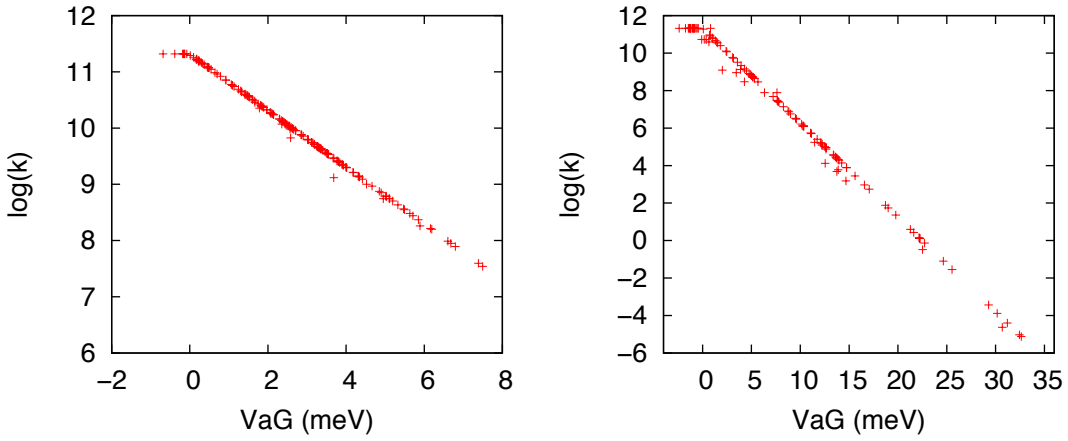

(a) (b)

Figure 7.13 Correlation of the hopping rate constant (k) of the local minima of D atom with the corresponding VAG barrier height on (a) crystalline I_h surface (b) amorphous ASW surface. The hopping rate constants are calculated using qq-HTST theory including exoergic and endoergic corrections at 10 K.

7.3.6 Diffusion Constants

The Adaptive kinetic Monte Carlo [89, 90] method is used for long timescale simulation in crystalline and amorphous ice surface for determining kinetic processes like diffusion of deuterium atom for the present study. AKMC method has already been discussed in detail in Chapter 2, Section 2.1.4.1.

The KMC trajectories give the position (*r*) of the deuterium atom on the ice surface as a function of time (*t*). Thus, we can calculate the diffusion coefficients, D, using the Einstein-Smoluchowski Equation (7.7) for two-dimensional diffusion.

$$D = \lim_{t\to\infty} \frac{1}{4t} \langle |r(0) - r(t)|^2 \rangle \tag{7.7}$$

where $\langle |r(0) - r(t)|^2 \rangle$ is the mean-squared displacement.

As discussed above, the rate constant (*k*) depends on the sign of the VAG barrier height (ΔE^{VAG}), which in turn can effect diffusion contants (D). Therefore, we have considered both cases:

Case (1): rate constants are calculated using qq-HTST theory only, irrespective of the sign of the VAG barrier height (ΔE^{VAG}) and ; *Case (2)*: rate constants are calculated using qq-HTST theory with enoergic and exoergic transitions correction, i.e. considering the sign of VAG barrier height (ΔE^{VAG}).

Using an Arrhenius Equation (7.8), we have calculated the effective diffusion energy barrier (E_{diff}) and pre-exponential factor (D_o) for deuterium diffusion on I_h surface.

$$D = D_o \exp\left(-E_{diff}/k_B T\right) \tag{7.8}$$

The activation energy for diffusion (E_{diff}) can be interpreted, as an average effective diffusion barrier a deuterium has to cross along the minimum energy path across the surface. By plotting ln(D) versus 1/T (K^{-1}), we observe an Arrhenius type behaviour as shown in Figure 7.18 and Figure 7.19 for *case (1)* and *case (2),* respectively, and the calculated E_{diff} is nearly same for both cases, i.e. about 7.166 meV for *case (1)* and 7.162 meV for *case (2).*

7.3.6.1 Diffusion constants of deuterium on crystalline (I_h) ice

The surface diffusion constants of the deuterium atom on crystalline (I_h) ice surface are calculated from the mean squared displacements in the KMC trajectories at different temperatures (T = 8 K, 10 K, 15 K, 20K, 25 K, and 30 K) using Equation (7.7). For example : By plotting RMS distance ($Å^2$) on the y-axis versus time (sec) on the x-axis, we get a slope (*m*) which is equal to 4 times the diffusion constant (D), for two-dimensional deuterium atom diffusion, as shown in Figures 7.14 and 7.15 for *case (1)* at

temperatures of 10 K and 20 K, respectively. Also refer to Figures 7.16 and 7.17 for *case (2)*. Thus we can calculate diffusion constants of the deterium atom on the crystalline I_h surface, and all resulting diffusion constants (D) obtained at a range of temperatures are listed in Table 7.2 for *case (1),* and in Table 7.3 for *case (2)*.

It is seen from the results that value of diffusion constant (D) increases with increase in temperature, which shows that diffusion of deuterium atom is faster at higher temperatures. The diffusion constant D at T=10 K is about 5.00×10^{-7} cm^2s^{-1}. The diffusion constant D is about 5×10^3 times higher at 30 K i.e. 1.00×10^{-4} cm^2s^{-1} as compared to that at 10 K.

It is also observed that similar results are obtained for the diffusion constants in both cases (1) and (2) (See Tables 7.2-7.3 & Figure 7.14-7.17). Thus, the sign of the VAG barrier heights (ΔE^{VAG}) is not found to influence rate constants (k), and hence diffusion constants (D) obtained using qq-HTST level of theory are consistent with the one obtained by considering endoergic and exoergic transition corrections in a crystalline ice surface.

Table 7.2 The diffusion constant for D atom diffusion on crystalline I_h surface at different temperatures T. The rate constants are calculated using qq-HTST theory.

Temperature (T)	***Slope m* ($Å^2$ s^{-1})**	**D ($Å^2$ s^{-1})**	**D (cm^2 s^{-1})**
8	1.811×10^9	4.528×10^8	4.528×10^{-8}
10	1.737×10^{10}	4.343×10^9	4.343×10^{-7}
15	2.834×10^{11}	7.085×10^{10}	7.085×10^{-6}
20	1.096×10^{12}	2.740×10^{11}	2.740×10^{-5}
25	2.385×10^{12}	5.963×10^{11}	5.963×10^{-5}
30	3.552×10^{12}	0.888×10^{12}	0.888×10^{-4}

Table 7.3 The diffusion constant for D atom diffusion on crystalline I_h surface at different temperatures. The rate constants are calculated using qq-HTST theory including endoergic and exoergic corrections.

Temperature (T)	*Slope m* ($Å^2\ s^{-1}$)	D ($Å^2\ s^{-1}$)	D ($cm^2\ s^{-1}$)
8	1.851×10^{9}	4.628×10^{8}	4.628×10^{-8}
10	1.664×10^{10}	4.160×10^{9}	4.160×10^{-7}
15	2.887×10^{11}	7.218×10^{10}	7.218×10^{-6}
20	1.085×10^{12}	2.713×10^{11}	2.713×10^{-5}
25	2.233×10^{12}	5.583×10^{11}	5.583×10^{-5}
30	3.721×10^{12}	0.930×10^{12}	0.930×10^{-4}

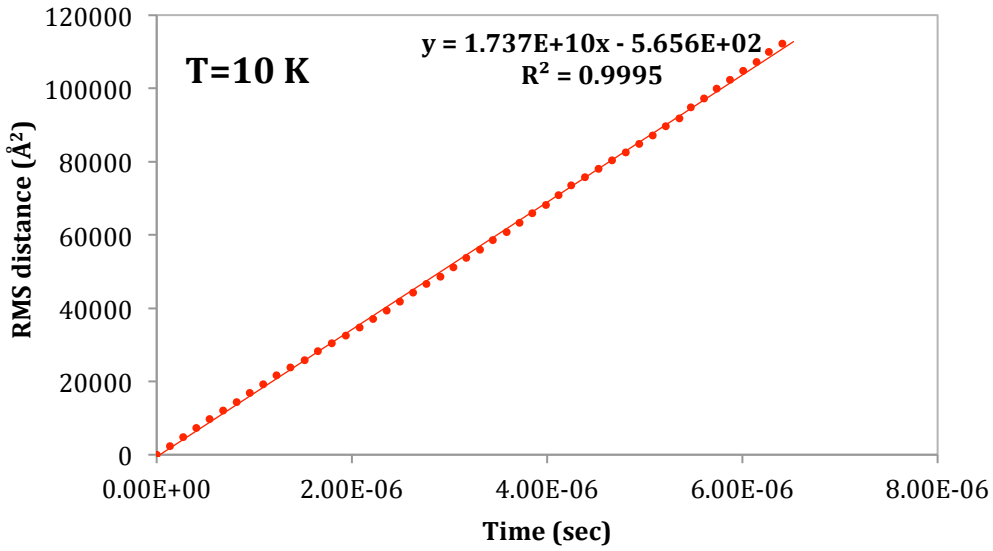

Figure 7.14 RMS distance ($Å^2$) versus time (sec) for D atom diffusion on crystalline I_h surface. The rate constants are calculated using qq-HTST theory at temperature of 10 K.

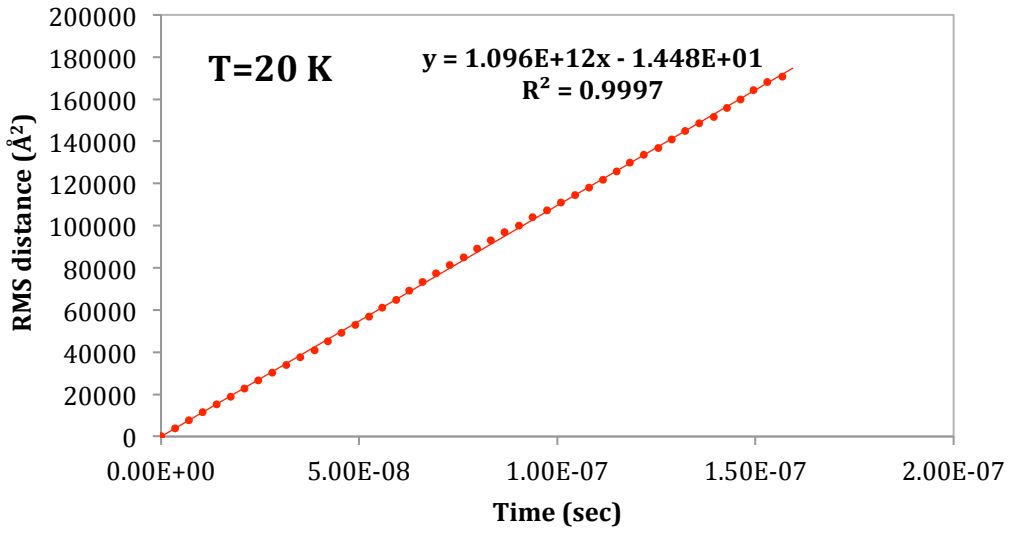

Figure 7.15 RMS distance (Å^2) versus time (sec) for D atom diffusion on crystalline I_h surface. The rate constants are calculated using qq-HTST theory at temperature of 20 K.

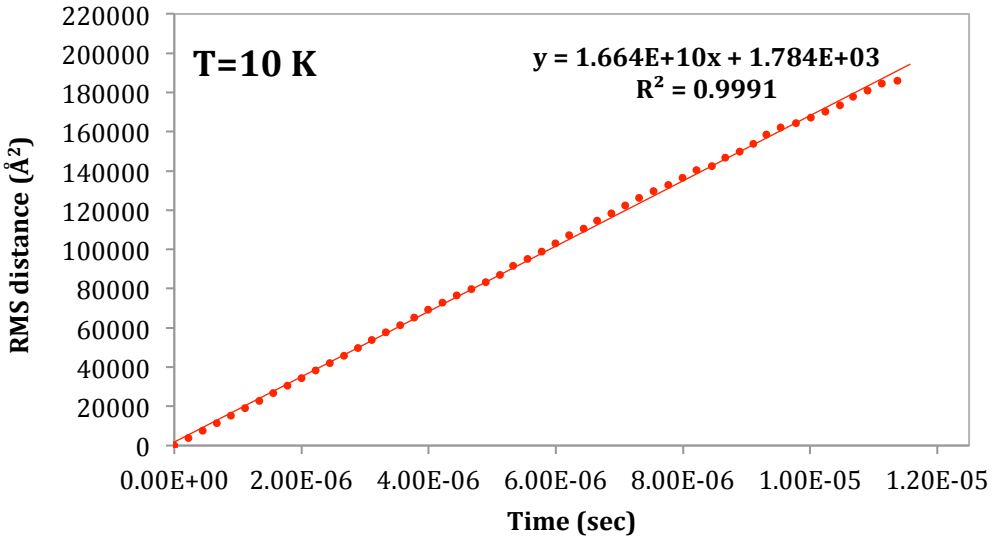

Figure 7.16 RMS distance (Å^2) versus time (sec) for D atom diffusion on crystalline I_h surface. The rate constants are calculated using qq-HTST theory including endoergic and exoergic transition corrections at temperature of 10 K.

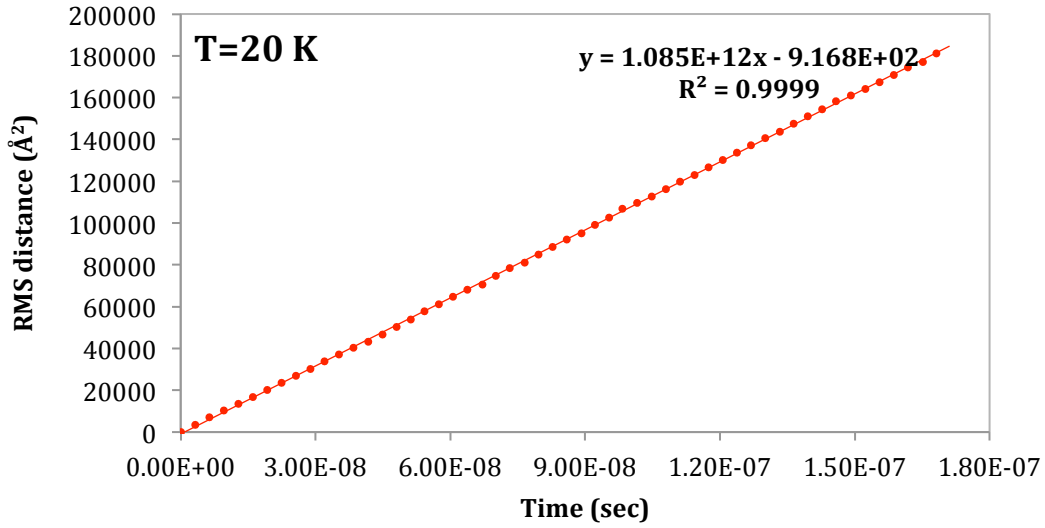

Figure 7.17 RMS distance ($Å^2$) versus time (sec) for D atom diffusion on crystalline I_h surface. The rate constants are calculated using qq-HTST theory including endoergic and exoergic transition corrections at temperature of 20 K.

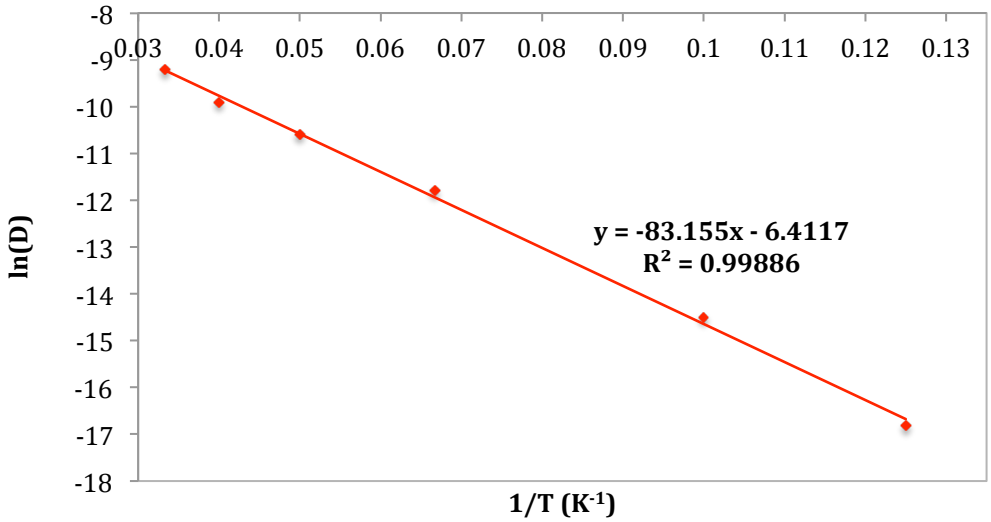

Figure 7.18 Arrhenius plot of the diffusion constants (D) of the deuterium atom on crystalline ice surface: ln(D) versus 1/T (K^{-1}). Temperature ranges from T = 8 K to 30 K. The rate constants are calculated using qq-HTST theory.

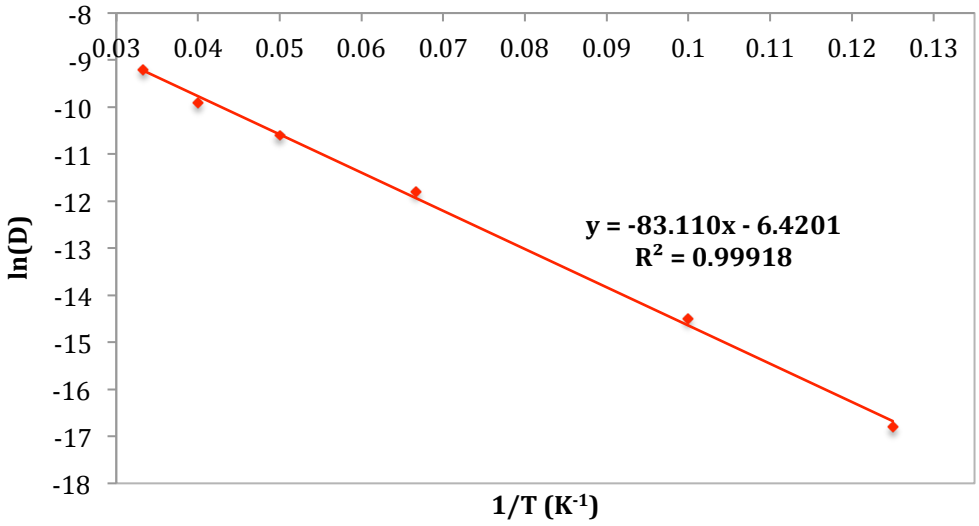

Figure 7.19 Arrhenius plot of the diffusion constants (D) of the deuterium atom on crystalline ice surface: ln(D) versus 1/T (K^{-1}). Temperature ranges from T = 8 K to 30 K. The rate constants are calculated using qq-HTST theory including endoergic and exoergic transition corrections.

7.3.6.2 Diffusion constants of deuterium on amorphous solid water (ASW)

Similar to diffusion constant calculations in crystalline surface as discussed in Section 7.3.6.1, we have calculated the surface diffusion constants of the deuterium atom on the ASW surface using Equation (7.7). Plots of RMS distance ($Å^2$) versus time (sec) for two-dimensional deuterium atom diffusion on the ASW are shown in Figures 7.20 and 7.21 for *case (1)* at temperatures 10 K and 20 K, respectively, also refer to Figures 7.22 and 7.23 for *case (2).* All resulting diffusion constants (D) obtained at a range of temperatures are listed in Table 7.4 for *case (1),* and in Table 7.5 for *case (2).*

Similar trends in diffusion constants are observed for the ASW as for the I_h surface. The diffusion constants are higher at higher temperatures, which indicate faster diffusion of deuterium atom at higher temperatures. The diffusion constants are in much broader range in ASW, which varies from about 5.00×10^{-23} cm^2s^{-1} at 8 K to about 5.00×10^{-8} cm^2s^{-1} at 30 K. The diffusion constant is about 10^{15} times higher at 30 K i.e. 5.00×10^{-8} cm^2s^{-1} as compared to that at 8 K.

It is found that results obtained are noticeably different for the diffusion constants at certain temperatures for *case (1)* (See Table 7.4 and Figures 7.20-7.21), and for *case (2)*

(See Table 7.5 and Figures 7.22-7.23). Thus, in ASW, signs of the VAG barrier heights (ΔE^{VAG}) influence rate constants (k), and hence diffusion constants (D) obtained using QQ-HTST level of theory are slightly higher compared to the one obtained by considering endoergic and exoergic transition corrections.

It is seen that the values of diffusion constants are much lower in ASW as compared to those in the I_h surface. The diffusion constant is 4.73×10^{-19} cm^2s^{-1} at 10 K for the ASW surface, while its much higher in I_h surface at same temperature i.e. 5.00×10^{-7} cm^2s^{-1}.

Using an Arrhenius Equation (7.8), the effective diffusion energy barrier (E_{diff}) and pre-exponential factor (D_o) for deuterium diffusion on the ASW surface are obtained. We observe an Arrhenius type behaviour for deuterium atom diffusion as shown in Figure 7.24 for *case (1)* and calculated E_{diff} is about 32.634 meV, whereas Figure 7.25 represents *case (2)* and calculated E_{diff} is slightly lower i.e. 32.493 meV.

It is evident from our results that an effective diffusion barrier E_{diff} for deuterium is very high on the ASW as compared to the crystalline I_h surface, and values are listed in Table 7.6.

Table 7.4 Diffusion constant for D atom diffusion on amorphous solid water (ASW) at different temperatures (T). The rate constants are calculated using qq-HTST theory.

Temperature (T)	***Slope m* ($Å^2$ s^{-1})**	**D ($Å^2$ s^{-1})**	**D (cm^2 s^{-1})**
8	1.811×10^{-6}	4.528×10^{-7}	4.528×10^{-23}
10	1.888×10^{-2}	4.720×10^{-3}	4.720×10^{-19}
15	5.118×10^{3}	1.279×10^{3}	1.279×10^{-13}
20	3.291×10^{6}	8.228×10^{5}	8.228×10^{-11}
25	1.639×10^{8}	4.098×10^{7}	4.098×10^{-9}
30	2.110×10^{9}	5.275×10^{8}	5.275×10^{-8}

Table 7.5 Diffusion constant for D atom diffusion on amorphous solid water (ASW) at different temperatures (T). The rate constants are calculated using qq-HTST theory including endoergic and exoergic corrections.

Temperature (T)	*Slope* m ($Å^2\ s^{-1}$)	D ($Å^2\ s^{-1}$)	D ($cm^2\ s^{-1}$)
8	1.857×10^{-6}	4.643×10^{-7}	4.643×10^{-23}
10	1.832×10^{-2}	4.580×10^{-3}	4.580×10^{-19}
15	4.670×10^{3}	1.168×10^{3}	1.168×10^{-13}
20	2.997×10^{6}	7.493×10^{5}	7.493×10^{-11}
25	1.322×10^{8}	3.305×10^{7}	3.305×10^{-9}
30	1.995×10^{9}	4.988×10^{8}	4.988×10^{-8}

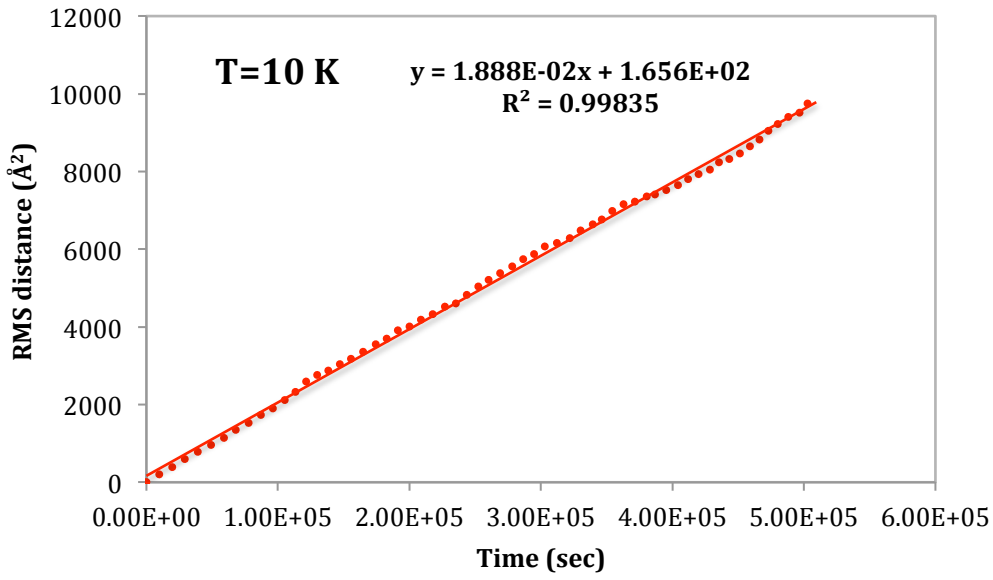

Figure 7.20 RMS distance ($Å^2$) versus time (sec) for D atom diffusion on ASW surface. The rate constants are calculated using qq-HTST theory at temperature of 10 K.

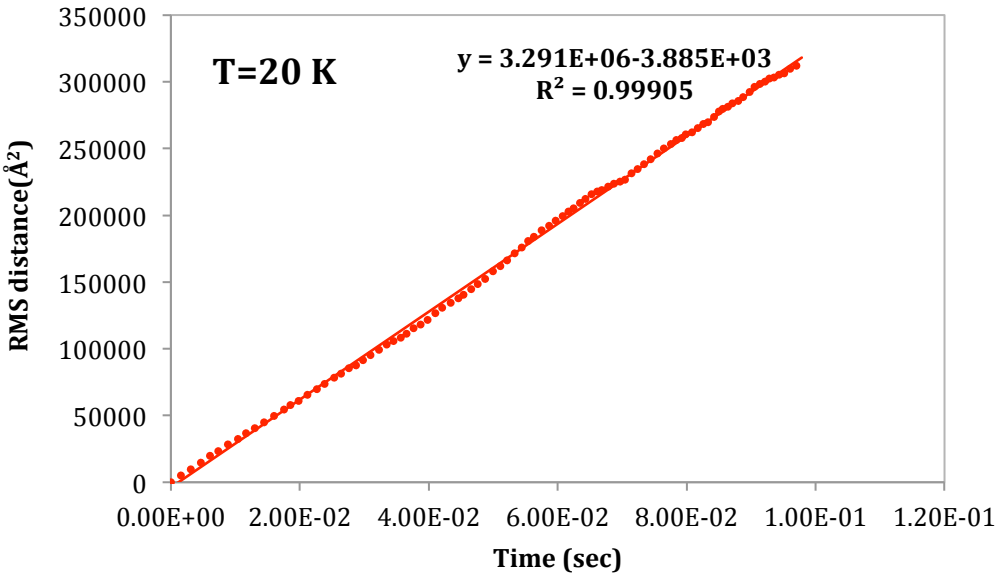

Figure 7.21 RMS distance (Å^2) versus time (sec) for D atom diffusion on ASW surface. The rate constants are calculated using qq-HTST theory at temperature of 20 K.

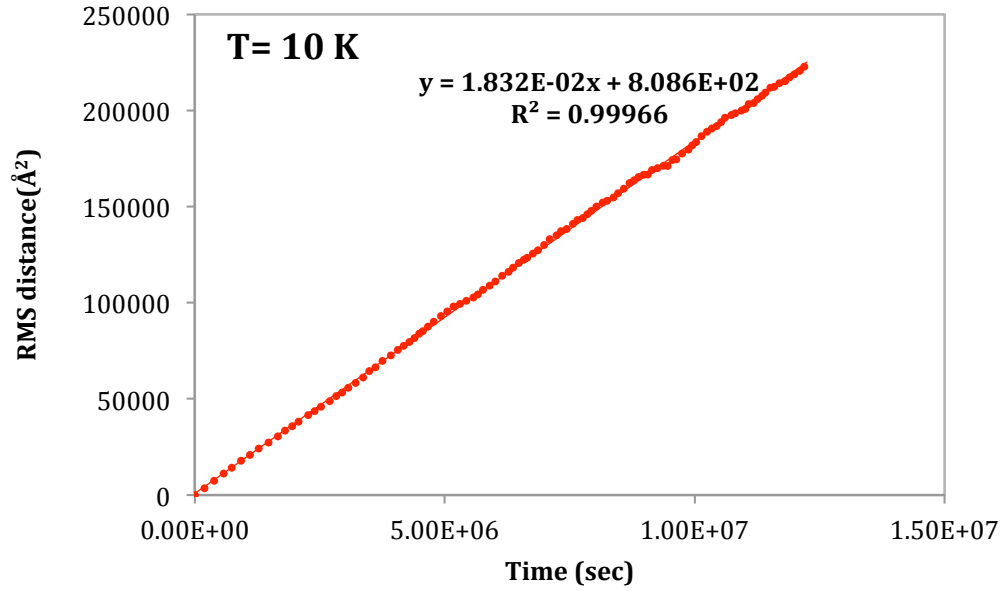

Figure 7.22 RMS distance (Å^2) versus time (sec) for D atom diffusion on ASW surface. The rate constants are calculated using qq-HTST theory including endoergic and exoergic corrections at temperature of 10 K.

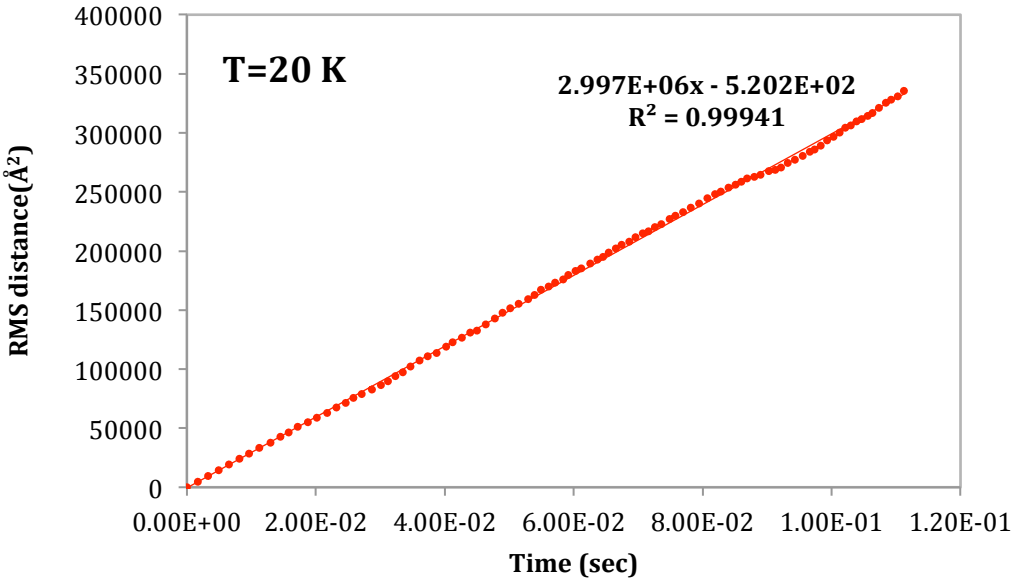

Figure 7.23 RMS distance ($Å^2$) versus time (sec) for D atom diffusion on ASW surface. The rate constants are calculated using qq-HTST theory including endoergic and exoergic corrections at temperature of 20 K.

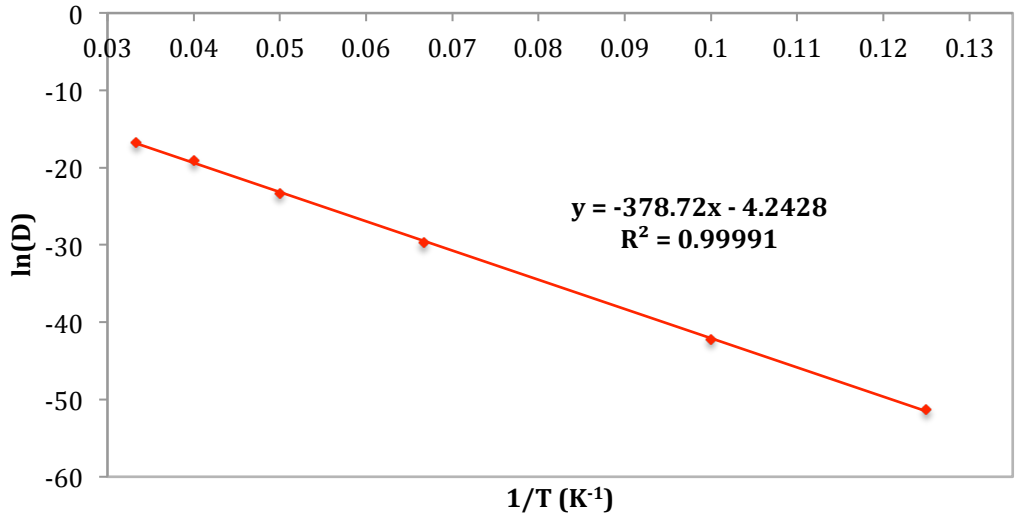

Figure 7.24 Arrhenius plot of the diffusion constants (D) of the deuterium on amorphous solid water (ASW): ln(D) versus 1/T (K^{-1}). Temperature ranges from T = 8 K to 30 K. The rate constants are calculated using qq-HTST theory.

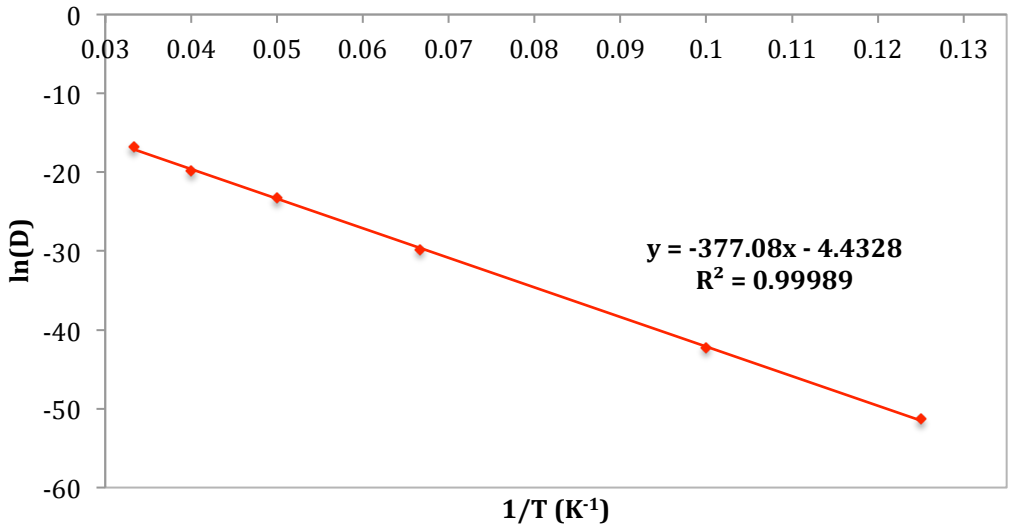

Figure 7.25 Arrhenius plot of the diffusion constants (D) of the deuterium on amorphous solid water (ASW): ln(D) versus 1/T (K^{-1}). Temperature ranges from T = 8 K to 30 K. The rate constants are calculated using qq-HTST theory including endoergic and exoergic corrections.

Table 7.6 Effective barrier height (meV) and pre-exponential factor (D_o) for the D atom diffusion on crystalline ice (I_h) and amorphous solid water (ASW) using QQHTST theory. Values in parenthesis are calculated using qq-HTST theory including endoergic and exoergic transitions corrections.

	Effective Barrier height (meV)	**Prefactor (D_o) ($cm^2\ s^{-1}$)**
I_h	7.166 (7.162)	1.64×10^{-3} (1.63×10^{-3})
ASW	32.634 (32.493)	1.44×10^{-2} (1.19×10^{-2})

7.4 Conclusions

Our results show significant difference in hopping characteristics of the deuterium atom on crystalline I_h and amorphous ASW ice surfaces. The morphology of an ice surface plays an important role in generating a different range of potential sites, which in turn influence classical binding energies, classical barrier heights, VAG barrier heights, rate constants, residence times, and diffusion constants. The classical binding energies and classical barrier heights are found to be significantly lower and in a narrow range for much smoother crystalline ice as compared to the complicated amorphous (ASW) surface. The classical binding energies of the deuterium atom are estimated to be in

range of 34.8-47.6 meV for crystalline surface while binding energy range of 39-79 meV is observed in amorphous ice surface.

The classical barrier height ranges are $\Delta E \leq 4.97$ meV and $\Delta E > 5$ meV for a crystalline ice surface, with a maximum barrier height of 13.9 meV. We show that different types of potential sites exist on ASW surface, where barrier heights ΔE are in range $\Delta E \leq 21$ meV, 26 meV, 30 meV and $\Delta E \geq 32$ meV, with a maximum barrier height of 48 meV which is much higher as compared to that for a crystalline surface. We observe that very shallow potential sites ($\Delta E \leq 21$ meV) dominate the diffusion of deuterium atom on the ASW on which atom diffuses rapidly, and in good agreement with the experimental results obtained by Hama *et al*. [319]. The activation energies for deuterium-atom diffusion on ASW surface are consistent with the experimental results [319], with barrier heights differences of about 2-3 meV are noticed. We notice that the deep potential sites with high barrier heights support slow diffusion while shallow potential sites with low barrier heights support fast diffusion. Thus, rate constants for deuterium-atom diffusion are higher at lower barrier heights and vice versa.

We observe shorter residence times in the crystalline I_h ice surface, which ranges from the picoseconds to the nanoseconds range, while the ASW surface gives comparatively longer residence times with a broader range from picoseconds to seconds at 10 K. In ASW, longer residence times indicate slow hopping of the deuterium atom between the local minima and the possibility of deuterium atom getting trapped in such sites. The fast hopping of deuterium atom on I_h surfaces indicate the rare possibility of deuterium atom to get trapped and therefore a very small possibility of recombination of diffusing deuterium atom with trapped deuterium atom to form deuterium molecule (D_2). However, due to the existence of a range of potential sites supporting both fast and slow diffusion, the recombination process is efficient on the ASW surface, where the diffusing deuterium atom can recombine with trapped deuterium atom to form D_2.

Long-timescale simulations using the adaptive kinetic Monte Carlo method on crystallline and amorphous solid water has predicted diffusion constants D , which are found to follow Arrhenius behaviour and the corresponding effective activation energy for diffusion of deuterium atom are found to be higher on the ASW as compared to the crystalline I_h surface. The effective diffusion energy barrier for deuterium is determined to be about 32.6 meV for the ASW surface, while a lower effective diffusion barrier of about 7.20 meV is calculated for the I_h surface. Our results show the temperature dependence of the diffusion constants, where diffusion constants increase with a rise in

temperature, which shows that diffusion of deuterium atom is faster at higher temperatures. The diffusion constants are also found to be much higher on the I_h surface ($D \approx 5.00\times10^{-7}$ cm^2s^{-1}) as compared to the ASW surface ($D \approx 4.73\times10^{-19}$ cm^2s^{-1}) at same surface temperature (at 10 K).

Chapter 8 - Overall Conclusions

The work presented in this thesis has provided insight into the UV spectroscopy and photochemistry of cyclic aromatic hydrocarbons such as benzene and naphthalene, as well as small water clusters and crystalline ice clusters. Firstly, smaller water clusters up to the water hexamer, and then larger crystalline ice cluster models were used, and their interactions with cyclic aromatic hydrocarbons were investigated. These were considered as astrophysically relevant systems to model polycyclic aromatic hydrocarbons (PAHs) interactions in interstellar ices, and to study their behaviour under UV field. Various computational chemistry techniques were used to study both ground and excited states of such systems, primarily excited states were studied, and further comparison with the available experimental data was presented. Surface diffusion of the deuterium (D) atom on both crystalline and amorphous ice at astronomically relevant temperatures was also investigated, which is also of astrophysical importance, to understand the hopping characteristics of the D atom, and eventually the D_2 formation on interstellar ice surfaces.

In Chapter 3, the benchmark computations using a wide range of electronic structure methods including linear response coupled cluster and TD-DFT methods were performed to study excited state properties of small water clusters from monomer up to the water pentamer. It was observed that electron correlation effects play an important role in such systems, with double excitations contributing significantly over singles, and lowers the excitation energies by about ≤ 2 eV. Thus CCS excitation energies were found to be higher by about ≤ 2 eV with respect to CCSD values, whereas triples excitation contributions were found to be very small such that CCSD and CC3 methods converge monotonically to similar energy values within ≤ 0.1 eV. Therefore, highly correlated CCSD and CC3 methods were found to perform better than the CCS method. TD-DFT excitation energies calculated were often too low by few eV (about 0.1-0.8 eV) as compared to the correlated coupled cluster CCSD and CC3 results. Similarly, TD-DFT oscillator strengths were also found to be too low in comparison to coupled cluster results. The coupled cluster excited state total dipole moments have shown reduction by about 13-37% with respect to ground state dipole moment in water monomer, depending on the excited state under study. In water dimer, total excited state dipole moments were found to increase by about 7-120% with respect to ground state whereas in water trimer, total excited state dipole moments were calculated to be about

three to five times larger than the ground state dipole moments. It was observed that excited states of water clusters exhibit a diffuse Rydberg type character. It is found that diffuse Rydberg type character increases with water cluster size for the lowest lying excited state, as quantified from the second moment of charge calculations. It was also shown that the lowest energy excitation associated with the central water molecule in water pentamer (C_{2v}) undergoes a blue shift of ~ 0.7 eV relative to water monomer (C_{2v}) at CCSD level, and compares well with the experimental blue shift of ~ 1 eV in condensed phase.

In Chapter 4, DFT and MP2 calculations were performed to obtain optimized ground state geometries and binding energies of the cage and the prism conformers of water W_6 clusters and Bz-W_6 clusters. The cage conformer of the Bz-W_6 system was found to be more stable than the prism conformer for all range of DFT functional and MP2. UV spectra of the cage clusters were found to differ noticeably from those of the prism geometries, as obtained by time dependent-DFT. Both M06-2X and CAM-B3LYP functionals performed consistently with each other. Benzene–mediated excitations of the water W_6 cluster towards longer wavelengths above 170 nm were noticed in both the cage and prism geometries of Bz-W_6 cluster, which were absent in the isolated water W_6 cluster. Benzene was also found to be influenced after interacting with the cage and prism W_6 geometries, and was seen to undergo a red shift in the main $\pi \rightarrow \pi^*$ electronic transition, in which the degeneracy is slightly broken. New charge transfer (CT) states and diffuse Rydberg-type states were also found to play an important role in the spectroscopy of such systems.

Similar studies were performed in Chapter 5 for naphthalene bound W_6 clusters. It was found by both MP2 and DFT calculations that the prism conformer of the naphthalene-bound water hexamer cluster is more stable with higher binding energy than the cage conformer, indicating strong binding preference of naphthalene for the prism conformer of the water hexamer. UV spectra obtained by M06-2X and CAM-B3LYP functionals are in good agreement with each other, while B3LYP spectra are slightly red-shifted towards longer wavelengths. Consistent with the UV spectra results for the Bz-W_6 cluster, the $\pi \rightarrow \pi^*$ electronic transition of naphthalene are found to be red-shifted in wavelengths and occur with lower intensities after interacting with the cage and prism-shaped W_6 clusters. We have predicted new electronic transition features that correspond to naphthalene charge transfer, and locally diffuse Rydberg type excitations, in addition to water excitations towards longer wavelengths in both the

cage and prism shaped geometries of the naphtha-W_6 cluster that are absent in isolated water W_6 cluster.

In Chapter 6, ground state geometries of benzene on a crystalline ice cluster model were systematically investigated by using the ONIOM(QM:AMOEBA) approach. It was found that the binding energies of benzene-bound ice complexes are sensitive to the dangling features of the binding sites. Benzene binding was found to be favourable for the binding sites containing both dangling-hydrogen and dangling-oxygen. It was observed that the size of the ice cluster and dangling features show minor effect on the UV spectral characteristics. The electronic excitations of water were noticed at wavelengths, where photon absorption cross section is negligible i.e. above 170 nm, indicating a benzene effect on excitations in water ice clusters, and are also in good agreement with experimental results. The intensities of peaks associated with water excitations in benzene-ice clusters were found to be higher than in isolated ice clusters. The $\pi \rightarrow \pi^*$ electronic transition of benzene in benzene-ice complexes undergoes a small red shift as compared to the isolated benzene molecule and this holds for all benzene-bound ice complexes.

In Chapter 7, the hopping characteristics of the deuterium atom on crystalline I_h and amorphous ASW ice surfaces were studied in detail. The different range of potential sites was found to be on I_h and amorphous ASW ice surfaces due to differences in the surface morphology. The classical binding energies and barrier heights calculated for the complicated amorphous (ASW) surface were significantly higher and in a broader range as compared to much smoother crystalline ice. The activation energies obtained for D-atom diffusion on ASW surface were in good agreement with the experimental results, within difference of about 2-3 meV. The range of potential sites was found to exist on ASW that support both fast and slow diffusion. It was found that deep potential sites with high barrier heights support the slow diffusion whereas shallow potential sites with low barrier heights support fast diffusion. The longer residence times were noticed in ASW that indicate the possibility of the deuterium atom to get trapped in such sites, while fast hopping on I_h surfaces makes it a rare possibility for deuterium atom to get trapped. Thus, the recombination process was found to be efficient on ASW surface, where the diffusing D atom can recombine with trapped D atom to form D_2 molecule. The diffusion constants (D) obtained using the adaptive kinetic Monte Carlo method were shown to follow Arrhenius behaviour and the corresponding effective diffusion enery barrier was found to be significantly higher for ASW as compared to the

crystalline I_h surface. The diffusion constants D were found to be much higher on I_h surface as compared to ASW surface at same surface temperature (10 K). It was also shown that diffusion constants increase with increase in temperature, which shows faster diffusion of the deuterium atom at higher temperatures.

References

[1] Brown, J.M., *Molecular spectroscopy*. Oxford chemistry primers. 1998, Oxford: Oxford University Press. vi, 89 p.

[2] Harris, D.C. and M.D. Bertolucci, *Symmetry and spectroscopy : an introduction to vibrational and electronic spectroscopy*. Dover classics of science and mathematics. 1989, New York: Dover. xii, 550 p.

[3] Hartquist, T.W. and D.A. Williams, *The chemically controlled cosmos : astronomical molecules from the Big Bang to exploding stars*. 1995, Cambridge: Cambridge University Press. xv, 169 p.

[4] Greenberg, J.M., *Cosmic dust and our origins*. Surf. Sci., 2002, **500**, 793-822.

[5] Williams, D.A. and E. Herbst, *It's a dusty Universe: surface science in space*. Surf. Sci., 2002, **500**, 823-837.

[6] Fraser, H.J., M.R.S. McCoustra, and D.A. Williams, *The molecular universe*. Astron. Geophys., 2002, **43**, 10-18.

[7] Tielens, A.G.G.M., *The physics and chemistry of the interstellar medium*. 2005, Cambridge: Cambridge University Press. xiii, 495 p.

[8] Herbst, E., *Chemistry in the Cold, Warm, and Hot Interstellar Medium*. AIP Conf. Proc., 2013, **1543**, 15-30.

[9] Herbst, E., *Chemistry in the Interstellar-Medium*. Annu. Rev. Phys. Chem., 1995, **46**, 27-53.

[10] Anderson, L.D., T.M. Bania, J.M. Jackson, D.P. Clemens, M. Heyer, R. Simon, R.Y. Shah, and J.M. Rathborne, *The Molecular Properties of Galactic H Ii Regions*. Astrophys. J. Suppl. S., 2009, **181**, 255-271.

[11] Allamandola, L.J., M.P. Bernstein, S.A. Sandford, and R.L. Walker, *Evolution of interstellar ices*. Space. Sci. Rev., 1999, **90**, 219-232.

[12] Trumpler, R.J., *Absorption of Light in the Galactic System (Reprinted from Publications of the Astronomical Society of the Pacific, Vol 42, 1930)*. Publ. Astron. Soc. Pac., 1988, **100**, 297-309.

[13] Snow, T.P., J.H. Black, E.F. vanDishoeck, G. Burks, R.M. Crutcher, B.L. Lutz, M.M. Hanson, and R.Y. Shuping, *The translucent molecular clouds toward hd 154368 .1. Extinction, abundances, and depletions*. Astrophys. J., 1996, **465**, 245-263.

[14] Bergin, E.A., G.J. Melnick, J.R. Stauffer, M.L.N. Ashby, G. Chin, N.R. Erickson, P.F. Goldsmith, M. Harwit, J.E. Howe, S.C. Kleiner, D.G. Koch, D.A. Neufeld, B.M. Patten, R. Plume, R. Schieder, R.L. Snell, V. Tolls, Z. Wang, G. Winnewisser, and Y.F. Zhang, *Implications of Submillimeter Wave Astronomy Satellite observations for interstellar chemistry and star formation*. Astrophys. J., 2000, **539**, L129-L132.

[15] Gould, R.J. and E.E. Salpeter, *Interstellar Abundance of Hydrogen Molecule .1. Basic Processes*. Astrophys. J., 1963, **138**, 393.

[16] Gillett, F.C. and W.J. Forrest, *Spectra of Becklin-Neugebauer Point Source and Kleinmann-Low Nebula from 2.8 to 13.5 Microns*. Astrophys. J., 1973, **179**, 483-491.

[17] Henderson, M.A., *The interaction of water with solid surfaces: fundamental aspects revisited*. Surf. Sci. Rep., 2002, **46**, 1-308.

[18] Thiel, P.A. and T.E. Madey, *The Interaction of Water with Solid-Surfaces - Fundamental-Aspects*. Surf. Sci. Rep., 1987, **7**, 211-385.

[19] Gibb, E.L., D.C.B. Whittet, W.A. Schutte, A.C.A. Boogert, J.E. Chiar, P. Ehrenfreund, P.A. Gerakines, J.V. Keane, A.G.G.M. Tielens, E.F. van Dishoeck, and O. Kerkhof, *An inventory of interstellar ices toward the embedded protostar W33A*. Astrophys. J., 2000, **536**, 347-356.

[20] van Dishoeck, E.F., *ISO spectroscopy of gas and dust: From molecular clouds to protoplanetary disks*. Annu. Rev. Astron. Astr., 2004, **42**, 119-167.

[21] Mathis, J.S., P.G. Mezger, and N. Panagia, *Interstellar Radiation-Field and Dust Temperatures in the Diffuse Interstellar Matter and in Giant Molecular Clouds*. Astron. Astrophys., 1983, **128**, 212-229.

[22] Hollenbach, D., M.J. Kaufman, E.A. Bergin, and G.J. Melnick, *Water, O-2, and Ice in Molecular Clouds*. Astrophys. J., 2009, **690**, 1497-1521.

[23] Dominik, C., C. Ceccarelli, D. Hollenbach, and M. Kaufman, *Gas-phase water in the surface layer of protoplanetary disks*. Astrophys. J., 2005, **635**, L85-L88.

[24] Shen, C.J., J.M. Greenberg, W.A. Schutte, and E.F. van Dishoeck, *Cosmic ray induced explosive chemical desorption in dense clouds*. Astron. Astrophys., 2004, **415**, 203-215.

[25] Allamandola, L.J., *Interstellar PAHs: Yesterday, today, and tomorrow*. Abstr. Pap. Am. Chem. Soc., 2006, **231**.

[26] Allamandola, L.J., A.G.G.M. Tielens, and J.R. Barker, *Interstellar Polycyclic Aromatic-Hydrocarbons - the Infrared-Emission Bands, the Excitation Emission Mechanism, and the Astrophysical Implications*. Astrophys. J. Suppl. S., 1989, **71**, 733-775.

[27] Leger, A. and J.L. Puget, *Identification of the Unidentified Ir Emission Features of Interstellar Dust*. Astron. Astrophys., 1984, **137**, L5-L8.

[28] Hudgins, D.M. and L.J. Allamandola, *Interstellar PAH emission in the 11-14 micron region: New insights from laboratory data and a tracer of ionized PAHs*. Astrophys. J., 1999, **516**, L41-L44.

[29] Gillett, F.C., W.J. Forrest, and K.M. Merrill, *8-13-Micron Spectra of Ngc-7027, Bd+30 Degrees 3639, and Ngc-6572*. Astrophys. J., 1973, **183**, 87-93.

[30] Peeters, E., S. Hony, C. Van Kerckhoven, A.G.G.M. Tielens, L.J. Allamandola, D.M. Hudgins, and C.W. Bauschlicher, *The rich 6 to 9 mu m spectrum of interstellar PAHs*. Astron. Astrophys., 2002, **390**, 1089-1113.

[31] Ehrenfreund, P., J. Cami, E. Dartois, and B.H. Foing, *Diffuse interstellar bands towards BD+63 degrees 1964 - A new reference target*. Astron. Astrophys., 1997, **318**, L28-L31.

[32] Herbig, G.H., *The Diffuse Interstellar Bands*. Annu. Rev. Astron. Astr., 1995, **33**, 19-73.

[33] Cernicharo, J., A.M. Heras, A.G.G.M. Tielens, J.R. Pardo, F. Herpin, M. Guelin, and L.B.F.M. Waters, *Infrared Space Observatory's discovery of C-4H2, C-6H2, and benzene in CRL 618*. Astrophys. J., 2001, **546**, L123-L126.

[34] Iglesias-Groth, S., A. Manchado, D.A. Garcia-Hernandez, J.I.G. Hernandez, and D.L. Lambert, *Evidence for the Naphthalene Cation in a Region of the Interstellar Medium with Anomalous Microwave Emission*. Astrophys. J. Lett., 2008, **685**, L55-L58.

[35] Krelowski, J., G.A. Galazutdinov, F.A. Musaev, and J. Nirski, *Identification of the naphthalene cation in space?* Mon. Not. R. Astron. Soc., 2001, **328**, 810-814.

[36] Snow, T.P., *On Ionized Naphthalene (C10h8+) as a Carrier of Diffuse Interstellar Bands*. Astrophys. J., 1992, **401**, 775-777.

[37] Hiraya, A. and K. Shobatake, *Direct Absorption-Spectra of Jet-Cooled Benzene in 130-260-Nm*. J. Chem. Phys., 1991, **94**, 7700-7706.
[38] Pantos, E., J. Philis, and A. Bolovinos, *Extinction Coefficient of Benzene Vapor in Region 4.6 to 36 Ev*. J. Mol. Spectrosc., 1978, **72**, 36-43.
[39] Newton, D., *Revise A2 chemistry for Salters*. New ed. Salters advanced chemistry. 2009, Oxford: Heinemann. 112 p.
[40] Hashimoto, T., H. Nakano, and K. Hirao, *Theoretical study of the valence pi->pi* excited states of polyacenes: Benzene and naphthalene*. J. Chem. Phys., 1996, **104**, 6244-6258.
[41] Kadantsev, E.S., M.J. Stott, and A. Rubio, *Electronic structure and excitations in oligoacenes from ab initio calculations*. J. Chem. Phys., 2006, **124**.
[42] Lopata, K., R. Reslan, M. Kowaska, D. Neuhauser, N. Govind, and K. Kowalski, *Excited-State Studies of Polyacenes: A Comparative Picture Using EOMCCSD, CR-EOMCCSD(T), Range-Separated (LR/RT)-TDDFT, TD-PM3, and TD-ZINDO*. J. Chem. Theory. Comput., 2011, **7**, 3686-3693.
[43] Packer, M.J., E.K. Dalskov, T. Enevoldsen, H.J.A. Jensen, and J. Oddershede, *A new implementation of the second-order polarization propagator approximation (SOPPA): The excitation spectra of benzene and naphthalene*. J. Chem. Phys., 1996, **105**, 5886-5900.
[44] Biermann, D. and W. Schmidt, *Diels-Alder Reactivity of Polycyclic Aromatic-Hydrocarbons .1. Acenes and Benzologs*. J. Am. Chem. Soc., 1980, **102**, 3163-3173.
[45] George, G.A. and G.C. Morris, *Intensity of Absorption of Naphthalene from 30 000 Cm-1 to 53 000 Cm-1*. J. Mol. Spectrosc., 1968, **26**, 67-71.
[46] Grimme, S. and M. Parac, *Substantial errors from time-dependent density functional theory for the calculation of excited states of large pi systems*. Chemphyschem, 2003, **4**, 292-295.
[47] Huebner, R.H., Mielczar.Sr, and C.E. Kuyatt, *Electron Energy-Loss Spectroscopy of Naphthalene Vapor*. Chem. Phys. Lett., 1972, **16**, 464-469.
[48] Westley, M.S., R.A. Baragiola, R.E. Johnson, and G.A. Baratta, *Photodesorption from Low-Temperature Water Ice in Interstellar and Circumsolar Grains*. Nature, 1995, **373**, 405-407.
[49] Westley, M.S., R.A. Baragiola, R.E. Johnson, and G.A. Baratta, *Ultraviolet Photodesorption from Water Ice*. Planet. Space Sci., 1995, **43**, 1311-1315.
[50] Nishi, N., H. Shinohara, and T. Okuyama, *Photodetachment, Photodissociation, and Photochemistry of Surface Molecules of Icy Solids Containing Nh3 and Pure H2o Ices*. J. Chem. Phys., 1984, **80**, 3898-3910.
[51] Oberg, K.I., H. Linnartz, R. Visser, and E.F. van Dishoeck, *Photodesorption of Ices. Ii. H2o and D2o*. Astrophys. J., 2009, **693**, 1209-1218.
[52] Andersson, S., A. Al-Halabi, G.J. Kroes, and E.F. van Dishoeck, *Molecular-dynamics study of photodissociation of water in crystalline and amorphous ices*. J. Chem. Phys., 2006, **124**.
[53] Yabushita, A., T. Hama, M. Yokoyama, M. Kawasaki, S. Andersson, R.N. Dixon, M.N.R. Ashfold, and N. Watanabe, *Translational and Rotational Energy Measurements of Photodesorbed Water Molecules in Their Vibrational Ground State from Amorphous Solid Water*. Astrophys. J. Lett., 2009, **699**, L80-L83.
[54] Baratta, G.A., G. Leto, F. Spinella, G. Strazzulla, and G. Foti, *The 3.1 Mu-M Feature in Ion-Irradiated Water Ice*. Astron. Astrophys., 1991, **252**, 421-424.

[55] Leto, G. and G.A. Baratta, *Ly-alpha photon induced amorphization of Ic water ice at 16 Kelvin - Effects and quantitative comparison with ion irradiation*. Astron. Astrophys., 2003, **397**, 7-13.

[56] Moore, M.H. and R.L. Hudson, *Far-Infrared Spectral Studies of Phase-Changes in Water Ice Induced by Proton Irradiation*. Astrophys. J., 1992, **401**, 353-360.

[57] Bernstein, M.P., S.A. Sandford, L.J. Allamandola, S. Chang, and M.A. Scharberg, *Organic-Compounds Produced by Photolysis of Realistic Interstellar and Cometary Ice Analogs Containing Methanol*. Astrophys. J., 1995, **454**, 327-344.

[58] Bernstein, M.P., S.A. Sandford, L.J. Allamandola, J.S. Gillette, S.J. Clemett, and R.N. Zare, *UV irradiation of polycyclic aromatic hydrocarbons in ices: Production of alcohols, quinones, and ethers*. Science, 1999, **283**, 1135-1138.

[59] Woon, D.E. and J.Y. Park, *Photoionization of benzene and small polycyclic aromatic hydrocarbons in ultraviolet-processed astrophysical ices: A computational study*. Astrophys. J., 2004, **607**, 342-345.

[60] Kobayashi, K., *Optical-Spectra and Electronic-Structure of Ice*. J. Phys. Chem., 1983, **87**, 4317-4321.

[61] Mota, R., R. Parafita, A. Giuliani, M.J. Hubin-Franskin, J.M.C. Lourenco, G. Garcia, S.V. Hoffmann, N.J. Mason, P.A. Ribeiro, M. Raposo, and P. Limao-Vieira, *Water VUV electronic state spectroscopy by synchrotron radiation*. Chem. Phys. Lett., 2005, **416**, 152-159.

[62] Chipman, D.M., *Excited electronic states of small water clusters*. J. Chem. Phys., 2005, **122**.

[63] do Couto, P.C. and D.M. Chipman, *Insights into the ultraviolet spectrum of liquid water from model calculations*. J. Chem. Phys., 2010, **132**.

[64] do Couto, P.C. and D.M. Chipman, *Insights into the ultraviolet spectrum of liquid water from model calculations: The different roles of donor and acceptor hydrogen bonds in water pentamers*. J. Chem. Phys., 2012, **137**.

[65] Pribble, R.N. and T.S. Zwier, *Probing Hydrogen-Bonding in Benzene-(Water)(N) Clusters Using Resonant Ion-Dip Ir Spectroscopy*. Faraday Discuss., 1994, **97**, 229-241.

[66] Garrett, A.W. and T.S. Zwier, *Multiphoton Ionization Studies of Clusters of Immiscible Liquids .2. C6h6-(H2o)N, N=3-8 and (C6h6)2-(H2o)1,2*. J. Chem. Phys., 1992, **96**, 3402-3410.

[67] Gotch, A.J. and T.S. Zwier, *Multiphoton Ionization Studies of Clusters of Immiscible Liquids .1. C6h6-(H2o)N, N=1,2*. J. Chem. Phys., 1992, **96**, 3388-3401.

[68] Elsila, J.E., M.R. Hammond, M.P. Bernstein, S.A. Sandford, and R.N. Zare, *UV photolysis of quinoline in interstellar ice analogs*. Meteorit. Planet. Sci., 2006, **41**, 785-796.

[69] Oberg, K.I., G.W. Fuchs, Z. Awad, H.J. Fraser, S. Schlemmer, E.F. Van Dishoeck, and H. Linnartz, *Photodesorption of CO ice*. Astrophys. J., 2007, **662**, L23-L26.

[70] Thrower, J.D., A.G.M. Abdulgalil, M.P. Collings, M.R.S. McCoustra, D.J. Burke, W.A. Brown, A. Dawes, P.J. Holtom, P. Kendall, N.J. Mason, F. Jamme, H.J. Fraser, and F.J.M. Rutten, *Photon- and electron-stimulated desorption from laboratory models of interstellar ice grains*. J. Vac. Sci. Technol. A, 2010, **28**, 799-806.

[71] Thrower, J.D., D.J. Burke, M.P. Collings, A. Dawes, P.D. Holtom, F. Jamme, P. Kendall, W.A. Brown, I.P. Clark, H.J. Fraser, M.R.S. McCoustra, N.J. Mason, and A.W. Parker, *Desorption of hot molecules from photon irradiated interstellar ices*. Astrophys. J., 2008, **673**, 1233-1239.
[72] Thrower, J.D., M.P. Collings, M.R.S. McCoustra, D.J. Burke, W.A. Brown, A. Dawes, P.D. Holtom, P. Kendall, N.J. Mason, F. Jamme, H.J. Fraser, I.P. Clark, and A.W. Parker, *Surface science investigations of photoprocesses in model interstellar ices*. J. Vac. Sci. Technol. A, 2008, **26**, 919-924.
[73] Bouwman, J., H.M. Cuppen, A. Bakker, L.J. Allamandola, and H. Linnartz, *Photochemistry of the PAH pyrene in water ice: the case for ion-mediated solid-state astrochemistry*. Astron. Astrophys., 2010, **511**.
[74] Bouwman, J., H.M. Cuppen, M. Steglich, L.J. Allamandola, and H. Linnartz, *Photochemistry of polycyclic aromatic hydrocarbons in cosmic water ice II. Near UV/VIS spectroscopy and ionization rates*. Astron. Astrophys., 2011, **529**.
[75] Upadhyay, D.M. and P.C. Mishra, *Binding of benzene with water clusters (H2O)(n), n=1-6, in the ground and lowest singlet excited states*. J. Mol. Struc-TheoChem., 2002, **584**, 113-133.
[76] Atkins, P.W. and R. Friedman, *Molecular quantum mechanics*. 5th ed. 2011, Oxford: Oxford University Press. xiv, 537 p.
[77] Szabo, A. and N.S. Ostlund, *Modern quantum chemistry : introduction to advanced electronic structure theory*. 1996, Mineola, N.Y London: Dover ;Constable and Company [distributor]. xiv, 466 p.
[78] Cramer, C.J., *Essentials of computational chemistry : theories and models*. 2nd ed. 2004, Chichester Hoboken, NJ: Wiley. xx, 596 p.
[79] Worth, G.A. and L.S. Cederbaum, *Beyond Born-Oppenheimer: Molecular dynamics through a conical intersection*. Annu. Rev. Phys. Chem., 2004, **55**, 127-158.
[80] Simons, J., *An introduction to theoretical chemistry*. xiii, 461 pages.
[81] Mousseau, N. and G.T. Barkema, *Traveling through potential energy landscapes of disordered materials: The activation-relaxation technique*. Phys. Rev. E, 1998, **57**, 2419-2424.
[82] Barkema, G.T. and N. Mousseau, *Event-based relaxation of continuous disordered systems*. Phys. Rev. Lett., 1996, **77**, 4358-4361.
[83] Malek, R. and N. Mousseau, *Dynamics of Lennard-Jones clusters: A characterization of the activation-relaxation technique*. Phys. Rev. E, 2000, **62**, 7723-7728.
[84] Sankey, O.F., D.A. Drabold, and A. Gibson, *Projected Random Vectors and the Recursion Method in the Electronic-Structure Problem*. Phys. Rev. B, 1994, **50**, 1376-1381.
[85] Press, W.H. and W.T. Vetterling, *Numerical recipes in C : the art of scientific computing*. 1988, Cambridge: Cambridge University Press.
[86] Steinfeld, J.I., J.S. Francisco, and W.L. Hase, *Chemical kinetics and dynamics*. 1989, Englewood Cliffs: Prentice-Hall. xii, 548 p.
[87] Hanggi, P., P. Talkner, and M. Borkovec, *Reaction-Rate Theory - 50 Years after Kramers*. Rev. Mod. Phys., 1990, **62**, 251-341.
[88] Vineyard, G.H., *Frequency Factors and Isotope Effects in Solid State Rate Processes*. J. Phys. Chem. Solids, 1957, **3**, 121-127.

[89] Henkelman, G. and H. Jonsson, *Long time scale kinetic Monte Carlo simulations without lattice approximation and predefined event table*. J. Chem. Phys., 2001, **115**, 9657-9666.
[90] Pedersen, A. and H. Jonsson, *Distributed implementation of the adaptive kinetic Monte Carlo method*. Math. Comput. Simulat., 2010, **80**, 1487-1498.
[91] http://www.theochem.org/EON.
[92] Karssemeijer, L.J., A. Pedersen, H. Jonsson, and H.M. Cuppen, *Long-timescale simulations of diffusion in molecular solids*. Phys Chem Chem Phys, 2012, **14**, 10844-10852.
[93] Koch, W. and M.C. Holthausen, *A chemist's guide to density functional theory*. 2nd ed. 2001, Weinheim ; Chichester: Wiley-VCH. xiii, 300 p.
[94] Jensen, F., *Introduction to computational chemistry*. 1999, Chichester: Wiley. xvi, 429 p.
[95] Piela, L., *Ideas of quantum chemistry*. 2007, Amsterdam ; London: Elsevier. xxxiv, 1086 p.
[96] Roothaan, C.C.J., *New Developments in Molecular Orbital Theory*. Rev. Mod. Phys., 1951, **23**, 69-89.
[97] Slater, J.C., *Atomic shielding constants*. Phys. Rev., 1930, **36**, 0057-0064.
[98] Hehre, W.J., R.F. Stewart, and J.A. Pople, *Self-Consistent Molecular-Orbital Methods .I. Use of Gaussian Expansions of Slater-Type Atomic Orbitals*. J. Chem. Phys., 1969, **51**, 2657-&.
[99] Binkley, J.S., J.A. Pople, and W.J. Hehre, *Self-Consistent Molecular-Orbital Methods .21. Small Split-Valence Basis-Sets for 1st-Row Elements*. J. Am. Chem. Soc., 1980, **102**, 939-947.
[100] Hehre, W.J., Ditchfie.R, and J.A. Pople, *Self-Consistent Molecular-Orbital Methods .12. Further Extensions of Gaussian-Type Basis Sets for Use in Molecular-Orbital Studies of Organic-Molecules*. J. Chem. Phys., 1972, **56**, 2257.
[101] Krishnan, R., J.S. Binkley, R. Seeger, and J.A. Pople, *Self-Consistent Molecular-Orbital Methods .20. Basis Set for Correlated Wave-Functions*. J. Chem. Phys., 1980, **72**, 650-654.
[102] Francl, M.M., W.J. Pietro, W.J. Hehre, J.S. Binkley, M.S. Gordon, D.J. Defrees, and J.A. Pople, *Self-Consistent Molecular-Orbital Methods .23. A Polarization-Type Basis Set for 2nd-Row Elements*. J. Chem. Phys., 1982, **77**, 3654-3665.
[103] Harihara.Pc and J.A. Pople, *Influence of Polarization Functions on Molecular-Orbital Hydrogenation Energies*. Theor. Chem. Acc., 1973, **28**, 213-222.
[104] Frisch, M.J., J.A. Pople, and J.S. Binkley, *Self-Consistent Molecular-Orbital Methods .25. Supplementary Functions for Gaussian-Basis Sets*. J. Chem. Phys., 1984, **80**, 3265-3269.
[105] Dunning, T.H., *Gaussian-Basis Sets for Use in Correlated Molecular Calculations .1. The Atoms Boron through Neon and Hydrogen*. J. Chem. Phys., 1989, **90**, 1007-1023.
[106] Kendall, R.A., T.H. Dunning, and R.J. Harrison, *Electron-Affinities of the 1st-Row Atoms Revisited - Systematic Basis-Sets and Wave-Functions*. J. Chem. Phys., 1992, **96**, 6796-6806.
[107] Woon, D.E. and T.H. Dunning, *Gaussian-Basis Sets for Use in Correlated Molecular Calculations .3. The Atoms Aluminum through Argon*. J. Chem. Phys., 1993, **98**, 1358-1371.

[108] van Duijneveldt, F.B., J.G.C.M. van Duijneveldt-van de Rijdt, and J.H. van Lenthe, *State of the Art in Counterpoise Theory*. Chem. Rev., 1994, **94**, 1873-1885.
[109] Moller, C. and M.S. Plesset, *Note on an approximation treatment for many-electron systems*. Phys. Rev., 1934, **46**, 0618-0622.
[110] Friesner, R.A., *Ab initio quantum chemistry: Methodology and applications*. P. Natl. Acad. Sci. USA., 2005, **102**, 6648-6653.
[111] Tkatchenko, A., R.A. DiStasio, M. Head-Gordon, and M. Scheffler, *Dispersion-corrected Moller-Plesset second-order perturbation theory*. J. Chem. Phys., 2009, **131**.
[112] Riley, K.E. and P. Hobza, *Assessment of the MP2 method, along with several basis sets, for the computation of interaction energies of biologically relevant hydrogen bonded and dispersion bound complexes*. J. Phys. Chem. A, 2007, **111**, 8257-8263.
[113] Murphy, R.B., M.D. Beachy, R.A. Friesner, and M.N. Ringnalda, *Pseudospectral Localized Moller-Plesset Methods - Theory and Calculation of Conformational Energies*. J. Chem. Phys., 1995, **103**, 1481-1490.
[114] Tsuzuki, S., T. Uchimaru, K. Matsumura, M. Mikami, and K. Tanabe, *Effects of basis set and electron correlation on the calculated interaction energies of hydrogen bonding complexes: MP2/cc-pV5Z calculations of H2O-MeOH, H2O-Me2O, H2O-H2CO, MeOH-MeOH, and HCOOH-HCOOH complexes*. J. Chem. Phys., 1999, **110**, 11906-11910.
[115] Tsuzuki, S., T. Uchimaru, and K. Tanabe, *Intermolecular interaction potentials of methane and ethylene dimers calculated with the Moller-Plesset, coupled cluster and density functional methods*. Chem. Phys. Lett., 1998, **287**, 202-208.
[116] Purvis, G.D. and R.J. Bartlett, *A Full Coupled-Cluster Singles and Doubles Model - the Inclusion of Disconnected Triples*. J. Chem. Phys., 1982, **76**, 1910-1918.
[117] Noga, J. and R.J. Bartlett, *The Full Ccsdt Model for Molecular Electronic-Structure*. J. Chem. Phys., 1987, **86**, 7041-7050.
[118] Christiansen, O., H. Koch, and P. Jorgensen, *The 2nd-Order Approximate Coupled-Cluster Singles and Doubles Model Cc2*. Chem. Phys. Lett., 1995, **243**, 409-418.
[119] Koch, H., O. Christiansen, P. Jorgensen, A.M.S. deMeras, and T. Helgaker, *The CC3 model: An iterative coupled cluster approach including connected triples*. J. Chem. Phys., 1997, **106**, 1808-1818.
[120] Christiansen, O., H. Koch, and P. Jorgensen, *Response Functions in the Cc3 Iterative Triple Excitation Model*. J. Chem. Phys., 1995, **103**, 7429-7441.
[121] Hohenberg, P. and W. Kohn, *Inhomogeneous Electron Gas*. Phys. Rev. B, 1964, **136**, B864.
[122] Kohn, W. and L.J. Sham, *Self-Consistent Equations Including Exchange and Correlation Effects*. Phys. Rev., 1965, **140**, 1133-&.
[123] Perdew, J.P. and Y. Wang, *Accurate and Simple Analytic Representation of the Electron-Gas Correlation-Energy*. Phys. Rev. B, 1992, **45**, 13244-13249.
[124] Becke, A.D., *Density-Functional Exchange-Energy Approximation with Correct Asymptotic-Behavior*. Phys. Rev. A, 1988, **38**, 3098-3100.
[125] Lee, C.T., W.T. Yang, and R.G. Parr, *Development of the Colle-Salvetti Correlation-Energy Formula into a Functional of the Electron-Density*. Phys. Rev. B, 1988, **37**, 785-789.

[126] Becke, A.D., *A New Mixing of Hartree-Fock and Local Density-Functional Theories*. J. Chem. Phys., 1993, **98**, 1372-1377.
[127] Stephens, P.J., F.J. Devlin, C.F. Chabalowski, and M.J. Frisch, *Ab-Initio Calculation of Vibrational Absorption and Circular-Dichroism Spectra Using Density-Functional Force-Fields*. J. Phys. Chem., 1994, **98**, 11623-11627.
[128] Zhao, Y., N.E. Schultz, and D.G. Truhlar, *Design of density functionals by combining the method of constraint satisfaction with parametrization for thermochemistry, thermochemical kinetics, and noncovalent interactions*. J. Chem. Theory. Comput., 2006, **2**, 364-382.
[129] Zhao, Y. and D.G. Truhlar, *The M06 suite of density functionals for main group thermochemistry, thermochemical kinetics, noncovalent interactions, excited states, and transition elements: two new functionals and systematic testing of four M06-class functionals and 12 other functionals*. Theor. Chem. Acc., 2008, **120**, 215-241.
[130] Chai, J.D. and M. Head-Gordon, *Long-range corrected hybrid density functionals with damped atom-atom dispersion corrections*. Phys. Chem. Chem. Phys., 2008, **10**, 6615-6620.
[131] Yanai, T., D.P. Tew, and N.C. Handy, *A new hybrid exchange-correlation functional using the Coulomb-attenuating method (CAM-B3LYP)*. Chem. Phys. Lett., 2004, **393**, 51-57.
[132] Tawada, Y., T. Tsuneda, S. Yanagisawa, T. Yanai, and K. Hirao, *A long-range-corrected time-dependent density functional theory*. J. Chem. Phys., 2004, **120**, 8425-8433.
[133] Schwabe, T. and S. Grimme, *Double-hybrid density functionals with long-range dispersion corrections: higher accuracy and extended applicability*. Phys. Chem. Chem. Phys., 2007, **9**, 3397-3406.
[134] Allinger, N.L., *Conformational-Analysis .130. Mm2 - Hydrocarbon Force-Field Utilizing V1 and V2 Torsional Terms*. J. Am. Chem. Soc., 1977, **99**, 8127-8134.
[135] Lii, J.H. and N.L. Allinger, *Molecular Mechanics - the Mm3 Force-Field for Hydrocarbons .3. The Vanderwaals Potentials and Crystal Data for Aliphatic and Aromatic-Hydrocarbons*. J. Am. Chem. Soc., 1989, **111**, 8576-8582.
[136] Cornell, W.D., P. Cieplak, C.I. Bayly, I.R. Gould, K.M. Merz, D.M. Ferguson, D.C. Spellmeyer, T. Fox, J.W. Caldwell, and P.A. Kollman, *A 2nd Generation Force-Field for the Simulation of Proteins, Nucleic-Acids, and Organic-Molecules*. J. Am. Chem. Soc., 1995, **117**, 5179-5197.
[137] Casewit, C.J., K.S. Colwell, and A.K. Rappe, *Application of a Universal Force-Field to Main Group Compounds*. J. Am. Chem. Soc., 1992, **114**, 10046-10053.
[138] Casewit, C.J., K.S. Colwell, and A.K. Rappe, *Application of a Universal Force-Field to Organic-Molecules*. J. Am. Chem. Soc., 1992, **114**, 10035-10046.
[139] Brooks, B.R., R.E. Bruccoleri, B.D. Olafson, D.J. States, S. Swaminathan, and M. Karplus, *Charmm - a Program for Macromolecular Energy, Minimization, and Dynamics Calculations*. J. Comput. Chem., 1983, **4**, 187-217.
[140] Hwang, M.J., T.P. Stockfisch, and A.T. Hagler, *Derivation of Class-Ii Force-Fields .2. Derivation and Characterization of a Class-Ii Force-Field, Cff93, for the Alkyl Functional-Group and Alkane Molecules*. J. Am. Chem. Soc., 1994, **116**, 2515-2525.
[141] Scott, W.R.P., P.H. Hunenberger, I.G. Tironi, A.E. Mark, S.R. Billeter, J. Fennen, A.E. Torda, T. Huber, P. Kruger, and W.F. van Gunsteren, *The GROMOS*

biomolecular simulation program package. J. Phys. Chem. A, 1999, **103**, 3596-3607.
[142] Damm, W., A. Frontera, J. TiradoRives, and W.L. Jorgensen, *OPLS all-atom force field for carbohydrates*. J. Comput. Chem., 1997, **18**, 1955-1970.
[143] Shi, Y., Z. Xia, J.J. Zhang, R. Best, C.J. Wu, J.W. Ponder, and P.Y. Ren, *Polarizable Atomic Multipole-Based AMOEBA Force Field for Proteins*. J. Chem. Theory. Comput., 2013, **9**, 4046-4063.
[144] Ponder, J.W., C.J. Wu, P.Y. Ren, V.S. Pande, J.D. Chodera, M.J. Schnieders, I. Haque, D.L. Mobley, D.S. Lambrecht, R.A. DiStasio, M. Head-Gordon, G.N.I. Clark, M.E. Johnson, and T. Head-Gordon, *Current Status of the AMOEBA Polarizable Force Field*. J. Phys. Chem. B, 2010, **114**, 2549-2564.
[145] Ren, P.Y. and J.W. Ponder, *Temperature and pressure dependence of the AMOEBA water model*. J. Phys. Chem. B, 2004, **108**, 13427-13437.
[146] Ren, P.Y. and J.W. Ponder, *Polarizable atomic multipole water model for molecular mechanics simulation*. J. Phys. Chem. B, 2003, **107**, 5933-5947.
[147] Shi, Y., C.J. Wu, J.W. Ponder, and P.Y. Ren, *Multipole Electrostatics in Hydration Free Energy Calculations*. J. Comput. Chem., 2011, **32**, 967-977.
[148] Halgren, T.A., *Representation of Vanderwaals (Vdw) Interactions in Molecular Mechanics Force-Fields - Potential Form, Combination Rules, and Vdw Parameters*. J. Am. Chem. Soc., 1992, **114**, 7827-7843.
[149] Stone, A.J., *Distributed Multipole Analysis, or How to Describe a Molecular Charge-Distribution*. Chem. Phys. Lett., 1981, **83**, 233-239.
[150] Stone, A.J., *Distributed Polarizabilities*. Mol. Phys., 1985, **56**, 1065-1082.
[151] Williams, D.E., *Representation of the Molecular Electrostatic Potential by Atomic Multipole and Bond Dipole Models*. J. Comput. Chem., 1988, **9**, 745-763.
[152] Vignemaeder, F. and P. Claverie, *The Exact Multicenter Multipolar Part of a Molecular Charge-Distribution and Its Simplified Representations*. J. Chem. Phys., 1988, **88**, 4934-4948.
[153] Day, P.N., J.H. Jensen, M.S. Gordon, S.P. Webb, W.J. Stevens, M. Krauss, D. Garmer, H. Basch, and D. Cohen, *An effective fragment method for modeling solvent effects in quantum mechanical calculations*. J. Chem. Phys., 1996, **105**, 1968-1986.
[154] Ren, P.Y. and J.W. Ponder, *Consistent treatment of inter- and intramolecular polarization in molecular mechanics calculations*. J. Comput. Chem., 2002, **23**, 1497-1506.
[155] Thole, B.T., *Molecular Polarizabilities Calculated with a Modified Dipole Interaction*. Chem. Phys., 1981, **59**, 341-350.
[156] Abascal, J.L.F., E. Sanz, R.G. Fernandez, and C. Vega, *A potential model for the study of ices and amorphous water: TIP4P/Ice*. J. Chem. Phys., 2005, **122**.
[157] Abascal, J.L.F. and C. Vega, *A general purpose model for the condensed phases of water: TIP4P/2005*. J. Chem. Phys., 2005, **123**.
[158] Horn, H.W., W.C. Swope, J.W. Pitera, J.D. Madura, T.J. Dick, G.L. Hura, and T. Head-Gordon, *Development of an improved four-site water model for biomolecular simulations: TIP4P-Ew*. J. Chem. Phys., 2004, **120**, 9665-9678.
[159] Jorgensen, W.L., *Quantum and Statistical Mechanical Studies of Liquids .24. Revised Tips for Simulations of Liquid Water and Aqueous-Solutions*. J Chem Phys, 1982, **77**, 4156-4163.

[160] Jorgensen, W.L., J. Chandrasekhar, J.D. Madura, R.W. Impey, and M.L. Klein, *Comparison of Simple Potential Functions for Simulating Liquid Water*. J. Chem. Phys., 1983, **79**, 926-935.
[161] Berendsen, H.J.C., J.R. Grigera, and T.P. Straatsma, *The Missing Term in Effective Pair Potentials*. J. Phys. Chem., 1987, **91**, 6269-6271.
[162] Jorgensen, W.L., *Quantum and Statistical Mechanical Studies of Liquids .10. Transferable Intermolecular Potential Functions for Water, Alcohols, and Ethers - Application to Liquid Water*. J. Am. Chem. Soc., 1981, **103**, 335-340.
[163] MacKerell, A.D., *Developments in the CHARMM all-atom empirical energy function for biological molecules.* Abstr. Pap. Am. Chem. Soc., 1998, **216**, U696-U696.
[164] Gonzalez, M.A. and J.L.F. Abascal, *A flexible model for water based on TIP4P/2005*. J. Chem. Phys., 2011, **135**.
[165] Jorgensen, W.L. and J.D. Madura, *Temperature and Size Dependence for Monte-Carlo Simulations of Tip4p Water*. Mol. Phys., 1985, **56**, 1381-1392.
[166] Gonzalez, M.A. and J.L.F. Abascal, *A flexible model for water based on TIP4P/2005*. J. Chem. Phys., 2011, **135**.
[167] Field, M.J., P.A. Bash, and M. Karplus, *A Combined Quantum-Mechanical and Molecular Mechanical Potential for Molecular-Dynamics Simulations*. J. Comput. Chem., 1990, **11**, 700-733.
[168] Maseras, F. and K. Morokuma, *Imomm - a New Integrated Ab-Initio Plus Molecular Mechanics Geometry Optimization Scheme of Equilibrium Structures and Transition-States.* J. Comput. Chem., 1995, **16**, 1170-1179.
[169] Singh, U.C. and P.A. Kollman, *A Combined Abinitio Quantum-Mechanical and Molecular Mechanical Method for Carrying out Simulations on Complex Molecular-Systems - Applications to the Ch3cl + Cl- Exchange-Reaction and Gas-Phase Protonation of Polyethers*. J. Comput. Chem., 1986, **7**, 718-730.
[170] Warshel, A. and M. Levitt, *Theoretical Studies of Enzymic Reactions - Dielectric, Electrostatic and Steric Stabilization of Carbonium-Ion in Reaction of Lysozyme*. J. Mol. Biol., 1976, **103**, 227-249.
[171] Humbel, S., S. Sieber, and K. Morokuma, *The IMOMO method: Integration of different levels of molecular orbital approximations for geometry optimization of large systems: Test for n-butane conformation and S(N)2 reaction: RCl+Cl-*. J. Chem. Phys., 1996, **105**, 1959-1967.
[172] Svensson, M., S. Humbel, R.D.J. Froese, T. Matsubara, S. Sieber, and K. Morokuma, *ONIOM: A multilayered integrated MO+MM method for geometry optimizations and single point energy predictions. A test for Diels-Alder reactions and Pt(P(t-Bu)(3))(2)+H-2 oxidative addition*. J. Phys. Chem., 1996, **100**, 19357-19363.
[173] Vreven, T. and K. Morokuma, *Hybrid Methods: ONIOM(QM:MM) and QM/MM*. Annu. Rep. Comp. Chem., 2006, **2**, 35-51.
[174] Ananikov, V.P., D.G. Musaev, and K. Morokuma, *Real size of ligands, reactants and catalysts: Studies of structure, reactivity and selectivity by ONIOM and other hybrid computational approaches*. J. Mol. Catal. A:Chem., 2010, **324**, 104-119.
[175] Sameera, W.M.C. and F. Maseras, *Quantum mechanics/molecular mechanics methods can be more accurate than full quantum mechanics in systems involving dispersion correlations*. Phys. Chem. Chem. Phys., 2011, **13**, 10520-10526.

[176] Vreven, T., K. Morokuma, S.J. Zhong, G.A. Petersson, and M.J. Frisch, *Using compound model chemistries in ONIOM.* Abstr. Pap. Am. Chem. Soc., 2003, **226**, U307-U307.
[177] Chung, L.W., H. Hirao, X. Li, and K. Morokuma, *The ONIOM method: its foundation and applications to metalloenzymes and photobiology*. WIREs Comput. Mol. Sci., 2012, **2**, 327-350.
[178] Norman, P., *A perspective on nonresonant and resonant electronic response theory for time-dependent molecular properties*. Phys. Chem. Chem. Phys., 2011, **13**, 20519-20535.
[179] Sneskov, K. and O. Christiansen, *Excited state coupled cluster methods*. WIREs Comput. Mol. Sci., 2012, **2**, 566-584.
[180] Casida, M.E., *Time-dependent density-functional theory for molecules and molecular solids*. J. Mol. Struc-TheoChem., 2009, **914**, 3-18.
[181] Stanton, J.F. and R.J. Bartlett, *The Equation of Motion Coupled-Cluster Method - a Systematic Biorthogonal Approach to Molecular-Excitation Energies, Transition-Probabilities, and Excited-State Properties*. J. Chem. Phys., 1993, **98**, 7029-7039.
[182] Koch, H. and P. Jorgensen, *Coupled Cluster Response Functions*. J. Chem. Phys., 1990, **93**, 3333-3344.
[183] Christiansen, O., H. Koch, and F. Jorgensen, *Perturbative triple excitation corrections to coupled cluster singles and doubles excitation energies*. J. Chem. Phys., 1996, **105**, 1451-1459.
[184] Runge, E. and E.K.U. Gross, *Density-Functional Theory for Time-Dependent Systems*. Phys. Rev. Lett., 1984, **52**, 997-1000.
[185] Bauernschmitt, R. and R. Ahlrichs, *Treatment of electronic excitations within the adiabatic approximation of time dependent density functional theory*. Chem. Phys. Lett., 1996, **256**, 454-464.
[186] Burke, K., J. Werschnik, and E.K.U. Gross, *Time-dependent density functional theory: Past, present, and future*. J. Chem. Phys., 2005, **123**.
[187] Marques, M.A.L. and E.K.U. Gross, *Time-dependent density functional theory*. Annu. Rev. Phys. Chem., 2004, **55**, 427-455.
[188] Eisenberg, D.S. and W. Kauzmann, *The structure and properties of water*. 1969, Oxford: Clarendon Press. xii, 296 p.
[189] Cheng, B.M., E.P. Chew, C.P. Liu, M. Bahou, Y.P. Lee, Y.L. Yung, and M.F. Gerstell, *Photo-induced fractionation of water isotopomers in the Martian atmosphere*. Geophys. Res. Lett., 1999, **26**, 3657-3660.
[190] Engel, V., V. Staemmler, R.L. Vanderwal, F.F. Crim, R.J. Sension, B. Hudson, P. Andresen, S. Hennig, K. Weide, and R. Schinke, *Photodissociation of Water in the 1st Absorption-Band - a Prototype for Dissociation on a Repulsive Potential-Energy Surface*. J. Phys. Chem., 1992, **96**, 3201-3213.
[191] van Harrevelt, R. and M.C. van Hemert, *Photodissociation of water in the (A)over-tilde band revisited with new potential energy surfaces*. J. Chem. Phys., 2001, **114**, 9453-9462.
[192] Votava, O., D.F. Plusquellic, and D.J. Nesbitt, *Vibrationally mediated photolysis dynamics of H2O in the v(OH)=3 manifold: Far off resonance photodissociation cross sections and OH product state distributions*. J. Chem. Phys., 1999, **110**, 8564-8576.
[193] Hayashi, H., N. Watanabe, Y. Udagawa, and C.C. Kao, *The complete optical spectrum of liquid water measured by inelastic x-ray scattering*. P. Natl. Acad. Sci. USA., 2000, **97**, 6264-6266.

[194] Quickenden, T.I., J.A. Irvin, and D.F. Sangster, *A Search for Non-Cerenkov Uv Emission from Liquid Water Irradiated with Pulsed Electrons*. J. Chem. Phys., 1980, **73**, 3632-3634.
[195] Chergui, M. and N. Schwentner, *Experimental-Evidence to Rydbergization of Antibonding Molecular-Orbitals*. Chem. Phys. Lett., 1994, **219**, 237-242.
[196] Han, P. and D.M. Bartels, *H/D Isotope Effects in Water Radiolysis .2. Dissociation of Electronically Excited Water*. J. Phys. Chem., 1990, **94**, 5824-5833.
[197] Klein, S., E. Kochanski, A. Strich, and A.J. Sadlej, *Electric properties of the water molecule in (1)A(1),B-1(1), and B-3(1) electronic states: Refined CASSCF and CASPT2 calculations*. Theor. Chem. Acc., 1996, **94**, 75-91.
[198] Vaval, N. and S. Pal, *Molecular property calculations for excited states using a multireference coupled-cluster approach*. Chem. Phys. Lett., 1999, **300**, 125-130.
[199] Ikehata, A., N. Higashi, and Y. Ozaki, *Direct observation of the absorption bands of the first electronic transition in liquid H2O and D2O by attenuated total reflectance far-UV spectroscopy*. J. Chem. Phys., 2008, **129**.
[200] Marin, T.W., K. Takahashi, and D.M. Bartels, *Temperature and density dependence of the light and heavy water ultraviolet absorption edge*. J. Chem. Phys., 2006, **125**.
[201] Christiansen, O., T.M. Nymand, and K.V. Mikkelsen, *A theoretical study of the electronic spectrum of water*. J. Chem. Phys., 2000, **113**, 8101-8112.
[202] Harvey, J.N., J.O. Jung, and R.B. Gerber, *Ultraviolet spectroscopy of water clusters: Excited electronic states and absorption line shapes of (H2O)(n), n=2-6*. J. Chem. Phys., 1998, **109**, 8747-8750.
[203] Miller, Y., E. Fredj, J.N. Harvey, and R.B. Gerber, *Ultraviolet spectroscopy of large water clusters: Model and calculations for (H2O)(n), for n=8, 11, 20, 40, and 50*. J. Phys. Chem. A, 2004, **108**, 4405-4411.
[204] Svoboda, O., M. Oncak, and P. Slavicek, *Simulations of light induced processes in water based on ab initio path integrals molecular dynamics. II. Photoionization*. J. Chem. Phys., 2011, **135**.
[205] Mata, R.A., H. Stoll, and B.J.C. Cabral, *A Simple One-Body Approach to the Calculation of the First Electronic Absorption Band of Water*. J. Chem. Theory. Comput., 2009, **5**, 1829-1837.
[206] Petrik, N.G. and G.A. Kimmel, *Electron-stimulated reactions at the interfaces of amorphous solid water films driven by long-range energy transfer from the bulk*. Phys. Rev. Lett., 2003, **90**.
[207] Temelso, B., K.A. Archer, and G.C. Shields, *Benchmark Structures and Binding Energies of Small Water Clusters with Anharmonicity Corrections*. J. Phys. Chem. A, 2011, **115**, 12034-12046.
[208] Dalgaard, E. and H.J. Monkhorst, *Some Aspects of the Time-Dependent Coupled-Cluster Approach to Dynamic-Response Functions*. Phys. Rev. A, 1983, **28**, 1217-1222.
[209] Stanton, J.F. and R.J. Bartlett, *A Coupled-Cluster Based Effective Hamiltonian Method for Dynamic Electric Polarizabilities*. J. Chem. Phys., 1993, **99**, 5178-5183.
[210] Delbene, J.E., Ditchfie.R, and J.A. Pople, *Self-Consistent Molecular Orbital Methods .10. Molecular Orbital Studies of Excited States with Minimal and Extended Basis Sets*. J. Chem. Phys., 1971, **55**, 2236.

[211] Foresman, J.B., M. Headgordon, J.A. Pople, and M.J. Frisch, *Toward a Systematic Molecular-Orbital Theory for Excited-States*. J. Phys. Chem., 1992, **96**, 135-149.

[212] Headgordon, M., R.J. Rico, M. Oumi, and T.J. Lee, *A Doubles Correction to Electronic Excited-States from Configuration-Interaction in the Space of Single Substitutions*. Chem. Phys. Lett., 1994, **219**, 21-29.

[213] Aidas, K., C. Angeli, K.L. Bak, V. Bakken, R. Bast, L. Boman, O. Christiansen, R. Cimiraglia, S. Coriani, P. Dahle, E.K. Dalskov, U. Ekstrom, T. Enevoldsen, J.J. Eriksen, P. Ettenhuber, B. Fernandez, L. Ferrighi, H. Fliegl, L. Frediani, K. Hald, A. Halkier, C. Hattig, H. Heiberg, T. Helgaker, A.C. Hennum, H. Hettema, E. Hjertenaes, S. Host, I.M. Hoyvik, M.F. Iozzi, B. Jansik, H.J.A. Jensen, D. Jonsson, P. Jorgensen, J. Kauczor, S. Kirpekar, T. Kjrgaard, W. Klopper, S. Knecht, R. Kobayashi, H. Koch, J. Kongsted, A. Krapp, K. Kristensen, A. Ligabue, O.B. Lutnaes, J.I. Melo, K.V. Mikkelsen, R.H. Myhre, C. Neiss, C.B. Nielsen, P. Norman, J. Olsen, J.M.H. Olsen, A. Osted, M.J. Packer, F. Pawlowski, T.B. Pedersen, P.F. Provasi, S. Reine, Z. Rinkevicius, T.A. Ruden, K. Ruud, V.V. Rybkin, P. Salek, C.C.M. Samson, A.S. de Meras, T. Saue, S.P.A. Sauer, B. Schimmelpfennig, K. Sneskov, A.H. Steindal, K.O. Sylvester-Hvid, P.R. Taylor, A.M. Teale, E.I. Tellgren, D.P. Tew, A.J. Thorvaldsen, L. Thogersen, O. Vahtras, M.A. Watson, D.J.D. Wilson, M. Ziolkowski, and H. Agren, *The Dalton quantum chemistry program system*. WIREs Comput. Mol. Sci., 2014, **4**, 269-284.

[214] Frisch, M.J., G.W. Trucks, H.B. Schlegel, G.E. Scuseria, M.A. Robb, J.R. Cheeseman, G. Scalmani, V. Barone, B. Mennucci, G.A. Petersson, H. Nakatsuji, M.L. Caricato, X., H.P. Hratchian, A.F. Izmaylov, J. Bloino, G. Zheng, J.L. Sonnenberg, M. Hada, M. Ehara, K. Toyota, R. Fukuda, J. Hasegawa, M. Ishida, T. Nakajima, Y. Honda, O. Kitao, H. Nakai, T. Vreven, J.A.J. Montgomery, J.E. Peralta, F. Ogliaro, M. Bearpark, J.J. Heyd, E. Brothers, K.N. Kudin, V.N. Staroverov, R. Kobayashi, J. Normand, K. Raghavachari, A. Rendell, J.C. Burant, S.S. Iyengar, J. Tomasi, M. Cossi, N. Rega, M.J. Millam, M. Klene, J.E. Knox, J.B. Cross, V. Bakken, C. Adamo, J. Jaramillo, R. Gomperts, R.E. Stratmann, O. Yazyev, A.J. Austin, R.P. Cammi, C., J.W. Ochterski, R.L. Martin, K. Morokuma, V.G. Zakrzewski, G.A. Voth, P. Salvador, J.J. Dannenberg, S. Dapprich, A.D. Daniels, Ö. Farkas, J.B. Foresman, J.V. Ortiz, J. Cioslowski, and D.J. Fox. Gaussian 09, Revision D.01, Gaussian Inc., Wallingford CT, 2009.

[215] Benedict, W.S., N. Gailar, and E.K. Plyler, *Rotation-Vibration Spectra of Deuterated Water Vapor*. J. Chem. Phys., 1956, **24**, 1139-1165.

[216] Odutola, J.A. and T.R. Dyke, *Partially Deuterated Water Dimers - Microwave-Spectra and Structure*. J. Chem. Phys., 1980, **72**, 5062-5070.

[217] Halkier, A., H. Koch, P. Jorgensen, O. Christiansen, I.M.B. Nielsen, and T. Helgaker, *A systematic ab initio study of the water dimer in hierarchies of basis sets and correlation models*. Theor. Chem. Acc., 1997, **97**, 150-157.

[218] Kim, K. and K.D. Jordan, *Comparison of Density-Functional and Mp2 Calculations on the Water Monomer and Dimer*. J. Phys. Chem., 1994, **98**, 10089-10094.

[219] Xantheas, S.S., C.J. Burnham, and R.J. Harrison, *Development of transferable interaction models for water. II. Accurate energetics of the first few water clusters from first principles*. J. Chem. Phys., 2002, **116**, 1493-1499.

[220] Keutsch, F.N. and R.J. Saykally, *Water clusters: Untangling the mysteries of the liquid, one molecule at a time*. P. Natl. Acad. Sci. USA., 2001, **98**, 10533-10540.
[221] Chutjian, A., R.I. Hall, and S. Trajmar, *Electron-Impact Excitation of H2o and D2o at Various Scattering Angles and Impact Energies in Energy-Loss Range 4.2-12 Ev*. J. Chem. Phys., 1975, **63**, 892-898.
[222] Knoop, F.W.E., Brongers.Hh, and Oosterho.Lj, *Triplet Excitation of Water and Methanol by Low-Energy Electron-Impact Spectroscopy*. Chem. Phys. Lett., 1972, **13**, 20-&.
[223] Schulz, G.J., *Excitation and Negative Ions in H2o*. J. Chem. Phys., 1960, **33**, 1661-1665.
[224] Dutuit, O., A. Tabchefouhaile, I. Nenner, H. Frohlich, and P.M. Guyon, *Photodissociation Processes of Water-Vapor Below and above the Ionization-Potential*. J. Chem. Phys., 1985, **83**, 584-596.
[225] Reisler, H. and A.I. Krylov, *Interacting Rydberg and valence states in radicals and molecules: experimental and theoretical studies*. Int. Rev. Phys. Chem., 2009, **28**, 267-308.
[226] Dyke, T.R. and J.S. Muenter, *Electric Dipole-Moments of Low J States of H2o and D2o*. J. Chem. Phys., 1973, **59**, 3125-3127.
[227] Dyke, T.R., K.M. Mack, and J.S. Muenter, *Structure of Water Dimer from Molecular-Beam Electric Resonance Spectroscopy*. J. Chem. Phys., 1977, **66**, 498-510.
[228] Heller, J.M., R.N. Hamm, R.D. Birkhoff, and L.R. Painter, *Collective Oscillation in Liquid Water*. J. Chem. Phys., 1974, **60**, 3483-3486.
[229] Michaud, M., P. Cloutier, and L. Sanche, *Low-Energy Electron-Energy-Loss Spectroscopy of Amorphous Ice - Electronic Excitations*. Phys. Rev. A, 1991, **44**, 5624-5627.
[230] Kim, K., K.D. Jordan, and T.S. Zwier, *Low-Energy Structures and Vibrational Frequencies of the Water Hexamer - Comparison with Benzene-(H2o)(6)*. J. Am. Chem. Soc., 1994, **116**, 11568-11569.
[231] Tissandier, M.D., S.J. Singer, and J.V. Coe, *Enumeration and evaluation of the water hexamer cage structure*. J. Phys. Chem. A, 2000, **104**, 752-757.
[232] Liu, K., M.G. Brown, C. Carter, R.J. Saykally, J.K. Gregory, and D.C. Clary, *Characterization of a cage form of the water hexamer*. Nature, 1996, **381**, 501-503.
[233] Maheshwary, S., N. Patel, N. Sathyamurthy, A.D. Kulkarni, and S.R. Gadre, *Structure and stability of water clusters (H2O)(n), n=8-20: An ab initio investigation*. J. Phys. Chem. A, 2001, **105**, 10525-10537.
[234] Upadhyay, D.M., M.K. Shukla, and P.C. Mishra, *An ab initio study of water clusters in gas phase and bulk aqueous media: (H2O)(n), n=1-12*. Int. J Quantum Chem., 2001, **81**, 90-104.
[235] Lenz, A. and L. Ojamae, *A theoretical study of water clusters: the relation between hydrogen-bond topology and interaction energy from quantum-chemical computations for clusters with up to 22 molecules*. Phys. Chem. Chem. Phys., 2005, **7**, 1905-1911.
[236] Lenz, A. and L. Ojamae, *Theoretical IR spectra for water clusters (H2O)(n) (n=6-22, 28, 30) and identification of spectral contributions from different H-bond conformations in gaseous and liquid water*. J. Phys. Chem. A, 2006, **110**, 13388-13393.

[237] Lenz, A. and L. Ojamae, *On the stability of dense versus cage-shaped water clusters: Quantum-chemical investigations of zero-point energies, free energies, basis-set effects and IR spectra of (H2O)(12) and (H2O)(20)*. Chem. Phys. Lett., 2006, **418**, 361-367.
[238] Bates, D.M. and G.S. Tschumper, *CCSD(T) complete basis set limit relative energies for low-lying water hexamer structures*. J. Phys. Chem. A, 2009, **113**, 3555-3559.
[239] Wang, Y., V. Babin, J.M. Bowman, and F. Paesani, *The water hexamer: cage, prism, or both. Full dimensional quantum simulations say both*. J. Am. Chem. Soc., 2012, **134**, 11116-11119.
[240] Neela, Y.I., A.S. Mahadevi, and G.N. Sastry, *Hydrogen Bonding in Water Clusters and Their Ionized Counterparts*. J. Phys. Chem. B, 2010, **114**, 17162-17171.
[241] Baron, M. and V.J. Kowalewski, *The liquid water-benzene system*. J. Phys. Chem. A, 2006, **110**, 7122-7129.
[242] Feller, D., *Strength of the benzene-water hydrogen bond*. J. Phys. Chem. A, 1999, **103**, 7558-7561.
[243] Fredericks, S.Y., J.M. Pedulla, K.D. Jordan, and T.S. Zwier, *OH stretch IR spectra of (H2O)(3) and benzene-(H2O)(3)*. Theor. Chem. Acc., 1997, **96**, 51-55.
[244] Jedlovszky, P., A. Kereszturi, and G. Horvai, *Orientational order of the water molecules at the vicinity of the water-benzene interface in a broad range of thermodynamic states, as seen from Monte Carlo simulations*. Faraday Discuss., 2005, **129**, 35-46.
[245] Prakash, M., K.G. Samy, and V. Subramanian, *Benzene-Water (BZW(n) (n=1-10)) Clusters*. J. Phys. Chem. A, 2009, **113**, 13845-13852.
[246] Pribble, R.N., A.W. Garrett, K. Haber, and T.S. Zwier, *Resonant Ion-Dip Infrared-Spectroscopy of Benzene-H2o and Benzene-Hod*. J. Chem. Phys., 1995, **103**, 531-544.
[247] Pribble, R.N. and T.S. Zwier, *Size-Specific Infrared-Spectra of Benzene-(H2o)(N) Clusters (N=1 through 7) - Evidence for Noncyclic (H2o)(N) Structures*. Science, 1994, **265**, 75-79.
[248] Tarakeshwar, P., H.S. Choi, S.J. Lee, J.Y. Lee, K.S. Kim, T.K. Ha, J.H. Jang, J.G. Lee, and H. Lee, *A theoretical investigation of the nature of the pi-H interaction in ethene-H2O, benzene-H2O, and benzene-(H2O)(2)*. J. Chem. Phys., 1999, **111**, 5838-5850.
[249] Gruenloh, C.J., J.R. Carney, C.A. Arrington, T.S. Zwier, S.Y. Fredericks, and K.D. Jordan, *Infrared spectrum of a molecular ice cube: The S-4 and D-2d water octamers in benzene-(water)(8)*. Science, 1997, **276**, 1678-1681.
[250] Gruenloh, C.J., J.R. Carney, F.C. Hagemeister, C.A. Arrington, T.S. Zwier, S.Y. Fredericks, J.T. Wood, and K.D. Jordan, *Resonant ion-dip infrared spectroscopy of the S-4 and D-2d wafer octamers in benzene-(water)(8) and benzene(2)-(water)(8)*. J. Chem. Phys., 1998, **109**, 6601-6614.
[251] Allamandola, L.J., D.M. Hudgins, C.W. Bauschlicher, and S.R. Langhoff, *Carbon chain abundance in the diffuse interstellar medium*. Astron. Astrophys., 1999, **352**, 659-664.
[252] Woods, P.M., T.J. Millar, and A.A. Zijlstra, *The synthesis of benzene in the proto-planetary nebula CRL 618*. Astrophys. J., 2002, **574**, L167-L170.

[253] Cherchneff, I., J.R. Barker, and A.G.G.M. Tielens, *Polycyclic Aromatic Hydrocarbon Formation in Carbon-Rich Stellar Envelopes*. Astrophys. J., 1992, **401**, 269-287.
[254] Woods, P.M. and K. Willacy, *Benzene formation in the inner regions of protostellar disks*. Astrophys. J., 2007, **655**, L49-L52.
[255] Frenklach, M. and E.D. Feigelson, *Formation of Polycyclic Aromatic-Hydrocarbons in Circumstellar Envelopes*. Astrophys. J., 1989, **341**, 372-384.
[256] Willacy, K. and D.A. Williams, *Desorption Processes in Molecular Clouds - Quasi-Steady-State Chemistry*. Mon. Not. R. Astron. Soc., 1993, **260**, 635-642.
[257] Rana, S.V.S. and Y. Verma, *Biochemical toxicity of benzene*. J. Environ. Biol., 2005, **26**, 157-168.
[258] Duarte-Davidson, R., C. Courage, L. Rushton, and L. Levy, *Benzene in the environment: an assessment of the potential risks to the health of the population*. Occup. Environ. Med., 2001, **58**, 2-13.
[259] Ma, J., D. Alfe, A. Michaelides, and E. Wang, *The water-benzene interaction: Insight from electronic structure theories*. J. Chem. Phys., 2009, **130**.
[260] Pribble, R.N. and T.S. Zwier, *Size-Specific Infrared Spectra of Benzene-(H2O)n Clusters (n = 1 through 7): Evidence for Noncyclic (H2O)n Structures*. Science, 1994, **265**, 75-79.
[261] Kim, S.J., H.I. Seo, and B.H. Boo, *Theoretical investigations for the molecular structures and binding energies for C(6)H(6)(H(2)O)(n), (n=1-7) complexes*. Mol. Phys., 2009, **107**, 1261-1270.
[262] Alberti, M., N.F. Lago, and F. Pirani, *Benzene water interaction: From gaseous dimers to solvated aggregates*. Chem. Phys., 2012, **399**, 232-239.
[263] Slipchenko, L.V. and M.S. Gordon, *Water-Benzene Interactions: An Effective Fragment Potential and Correlated Quantum Chemistry Study*. J. Phys. Chem. A, 2009, **113**, 2092-2102.
[264] Perez, C., M.T. Muckle, D.P. Zaleski, N.A. Seifert, B. Temelso, G.C. Shields, Z. Kisiel, and B.H. Pate, *Structures of cage, prism, and book isomers of water hexamer from broadband rotational spectroscopy*. Science, 2012, **336**, 897-901.
[265] Lee, J.Y., J. Kim, H.M. Lee, P. Tarakeshwar, and K.S. Kim, *Structures, vibrational frequencies, and infrared spectra of the hexa-hydrated benzene clusters*. J. Chem. Phys., 2000, **113**, 6160-6168.
[266] Kim, J. and K.S. Kim, *Structures, binding energies, and spectra of isoenergetic water hexamer clusters: Extensive ab initio studies*. J. Chem. Phys, 1998, **109**, 5886-5895.
[267] Kelkkanen, A.K., B.I. Lundqvist, and J.K. Norskov, *Density functional for van der Waals forces accounts for hydrogen bond in benchmark set of water hexamers*. J. Chem. Phys., 2009, **131**, 046102.
[268] Santra, B., A. Michaelides, M. Fuchs, A. Tkatchenko, C. Filippi, and M. Scheffler, *On the accuracy of density-functional theory exchange-correlation functionals for H bonds in small water clusters. II. The water hexamer and van der Waals interactions*. J. Chem. Phys., 2008, **129**, 194111.
[269] Telle, H.H., R.J. Donovan, and A. Gonzalez Urena, *Laser chemistry : spectroscopy, dynamics and applications*. 2007, Chichester: John Wiley & Sons. xiv, 502 p.

[270] Lassettr.En, A. Skerbele, M.A. Dillon, and K.J. Ross, *High-Resolution Study of Electron-Impact Spectra at Kinetic Energies between 33 and 100 Ev and Scattering Angles to 16 Degrees*. J. Chem. Phys., 1968, **48**, 5066-&.
[271] Williams, M.W., R.A. Macrae, R.N. Hamm, and E.T. Arakawa, *Collective Oscillations in Pure Liquid Benzene*. Phys. Rev. Lett., 1969, **22**, 1088-&.
[272] Goerigk, L. and S. Grimme, *A thorough benchmark of density functional methods for general main group thermochemistry, kinetics, and noncovalent interactions*. Phys. Chem. Chem. Phys., 2011, **13**, 6670-6688.
[273] Sharma, D. and M.J. Paterson, *The structure and UV spectroscopy of benzene–water (Bz–W6) clusters using time-dependent density functional theory*. Photochem.Photobiol.Sci., 2014, **13**, 1549-1560.
[274] Parker, D.S.N., F.T. Zhang, Y.S. Kim, R.I. Kaiser, A. Landera, V.V. Kislov, A.M. Mebel, and A.G.G.M. Tielens, *Low temperature formation of naphthalene and its role in the synthesis of PAHs (Polycyclic Aromatic Hydrocarbons) in the interstellar medium*. P. Natl. Acad. Sci. USA., 2012, **109**, 53-58.
[275] Preuss, R., J. Angerer, and H. Drexler, *Naphthalene - an environmental and occupational toxicant*. Int. Arch. Occup. Environ. Health., 2003, **76**, 556-576.
[276] Ehrenfreund, P. and M.A. Sephton, *Carbon molecules in space: from astrochemistry to astrobiology*. Faraday Discuss., 2006, **133**, 277-288.
[277] Kassis, M., J.D. Adams, M.F. Campbell, L.K. Deutsch, J.L. Hora, J.M. Jackson, and E.V. Tollestrup, *Mid-infrared emission at photodissociation regions in the Orion Nebula*. Astrophys. J., 2006, **637**, 823-837.
[278] Kaneda, H., T. Onaka, and I. Sakon, *Detection of PAH emission features from nearby elliptical galaxies with the Spitzer infrared spectrograph*. Astrophys. J., 2005, **632**, L83-L86.
[279] Lagadec, E., O. Chesneau, M. Matsuura, O. De Marco, J.A.D. Pacheco, A.A. Zijlstra, A. Acker, G.C. Clayton, and B. Lopez, *New insights on the complex planetary nebula Hen 2-113*. Astron. Astrophys., 2006, **448**, 203-212.
[280] Duley, W.W., *Polycyclic aromatic hydrocarbons, carbon nanoparticles and the diffuse interstellar bands*. Faraday Discuss., 2006, **133**, 415-425.
[281] Sandford, S.A., M.P. Bernstein, and L.J. Allamandola, *The mid-infrared laboratory spectra of naphthalene (C10H8) in solid H2O*. Astrophys. J., 2004, **607**, 346-360.
[282] Bernstein, M.P., S.A. Sandford, and L.J. Allamandola, *The mid-infrared absorption spectra of neutral polycyclic aromatic hydrocarbons in conditions relevant to dense interstellar clouds*. Astrophys. J. Suppl. S., 2005, **161**, 53-64.
[283] Bernstein, M.P., S.A. Sandford, A.L. Mattioda, and L.J. Allamandola, *Near- and mid-infrared laboratory spectra of PAH cations in solid H(2)O*. Astrophys. J., 2007, **664**, 1264-1272.
[284] Fletcher, N.H., *Reconstruction of Ice Crystal-Surfaces at Low-Temperatures*. Philos. Mag. B, 1992, **66**, 109-115.
[285] Pan, D., L.M. Liu, G.A. Tribello, B. Slater, A. Michaelides, and E. Wang, *Surface Energy and Surface Proton Order of Ice Ih*. Phys. Rev. Lett., 2008, **101**.
[286] Buch, V., H. Groenzin, I. Lit, M.J. Shultz, and E. Tosatti, *Proton order in the ice crystal surface*. P. Natl. Acad. Sci. USA., 2008, **105**, 5969-5974.
[287] Groenzin, H., I. Li, V. Buch, and M.J. Shultz, *The single-crystal, basal face of ice I(h) investigated with sum frequency generation*. J. Chem. Phys., 2007, **127**.
[288] Groenzin, H., I. Li, and M.J. Shultz, *Sum frequency generation on single-crystalline ice I-h*. Physics and Chemistry of Ice, 2007, 191-199.

[289] Silva, S.C. and J.P. Devlin, *Interaction of Acetylene, Ethylene, and Benzene with Ice Surfaces*. J. Phys. Chem., 1994, **98**, 10847-10852.
[290] Bahr, S. and V. Kempter, *Interaction of benzene with amorphous solid water adsorbed on polycrystalline Ag*. J. Chem. Phys., 2007, **127**.
[291] Jakob, P. and D. Menzel, *Benzene Multilayers - a Model for Their Anisotropic Growth from Vibrational Spectroscopy and Thermal-Desorption*. Surf. Sci., 1989, **220**, 70-95.
[292] Haq, S. and D.A. King, *Configurational transitions of benzene and pyridine adsorbed on Pt{111} and Cu{110} surfaces: An infrared study*. J. Phys. Chem., 1996, **100**, 16957-16965.
[293] Rockey, T.J., M.C. Yang, and H.L. Dai, *Adsorption energies, inter-adsorbate interactions, and the two binding sites within monolayer benzene on Ag(111)*. J. Phys. Chem. B, 2006, **110**, 19973-19978.
[294] Bo, C. and F. Maseras, *QM/MM methods in inorganic chemistry*. Dalton Trans., 2008, 2911-2919.
[295] Sameera, W.M.C. and F. Maseras, *Transition metal catalysis by density functional theory and density functional theory/molecular mechanics*. WIREs Comput. Mol. Sci., 2012, **2**, 375-385.
[296] Rivilla, I., W.M.C. Sameera, E. Alvarez, M.M. Diaz-Requejo, F. Maseras, and P.J. Perez, *Catalytic cross-coupling of diazo compounds with coinage metal-based catalysts: an experimental and theoretical study*. Dalton Trans., 2013, **42**, 4132-4138.
[297] Ponder, J.W. and F.M. Richards, *An Efficient Newton-Like Method for Molecular Mechanics Energy Minimization of Large Molecules*. J. Comput. Chem., 1987, **8**, 1016-1024.
[298] Kundrot, C.E., J.W. Ponder, and F.M. Richards, *Algorithms for Calculating Excluded Volume and Its Derivatives as a Function of Molecular-Conformation and Their Use in Energy Minimization*. J. Comput. Chem., 1991, **12**, 402-409.
[299] Ren, P.Y., C.J. Wu, and J.W. Ponder, *Polarizable Atomic Multipole-Based Molecular Mechanics for Organic Molecules*. J. Chem. Theory. Comput., 2011, **7**, 3143-3161.
[300] Ditchfie.R, W.J. Hehre, and J.A. Pople, *Self-Consistent Molecular-Orbital Methods .9. Extended Gaussian-Type Basis for Molecular-Orbital Studies of Organic Molecules*. J. Chem. Phys., 1971, **54**, 724-&.
[301] Neese, F., *The ORCA program system*. WIREs Comput. Mol. Sci., 2012, **2**, 73-78.
[302] Leverentz, H.R., H.W. Qi, and D.G. Truhlar, *Assessing the Accuracy of Density Functional and Semiempirical Wave Function Methods for Water Nanoparticles: Comparing Binding and Relative Energies of (H2O)(16) and (H2O)(17) to CCSD(T) Results*. J. Chem. Theory. Comput., 2013, **9**, 995-1006.
[303] Sameera, W.M.C. and D.A. Pantazis, *A Hierarchy of Methods for the Energetically Accurate Modeling of Isomerism in Monosaccharides*. J. Chem. Theory. Comput., 2012, **8**, 2630-2645.
[304] Vidali, G., L. Li, J.E. Roser, and R. Badman, *Catalytic activity of interstellar grains: Formation of molecular hydrogen on amorphous silicates*. Adv. Space Res., 2009, **43**, 1291-1298.
[305] Pirronello, V. and D. Averna, *Production of Molecular-Hydrogen by Cosmic-Rays in Interstellar Clouds - a Relevant Process*. Astron. Astrophys., 1988, **196**, 201-206.

[306] Hollenba.D and E.E. Salpeter, *Surface Recombination of Hydrogen Molecules*. Astrophys. J., 1971, **163**, 155.
[307] Millar, T., *Deuterium in interstellar clouds*. Astron. Geophys., 2005, **46**, 29-32.
[308] Roberts, H., E. Herbst, and T.J. Millar, *Enhanced deuterium fractionation in dense interstellar cores resulting from multiply deuterated H-3(+)*. Astrophys. J., 2003, **591**, L41-L44.
[309] Roberts, H., E. Herbst, and T.J. Millar, *The chemistry of multiply deuterated species in cold, dense interstellar cores*. Astron. Astrophys., 2004, **424**, 905-917.
[310] Watson, W.D., *Interstellar Molecule Reactions*. Rev. Mod. Phys., 1976, **48**, 513-552.
[311] Nagaoka, A., N. Watanabe, and A. Kouchi, *H-D substitution in interstellar solid methanol: A key route for D enrichment*. Astrophys. J., 2005, **624**, L29-L32.
[312] Nagaoka, A., N. Watanabe, and A. Kouchi, *Effective rate constants for the surface reaction between solid methanol and deuterium atoms at 10 K*. J. Phys. Chem. A, 2007, **111**, 3016-3028.
[313] Hidaka, H., M. Watanabe, A. Kouchi, and N. Watanabe, *Reaction Routes in the Co-H2co-D(N)-Ch3oh-D(M) System Clarified from H(D) Exposure of Solid Formaldehyde at Low Temperatures*. Astrophys. J., 2009, **702**, 291-300.
[314] Manico, G., G. Raguni, V. Pirronello, J.E. Roser, and G. Vidali, *Laboratory measurements of molecular hydrogen formation on amorphous water ice*. Astrophys. J., 2001, **548**, L253-L256.
[315] Hornekaer, L., A. Baurichter, V.V. Petrunin, D. Field, and A.C. Luntz, *Importance of surface morphology in interstellar H-2 formation*. Science, 2003, **302**, 1943-1946.
[316] Perets, H.B., O. Biham, G. Manico, V. Pirronello, J. Roser, S. Swords, and G. Vidali, *Molecular hydrogen formation on ice under interstellar conditions*. Astrophys. J., 2005, **627**, 850-860.
[317] Matar, E., E. Congiu, F. Dulieu, A. Momeni, and J.L. Lemaire, *Mobility of D atoms on porous amorphous water ice surfaces under interstellar conditions*. Astron. Astrophys., 2008, **492**, L17-L20.
[318] Watanabe, N., Y. Kimura, A. Kouchi, T. Chigai, T. Hama, and V. Pirronello, *Direct Measurements of Hydrogen Atom Diffusion and the Spin Temperature of Nascent H-2 Molecule on Amorphous Solid Water*. Astrophys. J. Lett., 2010, **714**, L233-L237.
[319] Hama, T., K. Kuwahata, N. Watanabe, A. Kouchi, Y. Kimura, T. Chigai, and V. Pirronello, *The Mechanism of Surface Diffusion of H and D Atoms on Amorphous Solid Water: Existence of Various Potential Sites*. Astrophys. J., 2012, **757**.
[320] Pirronello, V., G. Manico, J. Roser, and G. Vidali, *Dust chemistry in the laboratory*. Springer Proc. Phys, 2004, **91**, 525-532.
[321] Buch, V. and Q. Zhang, *Sticking Probability of H and D Atoms on Amorphous Ice - a Computational Study*. Astrophys. J., 1991, **379**, 647-652.
[322] Masuda, K., J. Takahashi, and T. Mukai, *Sticking probability and mobility of a hydrogen atom on icy mantle of dust grains*. Astron. Astrophys., 1998, **330**, 773-781.
[323] Al-Halabi, A. and E.F. Van Dishoeck, *Hydrogen adsorption and diffusion on amorphous solid water ice*. Mon. Not. R. Astron. Soc., 2007, **382**, 1648-1656.

[324] Hagen, W., A.G.G.M. Tielens, and J.M. Greenberg, *The Infrared-Spectra of Amorphous Solid Water and Ice Ic between 10-K and 140-K*. Chem. Phys., 1981, **56**, 367-379.
[325] Chakarov, D. and B. Kasemo, *Photoinduced crystallization of amorphous ice films on graphite*. Phys. Rev. Lett., 1998, **81**, 5181-5184.
[326] Malfait, K., C. Waelkens, L.B.F.M. Waters, B. Vandenbussche, E. Huygen, and M.S. de Graauw, *The spectrum of the young star HD 100546 observed with the Infrared Space Observatory*. Astron. Astrophys., 1998, **332**, L25-L28.
[327] Maldoni, M.M., M.P. Egan, R.G. Smith, G. Robinson, and C.M. Wright, *Crystalline water ice in OH32.8-0.3*. Mon. Not. R. Astron. Soc., 2003, **345**, 912-922.
[328] Karssemeijer, L.J., A. Pedersen, H. Jonsson, and H.M. Cuppen, *Long-timescale simulations of diffusion in molecular solids*. Phys. Chem. Chem. Phys., 2012, **14**, 10844-10852.